ON THE REACTIVITY OF NANOPARTICULATE ELEMENTAL SULFUR: EXPERIMENTATION AND FIELD OBSERVATIONS

Fotios Christos Kafantaris

Submitted to the faculty of the University Graduate School

in partial fulfillment of the requirements

for the degree

Doctor of Philosophy

in the Department of Earth Sciences,

Indiana University

December 2017

Accepted by the Graduate Faculty of Indiana University, in partial fulfillment of the requirements for the degree of Doctor of Philosophy.

Doctoral Committee

_____

Gregory K. Druschel, PhD, Chair

_____

Kevin Mandernack, PhD

_____

William P. Gilhooly III, PhD

_____

Gabriel Filippelli, PhD

_____

Steven E. Lacey, PhD

October 2, 2017

_____

Brandy M. Toner, PhD

DEDICATION

I would like to dedicate this work to three women. The first one is the Most Holy Theotokos and Ever-Virgin Mary, the most precious individual the human race has and will ever have, the Bridge from earth to Heaven and the Gate to Paradise. Through Her intercessions to the Holy Trinity I am still alive and safe.

The second woman is my mother, Eleni, who is the angel-on-earth that protects, nourishes, teaches, provides, inspires and guides me in life. Words would be poor to attempt to describe her and her virtues in an accurate manner. My mother is the main contributor of what I have become so far in life.

The third woman is my σύζυγος (spouse) Diana, who has given me life, as well as meaning for life. Diana is the main contributor of what I will hopefully do in life from this point onward, and through her help I will hopefully manage to be with the other two forever.

ACKNOWLEDGEMENTS

This work would not have been possible without the spiritual, psychological, financial and academic support of many people.

First and foremost, I thank the Holy, Co-substantial, Live-giving and Undivided Trinity for my existence and salvation, and for Her infinite and unconditional Love. I thank my parents Antonios-Pavlos and Eleni for being the reflectance of this unconditional love towards me and my family, and for always believing in me. My dad has always been a great-role model, a perfect example of optimism, motivation and hard work. My mother has been the perfect psychoanalyst and the person who would always make trouble go away with just one smile. Both of them make a perfect match and a superb model for couples and parents. I wish I become like them one day. Along with my parents, my grandfather, Fr.Theodoros, and grandmother, Chrysoula, have always been the continuity of my parents and a source of unconditional love. Without my parents and grandparents nothing would matter. Equal to my family, I thank the Most-Holy Theotokos, St. Nektarios, St. Nikolaos, St. Filothei, St. Anthony, St. Theodore the Warrior, Sts. Kostantine and Helen, St. Artemios, as well as Sts. Paisios, Porfyrios and Iakovos the newly proclaimed, as well as St. Luke of Krimea the Doctor. Glory be to God all of them are always with me wherever I go.

I thank my wife Diana for loving me so much above reason. She is the magnet that pulls me forward, the wind under my wings and the harissa in my lahmajoun. Thanks to my angelic kiddos, “Dino” Antoni and “Babyz” Eleni who teach me every day the meaning of life and along with “Mamacusat” help me discover and improve myself constantly. My dear mama-Sue is due special thanks due to her endless love and support, but mostly because of her patience and understanding, especially when things “sound Greek” to her. I love you dearly! I thank my sister Emilia-Anna for “μου 'βαλε τα γυαλιά” as an example of endurance, perseverance and motivation. She is a true descendant of those who said “ἢ τὰν ἢ ἐπὶ τᾶς”. I want to express infinite gratitude to my spiritual father, Fr. Dragan, and his family Vesna, Marija, Kristina, and Petar, as well as my best friends Fr. Marko and Biljana for welcoming me in Indy with open arms and being always there for me. Biljana

and Kara thank you for your patience at the cantor stand when I messed up the harmony for over 3 years continuously. Bosa and Dragan and the rest of St Nicholas Parish opened their arms to welcome me from the very first moment I entered the church. I thank my sister-in-law Amy, as well as Loren and Evangeline, for being in my life and for being supportive, patient, and having unconditional love for with me and my family. I thank Yanni and Suzanna for being my “grandparents-away-from-home” and being the first welcoming committee along with Fr. George Al-Dehneh, Mike Sifuentes, Roberto Velarde, and John Olgin when I first stepped foot on American soil in Texas. I don’t forget Fr. Georgios, Fr. Stavros, Dn. Dimitrios and all of the St Nicholas parish in London, as well as Fr. Athanasios, Fr. Timotheos, and Fr. Nabil for shadowing me with their prayers constantly. I thank my friends Dimitrios, Dimitrios and Katerina, Christos and Eleni for their true love towards me and my family and for their advice in life. Dr. Akin Akinwande has been a true and brotherly friend to me and my family on many occasions of our lives, and I thank him for that. Athanasios Godelitsas continued being a great support even after I graduated from his research group at the University of Athens. I thank him and his wife, Konstantina, for the late night Skype talks. In addition, I want to thank all past academic advisors since elementary school that contributed to the shaping of my personality and thought process. Some of those include Mr. Lazaros Maniakas, Mr. Kostas Pliasas, Mr. Pantelis, Mrs. Eleutheria, Mr. Rosakis, and many more. Fotios Fouskas is the academic brother that God sent to me so we can help and accompany each other on the track of science and life. Sue Epps was always there for me and my family full of energy and support. Finally, I want to thank my father-in-law Steve Dugger, my family members Niko, Maria, Vasili, Thodori, Panayoti, Roula, Gianni, as well as my academic family Theresa (Dits) Groth, Samapriya Roy, Nicole Bader, Clinton Broach, Shiva (Ladan) Ahrens, Mick Thomas, Beth Welke, Deborah Nichols, Amy Smith, Reina Hiramatsu, Renata Lafler, Igor Ogashawara, Christa Phelps, Melanie Perello, Kudzai Kaseke, James Harris, Nicolas Clercin, and Giorgos Bakoyannis for their constant love and support throughout the graduate school. Last but not least, I am thankful to Fr. Nikon of New Schete (Mount Athos), +Fr. Athanasios Mitilinaios, as well as Fr. Nikolaos Loudovikos, for accompanying me during long days and nights in the lab while I was listening to their lectures and sermons via youtube.

I want to express my gratitude to Prof. David Borrok, my first PhD advisor while I was still in UTEP, for taking another job in University of Louisiana and supporting my transition to Prof. Greg Druschel's lab at IUPUI where I finished the current dissertation. Apart from causing for me to dive in the world of sulfur, David unknowingly contributed for me to meet with my wife Diana.

This work was possible thanks to the research grants EAR1304352, EAR1261423, and OCE 1261424, given to Greg Druschel by NSF. Also special thanks are due to IUPUI graduate office for a travel fellowship given in 2016.

Within the framework of this work I have been graced to collaborate, interact and exchange ideas with a plethora of great scientists of all levels. With the fear of forgetting someone, I wish to thank Eric Boyd from MSU, Kirk Nordstrom, Blaine McCleskey, and Kate Campbell from USGS, as well as Axel Muller who made an expedition to Yellowstone a fun ride in the wilderness. I thank EJ Crane (Pomona College) for his academic advice, friendly discussions and the time he spent with me while he was visiting IUPUI for a year-long sabbatical. Special thanks are due to Philip Schmitt-Kopplin (Helmholtz Zentrum München) for his great hospitality while visiting his research group, in addition to Sabine Dvorski who shared with me her knowledge on sulfur organic chemistry. The most impressive experience was my immersion into the world of synchrotron chemistry at the facilities of Canadian Light Source thanks to Brandy Toner and Yongfeng Hu. My experience at Yongfeng's beamline was made much more productive due to his help as well as the help of Qunfeng Xiao and Aimee Maclennan. I would like to thank Brandy Toner and Brandi Kamermans for their great hospitality at University of Minnesota, and for their sharing of knowledge on XANES spectroscopy. Special thanks are due to Alexandra Walczak and Jennifer Houghton for the fruitful discussions on sulfur science as well as career development. David Fike has been a collaborator of my advisor's that I have met almost immediately when I started the doctorate program. David is a hospitable, generous, kind and inspiring person and I thank him for being in my academic life. I also feel very grateful for having met and worked with Don Nuzzio. Don is an inspiring person and knows how to calm you down when electrodes don't work. I want to thank Martin Kurek, John Shukle and Chase Howard for their

tremendous support in the lab and for their encouragement over the last months of my grad school. I want to thank Kevin Mandernack for the long academic and philosophical discussions and for the constant support. Special thanks to Bill Gilhooly, and Gabe Filippelli for being supportive and resourceful along the way of my career in IUPUI. Also I want to thank Steve Lacey for endorsing me in the world of Environmental Health Science. Special thanks are also due to Catherine Macris for her faith in me and her psychological support during the last two years of the program. Additionally, I thank Jake Mosely for his friendship and the fruitful discussions that ranged within the ternary diagram "Mineralogy-Demis Roussos-Ouzo effect".

Last but most importantly I want to thank my "academic father" Greg Druschel. Greg was always there for me, making sure he is an infinite source of intellectual resources whenever I needed them. Greg guided me through my PhD by letting me have self-discovery, without any micro-management, but at the same time he did not let me get lost and miss my target. In a phrase I can call him a "perfect buffer". He has been next to me, supporting me and my family, not only within the framework of this project – in which he made sure I have financial, academic and psychological support – but also in life experiences and trials, where he proved himself as an excellent advisor and friend. I thank him for all the sacrifice he offered in order to make this dissertation a reality, and I wish to him all the best.

“Я любил мученичество, которое так странно очищает душу”

“I loved martyrdom, which so strangely cleanses the soul”

St. Luke the Doctor and Archbishop of Crimea (1877-1961)

“...θεὸς δὲ ἀνθρώπῳ οὐ μείγνυται...”

“...God with man does not mingle...”

Plato, Symposium: 3 203A

Fotios Christos Kafantaris

ON THE REACTIVITY OF NANOPARTICULATE ELEMENTAL SULFUR: EXPERIMENTATION AND FIELD OBSERVATIONS

The reaction between elemental sulfur and sulfide is a lynchpin in the biotic and abiotic cycling of sulfur. This dissertation is focused on the reactivity of elemental sulfur nanoparticles ($S_{8weimarn}$, S_{8raffo}) among other forms of elemental sulfur (S_{8aq}, $S_{8aq\text{-}surfactant}$, α-S_8), and how the variation of their surface area, character and coatings reflect on the analytical, physical-chemical and geochemical processes involving sulfur cycling. A comprehensive electrochemical investigation utilizing mercury-surface electrodes showed that elemental sulfur compounds are represented by three main voltammetric signals, corresponding to potentials at -1.2V, -0.8V, and -0.6V in the absence of organics at circumneutral pH. Dissolved $S_{8aq\text{-}surfactant}$ signals can be found from -0.3V up to -1.0V, depending on the surfactant in the system. Variations in current response resulted from differences in electron transfer efficiency among the forms of S_8, due to their molecular structural variability. Based on this observation a new reaction pathway between S_8 and Hg-surface electrodes is proposed, involving an amalgam-forming intermediate step. The kinetics of the nucleophilic dissolution of S_{8nano} by sulfide, forming polysulfides, were investigated under varying surface area, surface character and presence or absence of surfactant coatings on S_{8nano}. Hydrophobic $S_{8weimarn}$ and hydrophilic S_{8raffo} show kinetic rate laws of $r_{S8weimarn} = 10^{-11.33}\left(e^{\frac{-700.65}{RT}}\right)$ (Molar(S_8)/second/dm^{-1}) and $r_{S8raffo} = 10^{-4.11}\, i^{-0.35}\left(e^{\frac{-615.77}{RT}}\right)$ (Molar(S_8)/second), respectively. The presence of surfactant molecules can influence the reaction pathways by dissolving S_{8nano} and releasing $S_{8aq\text{-}surfactant}$, evolving the rate-limiting step as a function of the degree of the solubilization of S_{8nano}. The reaction rate of $S_{8biological}$ can be compared with those of S_{8raffo} and $S_{8weimarn}$ in circumneutral pH values and T=50^{o}C, making the forms of S_{8nano} successful abiotic analogue models of microbially produced $S_{8biological}$. Field observations and geochemical kinetic modeling in the geothermal features of Yellowstone indicate that the nucleophilic dissolution reaction appears to be a key abiotic pathway for the cycling of sulfur

species and the enhancement of elemental sulfur bioavailability. Furthermore, in situ and ex situ voltammetry in the same geothermal waters disclosed chaotic variability in chemical gradients of sulfide (observed over small temporal and spatial scales) which can be considered as an ecological stressor capable of influencing single cell physiology and microbial community adaptation.

Gregory K. Druschel, PhD, Chair

TABLE OF CONTENTS

LIST OF TABLES

LIST OF FIGURES

LIST OF ABBREVIATIONS

CV	cyclic voltammetry
HDME	hanging-drop mercury electrode
BSDS	sodium dodecyl benzene sulphonate
SDS	sodium dodecyl sulfate
TX-100	polyethylene glycol octylphenyl ether
CTAB	hexadecyltrimethylammonium bromide

CHAPTER-1 – INTRODUCTION

Sulfur – Etymology, history and early uses

Mankind recognizes sulfur as a material since antiquity. Long before its discovery as an element, by Antoine-Laurent de Lavoisier in 1777, sulfur is mentioned in the Holy Bible, the Greek as well as the Latin literature. The oldest mention of a word with the same root as of "sulfur" is made by the Latin poet Ennius (239 to 169 BC). Ennius mentions the word "**sulpureus**" in his poem describing the sulfur-rich waters of the river Nar [river Nera in present day] in central Italy (Michie and Langslow, 1988). However, the etymology of the word "sulfur" is not fully understood. Even if the above mention is the oldest for the Latin language, there are possible linkages of sulfur with the Sanskritic language through the word "**sulvere**" (Ball, 1985). "**Brimstone**" was a synonym to sulfur in the West, originated from the Old English "bryne" (=burning) and "stān" (=stone). In the ancient Greek language sulfur translates to "**θεῖον**" or "**θέειον**", which means smoke (Hofmann, 1974). Its root is "θFεσ(ε)ιον[1]" (meaning "the substance that smokes") and is associated with the verb "θύω", which means "to offer sacrifice via incensing or burning" (Hofmann, 1974). The Greek translation of both the words "brimstone" and "sulfur" is "θεῖον/θέειον", and this is apparent in the Greek text of the Holy Bible:

> "καὶ Κύριος ἔβρεξεν ἐπὶ Σόδομα καὶ Γόμορρα **θεῖον**,
> καὶ πῦρ παρὰ Κυρίου ἐξ οὐρανοῦ." (Γεν. 19:24),

which translates to:

> "Then the Lord rained upon Sodom and upon Gomorrah **brimstone**,
> and fire from the Lord out of Heaven." (Gen 19:24).

[1] The letter "F" found in the word "θFεσ(ε)ιον" is called digamma (δίγαμμα) and is the sixth letter of the archaic version of the Greek alphabet, being placed between the letters Εε (epsilon) and Ζζ (zeta). Digamma was muted out of the Greek alphabet gradually until its permanent exclusion from the Greek alphabet at 403BC, however its traces are being preserved in the Greek language. Jannaris, A. (1907) The Digamma, Koppa, and Sampi as Numerals in Greek. The Classical Quarterly 1, 37-40, Parry, M. (1934) The Traces of the Digamma in Ionic and Lesbian Greek. Language 10, 130-144, Smyth, H.W. (1891) On Digamma in Post-Homeric Ionic. The American Journal of Philology 12, 211-220.

The total number of citations of sulfur in the Holy Bible is sixteen. Most of them describe a setting where brimstone [sulfur] is burning or is combined with fire (Deut 29:22; 3Mac 2:5; Ps 10:6; Isa 30:33; 34:9; Eze 38:22; Luke 17:29; Rev 9:17-18; 14-10; 19:20; 20:10; 21:8), while one citation uses the word to describe the sulfur-yellow color (Rev 9:17). Similar context in which the word sulfur is used (combined with fire) is found in ancient Greek literature. Homer mentions in Odyssey (Book 22, verses 480-484)(Cauer, 1905):

> ".....αὐτὰρ ὅ γε προσέειπε φίλην τροφὸν Εὐρύκλειαν:
> «οἶσε **θέειον**, γρηΰ, κακῶν ἄκος, οἶσε δέ μοι πῦρ,
> ὄφρα **θεειώσω** μέγαρον…» ....."

which translates to:

> "...and he [Odysseus] spoke to Eurycleia, the trustworthy nurse:
> «Bring me **sulfur** here, eldress, which cleanses the evil,
> and bring fire, that I can **sulfurize [cleanse]** the room around…»..."

The above citations as well as the etymology of sulfur both in the Western ("brimstone") and the Eastern ("θεῖον") languages show that "cleansing" (physical-chemical-biological) properties of sulfur were known, even if not fully understood. The heating up of elemental sulfur causes it to melt into a blood-red liquid, while blue flame is produced. The combustion of elemental sulfur in the presence of oxygen produces sulfur dioxide (Müller, 2000):

$$S + O_2 \rightarrow SO_2,\ \Delta H = -297\ \text{kJ/mol} \qquad \text{(reaction 1)}$$

This exothermic reaction (1) releases more heat and can increase burning temperatures to greater than 1000^{o}C (Müller, 2000).

Gaseous sulfur dioxide is responsible for adverse health effects to both animals and humans (Pohl, 1998). The enhanced solubility of SO_2 results in its rapid absorption in the upper respiratory system. Hydrolysis of sulfur dioxide results in the formation of bisulfite

(HSO_3^-) and sulfite (SO_3^{2-}) at a ratio of 5:1, with subsequent passage to the bloodstream and distribution to the rest of the body. The nucleophilic character of bisulfite results in its reaction with biomolecules in the upper respiratory system and the causation of bronchoconstriction effects (Pohl, 1998). Detoxification of sulfite takes place in the liver by the activity of sulfite oxidase enzymes which form sulfates that can be excreted by the urine (Pohl, 1998). Lethal doses for rats (NS strain) have been reported during continuous exposure at 590ppm SO_2, with 8 out of 8 rats participating in the experiment dying at an average of 31 hours of exposure (Pohl, 1998). Another study reported the death of half the population of Swiss Albino mice after a 30min exposure at 3000ppm SO_2 (Pohl, 1998). Systemic clinical attributes due to exposure of humans to SO_2 include airway resistance, wheezing, chest tightness and dyspnea (difficulty to breathe) during exposure of 0.5ppm SO_2 for 3 minutes (Pohl, 1998). Human tracheal and bronchial cell necrosis occurred during exposure of humans to 800ppm SO_2 for 8 hours (Pohl, 1998). Furthermore, the fumigation practices by burning sulfur would keep away insects and rodents, such as mice, roaches, ticks, fleas and lice. Pliny the Elder (60 AD) discloses the important application of sulfur as a fumigant and insecticide by describing it as “pest-averting” (Gunther, 1966). Hence, this application of sulfur would be of vital importance for ancient people who had limited resources for cleaning and disinfecting their houses and personal belongings.

Apart from the applications of sulfur as a fumigant for the purposes of Public Health, it was vastly known in the medical community of Antiquity. Hippocrates of Cos (460 – 370 BC) utilizes sulfur in a mixture with other herbs or asphalt for the treatment of gynecological conditions related to the uterus, via fumigation or topical administration (Hippocrates, Nature of Women, 26, 30, 34; Barrenness, 23)(Potter, 1995). He also prescribes oral administration of sulfur-infused wine for the treatment of breathlessness (Hippocrates, Nature of Women, 68)(Potter, 1995). The external application of sulfur on the skin as a mixture with other (mineral or herbal) compounds was also prescribed by Hippocrates for the treatment of skin diseases (Hippocrates, Ulcers, 16)(Jones et al., 1995). This utilization of sulfur is based on its keratolytic, antibacterial and antifungal properties (Sgantzos et al., 2015). The skin disorders that are treated to day by sulfur administration include acne, seborrheic dermatitis, tinea versicolor, scabies, rosacea (Lin et al., 1988). External application of sulfur on the skin causes hyperkeratosis, acanthosis and dilation of

the dermal vasculature (Lin et al., 1988). More specifically, the reaction of sulfur with cysteine according to the reaction 2:

$$2\ \text{cysteine} + S_8 \rightarrow \text{cystine} + H_2S \qquad \text{(reaction 2)}$$

which would result in the formation of cystine and the consequent progression of normal keratinization of the skin system, as long as the dosage of elemental sulfur would be limited. In higher doses, the excessive hydrogen sulfide would break down keratin and cause irritation (keratolytic effect) (Lin et al., 1988).

During the 10th century Chinese scholars discovered the explosive properties of gunpowder, which was used initially in fireworks, but a few centuries later it was applied to military and mining applications (Britannica, 2017). Sulfur played a significant role in the formation of gunpowder, as it is one of its three components, along with saltpeter (or else Potassium Nitrate, KNO_3), and charcoal (Partington, 1960). The presence of oxygen in the $–NO_3$ group would void the necessity of molecular oxygen for the combustion reaction, therefore acting as an oxidant to sulfur and carbon. Carbon can combust by reacting with KNO_3, forming carbon dioxide (CO_2). The importance of sulfur aligns with its combustion by KNO_3 at lower temperatures resulting in the formation of SO_2 and the release of heat. The exergonic combustion of elemental sulfur will consequently induce the combustion of more carbon and sulfur, enhancing the kinetics of gas (CO_2 and SO_2) formation and heat release. Induction of a series of electron exchange reactions that generate heat and gases in a rapid manner is the origin of the actual explosion (Russell, 2009).

Present day applications of sulfur

Sulfur continues to contribute to numerous applications up to the modern day, which are related with the scientific, technological and industrial settings. Industrial applications of sulfur comprise a fundamental role in metallurgy (Habashi, 2009), construction materials (Vlahovic et al., 2011), catalysis (Lan et al., 2005), chemical engineering for the production of sulfuric acid (Ashar and Golwalkar, 2013), or water

purification practices (Soares, 2002). Recent developments in the manufacturing of advanced chemical compounds have been based on elemental sulfur chemistry that has assisted with advancements in battery technology (Simmonds et al., 2014; Zhang et al., 2012), optics (Griebel et al., 2014), and material science (Li et al., 2015; Lim et al., 2015). Last but not least, elemental sulfur has been used in agriculture both as a nutrient (Germida and Janzen, 1993) and a pesticide (Williams and Cooper, 2004). A few examples of elemental sulfur applications are discussed below.

Applications of sulfur in advanced materials

Elemental sulfur is utilized in the manufacturing of batteries, such of Li-SO_2 and Na-S battery systems. The Li-CO2 battery shows significant advantages compared to other conventional batteries (i.e. Zn-C battery) with higher cost needed for its production (Nehb and Vydra, 2006). The Na-S battery system is very promising in terms of its high electrical capacity and low weight efficiency which makes it a strong candidate for application in electric cars (Nehb and Vydra, 2006). Research and development in battery science continues to involve the utilization of elemental sulfur under various forms and conditions. Zhang et al. (2012) have achieved the formation of an advanced material to serve as a cathode in Li-S batteries, which is a nanocomposite comprised of sulfur being encapsulated within two hollow carbon spheres. The high surface area and pore space results in excellent electrochemical performance of the material (Zhang et al., 2012). Carbon coating of Li_2S_{nano} can also become utilized as a cathode in Li-S battery technology (Lim et al., 2015). Other advanced materials incorporating elemental sulfur include the sulfur-rich copolymers “poly(S-r-DIB)” which are also used as cathode materials for the Li-S battery apparatus (Simmonds et al., 2014). These materials contributed to enhanced charge capacity of rechargeable Li-S batteries (Simmonds et al., 2014).

Formation of polymeric molecules of elemental sulfur is achieved via inverse vulcanization (Griebel et al., 2016). Near-infrared optics utilize a sulfur rich copolymer with 50-80% w/w S content and a high refractive index (n ~1.8), capable for achieving thermal imaging (Griebel et al., 2014). Multicomponent polymerizations (MCPs) involving

elemental sulfur and aliphatic diamines have been executed for the synthesis of advanced material characterized of high refractive index and high luminescence, promoting their efficient and economic synthesis in addition to their valuable optoelectronic properties (Li et al., 2015). Catalysis of Au^{1+} reduction to Au^0 by the presence of elemental sulfur is shown to result in Au nanoparticle formation (Chung et al., 2011). The zero-valent Au^0 will bind with sulfur that acts as a ligand to form Au nanoparticles (Au_{nano}) or S-Au_{nano}-nanocomposites (Chung et al., 2011). Lithium-S nanoparticles could also be produced by the reduction of sulfur to sulfide and the formation of Li_2S_{nano}; when coated with carbon these can be applied to Li-S battery technology (see above)(Lim et al., 2015).

Agricultural applications of sulfur

Sulfur is the 4th major nutrient for plants (Jamal et al., 2010; Rasheed et al., 2004), hence its presence is of vital importance to successful agricultural practices. Addition of elemental sulfur or sulfur-containing fertilizers in soils is a major practice to counteract soils deficient in sulfur. Microbial sulfur oxidation produces sulfate by autotrophic or heterotrophic metabolisms, which can be incorporated by the plants due to its high bioavailability (Germida and Janzen, 1993). The efficiency of this process is influenced by various physical-chemical factors of the soil as well as the particle size of sulfur, controlling the oxidation rates of S and the consequent release of bioavailable sulfate (Boswell and Friesen, 1993; Germida and Janzen, 1993; Nor and Tabatabai, 1977). Biologically-produced sulfur is also important as a fertilizer due to its naturally occurring small particle size and its hydrophilic surface character (Kleinjan et al., 2003).

Elemental sulfur has been used as a pesticide since Antiquity (see above) and is still used for the same purpose (Nehb and Vydra, 2006). Apart from man-made administration, in some cases elemental sulfur is produced naturally by plants in order to counteract fungal attack (Cooper and Williams, 2004). The fungi-toxicity of elemental sulfur has not been fully understood, however the most possible mechanism involves the intracellular incorporation of elemental sulfur into the fungal cells, the consequent disturbance of the

mitochondrial respiratory chain and the possible linkage of the element with protons to form toxic di-hydrogen sulfide (Williams and Cooper, 2004).

Sulfur chemistry

Sulfur is a metalloid with atomic number 16 and atomic weight 32.065, that shows a valence state across 8 e^- transformations from S(-II) up to S(+VI). This large valence span allows it to participate in an array of oxidation, reduction and disproportionation reactions, both abiotic and linked to microbial metabolism (Figure 1-1). Key inorganic species of sulfur include: sulfide (HS^-), polysulfides (S_n^{2-}), elemental sulfur (S_8), thiosulfate ($S_2O_3^{2-}$), sulfite (SO_3^{2-}), polythionates ($S_nO_6^{2-}$) and sulfate (SO_4^{2-}). Intermediate species of sulfur form through numerous reaction pathways, often showing enhanced reactivity that contributes to the element's cycling in nature and its interaction with other element systems (Figure 1-1). Some of these reactions involve the polymerization of dissolved sulfur to homocyclic octasulfur rings (S_{8aq}), via formation of S-S bonding. $S_{8(aq)}$ then undergoes coarsening processes to form solid forms of sulfur (see below), causing the variety of solid forms of elemental sulfur, including nanoparticles (S_{8nano}). The interaction of sulfur with other elements' cycles, such as Fe and C, enhances the reaction pathways active in natural systems. The interactions of sulfur species with iron include the sulfide and polysulfide pathways of pyritization processes when these species react with iron sulfide phases (Rickard and Luther, 2007)(Figure 1-1; upper part). Furthermore, high and low sulfur-to-carbon ratio during the interaction of most sulfur species (apart from sulfate) with natural organic matter will lead either to sulfurization or electron-exchange reactions, respectively (Amrani, 2014; Heitmann and Blodau, 2006)(Figure 1-1; lower part).

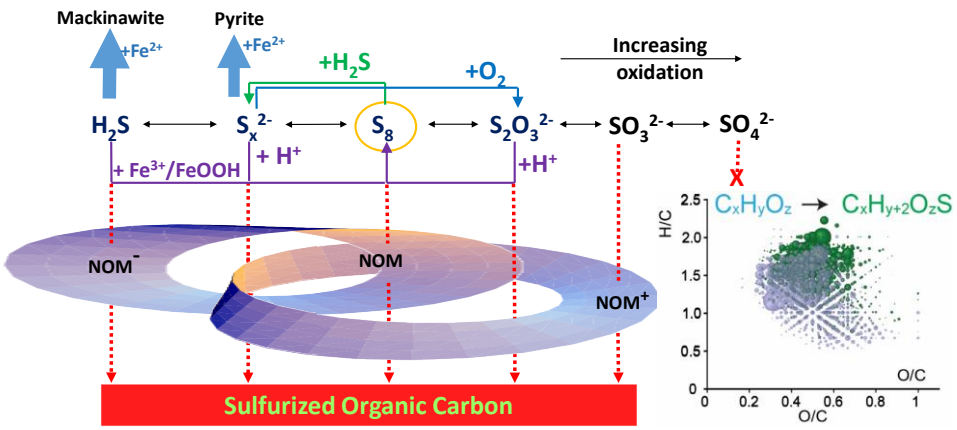

Figure 1-1: Sulfur redox reaction pathways in natural systems and their linkage to C and Fe cycles. The $8e^-$ span of the sulfur system is expressed via a plethora of oxidation, reduction and disproportionation reactions that transform sulfur from S(-2) to S(+6). The interaction of S with Fe cycles is expressed via many reactions, including the sulfide and polysulfides pathways of pyritization. The interaction of S and C cycles is expressed via the sulfurization of organic matter which results in the evolution of the chemistry of both sulfur and carbon species.

Microbial S_8^0 cycling: production and consumption

Elemental sulfur can be produced during microbial sulfide oxidation by anoxygenic phototrophs or anaerobic chemolithoautotrophs (Habicht et al., 1998; Kelly, 1989; Truper and Fischer, 1982; van den Ende and van Gemerden, 1993). Examples include members of the purple and green sulfur bacteria (Dahl and Friedrich, 2008; Wilbanks et al., 2014) as well as *Thiomargarita namibiensis* (Schulz and Schulz, 2005). *T. namibiensis* stores intracellular elemental sulfur, which is further oxidized to sulfate when the environment is sulfide-deprived (Schulz and Schulz, 2005). Wilbanks et al. (2014) discussed the metabolism of anoxygenic phototrophic Gammaproteobacteria (purple S bacteria), which consumed locally produced sulfide, oxidizing it to sulfate while maintaining intracellular stores of elemental sulfur. Dissimilatory sulfate reducers surviving in the same environment were producing the sulfide (Wilbanks et al., 2014). Elemental sulfur is also a

product of the reduction of sulfur oxyanions and sulfate (Lee et al., 2007; Milucka et al., 2012). Microbial metabolism increases the rate of this biological sulfide oxidation up to 4 orders of magnitude (Luther III et al., 2011). Biological elemental sulfur can precipitate and agglomerate as globules either intracellularly or extracellularly (Dahl and Prange, 2006; Kleinjan et al., 2003), and can be present within outer membrane vesicles (Gorlas et al., 2015). Other families of microbes that produce elemental sulfur include the *Thiobacilli* and the *Acidithiobacilli* (Kleinjan et al., 2003).

Elemental sulfur is consumed by autolithotrophic (both phototrophic and chemotrophic) and organoheterotrophic bacteria (Kleinjan et al., 2003). Examples of microbial species utilizing elemental sulfur include *Allochromatium vinosum* (purple sulfur bacteria)(Franz et al., 2007), *Sulfolobus acidocaldarius* (Shivvers and Brock, 1973), and *Thiobacillus ferrooxidans* (Konishi et al., 1994), among others. Elemental sulfur is oxidized to sulfite by *Thiobacillus thiooxidans* (Suzuki et al., 1992). The microbial species *Desulfovibrio desulfuricans, Desulfomicrobium baculatum,* and *Desulfobacterium autotrophicum* were considered to traditionally reduce sulfate. However the work of Lovley and Phillips (1994) showed that these species are also able to oxidize elemental sulfur to sulfate in presence of Mn^{4+} oxides (Lovley and Phillips, 1994).

Dissimilatory sulfur reduction is associated with thermophilic (Boyd et al., 2007) and anaerobic microbes (Moser and Nealson, 1996). Reduction of elemental sulfur takes place by the Archaea *Pyrococcus furiosus* (Blumentals et al., 1990), by the Crenarchaea *Caldisphaera draconis sp. Nov.* and *Acidilobus sulfurireducens sp. Nov.* (Boyd et al., 2007), which are all associated with high temperature environments. Zavarzina et al., 2000 report the reduction of elemental sulfur to sulfide by the thermophilic anaerobe *Thermanaerovibrio velox sp. nov*., whereas Moser and Nealson (1996) refer to the reduction of S^0 by *Shewanella putrefaciens*, a mesophile with facultative anaerobic metabolism (Moser and Nealson, 1996; Zavarzina et al., 2000).

Disproportionation of elemental sulfur to sulfate and sulfide is possible metabolically by species such as *Desulfocapsa thiozymogenes*, *Desulfocapsa sulfoexigens*, and *Desulfobulbus propionicus* (Canfield et al., 1998; Lovley and Phillips, 1994). *Desulfovibrio desulfuricans* – nominally a sulfate reducer – is able to disproportionate

thiosulfate to elemental sulfur and sulfite, which consequently undergo a second disproportionation cycle to sulfide and sulfate (Cypionka et al., 1998). *Desulfocapsa sulfoexigens sp. nov.* is a chemolithoautotrophic bacterium that also disproportionates elemental sulfur (in addition to thiosulfate and sulfite), while it is the first microbial species found to be able to survive exclusively by disproportionating other intermediates S^0, $S_2O_3^{2-}$, or SO_3^{2-} (Finster et al., 1998).

Elemental sulfur as a key species in the biogeochemical cycle of S

Elemental sulfur species contribute significantly to the biogeochemical cycling of sulfur over a vast array of terrestrial and extraterrestrial environments, during modern or ancient processes. In particular, redox reactions between the elemental form of sulfur and the rest of its species are prevalent in many systems containing sulfur, metals, and organics, influencing the transformation and distribution of their species (Aizenshtat et al., 1995; Böttcher et al., 2001; Boulègue and Michard, 1978; Druschel et al., 2004; Druschel et al., 2003; Kamyshny et al., 2004; Kamyshny et al., 2007; Luther III et al., 2003; Luther III et al., 2001; Slowey and Brown, 2007; Suzuki, 1999).

Seawater and porewaters of marine or lacustrine sediments incorporate elemental sulfur which participates in redox reactions abiotically or of microbial pathways. Wang et al. (1998) identified dissolved elemental sulfur (S_{8aq}) in pore waters of lake sediments using voltammetric techniques, while Ciglenečki et al., (1996) detected elemental sulfur in the water column of a euxinic (anoxic holomictic to meromictic) marine lake using similar techniques (Ciglenečki et al., 1996; Ciglenečki et al., 2017; Wang et al., 1998). Smith and Klug (1981) showed the contribution of sulfur species (including sulfate and elemental sulfur) in the pore waters and water column of a eutrophic lake. The microbial sulfur reduction rates were at 8.8μmol of S^0 per liter of sediment per day, contributing to the mineralization of organic carbon (Smith and Klug, 1981). Metabolic activities of cyanobacteria in a tropical salt lake resulted to the formation of elemental sulfur by sulfide oxidation during anoxygenic photosynthesis during the absence of oxygen (Jorgensen et al., 1979). Bura-Nakić et al., (2009) described the interactions between S and Fe cycling in

the anoxic waters of the monimolimnion layer of Lake Pavin. The increased concentrations of elemental sulfur result from the oxidation of sulfide by Fe^{3+} oxy-hydroxides resulting in the formation of S^0 (Bura-Nakić et al., 2009).

Ciglenečki and Ćosović (1996) mention an "unidentified" voltammetric peak at -0.6V when measuring seawater samples from the Andriatic Sea. Even though they were not able to identify and characterize the species resulting in this peak, it is not impossible that it belongs in one of the forms of elemental sulfur (see Chapter 2)(Ciglenečki and Ćosović, 1996). Glazer et al. (2006) discussed the redox profile of the suboxic zone of the Black Sea. They indicated the correlation of the increase of molecular oxygen and elemental sulfur with the presence of particulate Mn, explaining that Mn^{2+} was oxidized by O_2 and precipitated as Mn-oxides, which subsequently oxidized H_2S to polysulfide and elemental sulfur (Glazer et al., 2006). Luther et al. (1991) also reported concentrations of elemental sulfur in the Black Sea, among other sulfur species. The elemental sulfur amounts were detected below 90m, with a maximum at 120m reaching 60nM S^0, which was one order of magnitude lower than concentrations in other marine systems (Luther et al., 1991).

Elemental sulfur shows the highest relative abundance in coastal marine sediments among the sulfur intermediates (sulfite, thiosulfate, polythionates)(Zopfi et al., 2004). The peak concentration of S(0) is found in the bioturbation zone and the sediment water interface for the oxic and anoxic sediment zones, respectively (Zopfi et al., 2004). Holmer and Storkholm (2001) discuss the factors influencing the accumulation of reduced sulfur species in the sediments of lake systems, which include microbial sulfate reduction and sulfur re-oxidation (Holmer and Storkholm, 2001). Elemental sulfur is an important intermediate in the cycling of S in the sediments of lakes, whose accumulation is controlled by the oxidation of sulfides via abiotic or microbial pathways, associated with the Fe and Mn cycles (Holmer and Storkholm, 2001). The highest amounts of elemental sulfur are associated with the suboxic zone of lake sediments (Holmer and Storkholm, 2001).

Recent studies in glacier systems in the Canadian Arctic have detected concentrations of orthorhombic forms of elemental sulfur (α-S_8) as well as the rare monoclinic forms of β-S_8 and γ-S_8 (Lau et al., 2017). The sulfur allotropes of S_8 are sourced

by sulfidic supraglacial springs, where sulfide ascends and oxidizes to elemental sulfur (Lau et al., 2017), with sulfide oxidizing bacteria contributing to the precipitation of elemental sulfur (Gleeson et al., 2011; Grasby et al., 2003). In addition to elemental sulfur, gypsum and calcite are precipitated on the top of glacial ice (Gleeson et al., 2011). In the case of the β-S_8 and γ-S_8, they were found in association with organic matter (Lau et al., 2017). Sulfur cycling with elemental sulfur as an important intermediate also occurs in Soda Lakes (Poser et al., 2013). Microbial disproportionation of elemental sulfur to sulfide and sulfate takes place by haloalkaliphilic bacteria in soda lakes (Poser et al., 2013). They mention the bacterium *Dethiobacter alkaliphilus* was reported as the first member of the class Clostridia to be a sulfur disproportionator (Poser et al., 2013).

Geothermal environments also display biogeochemical S cycling that involves elemental sulfur (Boyd and Druschel, 2013; Nordstrom et al., 2009; Ward et al., 2017; Xu et al., 1998, 2000). Sulfur is contained in magmas in the form of hydrogen sulfide and sulfur dioxide. The degassing of magmatic material enriches the water bodies of hydrothermal systems such as Yellowstone with H_2S_{aq} which consequently oxidizes abiotically to elemental sulfur (Schoen and Rye, 1970). Microbial activities further oxidize elemental sulfur to sulfate (Schoen and Rye, 1970).

Elemental sulfur is contained in carbonaceous meteorites, such as the Orgueil meteorite, and is believed to have associations with organic compounds incorporated in extraterrestrial samples (Nagy and Bitz, 1963; Teresa Joseph Murphy and Nagy, 1966). Association of elemental sulfur with mineral surfaces on a similar type of meteorite has also been mentioned (Kaplan and Hulston, 1966). Sulfur isotope analyses have indicated the presence of elemental sulfur in planets since their early stages of formation during the differentiation of the solar system (Antonelli et al., 2014). Observations of Mercury, the smallest and innermost planet of our solar system, show accumulation of elemental sulfur in the north and south poles (Sprague et al., 1995). Iron sulfide accumulations enriched with reduced sulfur species exist in a regolith covering Mercury (Sprague et al., 1995). Io – Jupiter's satellite – is also carrying elemental sulfur on its surface in a mineralogical conformation that is different from cyclo-octasulfur (Nelson et al., 1990). Carlson et al. (2002) mention that elemental sulfur in the form of cyclo-octasulfur or zero-valent sulfur

chains (S_n) possibly exist on the surface of Europa, resulting in the formation of sulfuric acid through radiolysis (Carlson et al., 2002).

DeWitt et al. (2010) discuss the formation of elemental sulfur and organically bound sulfur in gaseous conditions resembling the atmosphere of Early Earth. Photolysis of a mixture of high S/C ratio results in formation of S_8, while the opposite results in the formation of organosulfur (DeWitt et al., 2010). Preservation of cyclo-octasulfur rings in the atmosphere of the Early Earth is believed to have played a beneficial role to the survival and evolution of life (Kasting et al., 1989). Due to the element's strong UV absorbance, elemental sulfur would provide an atmospheric radiation screen for the Earth's surface (Kasting et al., 1989). Elemental sulfur-based microbial metabolisms (on Earth's surface) are also believed to represent a possible metabolic pathway that would potentially support early microbial life in highly UV-exposed extraterrestrial environments (Schulze-Makuch et al., 2004).

Kerogen and bitumen incorporate zero-valent sulfur speciation in their sulfurized organic compounds, with the kerogen being more enriched in S^0 than bitumen (Pomerantz et al., 2014). Crude oil also contains sulfur in the zero-valent state (Al-Zahrani et al., 2015). Microstructures rich in S and C, with elemental sulfur being encapsulated by organic carbon and structured in linear or spherical patterns are able to be formed in the absence of biological activity (Cosmidis and Templeton, 2016). Their similarity to microbial intra- or extracellular sulfur-carbon precipitates makes them critical artifacts for the avoiding of misinterpretations of biogenic signatures in the rock record (Cosmidis and Templeton, 2016).

Nucleophilic dissolution reaction

Chemical systems in which sulfide and elemental sulfur are present simultaneously, result to the nucleophilic dissolution reaction (reaction 7) that produces polysulfide intermediates. Polysulfides are chainlike molecules that incorporate both zero-valent and sulfidic sulfur (1-), with the zero-valent sulfur atoms being in the interior of the chain and ending at two sulfidic atoms, one per each end of the chain. Polysulfides have a general formula of S_n^{2-}, with x ranging from 2 up to 8 in natural systems (Kamyshny et al., 2004).

$$HS^- + \frac{n-1}{8} S_8 \longleftrightarrow S_n^{2-} + H^+ \qquad \text{(reaction 7)}$$

Reaction 7 is a key component for the biogeochemical cycling of the sulfur system, representing a linchpin reaction that (re)cycles the reduced sulfur species – sulfide, elemental sulfur and polysulfides – causing the creation of the third species when the other two are present in any anoxic environment. This cycling is believed to contribute to the enhancing of the bioavailability of elemental sulfur by microbial cells via formation of polysulfides (forward) or cyclo-octasulfur (reverse reaction), both able to diffuse through the cell membrane (see discussion below). Furthermore, the importance of polysulfides has been shown during interactions of sulfur with other cycles, such as the Fe cycle during the pyritization pathways (polysulfide pathway)(Rickard and Luther, 2007).

The forward reaction describes the nucleophilic attack of the S_8 ring by the strong nucleophile HS^-, which opens the homocyclic ring and forms the polysulfide ion. Polysulfides are inherently unstable in acidic conditions decomposing to $S_{8(aq)}$ and sulfide, according to the reverse of reaction 7. At acidic conditions the polysulfide ions undergo a series of chain elongation and nucleophilic displacement reactions. During these reactions the one sulfidic end of the polysulfide chain acts as a nucleophile and attacks the other end, resulting in formation of the $S_{8(aq)}$ ring and the release of a sulfide molecule (reverse reaction 7). The reversibility of reaction 7 contributes to the re-arrangement of the solid form of zero valent sulfur. An example would be the nucleophilic dissolution of colloidal α-S_8 by reaction with HS^- to form polysulfide intermediates (forward reaction 7) followed

by acidification of the polysulfide (reverse of reaction 7) and formation of $S_{8(aq)}$ that can further coarsen to S_{8nano}. Considering both forward and reverse pathways of reaction 7, the elemental sulfur can be transformed from an original massive or colloidal α-S_8 form to the nanoparticulate form, through formation of $S_{8(aq)}$, changing in regards to size (surface area) and surface character.

At low temperatures, polysulfide formation due to nucleophilic dissolution of elemental sulfur has been noted during studies of sulfide oxidation by O_2 (Chen and Gupta, 1973; Chen and Morris, 1972). Steudel (1996) described the sulfide oxidation reaction by molecular oxygen as a 1 e^- step oxidation of sulfide toward radical molecules that undergo dimerization and elongation to form polysulfides (Steudel, 1996). However, in acidic to circumneutral pH range, and in absence of Fe^{3+}, a 1 e^- step is energetically unfavorable whereas the 2 e^- step oxidation of sulfide to elemental sulfur is energetically favorable (Luther III et al., 2011). That would lead to the reaction of elemental sulfur formed with remaining sulfide to form polysulfide intermediates, based on reaction 7.

The sulfur system includes reactions at higher temperatures that involve polysulfides as important intermediates (Giggenbach, 1974a, b). When elemental sulfur is contained in an aqueous acidic system it shows stability at low temperatures. Increase of temperatures in this system without change of pH conditions will lead to the hydrolysis of S_8 to form sulfide and bisulfate ion (Giggenbach, 1974a):

$$4S + 4H_2O \leftrightarrow 3H_2S + HSO_4^- + H^+ \qquad \text{(reaction 8)}$$

In the case where the pH conditions of the system evolve to circumneutral to alkaline values, elemental sulfur will react according to the nucleophilic reaction 7, presence of sulfide, and will form polysulfides (as mentioned above)(Kamyshny et al., 2004). Polysulfides in that case will be stable up to temperature values between 150º-200ºC (depending on pH), while above that temperature threshold will disproportionate to thiosulfate and sulfide (Giggenbach, 1974a, b):

$$4S_nS^{2-} + (3n-4)OH^- \leftrightarrow nS_2O_3^{2-} + (2n+4)HS^- \qquad \text{(reaction 9)}$$

The rate of the polysulfide decomposition (equation 9) is proportional to the temperature of the solution (Giggenbach, 1974b). Reaction 9 is fully reversible, with the reaction of thiosulfate and sulfide to form polysulfides (Giggenbach, 1974a, b):

$$nS_2O_3^{2-} + 2(n+2)HS^- \leftrightarrow 4S_nS^{2-} + 4(n-1)OH^- \qquad \text{(reaction 10)}$$

Furthermore, when the conditions in the initial S_8-rich acidic aqueous system were to change abruptly to higher temperatures and to higher pH values, the dissociation of elemental sulfur via reaction with hydroxide would lead to formation of thiosulfate and sulfide (Giggenbach, 1974a):

$$4S + 4OH^- \leftrightarrow S_2O_3^{2-} + 2HS^- + H_2O \qquad \text{(reaction 11)}$$

This reaction (11) takes place under conditions up to 250ºC, whereas in temperatures higher than 250ºC the disproportionation of thiosulfate (presence of hydroxide) to form sulfate and sulfide would take place (Giggenbach, 1974a):

$$S_2O_3^{2-} + OH^- \leftrightarrow SO_4^{2-} + HS^- \qquad \text{(reaction 12)}$$

In summary, polysulfides along with thiosulfate comprise important intermediates in reactions taking place in higher temperatures in the sulfur system. A summary figure of the above discussed reactions is shown below (*Figure 1-2*).

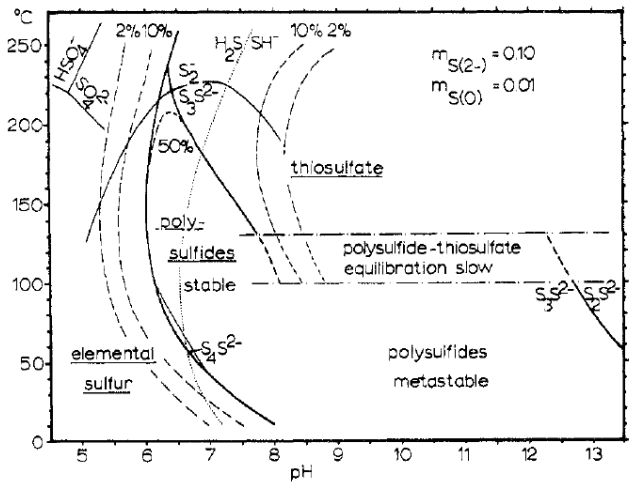

Figure 1-2: Temperature-pH diagram for the sulfur system (Giggenbach, 1974a).

Previous work has shown the kinetics as well as the thermodynamics of the nucleophilic dissolution of elemental sulfur by sulfide, using α-S_8 (Giggenbach, 1972; Giggenbach, 1974a, b; Hartler et al., 1967; Kamyshny et al., 2004; Kamyshny et al., 2003; Kamyshny et al., 2007; Licht and Davis, 1997; Teder, 1971), as well as biological produced sulfur (Kleinjan et al., 2005a, b). Teder (1971) measured the equilibrium constants of the nucleophilic reaction and found that the equilibrium constants would decrease with increasing temperature. Furthermore, Teder (1971) discussed that the stoichiometry of the polysulfide molecules (that is, their chain length) would be dependent on the pH of the solution, whereas the average chain length would not be influenced (Teder, 1971). The average distribution of aqueous polysulfides in equilibrium in standard conditions incorporates chain lengths of 2 to 8 sulfur atoms, with longer polysulfide chains possibly existing (lower confidence levels; Kamyshny et al., 2004). The molecules S_4^{2-}, S_5^{2-}, and S_6^{2-} show the highest abundance in solution, followed by the rest of the polysulfide molecules (S_7^{2-}, S_3^{2-}, S_8^{2-}, S_2^{2-}; Kamyshny et al., 2004). Pentasulfide (S_5^{2-}) will be the most abundant polysulfidic chain in high pH conditions, whereas HS_2^- is the most abundant species in acidic conditions (Kamyshny et al., 2004)(Figure 1-3). The identification of the specific chain length is possible due to the derivatization techniques developed by Kamyshny et al. (2006) where each polysulfide chain is stabilized after reaction with a methylating agent (Kamyshny et al., 2006). Polysulfide equilibria were found to be pH dependent with polysulfides decomposing via the reverse reaction 7 below pH 9 (Kamyshny et al., 2004), with the polysulfide decomposition kinetics being at a seconds-scale (experimental observations). Finally, Kamyshny et al (2007) discussed that with increasing temperature, both the concentration and the average chain length of polysulfide molecules increases, for solutions of pH 8 and above (Kamyshny et al., 2007).

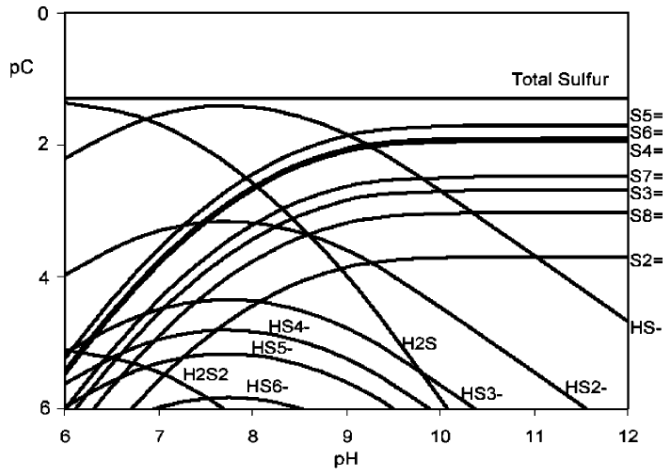

Figure 1-3: Distribution of sulfide and polysulfide species as a function of pH in 50mM polysulfide solution (I = 0.3)(Kamyshny et al., 2004).

Other studies have shown that the equilibrium constant of the nucleophilic dissolution of S_8 differs between conditions of α-S_8 and biologically produced sulfur (Kleinjan et al., 2005a; Teder, 1971). More specifically, the equilibrium between sulfide and $S_{8biological}$ at 21^0C shows a constant pK at 9.10±0.08, which is higher than that of the reaction involving sulfide and inorganic sulfur, which has pK at 8.82 (Kleinjan et al., 2005a). The higher value of pK during the reaction of $S_{8biological}$ with sulfide compared to that with inorganic sulfur (α-S_8) is attributed to the surface character of $S_{8biological}$ which is coated by an organic layer of negative charge, that makes it differ from the surface of α-S_8 (Kleinjan et al., 2005a).

The dissolution kinetics of α-S_8 are found to be influenced by the sulfide concentration and surface area effect, with the reaction rate being approximately second-order in respect to sulfide concentration (Hartler et al., 1967; Kleinjan et al., 2005b). Hartler et al. (1967) investigated the effect of specific surface area of sulfur granules, finding that the kinetics of the nucleophilic dissolution was enhanced at higher values of surface area (smaller diameters)(Hartler et al., 1967), which was expected based on observations of elemental sulfur reactivity in other studies (Lefroy and Blair, 1997; Sholeh et al., 1997). For the biologically produced sulfur, the kinetic rate law has also been established and takes the form:

$$\frac{d[S_5^{2-}]}{dt} = \frac{A_c[HS^-]}{[H^+]}(k_1^*[HS^-] + k_2^*[S_5^{2-}])$$

with k^{*1} and k^{*2} at $5.78*10^{-14}$ m s^{-1} and $1.33*10^{-10}$ m s^{-1} at 50°C.

The literature is missing information regarding the thermodynamics and kinetics of reaction 7 for nanoparticulate elemental sulfur of varying conditions of surface area (size of nanoparticles) as well as surface character. Surface character is influenced by the pathway (or recipe) of formation of elemental sulfur nanoparticles that results to either hydrophilic or hydrophobic nanoparticles (see below). Furthermore, surface character is influenced by the presence or absence of surfactant molecules that exist in natural systems as organic exudates from microbial activity, forming a coating onto the surface of the nanoparticle. Depending on the chemical conditions mentioned, the resulting elemental sulfur nanoparticles tend to resemble more or less sulfur particles that have resulted as precipitants of microbial metabolism. Since elemental sulfur nanoparticles are an important intermediate form of the coarsening evolution of elemental sulfur (from S_{8aq} up to α-S_8), it is worth looking into more detail on these forms of S_8. The furthering of the understanding of the reactivity of these nanoparticles particularly as a function of surface area/character, within the sulfur cycle as well as during the interaction of sulfur with carbon and metal cycles will contribute to a better understanding of the (biogeo)chemical processes of any natural environment that incorporates reduced sulfur species (i.e. Yellowstone, near-surface environments, anoxic water column of lakes or seawater, etc.).

The following subsections incorporate a mini review on the various forms of elemental sulfur, including their mineralogy, chemistry, surface character and properties, and microbiological origin. These subsections will give an emphasis on the nanoparticulate forms of elemental sulfur which are the focus on this thesis.

On the various forms of elemental sulfur (S_8^0)

Elemental sulfur allotropes

Sulfur occupies the chemical system with the vastest amount of allotropes in the solid phase, including unbranched cyclic molecules (S: 6 to 20 atoms) and polymeric ("branched") molecules (Meyer, 1964, 1976; Steudel and Eckert, 2003). The thermodynamically most stable form in ambient conditions is the orthorhombic allotrope of cyclo-octasulfur (α-S_8)(Steudel and Eckert, 2003), with the uncommon monoclinic allotropes of β-S_8 and γ-S_8 being found in arctic systems in association with natural organic matter (Lau et al., 2017). All three allotropes of S_8 (α, β, γ) are built by the same shape of the cyclo-octasulfur ring molecule. The crown shaped puckered conformation of cyclo-octasulfur is characterized by a D4d symmetry due to alternation of dihedral angles (Steudel and Eckert, 2003).

In the orthorhombic α-S_8, each four sulfur atoms form two groups that are placed in two parallel planes, forming the crown-shaped puckered conformation. The c crystallographic axis is perpendicular to those two planes. The unit cell contains four molecules of cyclo-octasulfur, while its dimensions are a=1046.4pm, b=1286.6pm, and c=2448.6pm (Meyer, 1976; Steudel and Eckert, 2003). This allotrope shows a large number of intermolecular contacts, that is 12 contacts per four non-equivalent sulfur atoms in each S_8 ring. In particular these contacts show short intermolecular distances, less than 370pm, leading to the high stability of this allotrope in STP (Steudel and Eckert, 2003).

The β-S_8 allotrope shows a crown shape puckered conformation similar to that of α-S_8, however with a flattening effect due to intermolecular forces. Two thirds of the amount of the rings in the crystals of β-S_8 being normal, whereas the one third being disordered by a 45^o rotation along the a axis. The unit cell incorporates six molecules of cyclo-octasulfur (four normal and two pseudocentered), while the cell dimensions are a=1092.6pm, b=1085.2pm, c=1079.0pm, and β=95.9^o (Meyer, 1976; Steudel and Eckert, 2003).

The γ-S_8 allotrope shows crystals of a “sheared penny roll” arrangement. The molecule of cyclo-octasulfur in this allotrope displays a pseudo-hexagonal close-packed structure. The unit cell includes four molecules, whereas its dimensions are a=845.5pm, b=1305.2pm, c=926.7pm, and β=124.9^o (Meyer, 1976; Steudel and Eckert, 2003). The bond lengths in γ-S_8 vary significantly, much more than the variation found in the bond lengths of α-S_8 and β-S_8 (Steudel and Eckert, 2003).

For more details on the solid sulfur allotropes, as well as their crystallographic, molecular and spectroscopic signatures, please refer to Appendix A.

Elemental sulfur nanoparticles (S_{8nano} or S-sols)

Formation and coarsening of solid phase intermediates of S_8

Aqueous elemental sulfur (S_{8aq}) is sparsely soluble in water (29±1nM S_{8aq} at 25^{o}C)(Kamyshny, 2009); when oversaturated, it forms nanoparticulate elemental sulfur solids (S_{8nano}) with a diameter of ~200nm within a few minutes (Garcia and Druschel, 2014; data from current study). S_{8nano}, as well as its consequent coarsened product, the sulfur "sols" (or S_{8sol}), show an attribute of very small droplets of liquid sulfur (or sulfur rich compounds)(Steudel, 2003) of a hydrophobic ($S_{8weimarn}$) or hydrophilic (S_{8raffo}) character (Garcia Jr and Druschel, 2014). All forms of sols are thermodynamically unstable (Steudel, 2003) and are coarsened via nucleation, aggregation and Ostwald ripening processes (Garcia Jr and Druschel, 2014), to turn into α-S_8, the thermodynamically most stable form in ambient conditions. α -S_8 is insoluble in water and precipitates as a sediment (Steudel, 2003).

Zero-valent sulfur (S^0) shows high enthalpy of formation in standard conditions, hence it is unstable (Kleinjan et al., 2003; Steudel, 2000b), catenating to form cyclo-octasulfur rings. Due to their hydrophobic character and sparse solubility, S_{8aq} homocycles tend to coalesce to form S_8 clusters that have a size range within the nano and micrometer scale (Garcia Jr and Druschel, 2014; Steudel, 2003). These sulfur-rich compounds are called sulfur sols (or S_{8sol}) and are described as being in the liquid phase, based on the observation of a "Maltese-cross pattern" via optical microscopy (Steudel, 2003). However, Raman spectroscopy on the S_{8sol} particles produced by Beggiatoa cultures indicated "extremely fine-grained microcrystalline, solid, elemental sulfur" (Pasteris et al., 2001). In reality both observations are correct, however the sulfur sols undergo a physical-chemical evolution by transitioning from the liquid to the solid state with the exact processes and kinetics of this transition not yet being fully understood. Capability for high resolution measurements of the diameter of nanoparticles as low as 1nm allowed for the determination of S_{8sols} passing through the nanometer scale and gradually coarsening to larger sizes. These forms of sols are called S_{8nano} and are the first form of sulfur particles formed after the coalescing of S_{8aq}. The initial stages of the coarsening process are represented by classical

nucleation through which the individual S_{8aq} molecules form clusters and nanocrystals of S_{8nano}, that reach diameters of up to 250nm within the first 5 minutes of aging (expressed as initial size of S_{8nano} in this work due to limitations in the instrumentation) (Garcia Jr and Druschel, 2014). Then, coarsening processes transition to Ostwald ripening and/or aggregation processes (Garcia Jr and Druschel, 2014). The definitions of S_{8nano} and S_{8sol} are overlapping at least in part of the ranges of size of particles they describe (Garcia Jr and Druschel, 2014). It is generally accepted that the sequence of elemental sulfur forms produced during coarsening processes are as shown in reaction 3:

$$S_nO_m^{2-} \rightarrow S_{8(aq)} \rightarrow S_{8(nano)} \rightarrow S_{8(sol)} \rightarrow \alpha\text{-}S_{8\ (bulk)} \qquad \text{(reaction 3)}$$

where the $S_nO_m^{2-}$ species might represent either the polysulfide, thiosulfate, polythionates or sulfane monosulfonic acids that undergo chain elongation reactions to form S_8 (Garcia Jr and Druschel, 2014).

Hydrophobic elemental sulfur nanoparticles ($S_{8weimarn}$)

$S_{8weimarn}$ is the result of dilution of elemental sulfur- saturated organic solvents in excess of water (Steudel, 2003). The cyclo-octasulfur dissolved in methanol (or ethanol or acetone) when in contact with water tends to avoid the aqueous environment and links with each other via the formation of Van der Waals bonding. Coarsening kinetics of various S-saturated methanol to H_2O ratios have been investigated within the scope of this work, showing that enhanced kinetics of coarsening of S_{8nano} takes place in higher ratios (i.e. 1:6 compared to 1:35). This possibly influences the overall time frame of the evolution of cyclo-octasulfur through the metastable S_{8nano} phase to the eventual precipitation of α-S_8, compared to the timeframe of days-scale described by Steudel (2003). In addition to methanol-to-water ratio, coarsening kinetics is influenced by temperature and surfactant coatings (Garcia Jr and Druschel, 2014). The color of the solution evolves along with the coarsening process, taking a blue-white opalescent color in young age of the suspension, while a milky-white color represents aged $S_{8weimarn}$ solutions (Steudel, 2003). The monodispersity of the $S_{8weimarn}$ solution originates from the particular method of mixing, which should be the introduction of water into the organic solution (Steudel, 2003). However, the electrochemical signal of $S_{8weimarn}$ results to be the same regardless on the

mixing method, as shown from electrochemical studies (see Chapter 2). Adsorption of negatively charged ions onto the surface of $S_{8weimarn}$ attributes a negative charge, which is measured by electrophoresis (Freundlich and Scholz, 1922).

Hydrophilic elemental sulfur nanoparticles (S_{8raffo})

S_{8raffo} (Raffo or LaMer sols) originate mainly from the acidification of thiosulfate or polysulfides (Raffo, 1908; Steudel, 2003), or reaction of sulfite and hydrogen sulfide, which in that case can be called Selmi sol (S_{8selmi})(Selmi, 1852; Steudel, 2003). S_{8raffo} is comprised of two forms of sulfur: Firstly, polythionates of a range of sulfur ions exist in an arrangement which allows the zero-valent sulfur interiors of the chains to occupy the interior of the nanoparticle, while the sulfonic moieties are exposed on the surface of the nanoparticle interacting with the aqueous phase (Figure 1-4)(Steudel, 2003; Steudel et al., 1987). Secondly, elemental sulfur homocycles of various numbers of sulfur atoms exist in the interior of the nanoparticle, as determined by liquid chromatography (Steudel, 2003; Steudel et al., 1981; Strauss and Steudel, 1987). The relative distribution of elemental sulfur homocycles follows the order $S_8 > S_7 > S_6$, with the following ring sizes being found in traces: $S_9 > S_{12} > S_{10}$, S_{11}, S_{13}, S_{14}, S_{15} (Steudel et al., 1988). An analysis of homocyclic ring distributions during the analysis of freshly formed S_{8raffo} showed 27.5mg/L S_8, 9.9mg/L S_7, 6.1mg/L S_6 and 0.2mg/L S_{12} (Steudel et al., 1988).The reactions describing the formation of sulfur homocycles due to the acidification of thiosulfate, as well as the formation of polythionates, is shown here (Steudel, 2003):

$$Na_2S_2O_3 + H_2SO_4 \rightarrow H_2S_2O_3 + Na_2SO_4 \qquad \text{(reaction 4)}$$

$$xH_2S_2O_3 \rightarrow yH_2O + zSO_2 + H_2S_mO_6 \qquad \text{(reaction 5)}$$

$$H_2S_mO_6 \rightarrow H_2S_{m-n}O_6 + S_n \ (n>5) \qquad \text{(reaction 6)}$$

Acidification of thiosulfate forms thiosulfuric acid (reaction 4), which consequently decomposes to polythionic acids, sulfur dioxide and water (reaction 5). The elongation of the sulfur chain in the polythionic acid (that produces polythionate ions) is due to the protonation of the thiosulfate ion, which is being attacked nucleophilically by the non-protonated thiosulfate ion (Steudel, 2003). The formation of S_{8raffo} takes place due to the

splitting of polythionic acid to a polythionic product of a shorter chain (lower amount of zero-valent sulfur), and sulfur homocycles (reaction 6).

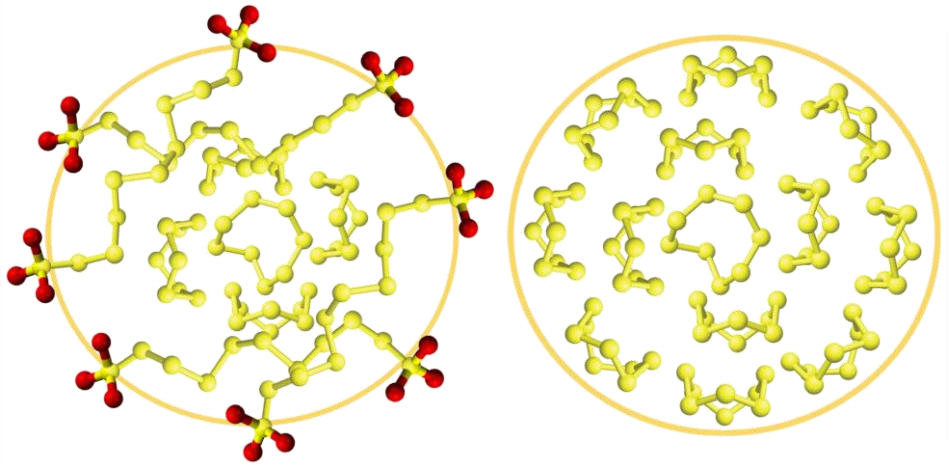

Figure 1-4: Schematic models on how we understand the structure of S_{8raffo} (left) and $S_{8weimarn}$ (right).

Biologically-produced elemental sulfur ($S_{8biological}$)

Biologically produced sulfur ($S_{8biological}$) is another particulate form of zero-valent sulfur species that is formed due to microbial metabolic activity. During dissimilatory sulfide oxidation by phototrophic or chemotrophic microbes, $S_{8biological}$ is an intermediate that is often produced and stored either intra- or extracellularly. $S_{8biological}$ shows in general a density value lower than that of orthorhombic α-S_8, while its surface character is hydrophilic (Kleinjan et al., 2003). The geometry of $S_{8biological}$ is that of a spherical or ellipsoidal shape, with a diameter of up to 1μm. X-ray diffraction analyses show in general a non-crystalline material with high concentrations in sulfur (not purely comprised of sulfur)(Steudel, 1989). The diameter sizes of $S_{8biological}$ range from a few hundreds of nanometers up to 1μm, for both intracellularly and extracellularly precipitated sulfur. However members of the *Beggiatoa* and *Allochromatium* families precipitate $S_{8biological}$ with diameter at 250μm (Kleinjan et al., 2003; Nicolson and Schmidt, 1971; Strohl et al., 1981).

The surface charge of the biological sulfur nanoparticle is influenced by the pH in solution (Kleinjan et al., 2003). This results from the protonation – deprotonation reactions that take place among surface functional groups present on the surface of $S_{8biological}$. Depending on their pK values various functional groups are deprotonated in different pH ranges, with the carboxylic (R-COOH) and amino ($R\text{-}NH3^{+}$) groups deprotonating at acidic and alkaline pH ranges, respectively (Bas et al., 2008). Hence, the surface charge of $S_{8biological}$ would be negative at environmentally relevant conditions, as the zero point of charge (ZPC) of $S_{8biological}$ has been measured at 2.3 (Kleinjan et al., 2003). Furthermore, this charge is distributed in a non-homogeneous manner on the surface of the biologically produced $S_{8biological}$ (Janssen et al., 1996). The existence of surface charge causes the attraction of oppositely charged ions and the formation of a "diffuse electrical double layer" (Kleinjan et al., 2003). The diffuse electrical double layer is a layer highly concentrated in ions that are charged oppositely to the surface charge of $S_{8biological}$, with the charge equalizing in distance from the surface. Surface charge on $S_{8biological}$ also contributes to biopolymer and surfactant adsorption which, depending on the charge of the biopolymer adsorbed, consequently influences the stabilization of these nanoparticles (Kleinjan et al., 2003).

Three main chemical forms of zero-valent sulfur are present in microbial sulfur globules (Dahl and Prange, 2006; George et al., 2008; Kleinjan et al., 2003; Pasteris et al., 2001; Prange et al., 2002): 1) cyclo-octasulfur rings, 2) sulfur chains with organic endmember moieties, and 3) polythionates. The globules can include more than one chemical type of sulfur. There can be a distinction between intracellularly and extracellularly deposited $S_{8biological}$ as a function of its depositional location to the cellular wall.

Extracellularly precipitated $S_{8biological}$

The structure of extracellularly precipitated $S_{8biological}$ has been investigated, using sulfur precipitates from *Thiobacillus sp.* as well as *Acidithiobacillus ferrooxidans*. The sulfur globules formed by *A. ferrooxidans* consist of polythionate molecules concentrated around the rim of the globule, forming a vesicle whose vacant space is occupied by water

molecules. X-ray absorption spectroscopy has declined the existence of sulfur homocycles, which was initially believed to take place in the biological colloids (Steudel, 1989; Steudel, 2003). However X-ray absorption spectroscopic studies have confirmed the liquid chromatography measurements that described the existence of polythionates in this type of $S_{8biological}$ (Prange et al., 2002; Steudel et al., 1987). There is a relationship between the pH conditions in the environments that *A. ferrooxidans* occupies and the stability of polythionates (Druschel et al., 2003). The very slow oxidation rate and consequent relative stability of polythionates in acidic conditions (Druschel et al., 2003) where the cells of *A. ferrooxidans* survive, makes this metabolic pathway very successful for this microbial species, as opposed to other species that occupy environments of higher pH range (Ingledew, 1982). Another example of microbial species precipitating extracellular $S_{8biological}$ is that of *Thiobacillus sp.* X-ray diffraction measurements have shown that the globule consists of cyclo-octasulfur (Kleinjan et al., 2003). Floatation experiments of this type of $S_{8biological}$ with α-S_8 on water and decahexane disclosed hydrophilic surface attributes of $S_{8biological}$ as it dispersed to water and not to the organic solvent (as opposed to α-S_8)(Janssen et al., 1999). This behavior results from the presence of organic coatings on the surface of $S_{8biological}$ that resulted from *Thiobacillus sp*., that has been proven by various methods (surface density and isoelectric point measurements; Kleinjan et al., 2003).

Intracellularly precipitated $S_{8biological}$

Intracellular $S_{8biological}$ is the result of metabolic activity of members from various families of microbes, with examples the families of *Allochromatum* and *Beggiatoa* (Frigaard and Dahl, 2008; Kleinjan et al., 2003; Wilbanks et al., 2014). The characterization of $S_{8biological}$ precipitate by *Al. vinosum* was initially conducted by Steudel as a particle of a structure similar to that of S_{8raffo} (Steudel et al., 1990). X-ray diffraction analyses showed non crystalline patterns similar to those of "liquid" sulfur and not of a crystalline material, while aging of the $S_{8biological}$ would result in the formation of orthorhombic α-S_8 (Hageage et al., 1970; Kleinjan et al., 2003; Trüper and Hathaway, 1967). X-ray absorption spectroscopy (specifically XANES) conducted by Prange et al. (1999, 2002) declined the presence of polythionates and cyclo-octasulfur and characterized

the material to be consistent with organic polysulfane phases with formula R-S_n-R. The presence of organic moieties at the ends of the polysulfane chains explains the lower density values for this model of $S_{8biological}$ (Guerrero et al., 1984; Mas and Van Gemerden, 1987). Density measurements on the same $S_{8biological}$ material resulted in values of 1.21 gcm^{-3} which is much less than the liquid sulfur density of 1.89$grcm^{-3}$ as well as of the crystalline sulfur density of 1.9-2.2gcm^{-3} (Guerrero et al., 1984; Mas and Van Gemerden, 1987; Steudel, 2000a). The model of Prange et al. (1999; 2002) matches the density data which suggest that $S_{8biological}$ formed by *Allochromatum* is not pure sulfur but has some impurities represented by the organic moieties (Kleinjan et al., 2003; Prange et al., 1999; Prange et al., 2002). Interestingly, XANES spectroscopy on sulfur globules from the same bacteria showed them to have a chemical signature that appears to resemble the cyclo-octasulfur crowns of α-S_8 (George et al., 2008).

$S_{8biological}$ precipitating intracellularly by *Beggiatoa alba* has also been investigated by Raman (Pasteris et al., 2001) and XANES spectroscopy (Prange et al., 2002). The analyses disclosed a composition entirely made by cyclo-octasulfur (Pasteris et al., 2001; Prange et al., 2002). The results of Pasteris et al. (2001) on the composition of $S_{8biological}$ of *Thioploca* and *Beggiatoa* suggest microcrystalline cyclo-octasulfur. This microcrystallinity does not originate from a single crystal but from an alignment of many microcrystallites, due to the lack of birefringence in optical microscopy, contributing to the high reactivity of the globule because of the high surface area (Pasteris et al., 2001). Prange et al. (2002) also studied cells of *Thiomargarita namibiensis* and found that the sulfur globules they form are also comprised of cyclo-octasulfur rings. The surprising differences on the interpretations of the chemistry and mineralogy of the sulfur globules between research groups might be a result of the vastly different nature of the analytical techniques used. Comparing Raman with X-ray absorption spectroscopies, we recognize a rigid separation on level of sensitivity between the two instrumental methods (Pasteris et al., 2001). Furthermore sample handling (wet state globules for in situ analysis versus dried globules) can also be detrimental to the preservation of the original chemical signature of the sulfur globules (Kleinjan et al., 2003).

Dahl and Prange (2006) note a correlation between the form of sulfur globules precipitating from various microbial species, as a function of their ecology, physiology and metabolism with respect to oxygen (Dahl and Prange, 2006). Specifically, during the absence of molecular oxygen the metabolic activity of anaerobic phototrophic bacteria results in the formation of a chemical signature representing sulfur chains (organic polysulfanes). Presence of molecular oxygen at aerobic metabolic pathways results in the precipitation of globules that include either cyclo-octasulfur (*B. alba, T. namibiensis*), or polythionates (*A. ferrooxidans*), both representing aerobic metabolic pathways. Furthermore, based on their chemistry, the $S_{8biological}$ resulting from *B. alba* or *T. namibiensis* would be more hydrophobic (due to the cyclo-octasulfur content) compared to the $S_{8biological}$ resulting from *A. ferrooxidans* (which would consist of polythionates)(Dahl and Prange, 2006; Kleinjan et al., 2003; Prange et al., 2002).

Surface character of elemental sulfur nanoparticles

The elemental sulfur sols represent a reasonable "inorganically-formed" approximation of $S_{8biological}$ (Steudel and Albertsen, 1999). $S_{8biological}$ can precipitate by forming a structure of polythionates (*A. ferrooxidans*), organic polysulfanes (*Allochromatum vinosum*), or even cyclo-octasulfur (*B. alba, T. namibiensis*), depending on the microbial species forming the sulfur intermediate (Kleinjan et al., 2003; Pasteris et al., 2001; Prange et al., 1999; Prange et al., 2002; Steudel et al., 1987). However, in the cases where $S_{8biological}$ incorporates a hydrophobic cyclo-octasulfur rich nucleus, organic/biological polymers adsorbed on the surface of the particles attenuate the hydrophobicity and attribute a hydrophilic character to $S_{8biological}$ (Janssen et al., 1994; Janssen et al., 1999). A hexadecane-water partition test has confirmed the hydrophilic character of $S_{8biological}$ (Janssen et al., 1999). Freshly formed $S_{8biological}$ originating by the activity of a *Thiobacillus*-like microbial consortium shows a diameter of approximately 100μm (Janssen et al., 1996), which is comparable to the scale of diameters of inorganic S_{8nano}. Furthermore, the surface charge of $S_{8biological}$ formed by the *Thiobacillus*-like consortium was found to be negatively charged in circumneutral conditions (ZPC at 5.6) (Janssen et al., 1996), whereas another measurement of the ZPC of $S_{8biological}$ formed under

similar conditions showed a value of 2.3 (Kleinjan et al., 2003). Hence, both $S_{8weimarn}$ and S_{8raffo} can resemble $S_{8biological}$ with the S_{8raffo} being closer to the model of the hydrophilic, negatively-charged surface of the $S_{8biological}$ mentioned above.

Surface coatings of elemental sulfur nanoparticles

Microbiological activity can cause the formation of surfactant molecules, which are released from the cell as organic exudates (George et al., 2008; Knickerbocker et al., 2000; Pasteris et al., 2001; Suzuki, 1999) and consequently react with S_{8nano} to form a surfactant coating. This coating can control the size distribution as well as the hydrophobicity of S_{8nano} (Kleinjan et al., 2003). Enhancement of hydrophilicity of $S_{8biological}$ due to its organic exudate coatings can lead to error associated with the quantification of S_8 based on chloroform extraction as utilized in Chapter 4, compared to other methods such that of cyanolysis (Kamyshny et al., 2009). Studies of coarsening kinetics of S_{8nano} has shown that surface coating and temperature influence dramatically the rate of the nanoparticulate growth (Garcia Jr and Druschel, 2014). More specifically, the coarsening rates of S_{8nano} diminish with decreasing temperatures as well as due to the presence of surfactant coatings (Garcia Jr and Druschel, 2014; Janssen et al., 1996).

Organic coatings are also believed to influence the solubility of elemental sulfur (Steudel and Holdt, 1988). The solubility of S_8 in pure water and seawater is calculated to be ~29.62nM and ~18.06nM at 25°C (Kamyshny, 2009). Solubility experiments of α-S_8 using neutral-charged surfactants showed that the concentration of elemental sulfur in water in presence of surfactant molecules increased dramatically, up to 5000 times higher than S_8 solubility in pure water (Steudel and Holdt, 1988).

The amount of surfactant molecules that is needed in order to fully cover the surface area of S_{8nano} is dictated by the critical micelle concentration (CMC). The CMC is defined as the concentration above which the surfactant molecules have covered all the surface area of the nanoparticle forming micelle-like structures, while any further addition of surfactants in the system does not affect the S_{8nano}. Recent studies have shown that particle size and growth rate of S_{8nano} decrease with increasing surfactant concentration, while the growth rate becomes constant at CMC (Chaudhuri and Paria, 2011). The value of CMC is

influenced by the type of surfactant; for example the CMC for S_{8nano} in presence of BSDS is calculated at 1.2mM at 28^{o}C, whereas for TX-100 and CTAB is 0.15 and 0.93mM, respectively (Chaudhuri and Paria, 2009, 2011). The concentration of surfactant in the system compared to the value of the CMC is influencing detrimentally the fate of S_{8nano}. If the surfactants in solution have a concentration higher than the CMC, this leads to the dissolution of S_{8nano} described as follows: The solubility of S_{8nano} by surfactants takes place as the nanoparticle is completely covered by surfactant molecules forming a micelle. Within that micelle the S_{8nano} is being dissolved by the interaction with the hydrophobic part of the surfactant, releasing aqueous $S_{8aq\text{-}surfactant}$ (Steudel, 2003; Steudel and Holdt, 1988). When the surfactants present in the system are at a concentration lower than that of the CMC, dissolution of S_{8nano} is not prominent, however its coarsening kinetics might change. Adsorption of biopolymer molecules or surfactants accelerates the coarsening and precipitation of $S_{8weimarn}$, as the amphiphilic molecules connect with their hydrophobic part on the $S_{8weimarn}$ surface, releasing the hydrophilic part interacting with the water, therefore making the interactions with other nanoparticles easier (enhancing inter-particulate interactions and therefore coarsening)(Steudel, 2003; Steudel and Albertsen, 1999).

Natural systems incorporate surfactant molecules with concentrations at the hundreds of parts per billion for marine systems (North Adriatic Sea) and correlate with the dissolved organic carbon content (Ćosović and Vojvodić, 1998). In natural systems where surfactants are utilized during pollutant remediation procedures, high concentrations are found that lead to adverse biological and ecological effects (Cserháti et al., 2002). Bacterial biofilms represent a source of surfactants which are released by extracellular polymeric substances of bacteria and influence the surface tension, gas exchange and overall stability of the biofilm structure (Flemming and Wingender, 2010). The presence of surfactants in natural systems will influence the S_{8nano} coarsening based on the relationship between the surfactant concentration and the CMC. The CMC is reversely proportional to ionic strength in aqueous systems (Fuguet et al., 2005), whereas sorption of surfactants on mineral surfaces as well as the sediment/mineral-to-water ratio influence considerably the CMC in each system (Zheng and Obbard, 2002; Zhu et al., 2003).

The nanoparticulate form of elemental sulfur that is used as a substrate by microbial cells is thought to be more bioavailable than the bulk α-S_8 form (Boyd and Druschel, 2013). When elemental sulfur is precipitating as a metabolic product of microbial activities, it also appears in small particle sizes (~100nm)(Kleinjan et al., 2003). Due to the abundance of S_{8nano} in biotic systems where sulfur cycling occurs, the size and surface character of S_{8nano} have to be considered on how they influence the reactivity in geological and environmental systems.

Importance of this study

This study sheds light on the cycling of sulfur in systems where its elemental form is present, especially in cases where interactions between microorganisms and elemental sulfur (nano)particles occur. We focus on the nucleophilic dissolution kinetics of elemental sulfur expressed via reaction 7, particularly considering the influence of the various forms of elemental sulfur nanoparticles participating in this reaction. We show the influence of surface area, surface character, and surfactant coatings of S_{8nano} on its dissolution kinetics via reaction 7. We also characterize the kinetic rate law(s) of reaction 7 when involving S_{8nano} with different size and surface characteristics. In addition, we observed the sulfur speciation in Yellowstone National Park thermal areas, which indicates the existence of elemental sulfur and polysulfide intermediates with a dynamic supply of hydrogen sulfide. Field observations and geochemical kinetic modeling indicate that reaction 7 appears to be a key abiotic pathway for the cycling of sulfur species and the enhancement of elemental sulfur bioavailability. Furthermore, an evaluation of the electroanalytical chemistry of elemental sulfur was conducted, necessary to better understand the dynamics of sulfur cycling in field and lab experiments, but also to demonstrate how various forms of elemental sulfur contribute to a diverse pathway of interaction with the mercury-surface electrodes. Voltammetric signals corresponding to specific forms of elemental sulfur – including dissolved, colloidal, nanoparticulate of various particle sizes, surface character, and surfactant coatings – have been investigated under appropriate physical-

chemical conditions. A database of voltammetric signals is provided for the better detection of elemental sulfur in aqueous systems.

References

Aizenshtat, Z., Krein, E.B., Vairavamurthy, M.A. and Goldstein, T.P. (1995) Role of sulfur in the transformations of sedimentary organic matter: A mechanistic overview, ACS Symposium Series. American Chemical Society, pp. 16-37.

Al-Zahrani, I., Aneel Mohammed, M.H., Basheer, C., Siddiqui, M.N. and Al-Arfaj, A. (2015) Membrane assisted simultaneous extraction and derivatization with triphenylphosphine of elemental sulfur in arabian crude samples by gas chromatography/mass spectrometry. Journal of Chemistry 2015.

Amrani, A. (2014) Organosulfur Compounds: Molecular and Isotopic Evolution from Biota to Oil and Gas. Annual Review of Earth and Planetary Sciences 42, 733-768.

Antonelli, M.A., Kim, S.-T., Peters, M., Labidi, J., Cartigny, P., Walker, R.J., Lyons, J.R., Hoek, J. and Farquhar, J. (2014) Early inner solar system origin for anomalous sulfur isotopes in differentiated protoplanets. Proceedings of the National Academy of Sciences 111, 17749-17754.

Ashar, N.G. and Golwalkar, K.R. (2013) Processes of Manufacture of Sulfuric Acid, A Practical Guide to the Manufacture of Sulfuric Acid, Oleums, and Sulfonating Agents. Springer International Publishing, Cham, pp. 9-30.

Ball, D.W. (1985) Elemental etymology: What's in a name? Journal of Chemical Education 62, 787.

Bas, D.C., Rogers, D.M. and Jensen, J.H. (2008) Very fast prediction and rationalization of pKa values for protein–ligand complexes. Proteins: Structure, Function, and Bioinformatics 73, 765-783.

Blumentals, I., Itoh, M., Olson, G. and Kelly, R. (1990) Role of polysulfides in reduction of elemental sulfur by the hyperthermophilic archaebacterium Pyrococcus furiosus. Applied and environmental microbiology 56, 1255-1262.

Boswell, C. and Friesen, D. (1993) Elemental sulfur fertilizers and their use on crops and pastures. Nutrient Cycling in Agroecosystems 35, 127-149.

Böttcher, M.E., Thamdrup, B. and Vennemann, T.W. (2001) Oxygen and sulfur isotope fractionation during anaerobic bacterial disproportionation of elemental sulfur. Geochimica et Cosmochimica Acta 65, 1601-1609.

Boulègue, J. and Michard, G. (1978) Constantes de formation des ions polysulfures S-26, S-25 et S-24 en phase aqueuse. Journal français d'hydrologie 9, 27-33.

Boyd, E.S. and Druschel, G.K. (2013) Involvement of intermediate sulfur species in biological reduction of elemental sulfur under acidic, hydrothermal conditions. Applied and environmental microbiology 79, 2061-2068.

Boyd, E.S., Jackson, R.A., Encarnacion, G., Zahn, J.A., Beard, T., Leavitt, W.D., Pi, Y., Zhang, C.L., Pearson, A. and Geesey, G.G. (2007) Isolation, characterization, and ecology of sulfur-respiring Crenarchaea inhabiting acid-sulfate-chloride-containing geothermal springs in Yellowstone National Park. Applied and environmental microbiology 73, 6669-6677.

Britannica, T.E.o.E. (2017) Gunpowder. Encyclopædia Britannica.

Bura-Nakić, E., Viollier, E., Jézéquel, D., Thiam, A. and Ciglenečki, I. (2009) Reduced sulfur and iron species in anoxic water column of meromictic crater Lake Pavin (Massif Central, France). Chemical Geology 266, 311-317.

Canfield, D.E., Thamdrup, B. and Fleischer, S. (1998) Isotope fractionation and sulfur metabolism by pure and enrichment cultures of elemental sulfur-disproportionating bacteria. Limnology and Oceanography 43, 253-264.

Carlson, R., Anderson, M., Johnson, R., Schulman, M. and Yavrouian, A. (2002) Sulfuric acid production on Europa: the radiolysis of sulfur in water ice. Icarus 157, 456-463.

Cauer, P. (1905) 'Omēroy'Odysseia: Homers Odyssee. B. Freytag.

Chaudhuri, R.G. and Paria, S. (2009) Dynamic contact angles on PTFE surface by aqueous surfactant solution in the absence and presence of electrolytes. Journal of colloid and interface science 337, 555-562.

Chaudhuri, R.G. and Paria, S. (2011) Growth kinetics of sulfur nanoparticles in aqueous surfactant solutions. Journal of colloid and interface science 354, 563-569.

Chen, K.Y. and Gupta, S.K. (1973) Formation of polysulfides in aqueous solution. Environmental letters 4, 187-200.

Chen, K.Y. and Morris, J.C. (1972) Kinetics of oxidation of aqueous sulfide by oxygen. Environmental Science & Technology 6, 529-537.

Chung, W.J., Simmonds, A.G., Griebel, J.J., Kim, E.T., Suh, H.S., Shim, I.-B., Glass, R.S., Loy, D.A., Theato, P., Sung, Y.-E., Char, K. and Pyun, J. (2011) Elemental Sulfur as a Reactive Medium for Gold Nanoparticles and Nanocomposite Materials. Angewandte Chemie International Edition 50, 11409-11412.

Ciglenečki, I. and Ćosović, B. (1996) Electrochemical study of sulfur species in seawater and marine phytoplankton cultures. Marine chemistry 52, 87-97.

Ciglenečki, I., Kodba, Z. and Ćosović, B. (1996) Sulfur species in Rogoznica lake. Marine chemistry 53, 101-110.

Ciglenečki, I., Ljubešić, Z., Janeković, I. and Batistić, M. (2017) Rogoznica Lake, a Euxinic Marine Lake on the Adriatic Coast (Croatia) that Fluctuates Between Anoxic Holomictic and Meromictic Conditions, in: Gulati, R.D., Zadereev, E.S., Degermendzhi, A.G. (Eds.), Ecology of Meromictic Lakes. Springer International Publishing, Cham, pp. 125-154.

Cooper, R.M. and Williams, J.S. (2004) Elemental sulphur as an induced antifungal substance in plant defence. Journal of experimental botany 55, 1947-1953.

Cosmidis, J. and Templeton, A.S. (2016) Self-assembly of biomorphic carbon/sulfur microstructures in sulfidic environments. Nature communications 7.

Ćosović, B. and Vojvodić, V. (1998) Voltammetric Analysis of Surface Active Substances in Natural Seawater. Electroanalysis 10, 429-434.

Cserháti, T., Forgács, E. and Oros, G. (2002) Biological activity and environmental impact of anionic surfactants. Environment international 28, 337-348.

Cypionka, H., Smock, A.M. and Böttcher, M.E. (1998) A combined pathway of sulfur compound disproportionation in Desulfovibrio desulfuricans. FEMS Microbiology Letters 166, 181-186.

Dahl, C. and Friedrich, C.G. (2008) Microbial sulfur metabolism. Springer.

Dahl, C. and Prange, A. (2006) Bacterial sulfur globules: occurrence, structure and metabolism, Inclusions in prokaryotes. Springer, pp. 21-51.

DeWitt, H.L., Hasenkopf, C.A., Trainer, M.G., Farmer, D.K., Jimenez, J.L., McKay, C.P., Toon, O.B. and Tolbert, M.A. (2010) The formation of sulfate and elemental sulfur aerosols under varying laboratory conditions: implications for early earth. Astrobiology 10, 773-781.

Druschel, G.K., Baker, B.J., Gihring, T.M. and Banfield, J.F. (2004) Acid mine drainage biogeochemistry at Iron Mountain, California. Geochemical Transactions 5, 13-32.

Druschel, G.K., Hamers, R.J., Luther, G.W. and Banfield, J.F. (2003) Kinetics and mechanism of trithionate and tetrathionate oxidation at low pH by hydroxyl radicals. Aquatic Geochemistry 9, 145-164.

Finster, K., Liesack, W. and Thamdrup, B. (1998) Elemental sulfur and thiosulfate disproportionation by Desulfocapsa sulfoexigens sp. nov., a new anaerobic bacterium isolated from marine surface sediment. Applied and Environmental Microbiology 64, 119-125.

Flemming, H.-C. and Wingender, J. (2010) The biofilm matrix. Nature reviews. Microbiology 8, 623.

Franz, B., Lichtenberg, H., Hormes, J., Modrow, H., Dahl, C. and Prange, A. (2007) Utilization of solid ‘elemental’sulfur by the phototrophic purple sulfur bacterium Allochromatium vinosum: a sulfur K-edge X-ray absorption spectroscopy study. Microbiology 153, 1268-1274.

Freundlich, H. and Scholz, P. (1922) Ueber hydrophobe und hydrophile Sole des Schwefels. Fortschrittsberichte über Kolloide und Polymere 16, 234-266.

Frigaard, N.-U. and Dahl, C. (2008) Sulfur metabolism in phototrophic sulfur bacteria. Advances in microbial physiology 54, 103-200.

Fuguet, E., Ràfols, C., Rosés, M. and Bosch, E. (2005) Critical micelle concentration of surfactants in aqueous buffered and unbuffered systems. Analytica Chimica Acta 548, 95-100.

Garcia Jr, A.A. and Druschel, G.K. (2014) Elemental sulfur coarsening kinetics. Geochemical Transactions 15, 11.

George, G.N., Gnida, M., Bazylinski, D.A., Prince, R.C. and Pickering, I.J. (2008) X-ray absorption spectroscopy as a probe of microbial sulfur biochemistry: the nature of bacterial sulfur globules revisited. Journal of bacteriology 190, 6376-6383.

Germida, J. and Janzen, H. (1993) Factors affecting the oxidation of elemental sulfur in soils. Nutrient Cycling in Agroecosystems 35, 101-114.

Giggenbach, W. (1972) Optical spectra and equilibrium distribution of polysulfide ions in aqueous solution at 20. deg. Inorganic Chemistry 11, 1201-1207.

Giggenbach, W.F. (1974a) Equilibriums involving polysulfide ions in aqueous sulfide solutions up to 240. deg. Inorganic Chemistry 13, 1724-1730.

Giggenbach, W.F. (1974b) Kinetics of the polysulfide-thiosulfate disproportionation up to 240. deg. Inorganic chemistry 13, 1730-1733.

Glazer, B.T., Luther, G.W., Konovalov, S.K., Friederich, G.E., Nuzzio, D.B., Trouwborst, R.E., Tebo, B.M., Clement, B., Murray, K. and Romanov, A.S. (2006) Documenting the suboxic zone of the Black Sea via high-resolution real-time redox profiling. Deep Sea Research Part II: Topical Studies in Oceanography 53, 1740-1755.

Gleeson, D., Williamson, C., Grasby, S., Pappalardo, R., Spear, J. and Templeton, A. (2011) Low temperature S0 biomineralization at a supraglacial spring system in the Canadian High Arctic. Geobiology 9, 360-375.

Gorlas, A., Marguet, E., Gill, S., Geslin, C., Guigner, J.-M., Guyot, F. and Forterre, P. (2015) Sulfur vesicles from Thermococcales: A possible role in sulfur detoxifying mechanisms. Biochimie 118, 356-364.

Grasby, S.E., Allen, C.C., Longazo, T.G., Lisle, J.T., Griffin, D.W. and Beauchamp, B. (2003) Supraglacial sulfur springs and associated biological activity in the Canadian high arctic—signs of life beneath the ice. Astrobiology 3, 583-596.

Griebel, J.J., Glass, R.S., Char, K. and Pyun, J. (2016) Polymerizations with elemental sulfur: A novel route to high sulfur content polymers for sustainability, energy and defense. Progress in Polymer Science 58, 90-125.

Griebel, J.J., Namnabat, S., Kim, E.T., Himmelhuber, R., Moronta, D.H., Chung, W.J., Simmonds, A.G., Kim, K.-J., van der Laan, J., Nguyen, N.A., Dereniak, E.L., Mackay, M.E., Char, K., Glass, R.S., Norwood, R.A. and Pyun, J. (2014) New Infrared Transmitting Material via Inverse Vulcanization of Elemental Sulfur to Prepare High Refractive Index Polymers. Advanced Materials 26, 3014-3018.

Guerrero, R., Mas, J. and Pedrós-Alió, C. (1984) Buoyant density changes due to intracellular content of sulfur in Chromatium warmingii and Chromatium vinosum. Archives of microbiology 137, 350-356.

Gunther, F.A. (1966) Advances in analytical detection of pesticides. Scientific aspects of pest control, 276-302.

Habashi, F. (2009) Recent trends in extractive metallurgy. Journal of Mining and Metallurgy, Section B: Metallurgy 45, 1-13.

Habicht, K.S., Canfield, D.E. and Rethmeier, J.o. (1998) Sulfur isotope fractionation during bacterial reduction and disproportionation of thiosulfate and sulfite. Geochimica et Cosmochimica Acta 62, 2585-2595.

Hageage, G., Eanes, E. and Gherna, R. (1970) X-ray diffraction studies of the sulfur globules accumulated by Chromatium species. Journal of bacteriology 101, 464-469.

Hartler, N., Libert, J. and Teder, A. (1967) Rate of sulfur dissolution in aqueous sodium sulfide. Industrial & Engineering Chemistry Process Design and Development 6, 398-406.

Heitmann, T. and Blodau, C. (2006) Oxidation and incorporation of hydrogen sulfide by dissolved organic matter. Chemical Geology 235, 12-20.

Hofmann, J.B. (1974) Ετυμολογικό λεξικό της Αρχαίας Ελληνικής. Atena.

Holmer, M. and Storkholm, P. (2001) Sulphate reduction and sulphur cycling in lake sediments: a review. Freshwater Biology 46, 431-451.

Ingledew, W.J. (1982) Thiobacillus ferrooxidans the bioenergetics of an acidophilic chemolithotroph. Biochimica et Biophysica Acta (BBA)-Reviews on Bioenergetics 683, 89-117.

Jamal, A., Moon, Y.-S. and Zainul Abdin, M. (2010) Sulphur-a general overview and interaction with nitrogen. Australian Journal of Crop Science 4, 523.

Jannaris, A. (1907) The Digamma, Koppa, and Sampi as Numerals in Greek. The Classical Quarterly 1, 37-40.

Janssen, A., De Keizer, A. and Lettinga, G. (1994) Colloidal properties of a microbiologically produced sulphur suspension in comparison to a LaMer sulphur sol. Colloids and surfaces B: Biointerfaces 3, 111-117.

Janssen, A., De Keizer, A., Van Aelst, A., Fokkink, R., Yangling, H. and Lettinga, G. (1996) Surface characteristics and aggregation of microbiologically produced sulphur particles in relation to the process conditions. Colloids and Surfaces B: Biointerfaces 6, 115-129.

Janssen, A., Lettinga, G. and De Keizer, A. (1999) Removal of hydrogen sulphide from wastewater and waste gases by biological conversion to elemental sulphur: colloidal and interfacial aspects of biologically produced sulphur particles. Colloids and Surfaces A: Physicochemical and Engineering Aspects 151, 389-397.

Jones, W.H.S., Potter, P., Withington, E.T. and Smith, W.D. (1995) Hippocrates VIII. Harvard University Press.

Jorgensen, B.B., Kuenen, J.G. and Cohen, Y. (1979) Microbial transformations of sulfur compounds in a stratified lake (Solar Lake, Sinai). Limnology and Oceanography 24, 799-822.

Kamyshny, A. (2009) Solubility of cyclooctasulfur in pure water and sea water at different temperatures. Geochimica et Cosmochimica Acta 73, 6022-6028.

Kamyshny, A., Borkenstein, C.G. and Ferdelman, T.G. (2009) Protocol for Quantitative Detection of Elemental Sulfur and Polysulfide Zero-Valent Sulfur Distribution in Natural Aquatic Samples. Geostandards and Geoanalytical Research 33, 415-435.

Kamyshny, A., Ekeltchik, I., Gun, J. and Lev, O. (2006) Method for the determination of inorganic polysulfide distribution in aquatic systems. Analytical chemistry 78, 2631-2639.

Kamyshny, A., Goifman, A., Gun, J., Rizkov, D. and Lev, O. (2004b) Equilibrium distribution of polysulfide ions in aqueous solutions at 25° C: a new approach for the study of polysulfides' equilibria. Environmental science & technology 38, 6633-6644.

Kamyshny, A., Goifman, A., Rizkov, D. and Lev, O. (2003) Kinetics of disproportionation of inorganic polysulfides in undersaturated aqueous solutions at environmentally relevant conditions. Aquatic Geochemistry 9, 291-304.

Kamyshny, A., Gun, J., Rizkov, D., Voitsekovski, T. and Lev, O. (2007) Equilibrium distribution of polysulfide ions in aqueous solutions at different temperatures by rapid single phase derivatization. Environmental science & technology 41, 2395-2400.

Kaplan, I.R. and Hulston, J.R. (1966) The isotopic abundance and content of sulfur in meteorites. Geochimica et Cosmochimica Acta 30, 479-496.

Kasting, J.F., Zahnle, K., Pinto, J. and Young, A. (1989) Sulfur, ultraviolet radiation, and the early evolution of life. Origins of Life and Evolution of Biospheres 19, 95-108.

Kelly, D. (1989) Oxidation of sulphur compounds, in: Cole, J.A.F., S. (Ed.), Society for General Microbiology Symposium 42. Cambridge University Press, pp. 65-98.

Kleinjan, W.E., de Keizer, A. and Janssen, A.J. (2003) Biologically produced sulfur. Elemental sulfur and sulfur-rich compounds I, 44-57.

Kleinjan, W.E., de Keizer, A. and Janssen, A.J. (2005a) Equilibrium of the reaction between dissolved sodium sulfide and biologically produced sulfur. Colloids and Surfaces B: Biointerfaces 43, 228-237.

Kleinjan, W.E., de Keizer, A. and Janssen, A.J. (2005b) Kinetics of the reaction between dissolved sodium sulfide and biologically produced sulfur. Industrial & engineering chemistry research 44, 309-317.

Knickerbocker, C., Nordstrom, D. and Southam, G. (2000) The role of "blebbing" in overcoming the hydrophobic barrier during biooxidation of elemental sulfur by Thiobacillus thiooxidans. Chemical Geology 169, 425-433.

Konishi, Y., Takasaka, Y. and Asai, S. (1994) Kinetics of growth and elemental sulfur oxidation in batch culture of Thiobacillus ferrooxidans. Biotechnology and bioengineering 44, 667-673.

Lan, Y., Deng, B., Kim, C., Thornton, E.C. and Xu, H. (2005) Catalysis of elemental sulfur nanoparticles on chromium (VI) reduction by sulfide under anaerobic conditions. Environmental science & technology 39, 2087-2094.

Lau, G.E., Cosmidis, J., Grasby, S.E., Trivedi, C.B., Spear, J.R. and Templeton, A.S. (2017) Low-temperature formation and stabilization of rare allotropes of cyclooctasulfur (β-S 8 and γ-S 8) in the presence of organic carbon at a sulfur-rich glacial site in the Canadian High Arctic. Geochimica et Cosmochimica Acta 200, 218-231.

Lee, Y.-J., Prange, A., Lichtenberg, H., Rohde, M., Dashti, M. and Wiegel, J. (2007) In situ analysis of sulfur species in sulfur globules produced from thiosulfate by Thermoanaerobacter sulfurigignens and Thermoanaerobacterium thermosulfurigenes. Journal of bacteriology 189, 7525-7529.

Lefroy, R. and Blair, G. (1997) Influence of sulfur and phosphorus placement, and sulfur particle size, on elemental sulfur oxidation and the growth response of maize (Zea mays). Australian journal of agricultural research.

Li, W., Wu, X., Zhao, Z., Qin, A., Hu, R. and Tang, B.Z. (2015) Catalyst-free, atom-economic, multicomponent polymerizations of aromatic diynes, elemental sulfur, and aliphatic diamines toward luminescent polythioamides. Macromolecules 48, 7747-7754.

Licht, S. and Davis, J. (1997) Disproportionation of aqueous sulfur and sulfide: kinetics of polysulfide decomposition. The Journal of Physical Chemistry B 101, 2540-2545.

Lim, J., Pyun, J. and Char, K. (2015) Recent approaches for the direct use of elemental sulfur in the synthesis and processing of advanced materials. Angewandte Chemie International Edition 54, 3249-3258.

Lin, A.N., Reimer, R.J. and Carter, D.M. (1988) Sulfur revisited. Journal of the American Academy of Dermatology 18, 553-558.

Lovley, D.R. and Phillips, E.J. (1994) Novel processes for anaerobic sulfate production from elemental sulfur by sulfate-reducing bacteria. Applied and Environmental Microbiology 60, 2394-2399.

Luther, G.W., Church, T.M. and Powell, D. (1991) Sulfur speciation and sulfide oxidation in the water column of the Black Sea. Deep Sea Research Part A. Oceanographic Research Papers 38, S1121-S1137.

Luther III, G.W., Findlay, A.J., MacDonald, D.J., Owings, S.M., Hanson, T.E., Beinart, R.A. and Girguis, P.R. (2011) Thermodynamics and kinetics of sulfide oxidation by oxygen: a look at inorganically controlled reactions and biologically mediated processes in the environment. Frontiers in microbiology 2.

Luther III, G.W., Glazer, B., Ma, S., Trouwborst, R., Shultz, B.R., Druschel, G. and Kraiya, C. (2003) Iron and sulfur chemistry in a stratified lake: Evidence for iron-rich sulfide complexes. Aquatic Geochemistry 9, 87-110.

Luther III, G.W., Glazer, B.T., Hohmann, L., Popp, J.I., Taillefert, M., Rozan, T.F., Brendel, P.J., Theberge, S.M. and Nuzzio, D.B. (2001) Sulfur speciation monitored in situ with solid state gold amalgam voltammetric microelectrodes: polysulfides as a special case in sediments, microbial mats and hydrothermal vent

watersPresented at the Whistler 2000 Speciation Symposium, Whistler Resort, BC, Canada, June 25–July 1, 2000. Electronic Supplementary Information available. See http://www. rsc. org/suppdata/em/b0/b006499h. Journal of Environmental Monitoring 3, 61-66.

Mas, J. and Van Gemerden, H. (1987) Influence of sulfur accumulation and composition of sulfur globule on cell volume and buoyant density of Chromatium vinosum. Archives of microbiology 146, 362-369.

Meyer, B. (1964) Solid allotropes of sulfur. Chemical Reviews 64, 429-451.

Meyer, B. (1976) Elemental sulfur. Chemical Reviews 76, 367-388.

Michie, C.A. and Langslow, D.R. (1988) Sulphur or sulfur? A tale of two spellings. BMJ : British Medical Journal 297, 1697-1699.

Milucka, J., Ferdelman, T.G., Polerecky, L., Franzke, D., Wegener, G., Schmid, M., Lieberwirth, I., Wagner, M., Widdel, F. and Kuypers, M.M. (2012) Zero-valent sulphur is a key intermediate in marine methane oxidation. Nature 491, 541.

Moser, D.P. and Nealson, K.H. (1996) Growth of the facultative anaerobe Shewanella putrefaciens by elemental sulfur reduction. Applied and Environmental Microbiology 62, 2100-2105.

Müller, H. (2000) Sulfur Dioxide, Ullmann's Encyclopedia of Industrial Chemistry. Wiley-VCH Verlag GmbH & Co. KGaA.

Nagy, B. and Bitz, S.M.C. (1963) Long-chain fatty acids from the Orgueil meteorite. Archives of Biochemistry and Biophysics 101, 240-248.

Nehb, W. and Vydra, K. (2006) Sulfur. Ullmann's Encyclopedia of Industrial Chemistry.

Nelson, R.M., Smythe, W.D., Hapke, B.W. and Cohen, A.J. (1990) On the effect of X rays on the color of elemental sulfur: Implications for Jupiter's satellite Io. Icarus 85, 326-334.

Nicolson, G.L. and Schmidt, G.L. (1971) Structure of the Chromatium sulfur particle and its protein membrane. Journal of bacteriology 105, 1142-1148.

Nor, Y.M. and Tabatabai, M. (1977) Oxidation of elemental sulfur in soils. Soil Science Society of America Journal 41, 736-741.

Nordstrom, D.K., McCleskey, R.B. and Ball, J.W. (2009) Sulfur geochemistry of hydrothermal waters in Yellowstone National Park: IV Acid–sulfate waters. Applied Geochemistry 24, 191-207.

Parry, M. (1934) The Traces of the Digamma in Ionic and Lesbian Greek. Language 10, 130-144.

Partington, J.R. (1960) A history of Greek fire and gunpowder. JHU Press.

Pasteris, J.D., Freeman, J.J., Goffredi, S.K. and Buck, K.R. (2001) Raman spectroscopic and laser scanning confocal microscopic analysis of sulfur in living sulfur-precipitating marine bacteria. Chemical Geology 180, 3-18.

Pohl, H.L., John; Iannucci, Annette (1998) Toxicological Profile for Sulfur Dioxide. U.S. Department of Helath and Human Services: Public Health Service - Agency for Toxic Substances and Disease Registry.

Pomerantz, A.E., Bake, K.D., Craddock, P.R., Kurzenhauser, K.W., Kodalen, B.G., Mitra-Kirtley, S. and Bolin, T.B. (2014) Sulfur speciation in kerogen and bitumen from gas and oil shales. Organic Geochemistry 68, 5-12.

Poser, A., Lohmayer, R., Vogt, C., Knoeller, K., Planer-Friedrich, B., Sorokin, D., Richnow, H.-H. and Finster, K. (2013) Disproportionation of elemental sulfur by haloalkaliphilic bacteria from soda lakes. Extremophiles 17, 1003.

Potter, P. (1995) Hippocrates. Harvard University Press.

Prange, A., Arzberger, I., Engemann, C., Modrow, H., Schumann, O., Trüper, H.G., Steudel, R., Dahl, C. and Hormes, J. (1999) In situ analysis of sulfur in the sulfur globules of phototrophic sulfur bacteria by X-ray absorption near edge spectroscopy. Biochimica et Biophysica Acta (BBA)-General Subjects 1428, 446-454.

Prange, A., Chauvistre, R., Modrow, H., Hormes, J., Trüper, H.G. and Dahl, C. (2002) Quantitative speciation of sulfur in bacterial sulfur globules: X-ray absorption spectroscopy reveals at least three different species of sulfur. Microbiology 148, 267-276.

Raffo, M. (1908) Ueber kolloiden Schwefel. Colloid & Polymer Science 2, 358-360.

Rasheed, M., Ali, H. and Mahmood, T. (2004) Impact of nitrogen and sulfur application on growth and yield of maize (Zea mays L.) crop. J. Res. Sci 15, 153-157.

Rickard, D. and Luther, G.W. (2007) Chemistry of Iron Sulfides. Chemical Reviews 107, 514-562.

Russell, M.S. (2009) The chemistry of fireworks. Royal Society of Chemistry.

Schoen, R. and Rye, R.O. (1970) Sulfur isotope distribution in solfataras, Yellowstone National Park. Science 170, 1082-1084.

Schulz, H.N. and Schulz, H.D. (2005) Large sulfur bacteria and the formation of phosphorite. Science 307, 416-418.

Schulze-Makuch, D., Grinspoon, D.H., Abbas, O., Irwin, L.N. and Bullock, M.A. (2004) A sulfur-based survival strategy for putative phototrophic life in the Venusian atmosphere. Astrobiology 4, 11-18.

Selmi, F. (1852) Sur le soufre pseudosoluble, sa pseudosolution et le soufre mou. Jour. f. prakt. Chem 57, 49-57.

Sgantzos, M., Tsoucalas, G., Karamanou, M., Giatsiou, S., Tsoukalas, I. and Androutsos, G. (2015) Hippocrates on Pediatric Dermatology. Pediatric Dermatology 32, 600-603.

Shivvers, D.W. and Brock, T.D. (1973) Oxidation of elemental sulfur by Sulfolobus acidocaldarius. Journal of bacteriology 114, 706-710.

Sholeh, Lefroy, R.D.B. and Blair, G.J. (1997) Effect of nutrients and elemental sulfur particle size on elemental sulfur oxidation and the growth of Thiobacillus thiooxidans. Australian Journal of Agricultural Research 48, 497-502.

Simmonds, A.G., Griebel, J.J., Park, J., Kim, K.R., Chung, W.J., Oleshko, V.P., Kim, J., Kim, E.T., Glass, R.S. and Soles, C.L. (2014) Inverse vulcanization of elemental sulfur to prepare polymeric electrode materials for Li–S batteries. ACS Macro Letters 3, 229-232.

Slowey, A.J. and Brown, G.E. (2007) Transformations of mercury, iron, and sulfur during the reductive dissolution of iron oxyhydroxide by sulfide. Geochimica et Cosmochimica Acta 71, 877-894.

Smith, R.L. and Klug, M.J. (1981) Reduction of sulfur compounds in the sediments of a eutrophic lake basin. Applied and Environmental Microbiology 41, 1230-1237.

Smyth, H.W. (1891) On Digamma in Post-Homeric Ionic. The American Journal of Philology 12, 211-220.

Soares, M. (2002) Denitrification of groundwater with elemental sulfur. Water Research 36, 1392-1395.

Sprague, A.L., Hunten, D.M. and Lodders, K. (1995) Sulfur at Mercury, elemental at the poles and sulfides in the regolith. Icarus 118, 211-215.

Steudel, R. (1989) On the nature of the "elemental sulfur"(S0) produced by sulfur-oxidizing bacteria—a model for S0 globules. Autotrophic bacteria, 289-303.

Steudel, R. (1996) Mechanism for the formation of elemental sulfur from aqueous sulfide in chemical and microbiological desulfurization processes. Industrial & engineering chemistry research 35, 1417-1423.

Steudel, R. (2000a) The chemical sulfur cycle. Environmental technologies to treat sulfur pollution, 1-31.

Steudel, R. (2000b) Environmental technologies to treat sulfur pollution. Edited by Lens PN, Hulshoff W. London: IWA Publishing 1, 31.

Steudel, R. (2003) Aqueous Sulfur Sols, in: Steudel, R. (Ed.), Elemental Sulfur and Sulfur-Rich Compounds I. Springer Berlin Heidelberg, Berlin, Heidelberg, pp. 153-166.

Steudel, R. and Albertsen, A. (1999) The chemistry of aqueous sulfur sols–models for bacterial sulfur globules. Biochemical Principles and Mechanisms of Biosynthesis and Biodegradation of Polymers, 17-26.

Steudel, R. and Eckert, B. (2003) Solid sulfur allotropes, Elemental sulfur and sulfur-rich compounds I. Springer, pp. 1-80.

Steudel, R., Göbel, T. and Holdt, G. (1988) The molecular composition of hydrophilic sulfur sols prepared by acid decomposition of thiosulfate [1]. Zeitschrift für Naturforschung B 43, 203-218.

Steudel, R. and Holdt, G. (1988) Solubilization of elemental sulfur in water by cationic and anionic surfactants. Angewandte Chemie International Edition 27, 1358-1359.

Steudel, R., Holdt, G., Göbel, T. and Hazeu, W. (1987) Chromatographic separation of higher polythionates SnO 62⊖(n= 3… 22) and their detection in cultures of Thiobacillus ferroxidans; Molecular composition of bacterial sulfur secretions. Angewandte Chemie International Edition 26, 151-153.

Steudel, R., Holdt, G., Visscher, P.T. and van Gemerden, H. (1990) Search for polythionates in cultures of Chromatium vinosum after sulfide incubation. Archives of Microbiology 153, 432-437.

Steudel, R., Mäusle, H.J., Rosenbauer, D., Möckel, H. and Freyholdt, T. (1981) Separation and determination of sulfur homocycles by high pressure liquid chromatography—Detection of novel sulfur rings. Angewandte Chemie International Edition 20, 394-395.

Strauss, R. and Steudel, R. (1987) Schnelle chromatographische Trennung und Bestimmung der Schwefel-Homocyclen S n (n= 6− 28) mittels HPLC. Fresenius' Journal of Analytical Chemistry 326, 543-546.

Strohl, W.R., Geffers, I. and Larkin, J.M. (1981) Structure of the sulfur inclusion envelopes from four Beggiatoas. Current Microbiology 6, 75-79.

Suzuki, I. (1999) Oxidation of inorganic sulfur compounds: chemical and enzymatic reactions. Canadian Journal of Microbiology 45, 97-105.

Suzuki, I., Chan, C. and Takeuchi, T. (1992) Oxidation of elemental sulfur to sulfite by Thiobacillus thiooxidans cells. Applied and environmental microbiology 58, 3767-3769.

Teder, A. (1971) The equilibrium between elementary sulfur and aqueous polysulfide solutions. Acta Chem. Scand 25.

Teresa Joseph Murphy, S.M. and Nagy, B. (1966) Analysis for sulfur compounds in lipid extracts from the orgueil meteorite. Journal of the American Oil Chemists' Society 43, 189-196.

Truper, H. and Fischer, U. (1982) Anaerobic oxidation of sulphur compounds as electron donors for bacterial photosynthesis. Philosophical Transactions of the Royal Society B: Biological Sciences 298, 529-542.

Trüper, H.G. and Hathaway, J.C. (1967) Orthorhombic sulphur formed by photosynthetic sulphur bacteria. Nature 215, 435-436.

van den Ende, F.P. and van Gemerden, H. (1993) Sulfide oxidation under oxygen limitation by a Thiobacillus thioparus isolated from a marine microbial mat. FEMS microbiology ecology 13, 69-77.

Vlahovic, M.M., Martinovic, S.P., Boljanac, T.D., Jovanic, P.B. and Volkov-Husovic, T.D. (2011) Durability of sulfur concrete in various aggressive environments. Construction and building materials 25, 3926-3934.

Wang, F., Tessier, A. and Buffle, J. (1998) Voltammetric determination of elemental sulfur in pore waters. Limnology and oceanography 43, 1353-1361.

Ward, L., Taylor, M.W., Power, J.F., Scott, B.J., McDonald, I.R. and Stott, M.B. (2017) Microbial community dynamics in Inferno Crater Lake, a thermally fluctuating geothermal spring. The ISME journal.

Wilbanks, E.G., Jaekel, U., Salman, V., Humphrey, P.T., Eisen, J.A., Facciotti, M.T., Buckley, D.H., Zinder, S.H., Druschel, G.K. and Fike, D.A. (2014) Microscale sulfur cycling in the phototrophic pink berry consortia of the Sippewissett Salt Marsh. Environmental microbiology 16, 3398-3415.

Williams, J. and Cooper, R. (2004) The oldest fungicide and newest phytoalexin–a reappraisal of the fungitoxicity of elemental sulphur. Plant Pathology 53, 263-279.

Xu, Y., Schoonen, M., Nordstrom, D., Cunningham, K. and Ball, J. (1998) Sulfur geochemistry of hydrothermal waters in Yellowstone National Park: I. The origin of thiosulfate in hot spring waters. Geochimica et Cosmochimica Acta 62, 3729-3743.

Xu, Y., Schoonen, M., Nordstrom, D., Cunningham, K. and Ball, J. (2000) Sulfur geochemistry of hydrothermal waters in Yellowstone National Park, Wyoming, USA. II. Formation and decomposition of thiosulfate and polythionate in Cinder Pool. Journal of Volcanology and Geothermal Research 97, 407-423.

Zavarzina, D., Zhilina, T., Tourova, T., Kuznetsov, B., Kostrikina, N. and Bonch-Osmolovskaya, E. (2000) Thermanaerovibrio velox sp. nov., a new anaerobic, thermophilic, organotrophic bacterium that reduces elemental sulfur, and emended description of the genus Thermanaerovibrio. International journal of systematic and evolutionary microbiology 50, 1287-1295.

Zhang, C., Wu, H.B., Yuan, C., Guo, Z. and Lou, X.W.D. (2012) Confining sulfur in double-shelled hollow carbon spheres for lithium–sulfur batteries. Angewandte Chemie 124, 9730-9733.

Zheng, Z. and Obbard, J.P. (2002) Evaluation of an elevated non-ionic surfactant critical micelle concentration in a soil/aqueous system. Water Research 36, 2667-2672.

Zhu, L., Yang, K., Lou, B. and Yuan, B. (2003) A multi-component statistic analysis for the influence of sediment/soil composition on the sorption of a nonionic surfactant (Triton X-100) onto natural sediments/soils. Water Research 37, 4792-4800.

Zopfi, J., Ferdelman, T. and Fossing, H. (2004) Distribution and fate of sulfur intermediates—sulfite, tetrathionate, thiosulfate, and elemental sulfur—in marine sediments. Geological Society of America Special Papers 379, 97-116.

CHAPTER-2 – ELECTROANALYTICAL CHEMISTRY OF ELEMENTAL SULFUR

Introduction

Elemental sulfur (S^0) is an important intermediate in the global sulfur cycle, playing a role in a wide range of geological and biological reactions. Sulfur is the zero-valent intermediate species (S^0) of the sulfur system, spanning 8 e^- transformations between S(-II) up to S(+VI). Elemental sulfur is present in numerous natural environments, including hydrothermal systems (Gartman et al., 2011), marine (Yücel et al., 2010) and freshwater aqueous bodies and sediments (Bura-Nakić et al., 2009; Nriagu and Soon, 1985), ice systems (Lau et al., 2017), soils (Nor and Tabatabai, 1977), as well as extraterrestrial systems such as meteorites (Kaplan and Hulston, 1966) and exoplanets (Antonelli et al., 2014). The formation of elemental sulfur is a result of several possible pathways, including oxidation, reduction and disproportionation reactions, both abiotic and linked to microbial metabolisms (Kleinjan et al., 2003; Luther III et al., 2011; Schulz and Schulz, 2005; Steudel, 1996). Microbial communities also utilize elemental sulfur as a key nutrient for the satisfaction of their metabolic needs (Böttcher et al., 2001; Canfield and Thamdrup, 1994; Dahl and Friedrich, 2008; Finster et al., 1998; Konishi et al., 1994; Poser et al., 2013; Shivvers and Brock, 1973; Suzuki et al., 1992). Due to its transformation via abiotic or microbially-mediated redox cycling, elemental sulfur can play a key role as an intermediate in the overall biogeochemical cycling of sulfur, which in turn influences other element cycles such as carbon and iron (Raven et al., 2015; Rickard and Luther, 2007).

Cyclic voltammetry on Au-amalgam working electrodes is a valuable *in situ* technique for the analysis of electroactive species of sulfur as well as other redox active systems with fine spatial and temporal resolution (Luther et al., 2008; Lutz et al., 2008; Yücel et al., 2013). Electroactive species able to be identified based on their peak potential (E_p) include: sulfide and polysulfides (E_p=~ -0.70 and ~-0.68V, respectively, with pH dependence), elemental sulfur (S^0, E_p=-0.78V), thiosulfate ($S_2O_3^{2-}$, E_p=-0.12V), sulfite (SO_3^{2-}, E_p=-0.60V), trithionate ($S_3O_6^{2-}$, E_p=-0.29V), tetrathionate ($S_4O_6^{2-}$, E_p=-0.37V),

disulfite ($S_2O_5^{2-}$, E_p=-0.50V), sulfurous acid (H_2SO_3, E_p=-0.42V), and hydrogen thiosulfate ($HS_2O_3^{2-}$, E_p=-0.20V), whereas the species Fe^{2+} (E_p=-1.43V), Fe^{3+} (E_p=-0.25V), FeS_{aq} (E_p=-1.1V), Mn^{2+} (E_p=-1.55), O_2 (E_p=-0.3V), and H_2O_2 (E_p=-1.3V) are also able to be identified (Ciglenečki and Ćosović, 1996; Druschel et al., 2003; Gartman et al., 2011; Luther et al., 1985; Luther et al., 2003; Rozan et al., 2000; Theberge and Luther III, 1997; Wang et al., 1998). The natural environments in which voltammetric techniques have been utilized include: lake and seawater columns (Bura-Nakić et al., 2009; Ciglenečki and Ćosović, 1996; Ciglenečki et al., 1996; Glazer et al., 2006; Luther et al., 1991; Luther et al., 2003), sediment pore waters (Carey and Taillefert, 2005; Wang et al., 1998; Yücel et al., 2010), deep and shallow marine hydrothermal systems (Gartman et al., 2011; Gilhooly et al., 2014; Luther et al., 2008; Luther III et al., 2001a; Luther III et al., 2001b), as well as terrestrial geothermal springs (Boyd and Druschel, 2013; Clingenpeel et al., 2009; D'Imperio et al., 2008).

Bura-Nagic et al., 2009 utilized voltammetry to identify reduced sulfur species, in the anoxic monimolimnion layer of Lake Pavin, and quantified S^0 at -0.60V peak by subtracting the intensities with and without acidification and N_2-purging (to remove all di-hydrogen sulfide)(Bura-Nakić et al., 2009). Ciglenecki et al., (1996) detected zero-valent sulfur by reduction peaks at approximately -0.65V and -0.35V in the water column of a sea lake. They attributed the accumulations of S^0 in the oxic and anoxic zone of the water column to S_8 and polysulfides, respectively (Ciglenečki et al., 1996). The same peak of ~-0.60V has been utilized for the detection of the zero-valent moieties of polysulfides in marine hydrothermal vents (Gartman et al., 2011; Waite et al., 2008), microbial mats (Glazer et al., 2002; Luther et al., 2008; Luther III et al., 2001b), and seawater columns (Glazer et al., 2006).

The absorption of S^0 onto Hg on a Hg-Au working electrode surface, due to its high affinity for Hg, results in the oxidation of elemental mercury to Hg^{2+} and the reduction of S^0 to sulfide, forming a HgS complex at potentials more positive than ~-0.60V. This is followed by the reduction of HgS and the consequent formation of elemental mercury and S^{2-} ions that allows for their detection at E_p= ~-0.60V (Batina et al., 1992; Gartman et al., 2011; Glazer et al., 2006; Luther et al., 2008):

$S^0 + Hg \rightarrow HgS$ (adsorption onto Hg; E_p= < -0.60V) (1)

$HgS + H^+ + 2e^- \leftrightarrow HS^- + Hg$ (E_p= ~-0.60V) (2)

The reactions 1 and 2 taking place on the surface of mercury-plated gold working electrodes (for details of working electrode preparation see (Luther et al., 2008)), are believed to involve not only the dissolved elemental sulfur (S_{8aq}), but also the zero-valent sulfur portion of the polysulfide ions (Rozan et al., 2000), as mentioned above. The voltammetric signal of powder elemental sulfur using linear sweep voltammetry on a Hanging Drop Mercury Electrode (HDME) has been found to incorporate the reduction peak at ~-0.7V, which is close to the reduction potential described at reaction 2, as well as two reduction peaks at -0.85V and -1.0V that are characteristic of the solid form of the elemental sulfur globules (Bura-Nakić et al., 2007). Furthermore, microcrystalline elemental sulfur (S_8) is represented by peaks in the area of -1.1V to -1.35V as a function of its size, with the more negative peak representing microcrystalline S_8 that passed through a 0.45μm filter (Boyd and Druschel, 2013; Luther III et al., 2001b). Voltammetric identification of elemental sulfur shows dependence on pH for the potential of the -0.6V signal of zero-valent sulfur (Wang et al., 1998).

In summary, extensive work has been conducted by many authors on the voltammetric characterization of aqueous S_{8aq}, microcrystalline α-S_8, as well as polysulfidic zero-valent S^0. However, there is lack of information regarding the voltammetric responses of various forms of nanoparticulate elemental sulfur, including the nanoparticulate forms of S_{8nano}, in which the surface area, character and coatings may vary. In this study, an evaluation of the electroanalytical chemistry of elemental sulfur has been established to better understand the dynamics of sulfur cycling in field and lab experiments. Voltammetric signals corresponding to specific forms of elemental sulfur of various particle sizes, surface character, and surfactant coatings, have been investigated under appropriate physical-chemical conditions. A database of voltammetric signals is provided for the accurate determination of elemental sulfur species in aqueous systems.

Experimental work

Cyclic voltammetry (CV) measurements took place by utilizing the Analytical Instrument Systems (AIS) model DLK-100 and DLK-70 electrochemical analyzers connected to the Princeton EG&G Model 303A Hanging-Drop Mercury Electrode (HDME) stand. The reference electrode used was an Ag/AgCl electrode, the counter electrode was a platinum wire. Scans were acquired in quintuplet groups (five replicates) at a scan rate of 1000mV/sec from -0.1V to -1.8V and back to -0.1V versus the Ag/AgCl reference, with a 2 seconds conditioning step at -0.1V (deposition step), and with a holding potential of -0.9 volts. For the experiments that evaluated the effect of deposition time, the duration of conditioning step at -0.1V was varied between zero and 10 seconds.

Solutions were made anaerobic by extensive purging with N_2, and anaerobic conditions were maintained during experiments with a constant stream of N_2 applied to the headspace above the reaction cell. Temperature effect experiments, and room-temperature S_{8aq} voltammetry analyses were conducted by adding sulfur flour (Fischer Scientific Inc.) in 0.1M KCl solution made of Milli-Q water (>18MΩ) which was equilibrated overnight with stirring. The α-S_8 suspension was allowed to settle for a few hours prior to removal of supernatant and its filtering through 0.22μm pore size filters. Dynamic Light Scattering measurements confirmed there were no particles in this supernatant. The desired temperature of the solution was achieved by the use of a temperature-controlled hot bath. The α-S_8/0.1M KCl suspension was also used without filtering and after homogenization (via shaking) in order to investigate the voltammetric signal of α-S_8. The voltammetric signal of α-S_8 presence of surfactant molecules took place via the addition of the corresponding surfactant in the above α-S_8/0.1M KCl suspension to prepare solutions of 1% w/w BSDS, SDS, CTAB, and TX-100 (Table 2-1). Weimarn sols were prepared by dilution of sulfur-saturated methanol into aqueous solutions. The aqueous solutions used for the preparation of the $S_{8weimarn}$ were made of Milli-Q water (>18MΩ), 27.37mM NaCl, and 13.23mM PIPES. Raffo nanoparticles were prepared by acidifying a 164mM thiosulfate solution by the addition of 500μL of 1M HCl to initiate the chain elongation and cyclization reactions that form S_{8raffo} (Steudel, 2003a). After the preparation of S_{8raffo},

an aliquot of the S_{8raffo} solution was added to a buffered solution including 0.041M $HCO3^-$, 0.018M NaOH, and 0.010M NaCl.

Table 2-1 : Surfactant compounds used in this study

Annotation	Name	Chemical Formula	Type
BSDS	sodium dodecyl benzene sulphonate	$CH_3(CH_2)_{11}C_6H_4SO_3Na$	Anionic
SDS	sodium dodecyl sulfate	$C_{12}H_{25}NaSO_4$	Anionic
CTAB	hexadecyltrimethylammonium bromide	$(C_{16}H_{33})N(CH_3)_3]Br$	Cationic
TX-100	polyethylene glycol octylphenyl ether	$C_{14}H_{22}O(C_2H_4O)_n$	Non-ionic

Elemental sulfur analyses took place by sampling aliquots from experimental solutions and diluting 50% in HPLC-grade methanol to dissolve all S_{8nano}. Then S_8 was detected with reverse phase HPLC using an Acclaim 120, 5 μm particle size, 100mm long C18 column, following an isocratic method with 100% MeOH as eluent at a flow rate of 1ml/min. Detection of S_8 took place at a retention time of 3min, whereas the linear calibration curve was established using standard solutions of cyclo-octasulfur (S_8) with concentrations ranging from 5μM to 2mM S^0.

Dynamic light scattering (DLS) was utilized in order to characterize the size of elemental sulfur nanoparticles using a Beckman-Coulter DelsaNano C which applies photo correlation spectroscopy (PCS) to estimate nanoparticle diameter (Pecora, 2000). Mean size and polydispersity (that is the degree of the "non-uniformity" of size in the population) of S_{8nano} were calculated after averaging 70 acquisitions of scattering intensity for each S_{8nano} suspension placed in a cuvette holder. The Delsa Nano software utilizes the CONTIG algorithm to determine particle size distributions, based on an inverse Laplace transformation (Li et al., 2011).

Results

Dissolved (S_{8aq}) and particulate (a-S_8) elemental sulfur

Particulate elemental sulfur in its rhombohedral form (α-S_8) is the most common solid form of sulfur in standard pressure and temperature conditions (Steudel and Eckert, 2003). The peak of α-S_8 located at -0.8V was identified under a turbulent flow of the aqueous medium, which was achieved by using a stirring bar for a few seconds before acquisition (Figure 2-1). Turbulent fluid flow is often found in natural systems such as in Evening Primrose spring of the Yellowstone geothermal system (See Chapter 4). The voltammetric signal of α-S_8 is compared with the S_{8aq} species (-0.55V) as well as the electrolyte solution blank. Similar signals to that of α-S_8 have been shown by Bura-Nakic et al. (2007) for elemental sulfur nanoparticles (Bura-Nakic et al., 2007).

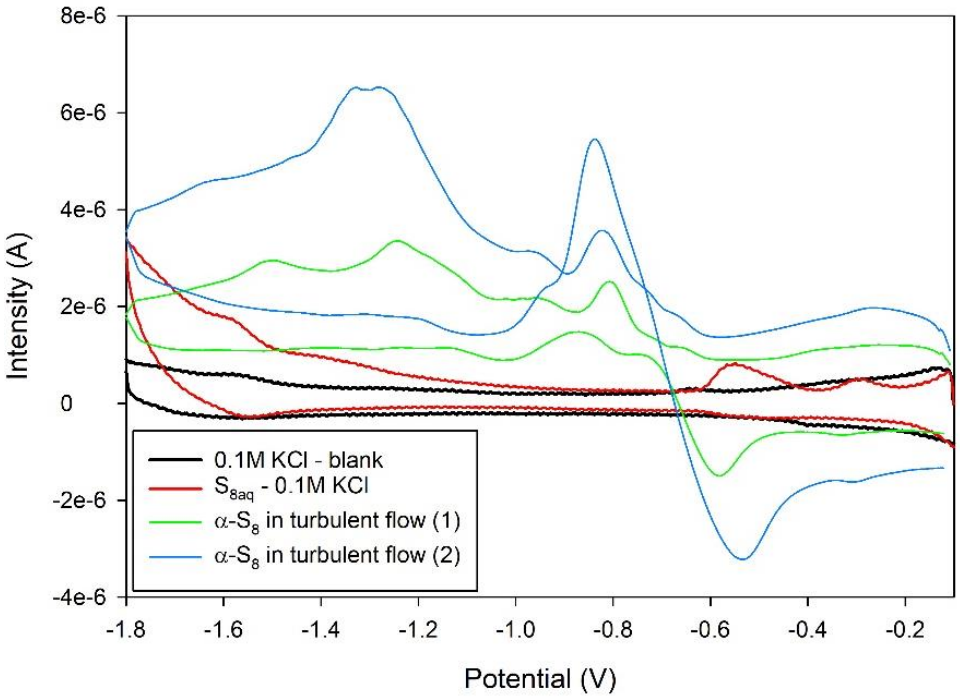

Figure 2-1 : Cyclic voltammetry signals of the a-S_8 suspension in 0.1M KCl with stirring bar to cause turbulent flow (blue and green lines). The signal of the S_{8aq} solution (red line) and the blank 0.1M KCl electrolyte solution (black line) are also shown.

Concentration and pH effects

The effects of elemental sulfur concentration and pH on the electrochemical signal of elemental sulfur compounds were investigated. Figure 2-2 shows the voltammograms of nanoparticulate elemental sulfur, both in the hydrophilic (S_{8raffo}) and the hydrophobic ($S_{8weimarn}$) forms, as well as the voltammetric signal of dissolved S_{8aq}, at pH 10 and 4 (Figure 2-2 top and bottom, respectively). Both $S_{8weimarn}$ and S_{8raffo} are of similar concentrations (864.4μM and 1000μM S^0, respectively), however their signal response is different. This is shown more clearly on their calibration curves of peak intensity (of -0.6V) as a function of concentration of S^0 (Figure 2-3-A). It is apparent that $S_{8weimarn}$ shows greater response in the -0.6V peak intensity as a function of increased concentration compared to S_{8raffo}, with slopes of $S_{8weimarn}$ and S_{8raffo} at 8.01E-09 and 3.34E-09 A/μM, respectively. The effect of intensity on the potential of the voltammetry peak for both S_{8nano} forms was also evaluated (Figure 2-3). Increasing current intensity results in a shift of the peak to more negative potentials for both $S_{8weimarn}$ and S_{8raffo}. $S_{8weimarn}$ has a steeper slope at 8.58E-05 A/V compared to the 3.45E-05 A/V of S_{8raffo} (Figure 2-3-B), corresponding to concentrations of 100 to 800μM S^0 for both types of S_{8nano}. All slopes were tested using a statistical test and found to be statistically significantly different to each other (One way ANCOVA with a p value at 0.0019).

The dependency of the voltammetric signal of various forms of elemental sulfur on pH was assessed. The observation of the overlays of $S_{8weimarn}$, S_{8raffo} and S_{8aq} under various pH conditions showed differences in the position of the -0.6V signal. The peak position of the sulfur species signals changes as a function of the pH conditions (Figure 2-4). Presence of thiosulfate due to the recipe of preparing the hydrophilic S_{8raffo}, is shown in the voltammetric signal at -0.2V (Figure 2-2).

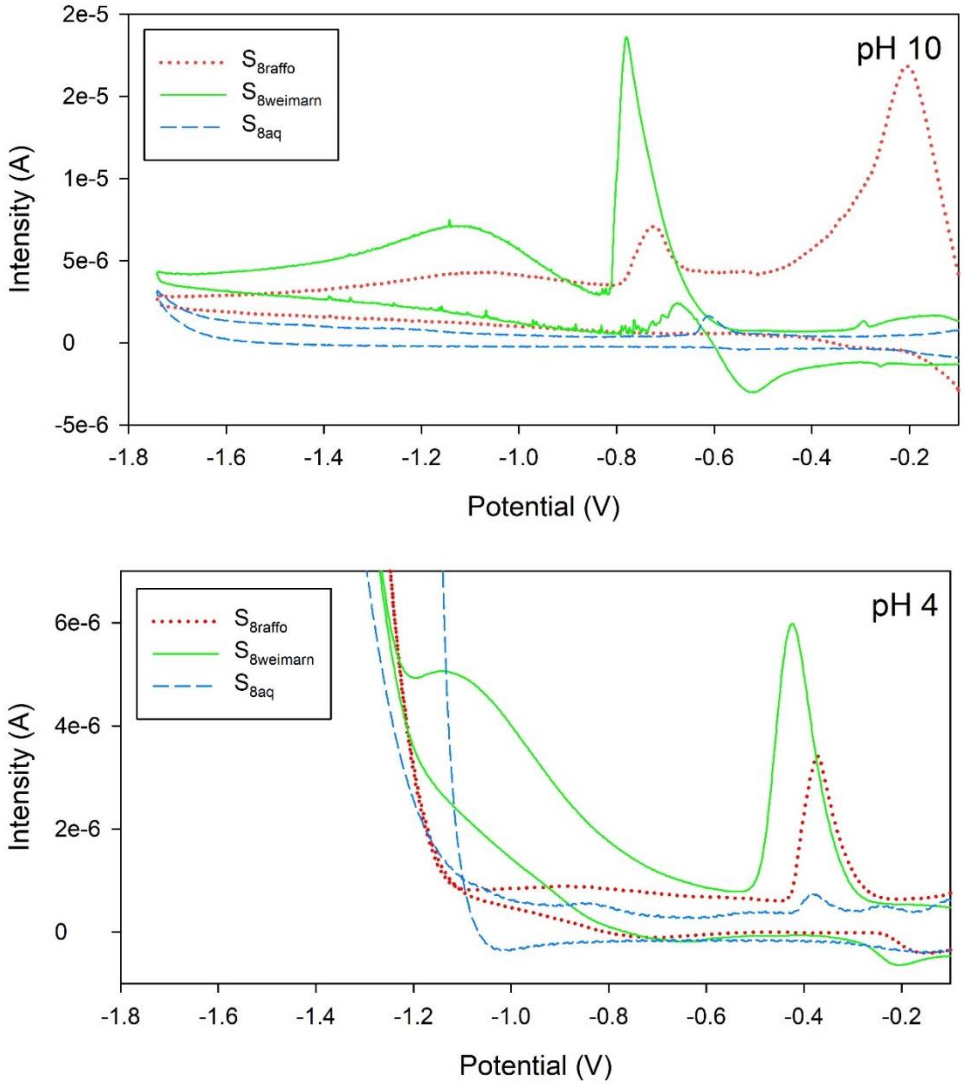

Figure 2-2: Cyclic voltammetry signals of S_{8aq}, 160.4µM S^0 (hydrophobic) $S_{8weimarn}$ and 174µM S^0 (hydrophilic) S_{8raffo} are shown at pH 4 and 10.

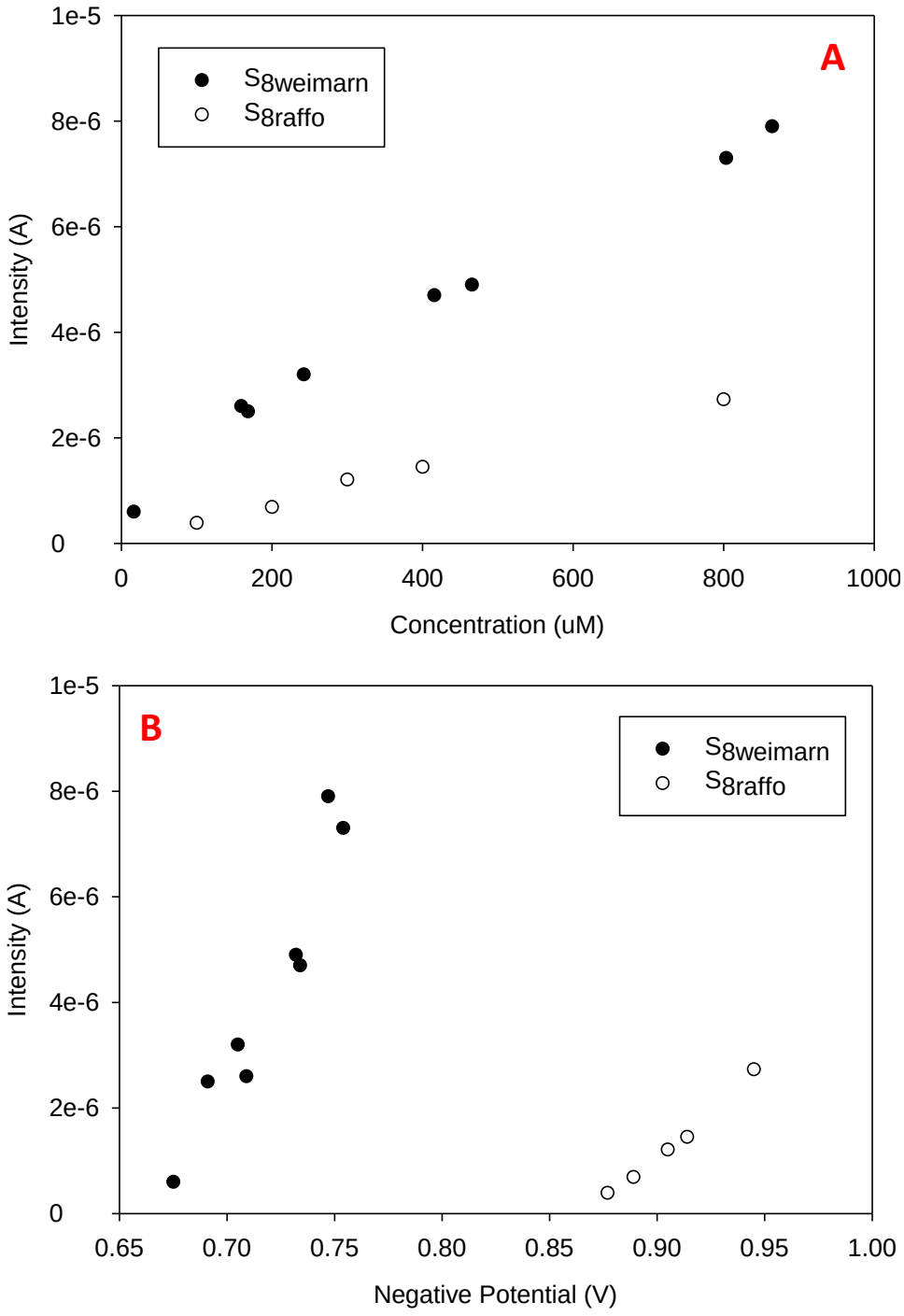

Figure 2-3: The calibration of intensity (A) as a function of concentration (µM S^0) for both (hydrophobic) $S_{8weimarn}$ and (hydrophilic) S_{8raffo} is shown in Figure 2-3-A. The relationship of intensity with negative potential for $S_{8weimarn}$ and S_{8raffo} is shown in Figure 2-3-B.

Figure 2-4 shows the correlation between the peak positions of both -0.6V and -1.2V signals for $S_{8weimarn}$, S_{8raffo} and S_{8aq} as a function of pH of the solution studied (Figure 2-4). The correlations between the position of the "-0.6V" signal and the pH conditions showed linear relationships for the $S_{8weimarn}$, S_{8raffo} as well as S_{8aq}, with slopes at 0.0544x, 0.0461x and 0.0634x, respectively. The slopes were found to be statistically significantly different from each other after being tested using one way ANCOVA test (p values less than 0.05). However the position of the "-1.2V" signal shows no variation with respect to pH of the solution for any form of elemental sulfur studied (Figure 2-4).

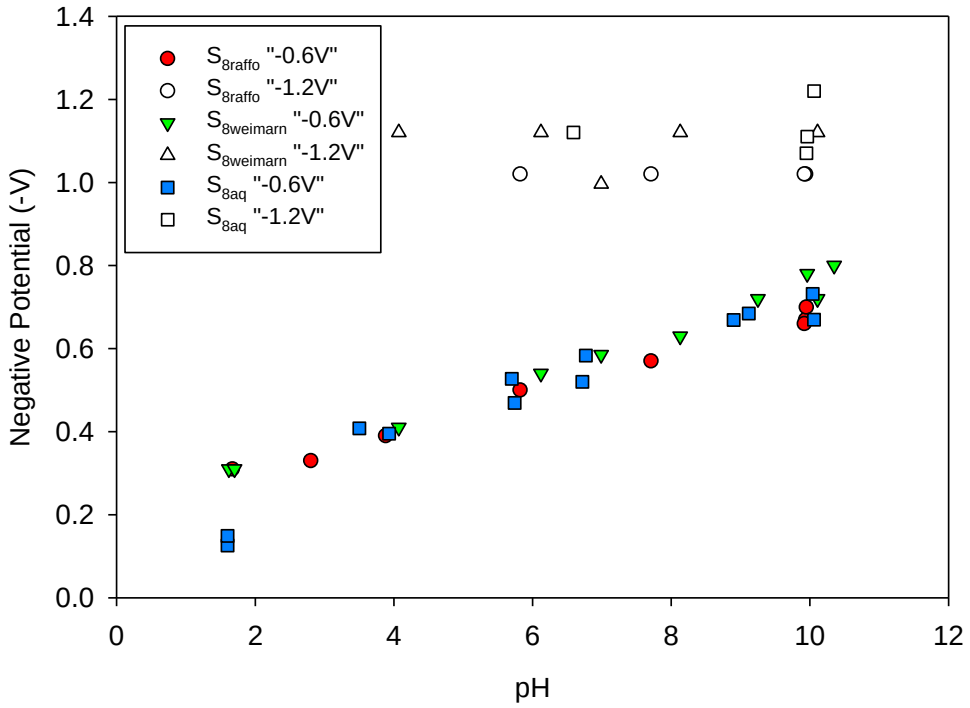

Figure 2-4: The calibration of the negative potential of the "-0.6V" and "-1.2V" signals as a function of pH are shown for S_{8aq}, (hydrophobic) $S_{8weimarn}$ and (hydrophilic) S_{8raffo}.

$S_{8weimarn}$ addition "direction" and methanol effects

$S_{8weimarn}$ is prepared by adding a sulfur-saturated organic phase to an aqueous phase. The direction of adding the aqueous phase into the organic phase has been established as the method that results in monodispersed particles according to (Steudel, 2003a). Furthermore, the (Steudel, 2003a) recipe for the preparation of $S_{8weimarn}$ describes the mixing of 35 parts of aqueous solution into 1 part of organic solution (1:35 ratio). In order to enhance the molarity of S_{total} in the system, a higher ratio of 1:6 has been used. This material has been characterized using DLS for the quantification of its coarsening kinetics, which in the absence of organics is the same with the material resulting from the 1:35 ratio recipe. Figure 2-5 shows the voltammetric signals of $S_{8weimarn}$ at 160.4μM and 864.4μM S^0 after mixing of the aqueous and organic solutions at a 1:6 ratio either organic to aqueous (normal) or aqueous to organic (reverse). Normal addition experiment showed size and polydispersity index of the $S_{8weimarn}$ population at 717.3nm and 0.135, respectively. Reverse addition resulted in size and polydispersity index values of the $S_{8weimarn}$ population at 743.9nm and 0.191, respectively. The voltammetry results show that both the "normal" and "reverse" recipe of $S_{8weimarn}$ result in identical signals at -0.6V and -1.2V, for each concentration of elemental sulfur, respectively.

Figure 2-6 shows the voltammetry signals of various ratios of methanol-to-water ratios under identical concentrations of S^0. The voltammetric signals show no statistically significant differences in potential or current, indicating that methanol does not influence the electrochemical reactions taking place between the cyclo-octasulfur and the mercury electrode, nor does it show any particular interaction with mercury.

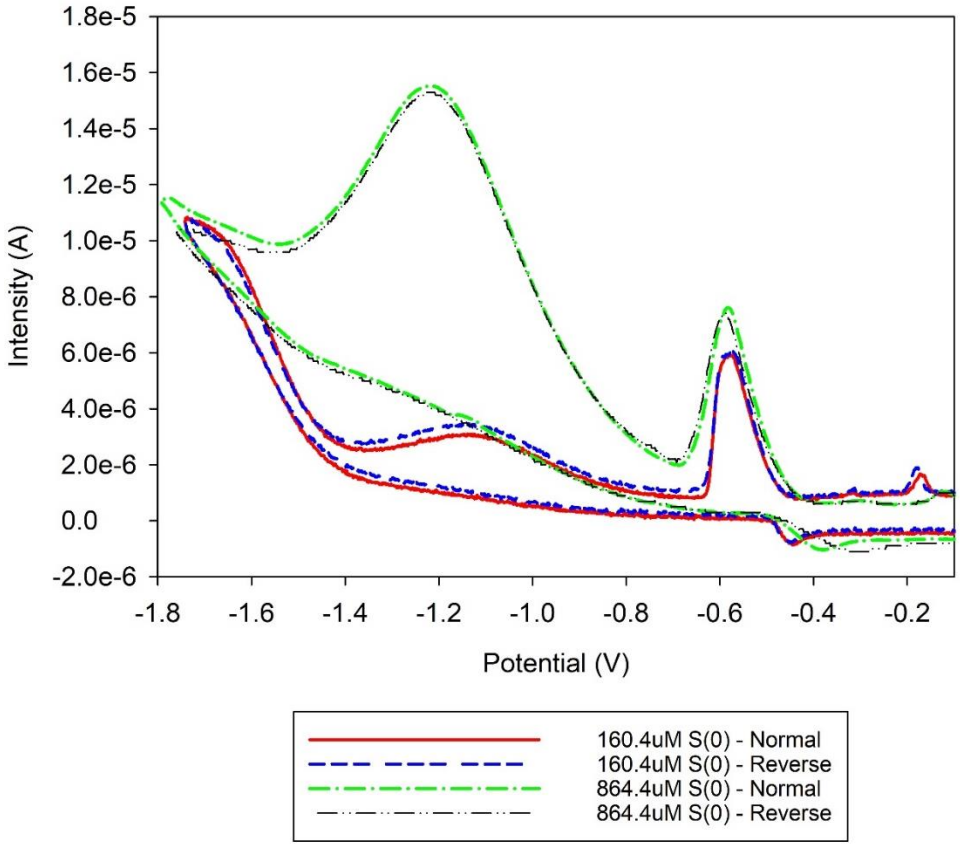

Figure 2-5: Cyclic voltammetry signals of (hydrophobic) $S_{8weimarn}$ at 864.4μM S^0 resulted by the mixing of sulfur-saturated methanol into water (blue dashed line) as well as water into the methanol fraction (solid red line). This experiment gives the observation that both mono- and polydispersed nanoparticles (resulted by the normal and reversed addition, respectively) result to identical signals.

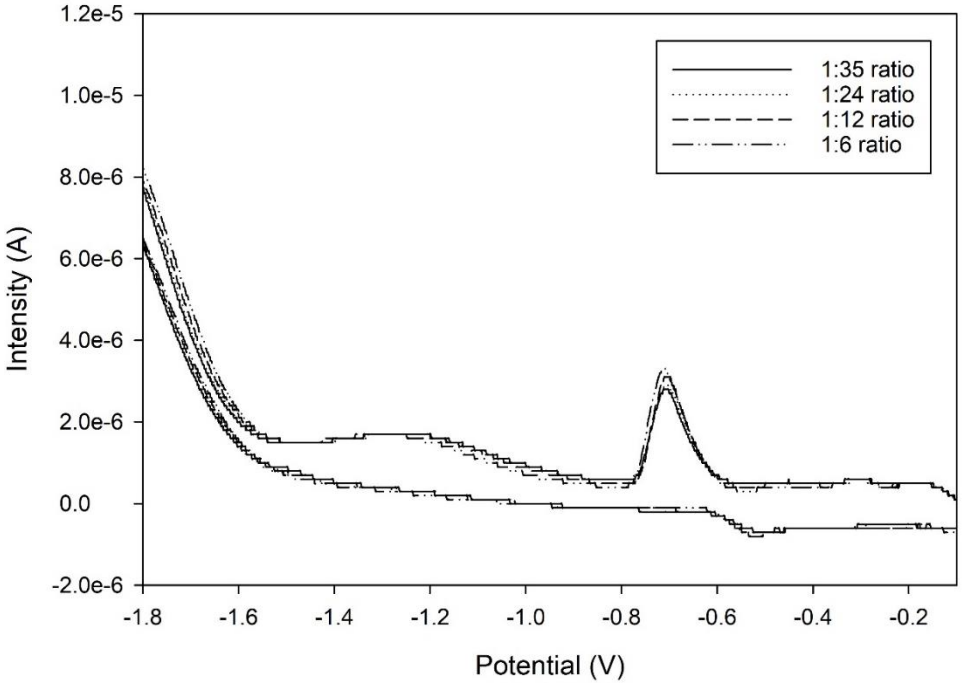

Figure 2-6: Cyclic voltammetry signals of 160.4μM S^0 (hydrophobic) $S_{8weimarn}$ prepared under various methanol to water ratios.

Temperature effect

The effect of temperature of the solution on the electrochemical signal of elemental sulfur compounds was investigated within the range of temperatures from 25ºC up to 50ºC (Figure 2-7). The S_{8aq} signal potential migrates to the more negative values, from -0.53V to -0.63V, corresponding to signal intensity from 6.15E-07A to 1.06E-06A, while temperature increases from 25ºC up to 50ºC, respectively (Table 2-2 and Figure 2-7). The S_{8aq} peak potential at 30ºC does not correlate with the corresponding temperature, for reasons that are not understood (Table 2-2 and Figure 2-7).

Table 2-2: Potential and intensity values of the voltammetric peak of S_{8aq} as a function of temperature.

Temperature (ºC)	Potential (V)	Intensity (A)
25	-0.53	6.15E-07
30	-0.634	6.70E-07
40	-0.606	6.79E-07
50	-0.623	1.06E-06

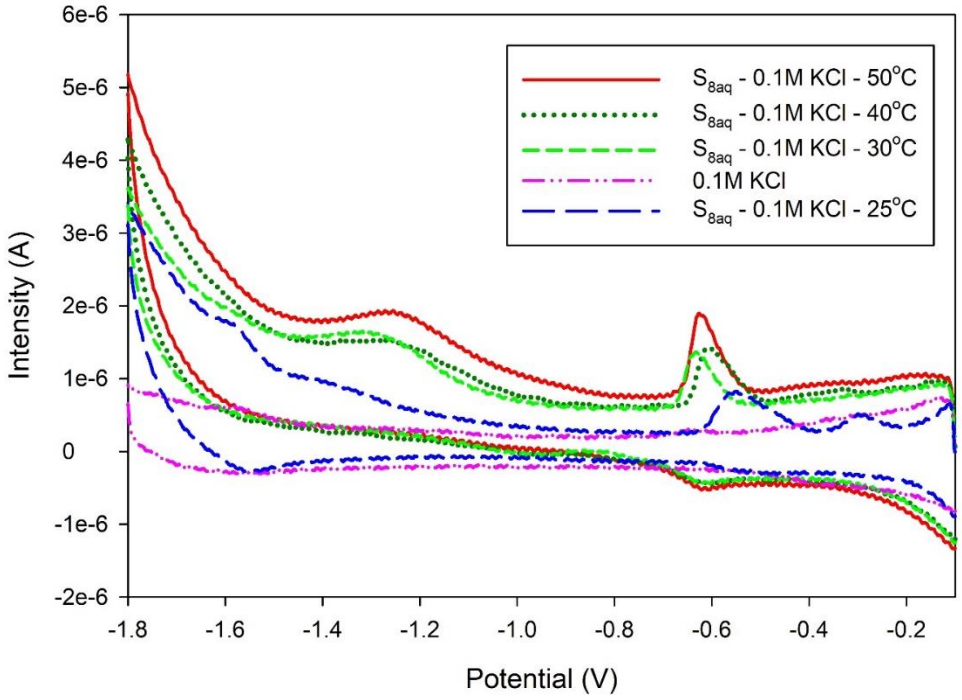

Figure 2-7: Temperature effect on the cyclic voltammetry signal of S_{8aq} in 0.1M KCl under various temperatures (25 to 50ºC). Blank signal is shown in pink.

Deposition (or conditioning) effect

Deposition or conditioning time is the period during which a potential of -0.1V (or other) is applied in the solution, resulting in the adsorption (plating) of the electroactive compound onto the surface of the electrode. The effect of increasing deposition times at -0.1V during the reaction of S_8 with the mercury electrode is shown in Figure 2-8-A. Elemental sulfur analyzed in this experiment was S_{8aq}, produced by the filtering (at 0.22μm filter pore size) of $S_{8weimarn}$. Peaks at -1.2 and -0.6V are formed by the interaction of S_{8aq} with the mercury on the electrode's surface. The deposition time increased from zero to ten seconds and the consequent increase in the intensity of the -0.6V peak is shown in Figure 2-8-B. However, the broad peak at -1.2V is not influenced by the deposition time.

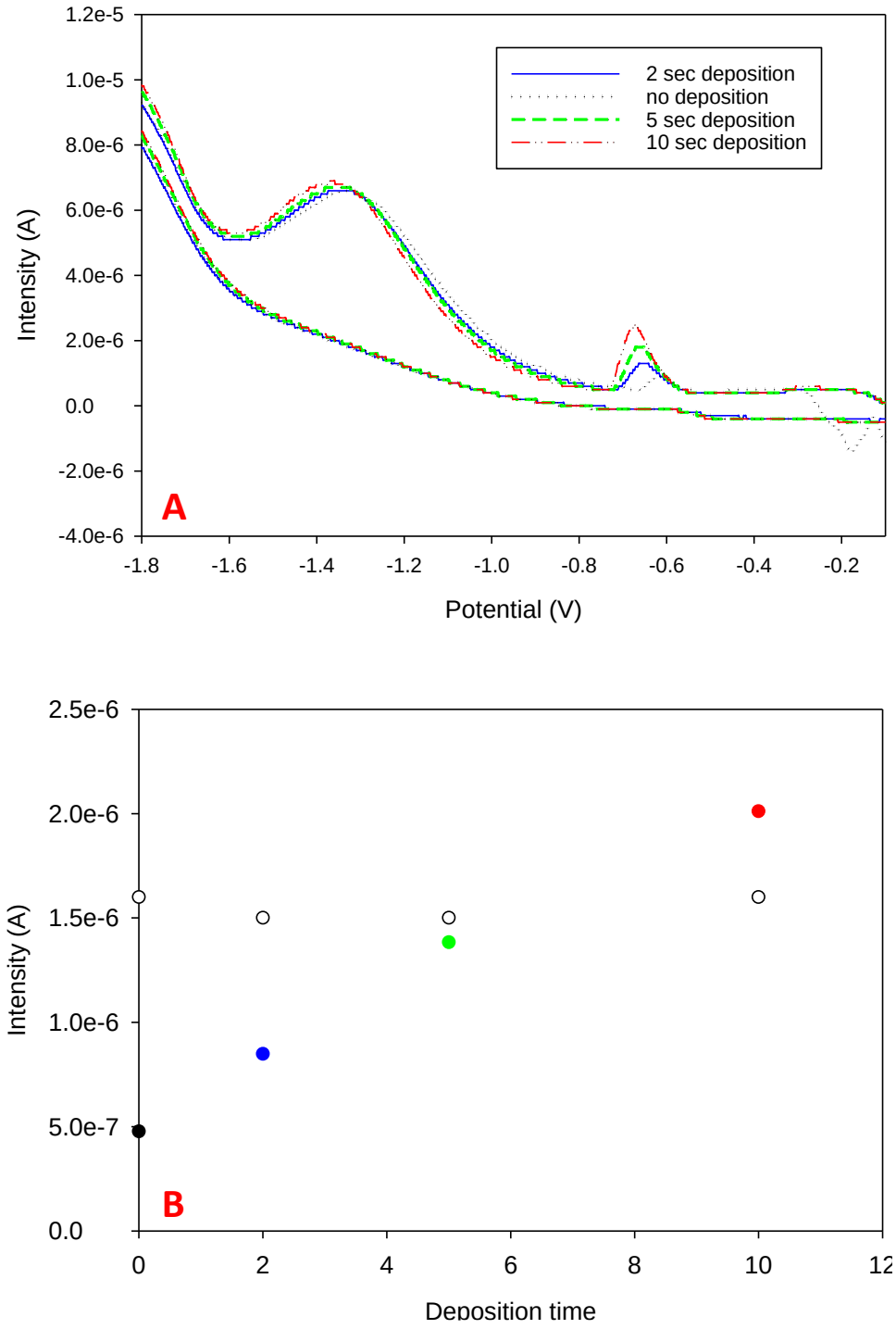

Figure 2-8: A. Cyclic voltammetry signal of an aqueous solution resulting by the filtration of (hydrophobic) $S_{8weimarn}$ (864.4µM S^0) at 0.22µm under various deposition times (at -0.1V)(top). B. The intensity of the -0.6V peak is linearly proportional to the deposition time at -0.1V, whereas the intensity of the -1.2V peak is not affected by deposition time.

Voltammetric signals of dissolved versus particulate S_8

Filtration through 0.22μm or 0.025μm pore filters was used to assess voltammetric signals for particulate versus dissolved elemental sulfur, using $S_{8weimarn}$ (1:6 ratio – 864.4μM S^0). The signal at -0.6V dropped significantly but never disappeared even after filtering at 0.025μm (Figure 2-9). The signal at -1.2V decreased much less than that of -0.6V even after the filtering at 0.025μm pore filters, supporting the idea that the -1.2V signal is strongly linked to the dissolved cyclo-octasulfur (S_{8aq}). It is worth noting that the coarsening process of the $S_{8weimarn}$ leads to the formation of particles of ~240nm within 5 minutes of aging of the solution, while the coarsening rate after that initial time period is at ~1.3nm/min. This shows that there are no significant particle sizes in the range of 25nm (corresponding to 0.025μm filter), allowing for the 0.025μm-filtered sample to correspond exclusively S_{8aq}.

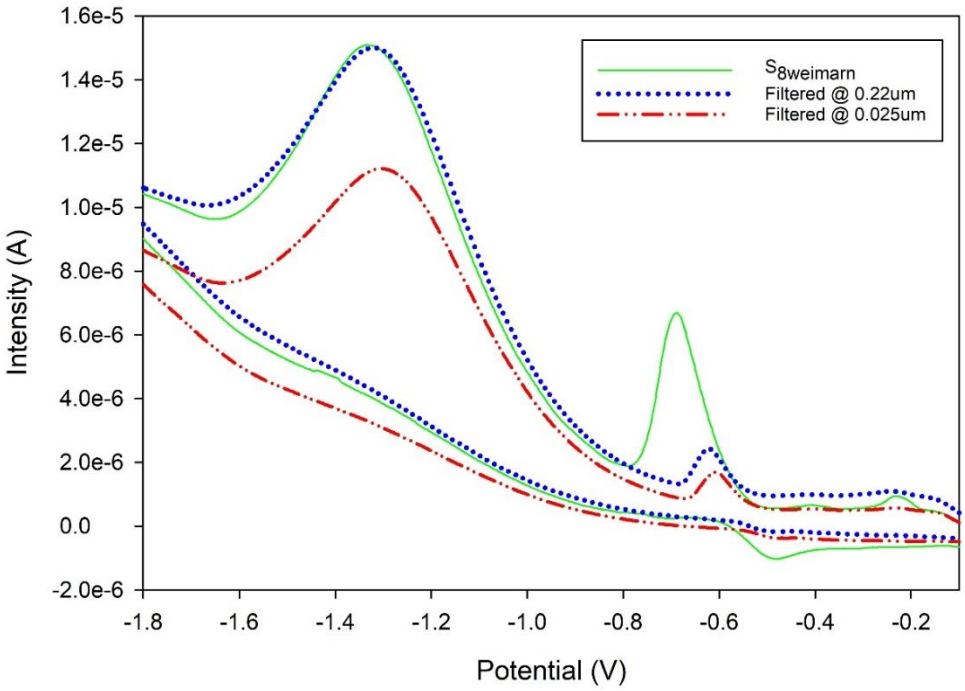

Figure 2-9: Cyclic voltammetry signals of (hydrophobic) $S_{8weimarn}$ (green solid line) after filtering at 0.22µm (blue dotted line) and 0.025µm (red dash-dot-dot line).

Surfactant effects

Figure 2-10 (A to D) shows the voltammetric signals of S_{8aq} solubilized with selected surfactants ($S_{8aq\text{-}surfactant}$). The voltammograms of $S_{8aq\text{-}surfactant}$ were overlaid in each case with the corresponding surfactant used to show the blank signal without elemental sulfur. The signal of the BSDS blank (Figure 2-10-A) shows two major peaks at -0.2 and -1.4V, whereas the $S_{8aq\text{-}BSDS}$ shows a small peak at -0.4V whereas a large wide peak at -0.8 that incorporates a small shoulder-peak at -0.6V. The signal of SDS is represented by two major peaks at ~-0.42V and -1.25V. The presence of $S_{8aq\text{-}SDS}$ results in the widening of the peak at -1.25V and shift of the more positive peak to -0.4V. The peaks representing $S_{8aq\text{-}SDS}$ are a large signal at -0.8V as well as a small peak at -0.6V (Figure 2-10-B). The voltammetric signal of CTAB is represented by a peak of strong intensity at -0.25V as well as two small signals at ~-0.5 and -1.65V. The presence of $S_{8aq\text{-}CTAB}$ in solution results in the appearance of signals at -0.3V and ~-0.67V, with the latter showing a shoulder-peak starting at potential close to -0.6V (Figure 2-10-C). The voltammetric signal of TX-100 is

represented by an intense peak at -0.55V as well as a very small peak at -0.2V (Figure 2-10-D). Presence of $S_{8aq\text{-}TX100}$ in solution resulted in a voltammetric signal similar to that of the blue line of Figure 2-10-D, showing a very broad peak, reaching a maximum at -0.9V. Ten times dilution of that solution resulted in the signal shown in red where the peak of $S_{8aq\text{-}TX100}$ is maximum at -1.0V (Figure 2-10-D). Undiluted $S_{8aq\text{-}TX\text{-}100}$ had a very large peak that was broad and difficult to define, a ten-fold dilution better identifies the position of the peak associated with dissolved elemental sulfur at -0.98V.

Figure 2-11 shows the calibration between the S_{8aq} as well as $S_{8aq\text{-}surfactant}$ at various concentrations, based on the voltammetric study discussed above. The response in current intensity of S_{8aq} as a function of concentration follows a hierarchy of increasing slope as: $S_{8aq\text{-}BSDS} < S_{8aq\text{-}TX100} < S_{8aq\text{-}SDS} < S_{8aq\text{-}CTAB} < S_{8aq}$.

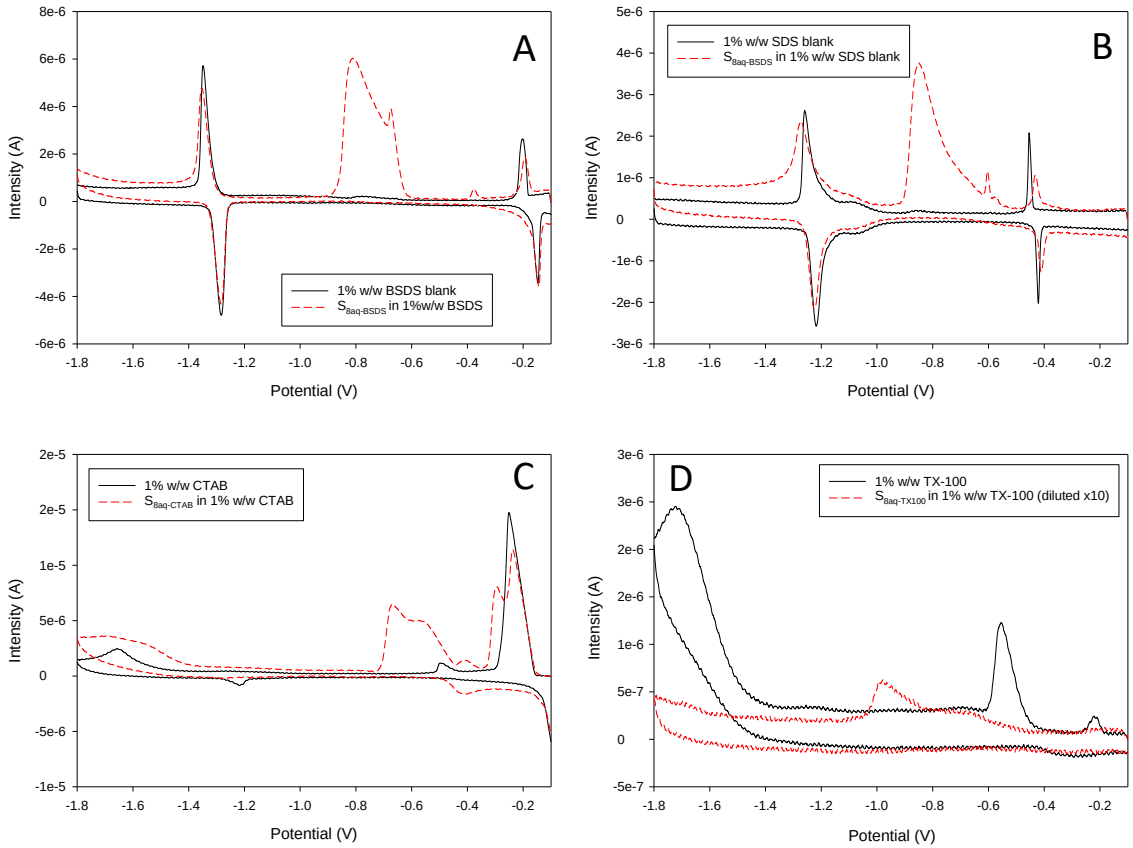

Figure 2-10: Cyclic voltammetry signals of $S_{8aq\text{-}surfactant}$ complexes are compared with the signals of their surfactant blank homologues, including the BSDS (A), SDS (B), CTAB (C) and TX-100 (D) surfactant system.

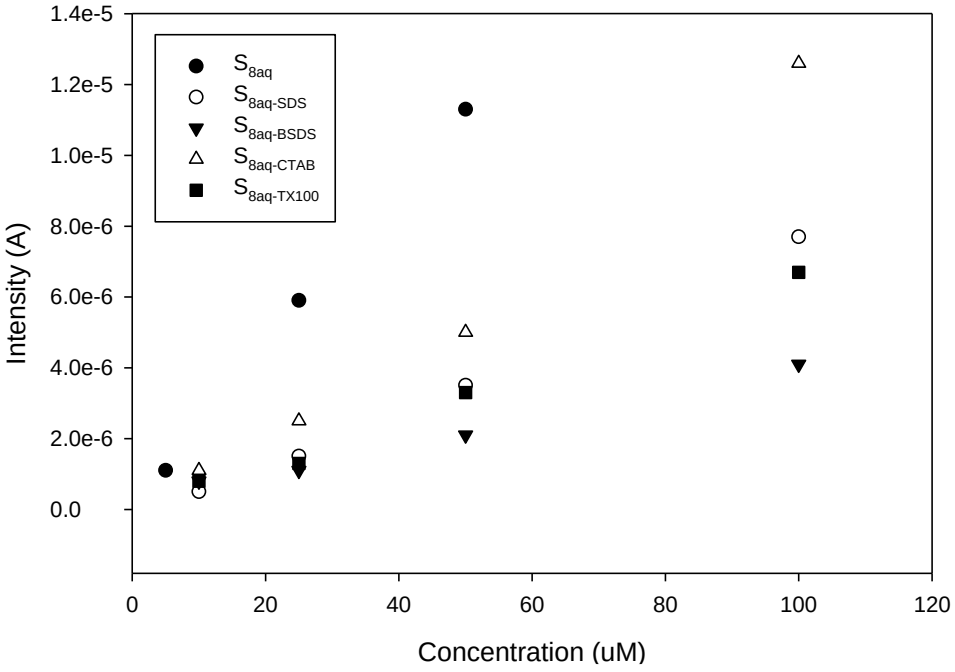

Figure 2-11: Calibration of the cyclic voltammetry signals (intensity in A) of S_{8aq}, as well as the $S_{8aq\text{-}surfactant}$ complexes as a function of their concentration (in μM).

Discussion

Elemental sulfur interaction with Au-amalgam or Hg electrodes is dependent on the soluble form, nanoparticulate, or colloidal forms present in any aqueous solution. Experiments show that deposition time as well as pH affect the interaction between the mercury electrode and elemental sulfur; and that different forms of elemental sulfur are described by more than one reaction. For inorganic sulfur forms this corresponds to the following voltammetric signals at different potentials (v. Ag/AgCl) signals:

- The most negative signal at -1.2 V shows no pH dependence, no removal by filtration, but is affected by surfactant coatings, and corresponds mainly to S_{8aq}.
- The peak found at -0.6V at circumneutral pH (for ease of communication we will refer to the less negative signal as "-0.6V") is mostly, but not completely, filtered out with 0.025 μm filtration. This signal is pH-dependent and is attributed to S_{8nano} as well as S_{8aq}.
- The signal of colloidal α-S_8 is found at a potential of ~-0.8V and is only a function of the physical transport and interaction of α-S_8 particles with the mercury surface.
- Surfactant-solubilized $S_{8aq\text{-}surfactant}$ signals show significant variability in both the voltammetric potential and in the voltammetric current response, different from the other signals for S_{8aq}, S_{8nano}, and α-S_8.

Deposition time influences the signal at -0.6V coming from filtered $S_{8weimarn}$ solutions (Figure 2-8), demonstrating that the reaction corresponding to the -0.6V potential is a stripping reaction. Stripping reactions between an electroactive analyte and the mercury electrode incorporate two steps and can be described analogous to sulfide voltammetric analysis. The first is the plating reaction, where the oxidation of Hg^0 to Hg^{2+} couples with the adsorption of sulfide on the surface of the electrode and the formation of HgS complexes:

$$HS^- + Hg^0 \leftrightarrow HgS + H^+ + 2e^- \qquad \text{(reaction 1)}$$

The plating step occurs at -0.1V, does not directly show any signal, but depends on the plating time as to how much HgS is formed at the electrode surface. The second reaction is the reduction of the HgS complex at -0.6V, where the Hg^{2+} is reduced back to Hg^0, releasing the sulfide in the aqueous medium.

$$HgS + H^+ + 2e^- \rightarrow HS^- + Hg \qquad \text{(reaction 2)}$$

The amount of the electroactive analyte is quantified by the peak of the stripping reaction at -0.6V. The work of Rozan et al. (2000) has expressed the reaction between mercury and elemental sulfur as adsorption of S^0 to the electrode's surface during the plating reaction (Rozan et al., 2000). Our understanding on the formation of the HgS complex (reaction 1) is that it is not a product of adsorption, rather a result of the reduction of S^0 to S^{2-} and the simultaneous oxidation of Hg^0 to Hg^{2+}, forming a HgS complex during the plating reaction:

$$S^0 + Hg^0 \rightarrow Hg^{2+}S^{2-} \qquad \text{(reaction 3)}$$

A similar, but not identical, adsorption product of "HgS" can be formed after a plating reaction that does not require electron exchange between the sulfur and the mercury, but rather is an amalgamation reaction that allows the two species to preserve their elemental form, as:

$$S^0 + Hg^0 \rightarrow Hg^0S^0 \qquad \text{(reaction 4)}$$

The stripping step would follow, consuming the HgS compound and releasing the sulfur as sulfide from the mercury which will remain as Hg^0 (stripping reaction):

$$HgS + H^+ + 2e^- \rightarrow HS^- + Hg \qquad \text{(reaction 5)}$$

The fact that the "-0.6V" signal is pH dependent for various forms of elemental sulfur can be explained by the presence of protons in reaction 5. The stoichiometry of the stripping reaction (5) is the same under both scenarios of plating of the mercury oxidation scenario (reaction 3) or the amalgam forming scenario (reaction 4). On the other hand, the redox

state of the sulfur and mercury in HgS is different between these two scenarios. In the case of reaction 3 being the predominant plating reaction, the mercury and the sulfide become oxidized (Hg^{2+}) and reduced (S^{2-}) states, respectively, allowing for the sulfide to be released as HS^- after it binds with a proton received from the solution (reaction 6).

$$Hg^{2+}S^{2-} + H^+ + 2e^- \rightarrow HS^- + Hg^0 \qquad \text{(reaction 6)}$$

On the contrary, during the amalgamation scenario (reaction 4) both mercury and sulfide represent their zero-valent states (Hg^0 and S^0, respectively), leading to the necessity of reduction of sulfur to sulfide during the stripping reaction 7.

$$Hg^0S^0 + H^+ + 2e^- \rightarrow HS^- + Hg^0 \qquad \text{(reaction 7)}$$

This significant difference in the pathways through which elemental sulfur can react with the surface of mercury cannot be identified via the a priori observation of signals, as the products of the stripping reaction (5) are identical regardless if reaction 3 or 4 have served in the platting step.

The stripping reactions (reactions 6 and 7) may be distinguishable if the different forms of elemental sulfur react differently at the electrode surface when reduced to sulfide. In the mercury oxidation scenario (reaction 6), the reduction of any form of elemental sulfur would take place during reaction 3, essentially reducing that elemental sulfur to form $Hg^{2+}S^{2-}$ at a time when the current is not being analyzed by voltammetry. The $Hg^{2+}S^{2-}$ would then react by reaction 6, and the signal potential and current response should be independent of the original form of elemental sulfur that was part of the plating reaction (reaction 3). During the amalgam-forming scenario the formation of an amalgam (reaction 4) between the mercury and any form of elemental sulfur would occur at a time when the current is not being analyzed by voltammetry. The Hg^0S^0 would then react by reaction 7, but any differences in the S^0 preserved from the original form of elemental sulfur involved with the amalgam formation (reaction 4), could cause differences in the signal potential and current response.

Within the framework of this study, various forms of elemental sulfur have interacted with the mercury surface electrodes, including S_{8aq}, S_{8nano} ($S_{8weimarn}$ and S_{8raffo}) and α-S_8. All of these forms of sulfur vary significantly in molecular structure, crystallinity, and association with organic molecules ($S_{8aq\text{-}surfactant}$ complexes). These structural differences can result in changes in electron transfer efficiency between these forms (Bard et al., 1980), which could be apparent during an electrochemical reduction influencing the current observed. More specifically, the current would show different response to same concentrations among the different forms of elemental sulfur, if reaction 7 was the stripping reaction. Indeed, the signal of the stripping reaction is different among the various forms of elemental sulfur used in this study (Figure 2-3-A, Figure 2-11), proving that the amalgam forming scenario and reduction of Hg^0S^0 most likely are the reactions occurring for elemental sulfur at Hg/Au-amalgam electrodes.

The interaction of elemental sulfur and mercury expressed as the signal at -1.2V has been described as a non-stripping reaction, since it is not influenced by the deposition time. The lack of a stripping step shows that the -1.2V signal is not related to the Hg surface directly, but only receives the electron flow that allows the reduction reactions to take place. Therefore, the reaction causing the -1.2V signal can probably be described by the reduction of cyclo-octasulfur to octasulfide by receiving 2 electrons, as shown:

$$S_8 + 2e^- \rightarrow S_8^{2-} \qquad \text{(reaction 8)}$$

The pH-independence cannot be fully explained as the pKa values for polysulfides can reach up to $pK_1 = 3.8$ and $pK_2 = 6.3$ for tetrasulfide, as well as $pK_1 = 3.5$ and $pK_2 = 5.7$ for pentasulfide (Steudel, 2003b). This means that in environmentally relevant conditions there could be a possibility for the octasulfide formed as a reduction product to be (partially) protonated (HS_8^-). That scenario would be similar to having sulfide as a reaction product, which has a pKa of 6.99 and 17 (Meyer et al., 1983) and will always be (singly or doubly) protonated in environmentally relevant conditions.

$$1/8\ S_8 + 2e^- + H+ \rightarrow HS^- \qquad \text{(reaction 9)}$$

In conclusion, since the experiments do not show any indication of pH-dependence for the signal at -1.2V (Figure 2-4), the reaction that explains this signal is considered to be reaction 8.

Conclusions

Elemental sulfur compounds in the absence of organics are represented by three main voltammetric signals, corresponding to potentials at -1.2V, -0.8V, and -0.6V at circumneutral pH. The most negative signal of sulfur at -1.2V, shows no pH dependence, no removal by filtration, but is affected by surfactant coatings and corresponds mainly to S_{8aq}. The signal at -0.6V (in circumneutral pH) is attributed to S_{8nano} as well as S_{8aq} and can mostly, but not completely, be filtered out with 0.025 μm filtration. Also, the signal of colloidal α-S_8 is found at a potential of ~-0.8V (at circumneutral pH). Surfactant-solubilized dissolved elemental sulfur ($S_{8aq\text{-}surfactant}$) signals show significant variability in both the voltammetric potential and in the voltammetric current response, different from the other signals for S_{8aq}, S_{8nano}, and α-S_8. These $S_{8aq\text{-}surfactant}$ signals can be found from -0.3V up to -1.0V, depending on the surfactant in the system.

The reactions through which elemental sulfur interacts with the mercury surface include a plating step at -0.1V that creates an Hg^0S^0 amalgam, a stripping reaction step that reduces the S^0 to HS^- at -0.6V (in circumneutral pH) and a non-stripping reaction of S_8 to S_8^{2-} at -1.2V. Colloidal S_8 and different forms of surfactant-solubilized S_{8aq} also react with the Au-amalgam or Hg electrode surface at different potentials and with different current responses. Functionally this suggests voltammetry to be a powerful way to distinguish different forms of elemental sulfur in natural waters, but calibration of the voltammetric signal requires knowledge of the form of elemental sulfur present in the sample.

References

Antonelli, M.A., Kim, S.-T., Peters, M., Labidi, J., Cartigny, P., Walker, R.J., Lyons, J.R., Hoek, J. and Farquhar, J. (2014) Early inner solar system origin for anomalous sulfur isotopes in differentiated protoplanets. Proceedings of the National Academy of Sciences 111, 17749-17754.

Bard, A.J., Faulkner, L.R., Leddy, J. and Zoski, C.G. (1980) Electrochemical methods: fundamentals and applications. wiley New York.

Batina, N., Ciglenečki, I. and Ćosović, B. (1992) Determination of elemental sulphur, sulphide and their mixtures in electrolyte solutions by ac voltammetry. Analytica chimica acta 267, 157-164.

Böttcher, M.E., Thamdrup, B. and Vennemann, T.W. (2001) Oxygen and sulfur isotope fractionation during anaerobic bacterial disproportionation of elemental sulfur. Geochimica et Cosmochimica Acta 65, 1601-1609.

Boyd, E.S. and Druschel, G.K. (2013) Involvement of intermediate sulfur species in biological reduction of elemental sulfur under acidic, hydrothermal conditions. Applied and environmental microbiology 79, 2061-2068.

Bura-Nakić, E., Krznarić, D., Jurašin, D., Helz, G.R. and Ciglenečki, I. (2007) Voltammetric characterization of metal sulfide particles and nanoparticles in model solutions and natural waters. Analytica Chimica Acta 594, 44-51.

Bura-Nakić, E., Viollier, E., Jézéquel, D., Thiam, A. and Ciglenečki, I. (2009) Reduced sulfur and iron species in anoxic water column of meromictic crater Lake Pavin (Massif Central, France). Chemical Geology 266, 311-317.

Canfield, D.E. and Thamdrup, B. (1994) The production of 34S-depleted sulfide during bacterial disproportionation of elemental sulfur. Science-AAAS-Weekly Paper Edition 266, 1973-1974.

Carey, E. and Taillefert, M. (2005) The role of soluble Fe (III) in the cycling of iron and sulfur in coastal marine sediments. Limnology and Oceanography 50, 1129-1141.

Ciglenečki, I. and Ćosović, B. (1996) Electrochemical study of sulfur species in seawater and marine phytoplankton cultures. Marine chemistry 52, 87-97.

Ciglenečki, I., Kodba, Z. and Ćosović, B. (1996) Sulfur species in Rogoznica lake. Marine chemistry 53, 101-110.

Clingenpeel, S.R., D'Imperio, S., Oduro, H., Druschel, G.K. and McDermott, T.R. (2009) Cloning and in situ expression studies of the Hydrogenobaculum arsenite oxidase genes. Applied and environmental microbiology 75, 3362-3365.

D'Imperio, S., Lehr, C.R., Oduro, H., Druschel, G., Kühl, M. and McDermott, T.R. (2008) Relative importance of H2 and H2S as energy sources for primary production in geothermal springs. Applied and environmental microbiology 74, 5802-5808.

Dahl, C. and Friedrich, C.G. (2008) Microbial sulfur metabolism. Springer.

Druschel, G.K., Hamers, R.J., Luther, G.W. and Banfield, J.F. (2003) Kinetics and mechanism of trithionate and tetrathionate oxidation at low pH by hydroxyl radicals. Aquatic Geochemistry 9, 145-164.

Finster, K., Liesack, W. and Thamdrup, B. (1998) Elemental sulfur and thiosulfate disproportionation by Desulfocapsa sulfoexigens sp. nov., a new anaerobic bacterium isolated from marine surface sediment. Applied and Environmental Microbiology 64, 119-125.

Gartman, A., Yücel, M., Madison, A.S., Chu, D.W., Ma, S., Janzen, C.P., Becker, E.L., Beinart, R.A., Girguis, P.R. and Luther, G.W. (2011) Sulfide oxidation across diffuse flow zones of hydrothermal vents. Aquatic Geochemistry 17, 583-601.

Gilhooly, W.P., Fike, D.A., Druschel, G.K., Kafantaris, F.-C.A., Price, R.E. and Amend, J.P. (2014) Sulfur and oxygen isotope insights into sulfur cycling in shallow-sea hydrothermal vents, Milos, Greece. Geochemical transactions 15, 12.

Glazer, B.T., Cary, S.C., Hohmann, L. and Luther III, G.W. (2002) In situ sulfur speciation using Au/Hg microelectrodes as an aid to microbial characterization of an intertidal salt marsh microbial mat. ACS Publications.

Glazer, B.T., Luther, G.W., Konovalov, S.K., Friederich, G.E., Nuzzio, D.B., Trouwborst, R.E., Tebo, B.M., Clement, B., Murray, K. and Romanov, A.S. (2006) Documenting the suboxic zone of the Black Sea via high-resolution real-time redox profiling. Deep Sea Research Part II: Topical Studies in Oceanography 53, 1740-1755.

Kaplan, I.R. and Hulston, J.R. (1966) The isotopic abundance and content of sulfur in meteorites. Geochimica et Cosmochimica Acta 30, 479-496.

Kleinjan, W.E., de Keizer, A. and Janssen, A.J. (2003) Biologically produced sulfur. Elemental sulfur and sulfur-rich compounds I, 44-57.

Konishi, Y., Takasaka, Y. and Asai, S. (1994) Kinetics of growth and elemental sulfur oxidation in batch culture of Thiobacillus ferrooxidans. Biotechnology and bioengineering 44, 667-673.

Lau, G.E., Cosmidis, J., Grasby, S.E., Trivedi, C.B., Spear, J.R. and Templeton, A.S. (2017) Low-temperature formation and stabilization of rare allotropes of cyclooctasulfur (β-S 8 and γ-S 8) in the presence of organic carbon at a sulfur-rich glacial site in the Canadian High Arctic. Geochimica et Cosmochimica Acta 200, 218-231.

Li, Y., Lubchenko, V. and Vekilov, P.G. (2011) The use of dynamic light scattering and Brownian microscopy to characterize protein aggregation. Review of Scientific Instruments 82, 053106.

Luther, G.W., Church, T.M. and Powell, D. (1991) Sulfur speciation and sulfide oxidation in the water column of the Black Sea. Deep Sea Research Part A. Oceanographic Research Papers 38, S1121-S1137.

Luther, G.W., Giblin, A.E. and Varsolona, R. (1985) Polarographic analysis of sulfur species in marine porewaters. Limnology and Oceanography 30, 727-736.

Luther, G.W., Glazer, B., Ma, S., Trouwborst, R., Shultz, B.R., Druschel, G. and Kraiya, C. (2003) Iron and sulfur chemistry in a stratified lake: Evidence for iron-rich sulfide complexes. Aquatic Geochemistry 9, 87-110.

Luther, G.W., Glazer, B.T., Ma, S., Trouwborst, R.E., Moore, T.S., Metzger, E., Kraiya, C., Waite, T.J., Druschel, G. and Sundby, B. (2008) Use of voltammetric solid-state (micro) electrodes for studying biogeochemical processes: laboratory measurements to real time measurements with an in situ electrochemical analyzer (ISEA). Marine Chemistry 108, 221-235.

Luther III, G.W., Rozan, T.F., Taillefert, M., Nuzzio, D.B., Di Meo, C., Shank, T.M., Lutz, R.A. and Cary, S.C. (2001a) Chemical speciation drives hydrothermal vent ecology. Nature 410, 813-816.

Luther III, G.W., Findlay, A.J., MacDonald, D.J., Owings, S.M., Hanson, T.E., Beinart, R.A. and Girguis, P.R. (2011) Thermodynamics and kinetics of sulfide oxidation by oxygen: a look at inorganically controlled reactions and biologically mediated processes in the environment. Frontiers in microbiology 2.

Luther III, G.W., Glazer, B.T., Hohmann, L., Popp, J.I., Taillefert, M., Rozan, T.F., Brendel, P.J., Theberge, S.M. and Nuzzio, D.B. (2001b) Sulfur speciation monitored in situ with solid state gold amalgam voltammetric microelectrodes: polysulfides as a special case in sediments, microbial mats and hydrothermal vent watersPresented at the Whistler 2000 Speciation Symposium, Whistler Resort, BC, Canada, June 25–July 1, 2000. Electronic Supplementary Information available. See http://www. rsc. org/suppdata/em/b0/b006499h. Journal of Environmental Monitoring 3, 61-66.

Lutz, R.A., Shank, T.M., Luther III, G.W., Vetriani, C., Tolstoy, M., Nuzzio, D.B., Moore, T.S., Waldhauser, F., Crespo-Medina, M. and Chatziefthimiou, A.D. (2008) Interrelationships between vent fluid chemistry, temperature, seismic activity, and biological community structure at a mussel-dominated, deep-sea hydrothermal vent along the East Pacific Rise. Journal of Shellfish Research 27, 177-190.

Meyer, B., Ward, K., Koshlap, K. and Peter, L. (1983) Second dissociation constant of hydrogen sulfide. Inorganic Chemistry 22, 2345-2346.

Nor, Y.M. and Tabatabai, M. (1977) Oxidation of elemental sulfur in soils. Soil Science Society of America Journal 41, 736-741.

Nriagu, J.O. and Soon, Y.K. (1985) Distribution and isotopic composition of sulfur in lake sediments of northern Ontario. Geochimica et Cosmochimica Acta 49, 823-834.

Pecora, R. (2000) Dynamic light scattering measurement of nanometer particles in liquids. Journal of nanoparticle research 2, 123-131.

Poser, A., Lohmayer, R., Vogt, C., Knoeller, K., Planer-Friedrich, B., Sorokin, D., Richnow, H.-H. and Finster, K. (2013) Disproportionation of elemental sulfur by haloalkaliphilic bacteria from soda lakes. Extremophiles 17, 1003.

Raven, M.R., Adkins, J.F., Werne, J.P., Lyons, T.W. and Sessions, A.L. (2015) Sulfur isotopic composition of individual organic compounds from Cariaco Basin sediments. Organic Geochemistry 80, 53-59.

Rickard, D. and Luther, G.W. (2007) Chemistry of Iron Sulfides. Chemical Reviews 107, 514-562.

Rozan, T.F., Theberge, S. and Luther, G. (2000) Quantifying elemental sulfur (S 0), bisulfide (HS−) and polysulfides (S x 2−) using a voltammetric method. Analytica Chimica Acta 415, 175-184.

Schulz, H.N. and Schulz, H.D. (2005) Large sulfur bacteria and the formation of phosphorite. Science 307, 416-418.

Shivvers, D.W. and Brock, T.D. (1973) Oxidation of elemental sulfur by Sulfolobus acidocaldarius. Journal of bacteriology 114, 706-710.

Steudel, R. (1996) Mechanism for the formation of elemental sulfur from aqueous sulfide in chemical and microbiological desulfurization processes. Industrial & engineering chemistry research 35, 1417-1423.

Steudel, R. (2003a) Aqueous Sulfur Sols, in: Steudel, R. (Ed.), Elemental Sulfur and Sulfur-Rich Compounds I. Springer Berlin Heidelberg, Berlin, Heidelberg, pp. 153-166.

Steudel, R. (2003b) Inorganic polysulfanes H2Sn with n> 1. Topics in Current Chemistry 231, 99-126.

Steudel, R. and Eckert, B. (2003) Solid sulfur allotropes sulfur allotropes, Elemental sulfur and sulfur-rich compounds I. Springer, pp. 1-80.

Suzuki, I., Chan, C. and Takeuchi, T. (1992) Oxidation of elemental sulfur to sulfite by Thiobacillus thiooxidans cells. Applied and environmental microbiology 58, 3767-3769.

Theberge, S.M. and Luther III, G.W. (1997) Determination of the electrochemical properties of a soluble aqueous FeS species present in sulfidic solutions. Aquatic Geochemistry 3, 191-211.

Waite, T.J., Moore, T.S., Childress, J.J., Hsu-Kim, H., Mullaugh, K.M., Nuzzio, D.B., Paschal, A.N., Tsang, J., Fisher, C.R. and Luther III, G.W. (2008) Variation in sulfur speciation with shellfish presence at a Lau Basin diffuse flow vent site. Journal of Shellfish Research 27, 163-168.

Wang, F., Tessier, A. and Buffle, J. (1998) Voltammetric determination of elemental sulfur in pore waters. Limnology and oceanography 43, 1353-1361.

Yücel, M., Konovalov, S.K., Moore, T.S., Janzen, C.P. and Luther, G.W. (2010) Sulfur speciation in the upper Black Sea sediments. Chemical Geology 269, 364-375.

Yücel, M., Sievert, S.M., Vetriani, C., Foustoukos, D.I., Giovannelli, D. and Le Bris, N. (2013) Eco-geochemical dynamics of a shallow-water hydrothermal vent system at Milos Island, Aegean Sea (Eastern Mediterranean). Chemical Geology 356, 11-20.

CHAPTER-3 – KINETICS OF THE NUCLEOPHILIC DISSOLUTION OF NANOPARTICULATE ELEMENTAL SULFUR (S_{8NANO}) BY SULFIDE

Introduction

When elemental sulfur is formed by the oxidation of sulfide in natural environments (Luther III et al., 2011), it can react with excess sulfide via the nucleophilic reaction one (1). Reaction 1 is a nucleophilic dissolution reaction where elemental sulfur is dissolved by sulfide to form polysulfides and protons (Kamyshny et al., 2014; Kamyshny et al., 2004). More specifically, the electron-rich nucleophile sulfide interacts with the electrophile elemental sulfur, causing the cleavage of the S-S covalent bond along with the addition of sulfide at the end of the 8-atom sulfur chain. The release of a proton as well as the redistribution of the charge causes the formation of an S_9^{2-} polysulfidic molecule.

$$HS^- + \frac{n-1}{8} S_8 \leftrightarrow S_n^{2-} + H^+ \qquad \textit{(Reaction 1)}$$

Polysulfides are chainlike molecules that incorporate both zero-valent and sulfidic sulfur (1-), with the zero-valent sulfur atoms being in the interior of the chain and ending at two sulfidic atoms, one per each end of the chain. Polysulfides have a general formula of S_n^{2-}, with x ranging from 2 up to 8 in natural systems (Kamyshny et al., 2004). This distribution of chain lengths of the polysulfides is established via reversible disproportionation reactions in aqueous systems, with the most dominant reaction being expressed as follows (Kamyshny et al., 2003):

$$S_4^{2-} + \frac{1}{4} H_2O \leftrightarrow \frac{3}{4} S_5^{2-} + \frac{1}{4} OH^- + \frac{1}{4} HS^- \qquad \textit{(Reaction 2)}$$

The kinetics of these reactions are in the order of 10 seconds at conditions that resemble the natural environment (Kamyshny et al., 2003). If reaction 1 is relatively fast, the nucleophilic dissolution of elemental sulfur by HS^- (Reaction 1) is likely the step forming polysulfides observed as intermediates during sulfide oxidation pathways by O_2 (Chen and Gupta, 1973; Chen and Morris, 1972). It is worth noting that polysulfide oxidation by O_2 is four times faster than the oxidation of sulfide by O_2, to form thiosulfate (Kleinjan et al., (2005b).

The importance of polysulfides – and consequently reaction 1, which forms polysulfides – is known throughout a vast array of natural environments, contributing to sulfur cycling and its interaction with other elements. In sedimentary systems, there are several different pathways by which pyrite can be formed (pyritization reactions). One pathway of pyritization is driven by sulfide (also called the Berzelius or Wachtershauser reaction) which involves the oxidation of ferrous sulfide (either as FeS_{aq} or FeS_m nanoparticles) by sulfide (H_2S) to form FeS_2 and H_2 (Berzelius, 1845; Rickard and Luther, 2007). Another pyritization pathway incorporates a polysulfide reaction – also called the Bunsen reaction – where a pentasulfide (S_5^{2-}) molecule reacts with FeS to give FeS_2 and S_8 (Bunsen, 1847; Rickard and Luther, 2007). In carbon-sulfur interactions, polysulfides interact with natural organic matter to produce sulfurized organic compounds (Amrani, 2014; Raven et al., 2015). As opposed to sulfide – which sulfurizes organic compounds forming S-containing rings, such as thiophene and thiane rings – the chemical structure of polysulfide is too large to achieve that (Raven et al., 2015). However, polysulfides are able to sulfurize organic molecules using both terminal sulfidic moieties, resulting in the interbridging of two organic molecules (Kohnen et al., 1990). Reactivity of organic carbon with sulfur species has been proven to also include redox reactions in addition to sulfurization reactions (Heitmann and Blodau, 2006; Raven et al., 2015; Schwarzenbach et al., 1985; Werne et al., 2000).

Previous work has shown the kinetics as well as the thermodynamics of the nucleophilic dissolution of elemental sulfur by sulfide, using α-S_8 (Giggenbach, 1972; Giggenbach, 1974a, b; Hartler et al., 1967; Kamyshny et al., 2004; Kamyshny et al., 2003; Kamyshny et al., 2007; Licht and Davis, 1997; Teder, 1971), as well as biological produced sulfur (Kleinjan et al., 2005a, c). These studies have shown that the equilibrium constant of the nucleophilic dissolution of S_8 differs between conditions of α-S_8 and biologically produced sulfur (Kleinjan et al., 2005a; Teder, 1971). Specifically, the equilibrium between sulfide and $S_{8biological}$ at 21^0C shows a constant pK at 9.10±0.08, which is higher than that of the reaction involving sulfide and α-S_8, which has pK at 8.82 (Kleinjan et al., 2005a). The higher value of pK during the reaction of $S_{8biological}$ with sulfide compared to that with inorganic sulfur is attributed to the presence of organic coatings on $S_{8biological}$, which results in less amounts of polysulfide being released in the aqueous solution as it is bound with

the organic moieties (Kleinjan et al., 2005a). Also the sulfide concentration and surface area effect have also been noted to influence the dissolution kinetics of α-S_8, with the reaction rate being approximately second-order with respect to sulfide concentration, and directly proportional to the α-S_8 surface area (Hartler et al., 1967; Kleinjan et al., 2005c). For the biologically produced sulfur, the rate of reaction 1 is known to take the form,

$$\frac{d[S_5^{2-}]}{dt} = \frac{A_c[HS^-]}{[H^+]}(k_1^*[HS^-] + k_2^*[S_5^{2-}])$$

with k^{*1} and k^{*2} at $5.78*10^{-14}$ m s^{-1} and $1.33*10^{-10}$ m s^{-1} at 50°C and pH 8.

Thermodynamic calculations in the S-O-H system have shown that temperature and activity of S_{total} (the summary of all sulfur species activities) are the two main factors that influence the distribution of the stability fields of elemental sulfur, sulfide and polysulfides, as expressed in Eh-pH diagrams. Specifically, increase of temperature leads to the expansion of the polysulfides stability fields relative to the the stability field of elemental sulfur. Figure 3-1 depicts a Log[HS^-] versus pH diagram of the S-O-H system at 25°C with S as basis species at 0.01, 1 and 10M activity at the grey, blue and red graphs, respectively. Increase of S_{total} leads to the expansion of the stability field of elemental sulfur and the contraction of the polysulfides' stability fields (Figure 3-1). The separating line between S and S_5^{2-} fields expresses the equilibrium of the nucleophilic reaction (Reaction 1), and it is shifted toward acidic pH values as temperature increases and as S_{total} drops. The presence of $S_{8biological}$ in the system results in the relocation of the equilibrium of reaction 1 to slightly lower pH values, compared to α-S_8. This results in the expansion of the stability field of pentasulfide ion when reacting with $S_{8biological}$ and approaching equilibrium at slightly lower HS^- and pH values than in the reaction with α-S_8.

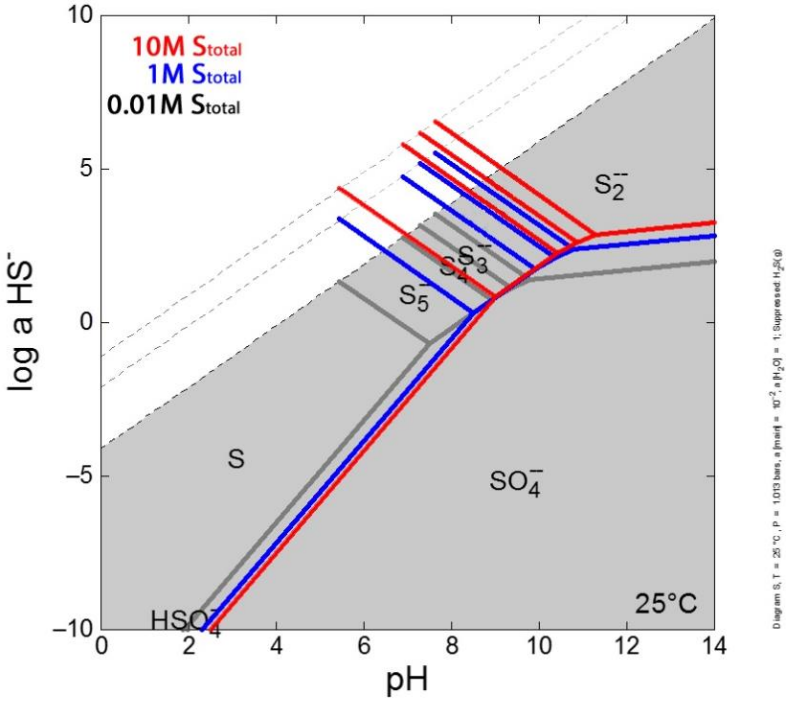

Figure 3-1 : Log[HS^-]-pH diagrams of the S-O-H system at 25ºC with S as basis species at 0.01, 1 and 10M activity at the grey, blue and red graphs, respectively. H_2S_g is suppressed on all graphs. This comparison shows the control of total S activity on the extent of the stability field of elemental sulfur and polysulfide species. As observed, an increase of the activity of S_{total} results in the expansion of the elemental sulfur and pentasulfide stability fields, as well as to the expansion and transposition of the separation line of these two fields to higher pH values. As a consequence, the equilibrium of the reaction 1 can be reached in higher sulfide and pH values.

Even though extensive work has been done on the kinetics and thermodynamics of α-S_8 and $S_{8biological}$, the literature is missing information regarding the thermodynamics and kinetics of reaction 1 for nanoparticulate elemental sulfur of various sizes and surface character. A better understanding on the chemical kinetics of the reaction 1 under these forms of elemental sulfur nanoparticles can elucidate on the cycling of reduced sulfur species as they comprise abiotic analogues of biologically produced elemental sulfur. This work shows how various forms of S_{8nano} affect the kinetics and thermodynamics of the nucleophilic dissolution of elemental sulfur. A range of sizes (and thus surface area values

of S_{8nano}) and surface characters (hydrophilic, hydrophobic surface) are considered on their reaction with HS^- (reaction 1). Experimental work on reaction kinetics of reaction 1 using S_{8nano} versus surfactant-coated S_{8nano} evaluates if the presence of surfactant coating on the nanoparticles increases the rate of elemental sulfur dissolution. This is displayed through an array of chromatographic, spectro-photometric and laser-based techniques in order to characterize the kinetics of the consumption of elemental sulfur by reaction 1.

Materials and methods

The chemical kinetics of the dissolution of S_{8nano} were investigated by using batch experiments in order to evaluate the rate of dissolution of S_{8nano} as a factor of specific surface area (or diameter), pH, ionic strength, molarity of sulfide and temperature (Table 3-1). The kinetic rate laws were established for both $S_{8weimarn}$ and S_{8raffo} using multiple linear regression calculations in R software (code included in Appendix B).

Table 3-1: Conditions of experiments conducted within the framework of this study. Black boxes indicate the variable under study using method of initial rates and pseudo-first order kinetic assumptions (Brezonik, 1993).

Variable	T (°C)	pH	Sulfide (M)	I (M)	SSA (dm2/dm3)	Diameter (nm)	type of S_{8nano}
Specific Surface Area	25	7.4	0.003	0.080			$S_{8weimarn}$
Ionic Strength	25	10.4	0.010		1927616	314	
Sulfide	25	11.9		0.080	1600419	375	
pH	25		0.002	0.100	990527	612	
Temperature		11.9	0.010	0.080	1445321	421	
sulfide	25	11.8		0.121	1494959	403	$S_{8weimarn-SDS}$
Temperature		7.4	0.003	0.121	2236483	271	
Specific Surface Area	25	8.5	0.005	0.040			S_{8raffo}
Ionic Strength	25	11.0	0.020		398216	1508	
Sulfide	25	11.0		0.029	754706	800	
pH	25		0.002	0.050	763142	793	
Temperature		8.6	0.005	0.040	604920	994	

Chemical compounds

Milli-Q water (>18MΩ purity) was obtained by a Thermo Scientific Barnstead GenPure xCAD Plus Ultrapure Water Purification System. Salts of sodium sulfide nonahydrate ($Na_2S \cdot 9H_2O$; >98% purity), sublimed elemental sulfur (>99.5% purity), sodium thiosulfate pentahydrate ($Na_2O_3S_2 \cdot 5\ H_2O$; >99.5% purity) as well as concentrated hydrochloric acid (ACS grade; 36.5-38% w/w), were purchased from Fischer Scientific. The preparation of sulfide and thiosulfate stock solutions took place by dissolving appropriate salts in water in which anoxia was established by purging using a nitrogen gas (N_2) stream. HPLC grade methanol (>99.9% purity) was also purchased by Fischer Scientific for use in both the liquid chromatography analyses as well as the preparation of $S_{8weimarn}$.

Sample characterization

Particle size information for S_{8nano} was measured with a DelsaNano HC Dynamic Light Scattering (DLS) instrument. The instrumental analysis was evaluated using a 100nm Latex bead standard. Consecutive analyses of the same standard over a period of one year showed reproducibility of 4.3nm at 2 standard deviations, with a mean diameter value at 99.8nm (of the 100nm standard). Specific Surface Area (SSA) values for each S_{8nano} population analyzed were converted from diameter values using the formula $SSA=[\pi r^2]/[4/3\pi r^3]$.

Nucleophilic dissolution kinetics were investigated by measuring the decrease of the blockage of light at the wavelength of 650nm caused by the suspension of S_{8nano}. The intensity of light was captured using an EPOCH 2 UV-VIS spectrophotometer with well plate reader and a heating element, using a 96 well glass plate, and was calibrated for the molarity of elemental sulfur for both $S_{8weimarn}$ and S_{8raffo} as shown in Figure 3-2.

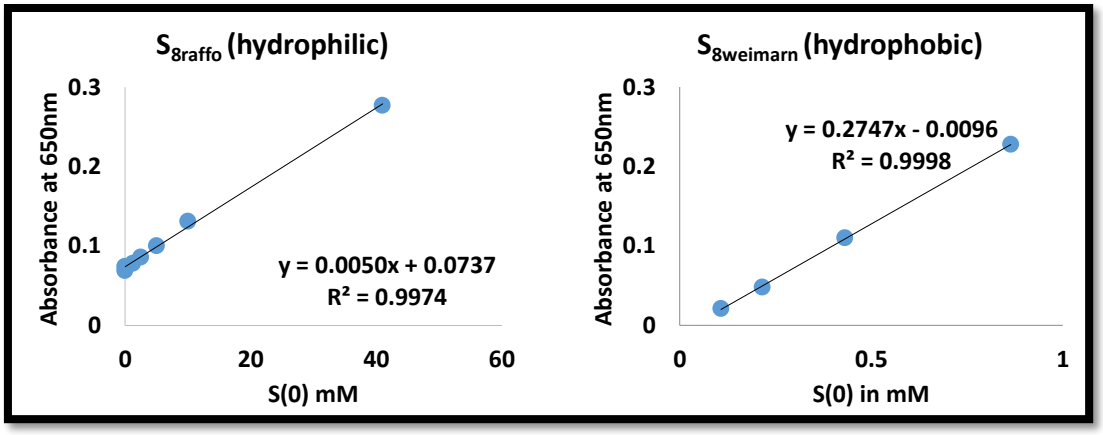

Figure 3-2: Absorption response measured at 650nm to varying concentrations (in mM S^0) of S_{8raffo} (left) and $S_{8weimarn}$ (right) suspensions.

Preparation of elemental sulfur nanoparticles

Elemental sulfur nanoparticles (S_{8nano}) of hydrophobic ($S_{8weimarn}$) and hydrophilic character (S_{8raffo}) were prepared after the recipes detailed in Steudel (2003). Briefly, the $S_{8weimarn}$ suspension was prepared by introducing buffer solutions (according to the desired pH for each kinetic experiment) in elemental sulfur-saturated methanol solution of ~6mM S^0. The ratio of saturated S^0-methanol-to-water was increased from 1:35 – which was indicated in the original recipe – to 1:6 in order to achieve a larger amount of S_{total} in the system. After the mixing of the water solution in the saturated S^0-methanol solution at a 1:6 ratio, the $S_{8weimarn}$ suspension had a concentration of 0.85mM S^0. The S_{8raffo} suspension was prepared by acidifying an $S_2O_3^{2-}$ stock solution with concentrated HCl to form S_{8raffo}. This suspension was then diluted in buffer solution of desired pH (according to the pH needed for each kinetic experiment). Ionic strength and pH significantly influence the coarsening kinetics in addition to temperature and presence of surfactants in solution (Garcia Jr and Druschel, 2014). Therefore, each time a kinetic experiment was initiated, a sample from the S_{8nano} suspension was sampled and analyzed by DLS to determine particle size. This was particularly important in order to capture kinetics data from experiments that

represented S_{8nano} of the same specific surface area when other factors were varied. Specific surface area is expressed as ratio of surface over volume of the nanoparticles (surface area divided by volume, in $dm^2/dm^3 = dm^{-1}$) assuming spherical geometry.

Kinetic experiments

Batch reactions to determine the rate of nucleophilic dissolution of elemental sulfur nanoparticles by sulfide were conducted under various specific surface area (hence variable diameter) values for both $S_{8weimarn}$ and S_{8raffo}, under variable pH, ionic strength, sulfide concentration and temperature conditions, and in the presence/absence of SDS surfactant ($S_{8weimarn-SDS}$) (Table 3-1). The experiments were carried out in 3 replicate wells of the EPOCH 2 UV-VIS spectrophotometer with a heating element, using a 96 well plate. The experimental solution had a volume of 300μL while each experiment had 3 replicates as well as 3 wells that served as a control sample where the S_{8nano} was analyzed without the addition of a sulfide aliquot. Each experiment was initiated when an aliquot of sulfide was spiked into the three wells containing S_{8nano} using a multi-channel pipette, and a single wavelength (650nm) kinetic analysis was initiated taking intensity measurements for 5 minutes with acquisitions every 4 seconds. For the kinetic experiments of $S_{8weimarn}$, the buffer solution and the S^0-methanol were made anoxic by bubbling of N_2 stream prior to their mixing. After the $S_{8weimarn}$ suspension was formed, the transfer to the well plate and the addition of sulfide were immediate for the nucleophilic reaction to be initiated. For S_{8raffo} experiments, the buffer and $S_2O_3^{2-}$ stock solutions were made anoxic by bubbling of N_2 stream prior to acidification and mixing. Anoxia was maintained by keeping an N_2 stream on the headspace of the beaker where the S_{8raffo} was prepared while the nanoparticles were aged for a few minutes, prior to the initiation of the kinetic experiments with the transfer to the wells and the addition of the sulfide aliquots. The same method was utilized for the preparation and maintaining of anoxia in the $S_{8weimarn-SDS}$, where due to the presence of surfactants the bubbling of N_2 was avoided in order not to cause mass loss of elemental sulfur nanoparticles due to the formation of surfactant bubbles.

The data were exported in excel files as intensity at 650nm versus time in seconds, for both the standard and the experiment data. Intensity data were converted to molarity values using calibration curves that had been established in the EPOCH2 spectrophotometer using both $S_{8weimarn}$ and S_{8raffo} solutions of known concentrations giving a linear relationship with r^2 values of >0.99 (Figure 3-2). In order to correct for intensity fluctuations due to slightly different size population of S_{8nano} between various experiments, the control data were subtracted from the raw experimental data. The corrected data were plotted versus time and the slope of initial rates of linear portion of the three curves (using the first few points defining the initial linear component of each curve) was averaged and recorded. This slope expressed the consumption of S_{8nano} in mol per liter per second (mol L^{-1} sec^{-1}) at each set of initial conditions. During the presentation of the experimental results (Results section) the consumption rate data are not normalized to SSA and are presented in Molar(S_8)/second for all types of nanoparticles. However, since the behavior of S_{8raffo} and $S_{8weimarn}$ in respect to the SSA was different, the rate data used by the linear regression modeling for the calculation of the kinetic rate law of $S_{8weimarn}$ only, were normalized to specific surface area (mol L^{-1} sec^{-1} dm^{-1})(see Results and Discussion).

The temperature effect on the kinetic dissolution of the S_{8nano} was investigated by utilizing the heating element of the spectrophotometer and letting the well plate equilibrate to the desired temperature prior to the initiation of the experiments by spiking with sulfide. Also, the $S_{8weimarn}$ and S_{8raffo} solutions were heated up using a hot bath and the diameter of the nanoparticles was determined by sampling a replicate aliquot originating from the same S_{8nano} solution and analyzing it in DLS immediately prior to the initiation of the kinetic experiments. Arrhenius plots were formed for the $S_{8weimarn}$, $S_{8weimarn\text{-}SDS}$ and S_{8raffo} and the activation energy for each reaction was extracted by the information of the slope of the lines formed (Arrhenius, 1889; Brezonik, 1993).

Results

A summary of all kinetics data can be found in Appendix B.

Results of dissolution kinetics of $S_{8weimarn}$

The effect of the surface area of $S_{8weimarn}$ on the rate of its nucleophilic dissolution is shown in Figure 3-3-A. The plot of the rate versus the diameter displays two sections: In the first segment, the rate of consumption of $S_{8weimarn}$ is increasing from 1.35E-07 up to 2.18E-07 Molar(S_8)/second, with decreasing diameter from 653.1 to 353.5nm (corresponding to increasing surface area from 9.18E+05 up to 1.69E+06 dm^2/dm^3, respectively), displaying a linear relationship between the rate and the surface area. The second segment shows a likely leveling off of the rate values, with the values reaching a maximum of 2.48E-107 Molar(S_8)/second at a diameter of 278.3nm (surface area value of 2.15E+06 dm^2/dm^3, respectively).

The effect of sulfide concentration on the rate of nucleophilic dissolution of $S_{8weimarn}$ is shown in Figure 3-4-A. The rate of elemental sulfur consumption increases with increasing sulfide concentration, ranging from 1.30E-07 Molar(S_8)/second up to 3.50E-07 Molar(S_8)/second for a sulfide concentration range between 2.77mM to 40mM HS^-. The relationship is linear for the experiments representing sulfide concentrations higher than 10mM, with the experiments representing the lower range of sulfide concentrations having a more curved correlation possibly due to shifts in pH, as the addition of the sulfide aliquots exceeded the buffering capacity of the buffer used in the solution. These pH values have been measured (Appendix B) and have been taken into consideration while calculating the kinetic rate law via multiple linear regression modeling.

The effect of the pH of the experimental solution on the consumption of $S_{8weimarn}$ is shown in Figure 3-4-C. The rate increased with increasing pH in a linear fashion with the rate values starting from 1.53E-07 Molar(S_8)/second at pH 7.11, increasing at 2.44E-07 at pH 8 and reaches 3.72E-07 at pH 10. The relationship between the pH and the rate of

reaction 1 for $S_{8weimarn}$ was tested using a linear model in R, showing statistical significance with a slope at 7.31E-08, intercept at -3.55E-07 and p value at 0.0059.

The effect of ionic strength of the experimental solution on the rate of nucleophilic dissolution of $S_{8weimarn}$ is shown in Figure 3-4-E. The rate varies over a range of values from 2.45E-08 up to 7.54E-07 Molar(S_8)/second, corresponding to a range of conditions of ionic strength with molarity from 0.059 up to 0.593 M. The ionic strength data on $S_{8weimarn}$ suggest that there is no statistically significant correlation between ionic strength and the rate (p value at 0.494), which is also apparent from the graphical representation of Figure 3-4-E.

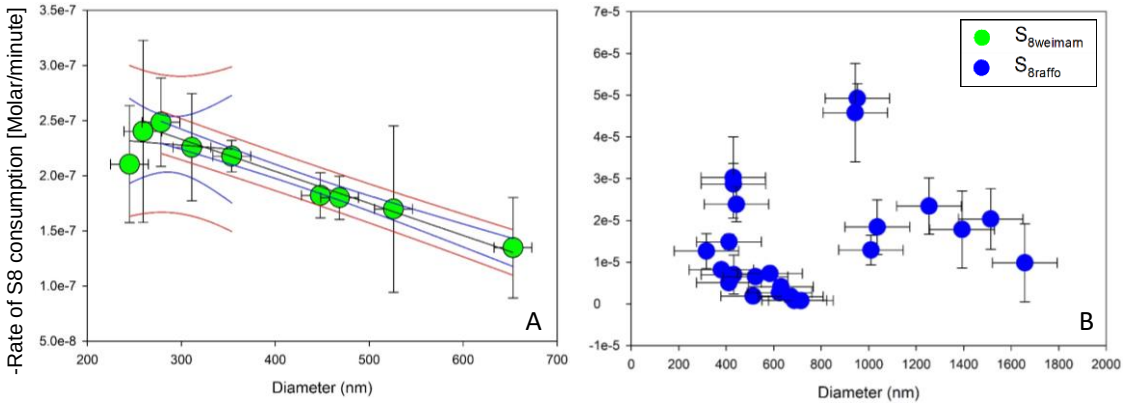

Figure 3-3: Specific surface area effect on the rate of the consumption of $S_{8weimarn}$ (A) and S_{8raffo} (B). For the $S_{8weimarn}$, the critical point where the surface-controlled zone intersects with the diffusion-controlled zone is at a diameter value of 325nm, corresponding to an SSA value of 1.85E+06 dm-1. This estimation has taken into consideration a conservative error of 95% confidence for both zones mentioned. The reactivity of S_{8raffo} shows independence on the surface area (or diameter) of the nanoparticles.

Results of dissolution kinetics of S_{8raffo}

The effect of the surface area of S_{8raffo} on reaction 1 is shown in Figure 3-3-B. The plot of the rate versus the diameter, shows the consumption rates range from 7.97E-07 up to 4.92E-05 Molar(S_8)/second over a range of diameter values from 316.7 to 1657.5nm (corresponding to surface area values of 18.9E+5 and 3.6E+05dm^2/dm^3, respectively). It is apparent that there is no linear relationship between the surface area and the consumption rate of S_{8raffo}.

The effect of sulfide concentration on the rate of consumption of S_{8raffo} is shown in Figure 3-4-B. The rate of S_{8raffo} consumption ranges between 4.79E-06 to 2.10E-05 Molar(S_8)/second for a range of sulfide concentration between 13.5mM up to 54mM HS^-. The rate of nucleophilic dissolution of S_{8raffo} is shown to be completely unaffected from the sulfide concentration, showing zero correlation as it has been shown graphically as well as statistically (P: 0.078).

The effect of the pH of the experimental solution on the nucleophilic dissolution of S_{8raffo} is shown in Figure 3-4-D. The S_{8raffo} consumption rate ranges from 6.47E-06 to 1.46E-05 Molar(S_8)/second, corresponding to pH values of 7.7 to 10, respectively. As shown in Figure 3-4 the relationship between S_{8raffo} and pH is proportional and follows a linear fashion, with slope at 3.88E-06 and intercept at -2.34E-05 (p value at 0.018).

The effect of ionic strength of the experimental solution on the rate of consumption of S_{8raffo} is shown in Figure 3-4-F. The rate displays a inversely proportional relationship with the ionic strength (expressed in molarity), with the rate values dropping from 1.90E-05 down to 5.73E-06 Molar(S_8)/second as the ionic strength increases from 0.029 up to 0.269M. The inversely proportional correlation between the rate and ionic strength for the S_{8raffo} showed a slope at -4.44E-05, intercept at 1.66E-05 and p value at 0.052. However, the p value of this parameter during the multiple linear regression model was at 0.049, therefore it is statistically significant and is included in the kinetic rate law (see below).

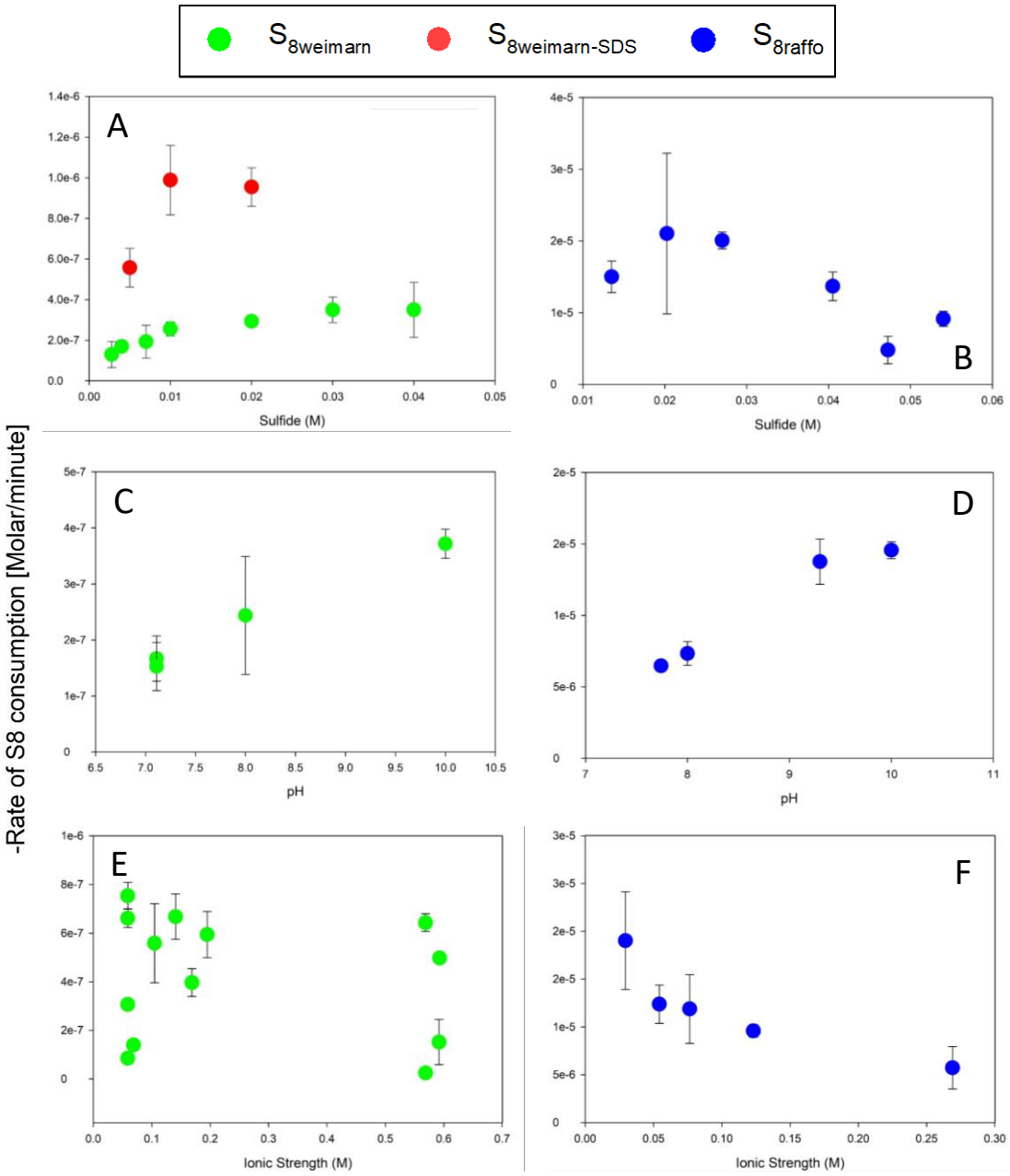

Figure 3-4: Influence of sulfide concentration (top), pH (middle) and ionic strength of solution (bottom) on the rate of consumption of $S_{8weimarn}$ (left - green circles) and S_{8raffo} (right - blue circles) expressed as Molar(S_8)/second.

Results of dissolution kinetics of surfactant coated S_{8nano} ($S_{8weimarn\text{-}SDS}$)

The reactivity of $S_{8weimarn\text{-}SDS}$ was compared with that of $S_{8weimarn}$ at Figure 3-4-A using the surface area normalized rates. The consumption rates of SDS-coated $S_{8weimarn\text{-}SDS}$ are more than three times higher than those of the non-surfactant coated $S_{8weimarn}$. The consumption rates of $S_{8weimarn\text{-}SDS}$ have also been compared with those of $S_{8weimarn}$ and S_{8raffo} at a sulfide concentration of 13.5mM HS^- (Table 3-2). Rates of S_{8raffo} consumption reach 1.6E-10 Molar(S_8)/second/dm^{-1}, whereas $S_{8weimarn\text{-}SDS}$ and $S_{8weimarn}$ show rates of 4.37E-12 and 1.37E-12 Molar(S_8)/second/dm^{-1}, respectively. The rates of S_{8raffo} were SSA-normalized for the shake of comparison with the rest of the forms of nanoparticles. However, non-normalized rate values show 1.2E-04 Molar(S_8)/second for the S_{8raffo}, whereas 6.99E-06 and 2.19E-06 Molar(S_8)/second for $S_{8weimarn\text{-}SDS}$ and $S_{8weimarn}$, respectively (Table 3-2).

Table 3-2: Consumption rates of various forms of elemental sulfur under same conditions.

Type of S_{8nano}	**Sulfide (mM)**	**SSA (dm^{-1})**	**-Rate (Molar/sec)**	**-Rate (Molar/sec/dm^{-1})**
S_{8raffo}	13.5	750,203.18	1.20E-04	1.60E-10
$S_{8weimarn\text{-}SDS}$	13.5	1,600,000.00	6.99E-06	4.37E-12
$S_{8weimarn}$	13.5	1,600,000.00	2.19E-06	1.37E-12
$\frac{S_{8raffo}}{S_{8weimarn}}\ ratio$	N/A	N/A	55	117
$\frac{S_{8weimarn-SDS}}{S_{8weimarn}}\ ratio$	N/A	N/A	3.2	3.2

Results of the temperature effect on the nucleophilic reaction

The effect of temperature on the rate of $S_{8weimarn}$ consumption is shown in Figure 3-5-A. The Arrhenius plot expressed as log[-mols/sec] versus the reciprocal of temperature shows a statistically significant inversely proportional relationship. The log[-mols/sec] values range from -10.10 to -9.19, representing rate values of 2.61E-07 and 2.15E-06 Molar(S_8)/second, and corresponding to temperature values of 27 to 65°C (299.96 and 338.06K), respectively. The activation energy has been calculated based on the equation $\ln K = -E_a/R$ (equation 1), with K being the slope of the linear regression of the data, R being 8.314 Joules/mol*K, and activation energy (E_a) in Joules/mol. The result was E_a = 43.01kJoules/mol or 10.28kcal/mol.

The effect of temperature on the rate of $S_{8weimarn\text{-}SDS}$ is shown in Figure 3-5-B. An Arrhenius plot of the log[-mols/sec] of $S_{8weimarn\text{-}SDS}$ is plotted versus the reciprocal of temperature (expressed in Kelvin). The consumption in log[-mols/sec] ranged from -10.30 to -9.80, representing 1.64E-07 and 5.19E-07 Molar(S_8)/second, and temperature values of 7.5^o and 35^{o}C (280.66 and 308.16K), respectively. The data showed an inversely proportional linear relationship between the consumption of $S_{8weimarn\text{-}SDS}$ and the reciprocal of temperature. The activation energy was calculated at 26.82kJoules/mol or 6.41kcal/mol.

The effect of temperature on the rate of nucleophilic dissolution of S_{8raffo} is shown Figure 3-5-C. The Arrhenius plot shows a statistically significant inversely proportional relationship, with rate values ranging between 1.29E-05 to 6.60E-05 Molar(S_8)/second, corresponding to -8.41 and -7.70 log[mols/sec], respectively, with temperature values ranging from 25 to 55^{o}C (298.16 to 328.16K), respectively. The activation energy of the reaction 1 specifically for S_{8raffo} has been calculated at 42.00kJoules/mol or 10.04kcal/mol, based on the slope of the data from the Arrhenius plot.

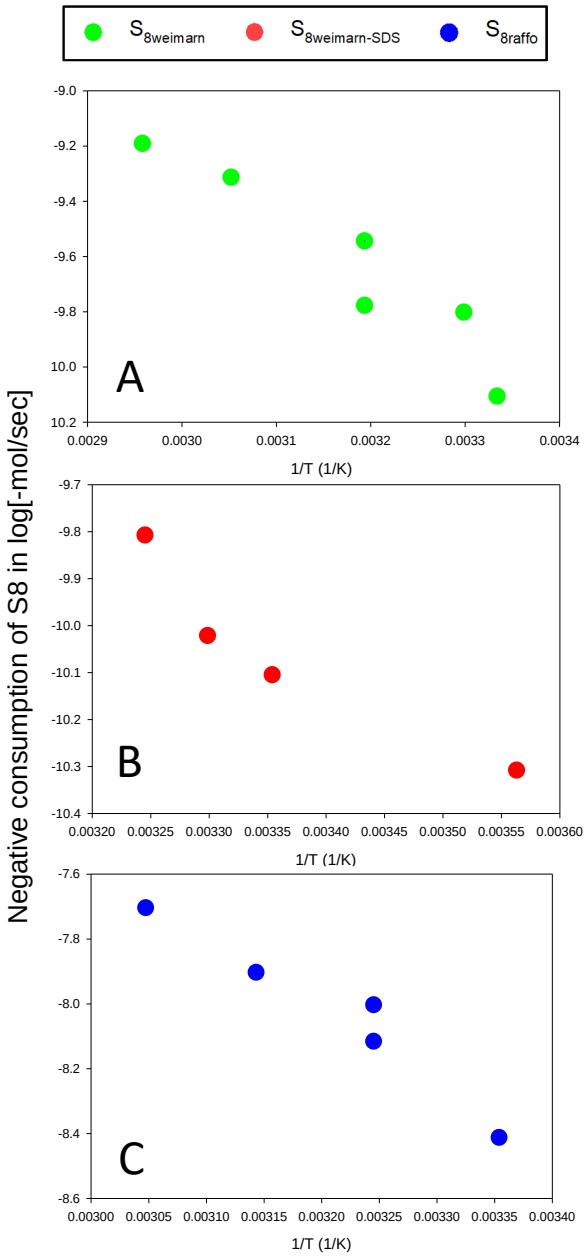

Figure 3-5: Effect of temperature on the rate of dissolution of $S_{8weimarn}$ (A), $S_{8weimarn\text{-}SDS}$ (B) and S_{8raffo} (C) is shown (temperature in Kelvin). The activation energy for each reaction is extracted from the slope of the linear relationship between log[-mols/sec] vs reciprocal of temperature (in ^{o}C)(Appendix B).

Kinetic rate laws

In order for the kinetic rate laws to be defined, key parameters were tested in order to evaluate their statistical significance (Table 3-3 and Table 3-4). The multiple linear regression is a statistical method calculating an equation through which the kinetic rate can be calculated by taking into consideration all parameters (pH, T, I, sulfide). The statistically significant parameters (probability less than 0.05) were included in the kinetic rate law. The rate for reaction 1 was surface area normalized for the $S_{8weimarn}$ as there was established a linear correlation between the specific surface area and the consumption rate for $S_{8weimarn}$ (Figure 3-3-A). However, the rate for reaction 1 involving S_{8raffo} was not surface area normalized since there was no linear correlation suggested by the data of the S_{8raffo} experiments (Figure 3-3-B). This observation for the S_{8raffo} nanoparticles was not able to be explained as these forms of nanoparticulate elemental sulfur are expected to result in surface area-controlled reactivity, similar to other chemical systems (Mitra and Rimstidt, 2009; Rimstidt, 2014).

The linear regression data of the parameters of $S_{8weimarn}$ and S_{8raffo} kinetics are shown in the Table 3-3 and Table 3-4, respectively. Apart from the intercept of the regression, and the temperature which show estimates that are statistically significant (probabilities $P<0.05$) in both $S_{8weimarn}$ and S_{8raffo} models, the rate of consumption of S_{8raffo} is statistically significantly influenced by the ionic strength of the solution (Table 3-4). The ionic strength does not show any statistically significant influence on the kinetic rate law of the $S_{8weimarn}$, which is expected from the graphical representation of the ionic strength effect experiments (Figure 3-4) as well as the hydrophobic nature of this type of nanoparticle.

Table 3-3: Statistical data from the multiple linear regression modeling of the parameters of the $S_{8weimarn}$ nucleophilic consumption reaction.

Coefficients	Estimate	Std. Error	t value	Pr(>|t|)
Intercept	-11.325337	0.965345	-11.732	1.68e-13
ph	0.002275	0.041433	0.055	0.957
h2s	0.083626	0.214750	0.389	0.699
i	-0.139622	0.166015	-0.841	0.406
Ret	-36.593721	8.242318	-4.440	9.03e-05

Table 3-4: Statistical data from the multiple linear regression modeling of the parameters of the S_{8raffo} nucleophilic consumption reaction.

Coefficients	Estimate	Std. Error	t value	Pr(>|t|)
Intercept	-4.112891	0.923489	-4.454	0.000464
ph	-0.002587	0.067108	-0.039	0.969763
h2s	-0.007300	0.188793	-0.039	0.969666
i	-0.354338	0.165565	-2.140	0.049182
ret	-32.160899	7.718962	-4.166	0.000827

Based on the above information the kinetic rate laws of the nucleophilic dissolution of $S_{8weimarn}$ and S_{8raffo} are calculated to be:

$$r_{S8weimarn} = 10^{-11.33}\left(e^{\frac{-700.65}{RT}}\right)$$

with $r_{weimarn}$ in Molar/second/dm^{-1} (T: 25 to 65°C, diameter: 325 to 653.1nm), and:

$$r_{S8raffo} = 10^{-4.11}\, i^{-0.35}\left(e^{\frac{-615.77}{RT}}\right)$$

with r_{raffo} in Molar/second (T: 25 to 55°C, ionic strength: 0.029 to 0.269 Molar).

Discussion

Surface area is a key control on the nucleophilic dissolution rates of $S_{8weimarn}$. The segment of the plot that displays linearity between the rate of consumption of $S_{8weimarn}$ and surface area, corresponds to a surface area-controlled region (Figure 3-3). Within this region, which based on 95% confidence calculations was found to range between diameter values of 653.1 and 325nm (corresponding to surface area values of 9.18E+05 up to 1.85E+06dm^2/dm^3), the rates are controlled by the surface area of the $S_{8weimarn}$. The increase of the surface area, representing finer diameters of nanoparticles, results in an increase of the nanoparticles' decomposition rate, due to the higher exposure of surface area per volume of $S_{8weimarn}$ to react. When the nanoparticles are below the diameter threshold of 325nm (surface area values are higher than 1.84E+06 dm^2/dm^3), the nucleophilic dissolution rates are not influenced by the surface area but are controlled purely by the diffusion of sulfide in the aqueous medium. Experiments defining the rates of S_{8raffo} consumption as a function of surface area do not indicate any correlation between the diameter (or surface area) of the nanoparticles and their consumption rates. There is no clear explanation on this observation. Based on the established importance of surface area for this reaction on $S_{8weimarn}$ and the practice of utilizing surface-area normalized rates in mineral reactions rates (Mitra and Rimstidt, 2009; Rimstidt, 2014), we have utilized all kinetic data for $S_{8weimarn}$ as surface-area normalized within the framework of the multiple linear regression modeling in order to calculate the kinetic rate law of $S_{8weimarn}$. However, since S_{8raffo} showed no SSA-dependence on the kinetic rates of consumption, the rate data utilized for the estimation of the kinetic rate law of S_{8raffo} consumption were not surface area normalized. In order to present the kinetics data between S_{8raffo} and $S_{8weimarn}$ in a comparable format, all the Figures included in the Results section are in Molar(S_8)/second, regardless on the type of nanoparticle.

Sulfide molarity is another parameter that showed no effect on the consumption rates of S_{8raffo}, as displayed graphically (Figure 3-4-B) and evaluated statistically ($p < 0.05$). Even if sulfide molarity was shown to be a key control on the nucleophilic dissolution of $S_{8weimarn}$ (based on statistical significance of slope; $p<0.05$) multiple linear regression

modeling on the datasets of both $S_{8weimarn}$ and S_{8raffo} suggested that the effect of sulfide was overall statistically insignificant, and was not included on either rate laws. However, even if linear relationship between either of S_{8nano} and sulfide concentration was not able to be established, it was clear that the S_{8raffo} is much more reactive than the $S_{8weimarn}$ under the same sulfide conditions (Table 3-2; Figure 3-4-A and Figure 3-4-B). This increase of reactivity in S_{8raffo} compared to that of $S_{8weimarn}$ might be related to the hydrophilic character of these nanoparticles, which is generated by the presence of sulfonic moieties on their surface due to the incorporation of polythionic chains in the structure of the nanoparticles.

The effect of ionic strength on the rates of S_{8nano} showed significant differences depending on the type of S_{8nano}. Ionic strength showed no statistically significant effect on the nucleophilic consumption of $S_{8weimarn}$, which coincides with the hydrophobic character of its surface. The inverse effect of ionic strength on the rate of consumption of S_{8raffo} indicates that the hydrophilic character of this type of nanoparticle is influenced by the amount of charged ions in solution. This suggests that (at least part of) the S components that comprise the S_{8raffo} (elemental sulfur rings and polythionate chains) participate in an electrostatic interaction, with potential reaction with neutral species being a possibility for the reactivity between the elemental sulfur rings with sulfide. This is consistent with the model S_{8raffo} where long-chained, negatively charged S polymers contribute surface charge to this type of nanoparticle (Steudel et al., 1988). A negative relationship between the consumption rates of S_{8raffo} and the square root of ionic strength was also established (linear relationship expressed as y = -3.36E-05x + 2.21E-05, with y = rate (in Molar(S_8)/sec) and $x = \sqrt{I}$, $R^2 = 0.862$ and p: 0.022; Appendix B). This information suggests a reaction between oppositely charged species according to the Bronsted equation (Brezonik, 1993). This characteristic seems counter to the chemical species involved where negatively charged moieties in S_{8raffo} (that make it more hydrophilic) should be interacting with neutral H_2S and charged HS^- ions. However, there may be other more specific electrostatic effects concerning specific sites or a more general electrostatic effect linked to the interaction of H^+ and OH^- ions with the nanoparticle surface (noting the pHzpc for S_{8raffo} is currently undefined).

The surface character and surface coatings of the S_{8nano} play a significant role in the reactivity of elemental sulfur nanoparticles (Figure 3-6 and Figure 3-7). $S_{8weimarn}$ and S_{8raffo} – the hydrophobic and hydrophilic end members of the elemental sulfur nanoparticles, respectively – were compared on their reactivity when all conditions were identical, resulting in rate changes spanning 2 orders of magnitude (Figure 3-4-A and Figure 3-4-B; Table 3-2). Furthermore, the presence of surfactant coatings (SDS) on the surface of the $S_{8weimarn-SDS}$, attributed a less hydrophobic character to the nanoparticles, compared to their non-surfactant-covered homologues ($S_{8weimarn}$), resulting in 3.2 times higher reactivity (Figure 3-4-A and Table 3-2). These observations lead to the understanding that increasing hydrophilicity enhances the reactivity of the nanoparticles (Figure 3-6).

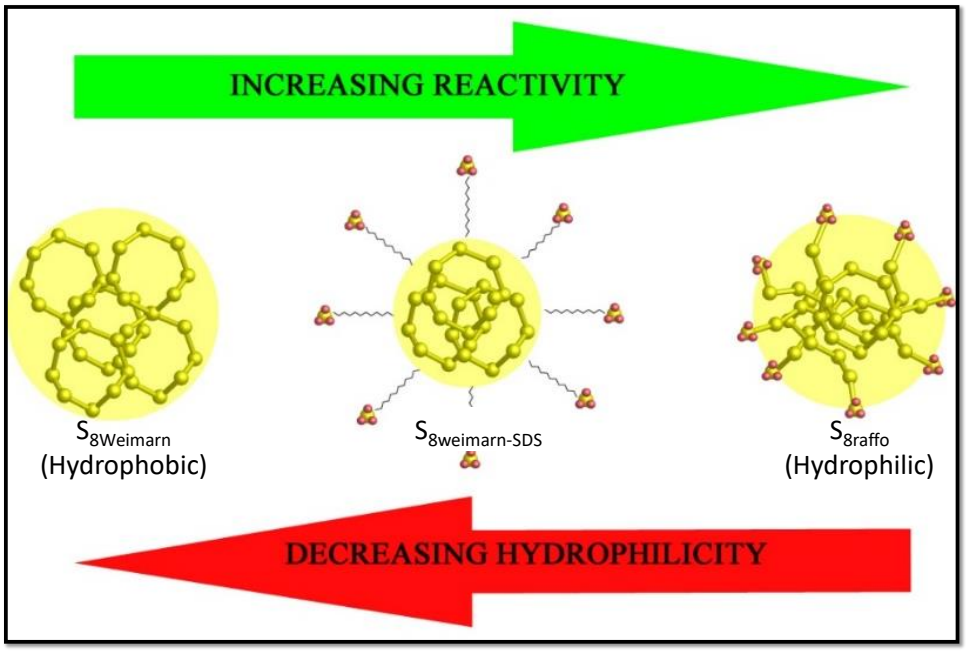

Figure 3-6: Elemental sulfur nanoparticles reactivity as a function of their surface character. Experimental data show that the reactivity of the elemental sulfur nanoparticles is proportional to their hydrophilicity. From left to right the hydrophilicity and reactivity increases as we move from the $S_{8weimarn}$ (hydrophobic nanoparticles) to surfactant coated $S_{8weimarn-SDS}$, and to S_{8raffo} (hydrophilic nanoparticles).

Activation energy values for $S_{8weimarn}$, S_{8raffo} and $S_{8weimarn\text{-}SDS}$ nanoparticles is Ea = 10.27, 10.04, and 6.41kcal/mol, respectively. Similar activation energy values have been estimated on the nucleophilic dissolution of α-S_8 (7.48kcal/mol)(Hartler et al., 1967) and the nucleophilic dissolution of $S_{8biological}$ (7.07kcal/mol)(Kleinjan et al., 2005c). These values suggest that the mechanism for the rate-controlling step is mineral dissolution, or mineral dissolution via surface reaction control (Langmuir, 1997). The results of the estimates of the activation energy are in agreement with the results of the multiple linear regression and the format of the kinetic rate laws, where temperature is the only parameter that controls the rate for both $S_{8weimarn}$ and S_{8raffo}, in addition to the ionic strength in the case of S_{8raffo}.

The pH conditions influence the initial consumption rates of both $S_{8weimarn}$ and S_{8raffo} in a linear fashion. The increase of rates with more alkaline pH is in agreement with the greater stability of polysulfides under these conditions (Figure 3-4-C and Figure 3-4-D) (Kamyshny et al., 2004), and the idea that polysulfides are also able to participate in the nucleophilic dissolution of elemental sulfur as an autocatalytic process (Hartler et al., 1967). The increase in proton concentration at lower pH forces the equilibrium of the reaction 1 to the left, where decomposition of polysulfides to S_8 and sulfide occurs. However, the pH conditions do not affect the overall reactivity of any of the S_{8nano} forms, as evaluated via the multiple linear regression modeling.

Rate data was gathered in this study on the particles and their reactivity – our discussion of mechanism and pathway reaction possibilities is focused on reactivity of the S_8 ring, but of course the particles are more complicated than this. Any elemental sulfur particle likely contains different size S(0) rings, and S_{8raffo} also includes polythionic molecules. Ab initio studies on the polarizability of sulfur clusters of various sizes (2 to 12 sulfur atoms) has shown that the increase of a molecule from 8 to 9 atoms of sulfur leads to a slight decrease of polarizability as well as increase of bond length (Millefiori and Alparone, 2001). In terms of the polythionic molecules, displacement reactions can take place between polythionates, polysulfane monosulfonic acids, thiosulfate and sulfide, but directly measuring this is very difficult in most experimental systems (Davis, 1958; Foss, 1958). Nevertheless, a nucleophilic interaction between the S_{8raffo} polythionates and sulfide

would lead to either the formation of polythionate chains of a different length, or to a sulfur homocycle. In addition, polythionates are most stable within acidic pH ranges, which are not related to the conditions used in our experiments. Therefore, our focus here is on the nucleophilic dissolution of the cyclo-octasulfur by sulfide which is represented by reaction one (1).

Three proposed mechanisms of the nucleophilic dissolution of elemental sulfur nanoparticles by sulfide (a and b) are shown in Figure 3-7. In the case where the nanoparticle has no surfactant coating (a), the sulfide attacks the cyclo-octasulfur ring at the S_{8nano} surface via nucleophilic degradation (Steudel, 2003), cleaving a covalent S-S bond as well as attaching itself to the end of the newly formed polysulfide chain, which is consequently released to the aqueous medium (Figure 3-7-A). Because of the significant change in polarity and the degree of electron delocalization between S_8 and S_n^{2-}, polysulfide is effectively released from the mineral into the surrounding aqueous solution. Polarizability is the ability of a molecule's electron cloud to be disturbed, with the molecule becoming polar. When this happens, it possibly can influence the compound's intermolecular interactions (Bruice, 2006). In the case of Van der Waals interactions, a slight change in the polarizability or the area of contact between two molecules being held together by Van der Waals bonds can influence the strength of the bond (Bruice, 2006). In our case where a nonasulfide is formed, both the change of polarizability as well as the contact area (comparing the contact area between two S_8 ring molecules versus an S_8 ring and a nonasulfide chain) would influence the van der Waals interactions making them weaker, and would support the idea of detachment from the S_{8nano} surface. The first polysulfide molecule, having the formula HS_9^{2-} will deprotonate and undergo a series of dissociation and dimerization reactions (similar to reaction 2, that comes to completion in 10 seconds at ambient conditions)(Kamyshny et al., 2003; Steudel, 2003). This would result in the formation of a wide range of chain lengths, ranging from S_2^{2-} to S_8^{2-}, with S_4^{2-} and S_5^{2-} being the most prevalent (Kamyshny et al., 2004).

Figure 3-7–B considers the role of organics, modeled as the surface of the nanoparticle coated by a surfactant (SDS)(Figure 3-7-B, left side). Surfactants can significantly enhance solubility of $S_{8(aq)}$ (up to 5000-fold)(Steudel and Holdt, 1988), as well

as considerably impact nanoparticle coarsening (Chaudhuri and Paria, 2010, 2011; Garcia Jr and Druschel, 2014). Therefore S_{8nano} reacts with sulfide either as an SDS-coated nanoparticle (Figure 3-7-B bottom), or as dissolved SDS-cyclooctasulfur complex ($S_{8aq\text{-}SDS}$; Figure 3-7-B top), or both. During the scenario where sulfide attacks nucleophilically the SDS-coated surface of the S_{8nano} (Figure 3-7-B bottom), the reaction takes place on the surface of the nanoparticle as the sulfur ring is attached to that surface. Rate data (Table 3-2) indicate that the presence of the surfactant coating enhances the reaction of sulfide with the $S_{8weimarn}$ surface, compared to the $S_{8weimarn}$ reaction without SDS.

In order to evaluate whether the scenario of surface reaction-controlled pathway versus the dissolution-controlled pathway is predominant, we considered the kinetics of dissolution of S_{8nano} presence of surfactants as well as the kinetics of reaction 1 on the $S_{8\text{-}surfactant}$ complex. Rates of $S_{8(aq)}$ dissolution with SDS are shown to take on the order of 30 minutes to equilibrate (Steudel and Holdt, 1988). Coarsening of $S_{8weimarn\text{-}SDS}$ at a pH 10 solution resulted in complete dissolution of the nanoparticles and their transformation to $S_{8aq\text{-}SDS}$ within 90 minutes. Therefore, both $S_{8weimarn\text{-}SDS}$ and $S_{8aq\text{-}SDS}$ are present in solution within the first 90 minutes (in these conditions). The kinetics of reaction 1 when $S_{8aq\text{-}SDS}$ is nucleophilically attached by sulfide at pH 10 show a production rate of S_5^{2-} at 4.73E-09 Molar(S_5^{2-})/second. When compared with S_{8raffo}, $S_{8weimarn}$, as well as $S_{8biological}$ (based on the rate law estimated by Kleinjan et al., 2005c), the dissolution of $S_{8aq\text{-}SDS}$ is shown to be very slow (Figure 3-8). This suggests that the rate of reaction 1 is controlled by the rate of the transport of sulfide directly to the S_{8nano} surface until the surfactant-induced dissolution of the nanoparticle and the complete release of $S_{8aq\text{-}SDS}$ are achieved. Then, the $S_{8aq\text{-}SDS}$ dissolution is the rate limiting step, and not on the transport of sulfide directly to the S_{8nano} surface. Furthermore, the comparison between the $S_{8biological}$ and the rest of its abiotic analogues (S_{8nano}) is achieved under pH 5, 8 and 10 using the "Kinetiscope – stochastic kinetics simulator". It is worth mentioning that the kinetic rate law for the nucleophilic dissolution of $S_{8biological}$ is empirically estimated for pH8, therefore the models for $S_{8biological}$ under pH values of 5 and 10 incorporate high error. The kinetic model at pH 8 and 10 suggested that the rate of consumption of $S_{8biological}$ is between those of S_{8raffo} and $S_{8weimarn}$, supporting the argument that these two forms of elemental sulfur nanoparticles are accurate

endmembers of a range of inorganic S_{8nano} structures, serving as promising abiotic analogues of the various forms of $S_{8biological}$ produced by microbial cells.

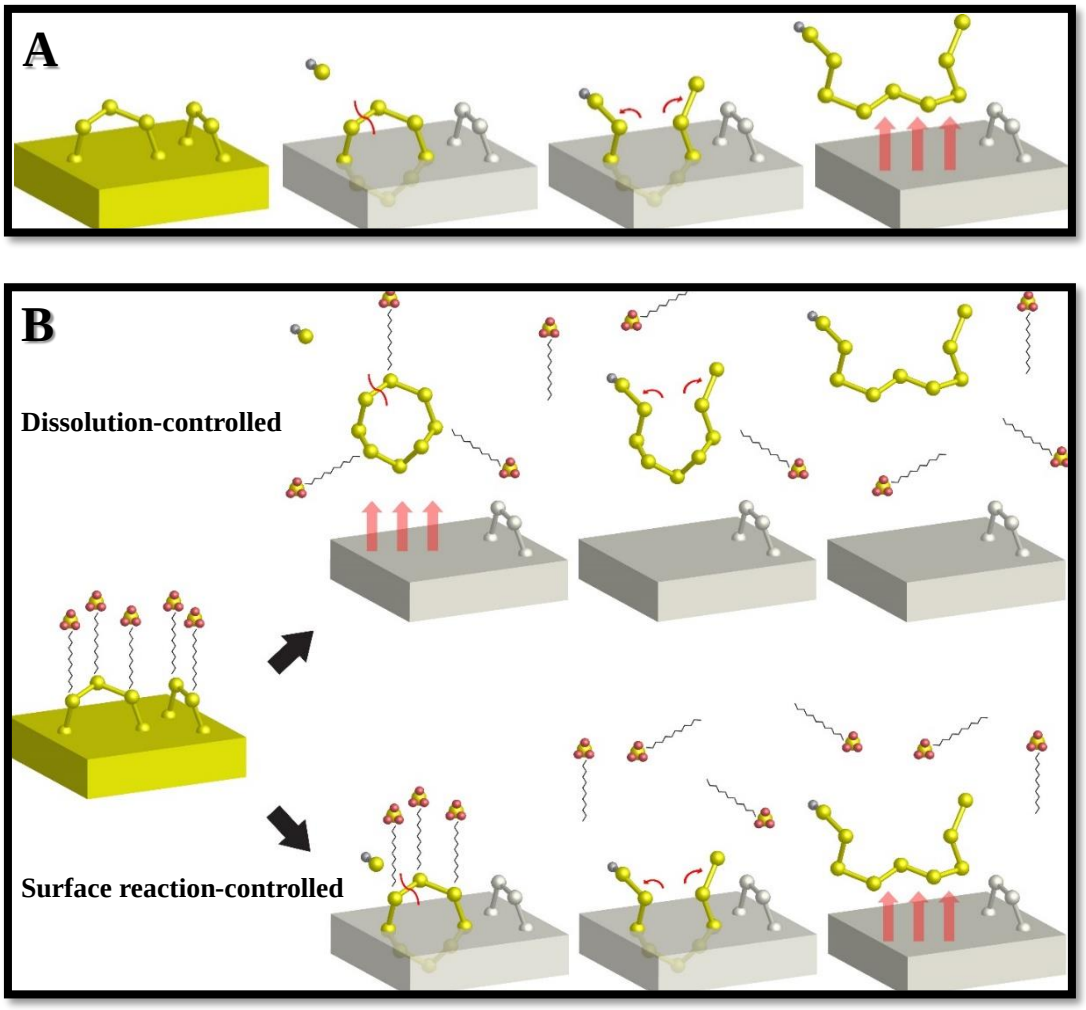

Figure 3-7: Proposed mechanisms of the nucleophilic dissolution of elemental sulfur nanoparticles by sulfide (a and b). In the case where the nanoparticle has no surface coating (a) the sulfide attacks the cyclo-octasulfur ring and cleaves a covalent S-S bond as well as attaches itself to the end of the newly formed polysulfide chain, which is released to the aqueous medium. In the case (b) that the surface of the nanoparticle is coated by surfactants (sodium dodecylsulfate), two pathways can take place: 1) the presence of surfactant can solubilize cyclo-octasulfur rings (top) which react with the sulfide to produce polysulfides in the aqueous medium. 2) The sulfide causes nucleophilic dissolution of S_8 on the surface of the nanoparticle similarly as in scenario a, though the kinetic rate of the reaction is much faster.

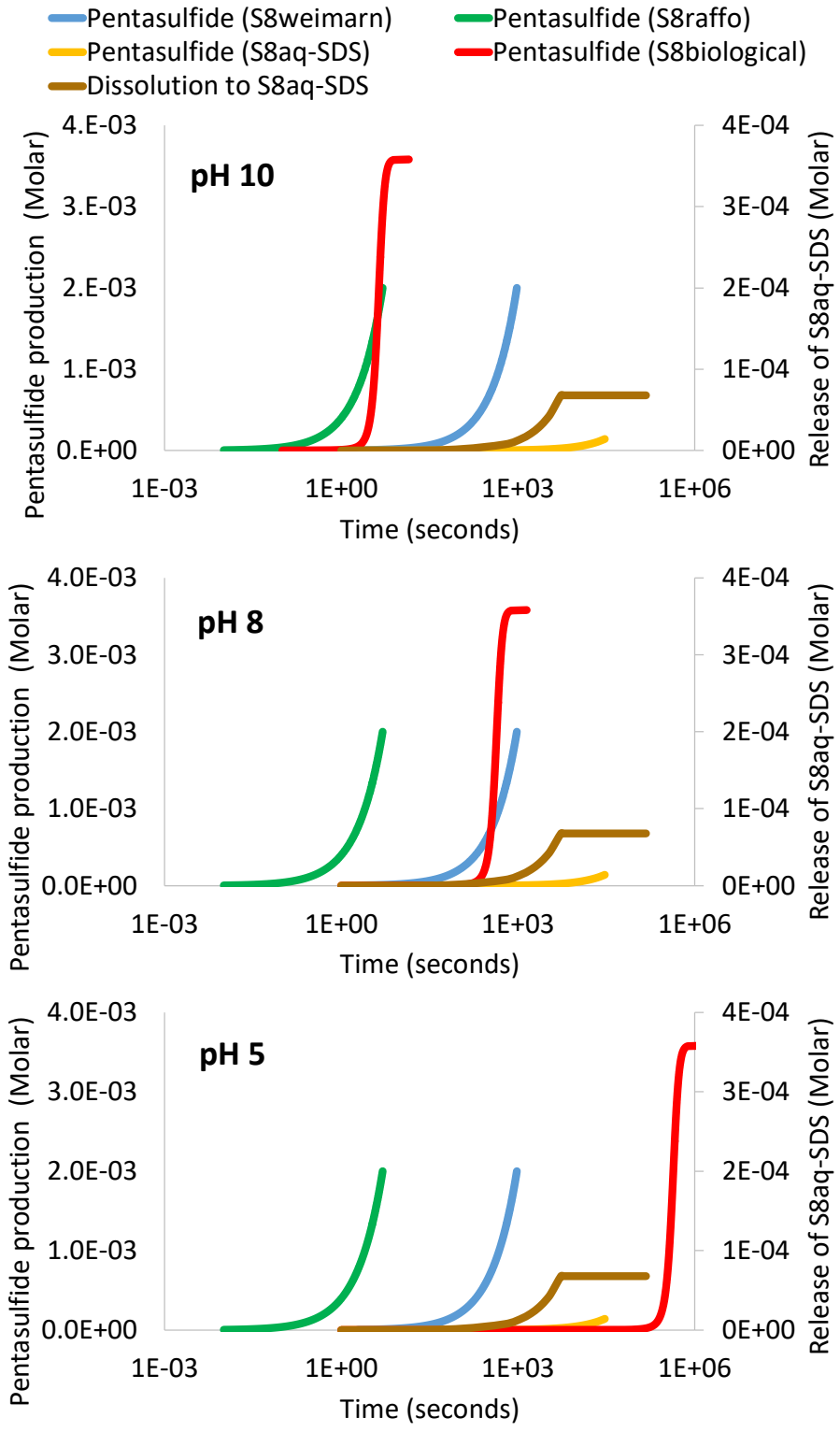

Figure 3-8: Geochemical kinetic modeling for the production kinetics of polysulfide ions during the nucleophilic dissolution of $S_{8weimarn}$ (blue), S_{8raffo} (orange), $S_{8biological}$ (red), and $S_{8aq\text{-}SDS}$ (yellow). The plots also display the kinetics of dissolution of $S_{8weimarn\text{-}SDS}$ to release

$S_{8aq\text{-}SDS}$ presence of SDS surfactants (not due to the nucleophilic reaction). The kinetics of both the release of $S_{8aq\text{-}SDS}$ as well as its nucleophilic reaction by sulfide to form polysulfides took place only at pH 10. The rate law utilized for the estimates of the kinetics of $S_{8biological}$ was derived by Kleinjan et al. (2005c). The limitation for the kinetics of $S_{8biological}$ is that the rate law is empirically estimated at pH 8 (middle) and therefore the calculations for pH 5 (bottom) and 10 (top) possibly enclose high error (Kleinjan et al. 2005c).

Conclusions

In summary, the current work has defined the rate laws for the hydrophobic and hydrophilic forms of elemental sulfur nanoparticles that is $S_{8weimarn}$ and S_{8raffo}, respectively. Both forms of nanoparticles are believed to serve as abiotic analogues to biologically produced sulfur. Depending on the bacteria that form elemental sulfur, $S_{8biological}$ can resemble the chemical structure and surface character of either $S_{8weimarn}$ or S_{8raffo}. The difference in hydrophilicity (surface character) between S_{8raffo} and $S_{8weimarn}$ influences significantly the rates of their nucleophilic dissolution by sulfide, with more hydrophilic surfaces of nanoparticles showing greater rate values. Surfactant coatings onto S_{8nano} (SDS used in this study) enhance the reactivity of the nanoparticles, where sulfide interacts with the cyclo-octasulfur on the surface of the $S_{8nano\text{-}surfactant}$ (Figure 3-7-B bottom). Furthermore, surfactant-induced solubility of S_{8nano} releases dissolved cyclo-octasulfur-surfactant complexes creating a pool of dissolved $S_{8aq\text{-}surfactant}$, which in our experiments is shown to take place in a relatively fast manner (using SDS at pH 10). The low reactivity of $S_{8aq\text{-}SDS}$ leads to a kinetic rate limiting step after the complete dissolution of S_{8nano}, presence of SDS surfactants, causing the mechanism of reaction 1 to be controlled by the interaction of sulfide with the released cyclo-octasulfur-surfactant complex (Figure 3-7-B top). However, until the surfactant-induced dissolution of the nanoparticle and the complete release of $S_{8aq\text{-}SDS}$ are achieved (both $S_{8weimarn\text{-}SDS}$ and $S_{8aq\text{-}SDS}$ in the system), the rate of reaction 1 is controlled by the rate of the transport of sulfide directly to the $S_{8weimarn\text{-}SDS}$ surface.

References

Amrani, A. (2014) Organosulfur compounds: molecular and isotopic evolution from biota to oil and gas. Annual Review of Earth and Planetary Sciences 42, 733-768.

Arrhenius, S. (1889) Über die Reaktionsgeschwindigkeit bei der Inversion von Rohrzucker durch Säuren. Zeitschrift für physikalische Chemie 4, 226-248.

Berzelius, J.J. (1845) Traité de Chimie, vol. 2. Didot, Paris.

Brezonik, P.L. (1993) Chemical kinetics and process dynamics in aquatic systems. CRC Press.

Bruice, P.Y. (2006) Essential organic chemistry. Pearson Education.

Bunsen, R. (1847) Ueber den innern Zusammenhang der pseudovulkanischen Erscheinungen Islands. European Journal of Organic Chemistry 62, 1-59.

Chaudhuri, R.G. and Paria, S. (2010) Synthesis of sulfur nanoparticles in aqueous surfactant solutions. Journal of colloid and interface science 343, 439-446.

Chaudhuri, R.G. and Paria, S. (2011) Growth kinetics of sulfur nanoparticles in aqueous surfactant solutions. Journal of colloid and interface science 354, 563-569.

Chen, K.Y. and Gupta, S.K. (1973) Formation of polysulfides in aqueous solution. Environmental letters 4, 187-200.

Chen, K.Y. and Morris, J.C. (1972) Kinetics of oxidation of aqueous sulfide by oxygen. Environmental Science & Technology 6, 529-537.

Davis, R.E. (1958) Displacement Reactions at the Sulfur Atom. I. An Interpretation of the Decomposition of Acidified Thiosulfate. Journal of the American Chemical Society 80, 3565-3569.

Foss, O. (1958) Remarks on the reactivities of the penta-and hexathionate ions. Acta Chem. Scand 12.

Garcia Jr, A.A. and Druschel, G.K. (2014) Elemental sulfur coarsening kinetics. Geochemical Transactions 15, 11.

Giggenbach, W. (1972) Optical spectra and equilibrium distribution of polysulfide ions in aqueous solution at 20. deg. Inorganic Chemistry 11, 1201-1207.

Giggenbach, W.F. (1974a) Equilibriums involving polysulfide ions in aqueous sulfide solutions up to 240. deg. Inorganic Chemistry 13, 1724-1730.

Giggenbach, W.F. (1974b) Kinetics of the polysulfide-thiosulfate disproportionation up to 240. deg. Inorganic Chemistry 13, 1730-1733.

Hartler, N., Libert, J. and Teder, A. (1967) Rate of sulfur dissolution in aqueous sodium sulfide. Industrial & Engineering Chemistry Process Design and Development 6, 398-406.

Heitmann, T. and Blodau, C. (2006) Oxidation and incorporation of hydrogen sulfide by dissolved organic matter. Chemical Geology 235, 12-20.

Kamyshny, A., Druschel, G., Mansaray, Z.F. and Farquhar, J. (2014) Multiple sulfur isotopes fractionations associated with abiotic sulfur transformations in Yellowstone National Park geothermal springs. Geochemical transactions 15, 7.

Kamyshny, A., Goifman, A., Gun, J., Rizkov, D. and Lev, O. (2004) Equilibrium distribution of polysulfide ions in aqueous solutions at 25 C: a new approach for the study of polysulfides' equilibria. Environmental science & technology 38, 6633-6644.

Kamyshny, A., Goifman, A., Rizkov, D. and Lev, O. (2003) Kinetics of disproportionation of inorganic polysulfides in undersaturated aqueous solutions at environmentally relevant conditions. Aquatic Geochemistry 9, 291-304.

Kamyshny, A., Gun, J., Rizkov, D., Voitsekovski, T. and Lev, O. (2007) Equilibrium distribution of polysulfide ions in aqueous solutions at different temperatures by rapid single phase derivatization. Environmental science & technology 41, 2395-2400.

Kleinjan, W.E., de Keizer, A. and Janssen, A.J. (2005a) Equilibrium of the reaction between dissolved sodium sulfide and biologically produced sulfur. Colloids and Surfaces B: Biointerfaces 43, 228-237.

Kleinjan, W.E., de Keizer, A. and Janssen, A.J. (2005b) Kinetics of the chemical oxidation of polysulfide anions in aqueous solution. Water research 39, 4093-4100.

Kleinjan, W.E., de Keizer, A. and Janssen, A.J. (2005c) Kinetics of the reaction between dissolved sodium sulfide and biologically produced sulfur. Industrial & engineering chemistry research 44, 309-317.

Kohnen, M.E.L., Damsté, J.S.S., Kock-van Dalen, A.C., Haven, H.L.T., Rullkötter, J. and De Leeuw, J.W. (1990) Origin and diagenetic transformations of C25 and C30

highly branched isoprenoid sulphur compounds: Further evidence for the formation of organically bound sulphur during early diagenesis. Geochimica et Cosmochimica Acta 54, 3053-3063.

Langmuir, D. (1997) Aqueous environmental geochemistry.

Licht, S. and Davis, J. (1997) Disproportionation of aqueous sulfur and sulfide: kinetics of polysulfide decomposition. The Journal of Physical Chemistry B 101, 2540-2545.

Luther III, G.W., Findlay, A.J., MacDonald, D.J., Owings, S.M., Hanson, T.E., Beinart, R.A. and Girguis, P.R. (2011) Thermodynamics and kinetics of sulfide oxidation by oxygen: a look at inorganically controlled reactions and biologically mediated processes in the environment. Frontiers in microbiology 2.

Millefiori, S. and Alparone, A. (2001) Ab Initio Study of the Structure and Polarizability of Sulfur Clusters, S n (n= 2− 12). The Journal of Physical Chemistry A 105, 9489-9497.

Mitra, A. and Rimstidt, J.D. (2009) Solubility and dissolution rate of silica in acid fluoride solutions. Geochimica et Cosmochimica Acta 73, 7045-7059.

Raven, M.R., Adkins, J.F., Werne, J.P., Lyons, T.W. and Sessions, A.L. (2015) Sulfur isotopic composition of individual organic compounds from Cariaco Basin sediments. Organic Geochemistry 80, 53-59.

Rickard, D. and Luther, G.W. (2007) Chemistry of Iron Sulfides. Chemical Reviews 107, 514-562.

Rimstidt, J.D. (2014) Geochemical rate models: an introduction to geochemical kinetics. Cambridge University Press.

Schwarzenbach, R.P., Giger, W., Schaffner, C. and Wanner, O. (1985) Groundwater contamination by volatile halogenated alkanes: abiotic formation of volatile sulfur compounds under anaerobic conditions. Environmental science & technology 19, 322-327.

Steudel, R. (2003) Aqueous Sulfur Sols, in: Steudel, R. (Ed.), Elemental Sulfur and Sulfur-Rich Compounds I. Springer Berlin Heidelberg, Berlin, Heidelberg, pp. 153-166.

Steudel, R., Göbel, T. and Holdt, G. (1988) The molecular composition of hydrophilic sulfur sols prepared by acid decomposition of thiosulfate [1]. Zeitschrift für Naturforschung B 43, 203-218.

Steudel, R. and Holdt, G. (1988) Solubilization of elemental sulfur in water by cationic and anionic surfactants. Angewandte Chemie International Edition 27, 1358-1359.

Teder, A. (1971) The equilibrium between elementary sulfur and aqueous polysulfide solutions. Acta Chem. Scand 25.

Werne, J.P., Hollander, D.J., Behrens, A., Schaeffer, P., Albrecht, P. and Damsté, J.S.S. (2000) Timing of early diagenetic sulfurization of organic matter: a precursor-product relationship in Holocene sediments of the anoxic Cariaco Basin, Venezuela. Geochimica et Cosmochimica Acta 64, 1741-1751.

CHAPTER 4 – DYNAMICS OF HYDROGEN SULFIDE INPUT AND BIOGEOCHEMICAL SULFUR CYCLING IN YELLOWSTONE HYDROTHERMAL WATERS

Introduction

Redox disequilibrium between sulfur species and oxidants (such as O_2) or reductants (such as H_2) provide the energy for chemotrophic metabolisms in a host of archaeal and bacterial species in Yellowstone National Park hydrothermal systems (Macur et al., 2013; Meyer-Dombard et al., 2005; Schubotz et al., 2013; Shock et al., 2005; Spear et al., 2005). Hydrothermal waters often contain elevated amounts of sulfide, which is degassed from the magmatic chamber and further dissolved in the aqueous phase (Nordstrom et al., 2009; Oppenheimer et al., 2011). Upon partial or full oxygenation of the hydrothermal waters, sulfide undergoes oxidation via abiotic or biotic reaction pathways, being transformed to higher oxidation states. These oxidized forms can vary between S(-1) and S(+6), including the zero-valent state of elemental sulfur with a dissolved form of S_{8aq} which quickly evolves through coarsening processes to S_{8nano} and eventually α-S_8, the thermodynamically most stable form in ambient conditions (Garcia and Druschel, 2014; Steudel, 2003). Sulfur transformations are often catalyzed by microbial activity, where microbial metabolic pathways involve oxidation (Hallberg et al., 1996; Taylor and Wirsen, 1997; Zerkle et al., 2009), reduction (Boyd et al., 2007; Lee et al., 2007; Schauder and Müller, 1993), or disproportionation (Hardisty et al., 2013; Thamdrup et al., 1993) of sulfur species. Photo-oxidation reactions also oxidize organic or inorganic forms of sulfide to higher oxidation states, both in modern and ancient systems (Farquhar et al., 2002; Foote and Peters, 1971; Gu and Foote, 1982; Ueno, 2014). Hydrogen sulfide is oxidized by molecular oxygen (O_2) to elemental sulfur (Chen and Morris, 1972; Luther III et al., 2011; Millero et al., 1987; O'Brien and Birkner, 1977; Steudel, 1996). The energetics of sulfide oxidation by O_2 suggest a 2 electron step that is exergonic over a wide range of pH values (Luther III et al., 2011). However, Luther III et al. (2011) showed that the kinetics of this reaction is slow when operated in metal free conditions (1μM day^{-1}). In the presence of

trace metals, the rate increases 50-fold, and when oxidized metabolically the rate increases up to 50,000 times (Luther III et al., 2011).

Elemental sulfur is a product of various metabolic pathways, including the oxidation of sulfide (Schulz and Schulz, 2005; Wilbanks et al., 2014) and the reduction of sulfur oxyanions and sulfate (Lee et al., 2007; Milucka et al., 2012). Biological elemental sulfur can precipitate and agglomerate as globules either intracellularly or extracellularly (Dahl and Prange, 2006; Kleinjan et al., 2003), and can be present within microbes for some time. Sulfur K-edge X-ray absorption spectroscopy data indicate in general that bacterial sulfur globules are in a "chemical form resembling S_8" (George et al., 2008), though other interpretations have included the presence of long-chain sulfur moieties also present in these globules (Kleinjan et al., 2003; Prange et al., 2002). The globules can include some combination of three main chemical forms of zero-valent sulfur (Dahl and Prange, 2006; George et al., 2008; Kleinjan et al., 2003; Pasteris et al., 2001; Prange et al., 2002): 1) cyclo-octasulfur rings, 2) sulfur chains with organic endmember moieties, and 3) polythionates.

The interaction of elemental sulfur with sulfide causes the formation of polysulfides, according to reaction 1 (Chen and Gupta, 1973; Kamyshny et al., 2004; Kleinjan et al., 2005a):

$$2HS^- + S_8 \leftrightarrows 2S_5^{2-} + 2H^+ \quad \text{(reaction 1)}$$

Polysulfides can further oxidize to thiosulfate by their interaction with O_2 in a rate that is faster than that of the oxidation of sulfide by O_2 (Kleinjan et al., 2005b). Thiosulfate, in turn, can oxidize further to higher oxidation states (Xu et al., 1996) or, in acidic solutions, disproportionate to sulfite and elemental sulfur (Johnston and McAmish, 1973; Xu et al., 1998). Reaction 1 may contribute to enhancing the bioavailability of elemental sulfur, either by the dissolution of S_8 to polysulfides, or by the formation of thiosulfate, either of which can pass through the cell wall as dissolved species. The decomposition of polysulfides in acidic conditions leads to the formation of S_{8aq} that subsequently coarsens to elemental sulfur nanoparticles (S_{8nano}), both thought to be significantly more bioavailable than α-S_8 (Boyd and Druschel, 2013). Reaction 1 also contributes to pyritization (Rickard and Luther, 2007) and to the sulfurization of organic matter (Raven et al., 2015).

Microbial sulfide oxidation is an important metabolic pathway affecting the microbial ecology of geothermal waters, especially in systems with a significant flux of hydrogen sulfide (Castenholz, 1977; Nakagawa and Fukui, 2003; Skirnisdottir et al., 2000). Most phototrophic bacteria that undergo anoxygenic photosynthesis, as well as many anaerobic and aerobic chemolitho-autotrophic bacteria, are able to utilize sulfide as their electron donor, transforming it to intermediate or oxidized sulfur species (polysulfides, elemental sulfur, thiosulfate, sulfite, sulfate)(Habicht et al., 1998; Kelly, 1989; Truper and Fischer, 1982; van den Ende and van Gemerden, 1993). Due to the hydrophobic nature of elemental sulfur, some microbes have evolved ways to excrete organic compounds that create surface coatings on or throughout elemental sulfur precipitates (Dahl and Prange, 2006; Knickerbocker et al., 2000). The sulfur globules inherit a hydrophilic surface character due to the existence of organic moieties comprised of glutathione when exposed to the surface of $S_{8biological}$ (Dahl and Prange, 2006). S_8 particles can also be actively dissolved by outer membrane 'blebs' to release bioavailable S_{8aq} (Knickerbocker et al., 2000), a reaction possibly analogous to the ability of various surfactant compounds to enhance solubility by several orders of magnitude (Steudel and Holdt, 1988).

Hydrothermal systems are studied for their chemistry and biology, as they are believed to represent natural analogue sites of primordial Earth (Holm, 1992; Shock and Schulte, 1998). Sulfur biogeochemical cycling has been extensively studied in hydrothermal systems, where the geochemical conditions existing in the geothermal waters have been linked to the structure of the microbial communities, using microbiological, genomic and phylogenetic methods, including terrestrial (Yellowstone National Park geothermal system, solfataric fields in SW Iceland, Japanese hot springs)(Castenholz, 1977; Inskeep et al., 2013; Nakagawa and Fukui, 2003; Skirnisdottir et al., 2000), shallow marine (hydrothermally influenced sediments in Papua New Guinea, hydrothermal system in Milos, GR)(Akerman et al., 2011; Sievert et al., 1999), and deep marine systems (Mothra Vent Field on the Juan de Fuca Ridge, Guaymas Basin, etc.)(Schrenk et al., 2003; Taylor et al., 1999). Bioenergetics modeling indicates a wide range of possible metabolic reactions involving multiple sulfur intermediates linked to a number of e^--acceptors, with sulfide oxidation being one of the prevalent metabolic pathways (Akerman et al., 2011; Amend et al., 2011; LaRowe et al., 2014; Shock et al., 2010; Spear et al., 2005). In most studies, the

chemical environment is sampled in a way that assumes the chemistry does not change significantly over short temporal or spatial scales.

A parallel approach for studying sulfur cycling in hydrothermal systems incorporates laboratory experiments where the microbial metabolic pathways that involve sulfide oxidation to sulfur or sulfate, among other pathways, can be interrogated. In these experiments, a microbial culture is exposed to sulfide for a period of time, and the reactants and products are measured. Sulfide concentrations are expressed and manipulated in different ways for several commonly utilized experimental designs: 1. Batch experiments, where a specific amount of sulfide is added to the culture, without being refreshed (Okabe et al., 2005); 2. chemostat experiments where the sulfide and other reactants and products are controlled to a "steady-state" by controlling the culture to a regulated flow (Buisman et al., 1991; Meulenberg et al., 1992; Taylor and Wirsen, 1997); 3. transient-state chemostat experiments where sulfide can be increased or decreased (Stefess et al., 1996; Visser et al., 1997); and 4. Gradient tube experiments where sulfide and molecular oxygen (or other electron acceptor) form a reverse vertical gradient (Botero et al., 2004; Kamp et al., 2006; Sievert et al., 2007). All of these approaches try to simulate natural environments with a relatively steady-state concentration of sulfide (either constant or changing in a somewhat linear fashion).

Physical, chemical, geological, and biological attributes of natural systems can show interlinked temporal variability. Yücel et al. (2013) conducted a 6 day long short term (minutes to hours) observation that indicated temporal variability in temperature, sulfide and sulfide:temperature ratio in a shallow-water hydrothermal vent system at Milos Island, Greece. The observations show a 12-hour and 15-hour periodicity on the sulfide and HS/T values changes that correlates with the waves of fresh seawater entering the system due to tidal activity. Other drivers of this variability include wave activity, meteoric conditions, subseafloor microearthquakes, convective flow and seawater-hydrothermal water mixing (Yücel et al., 2013). Lutz et al. (2008) linked the fluid chemistry and seismic activity of hydrothermal vents with the biological characteristics of mussels inhabiting those vents located along the East Pacific Rise. The workers observed short term temporal dynamics (within a 10-hour period) of sulfide in the deep sea hydrothermal system along the East

Pacific rise, which is correlated with the seismic activity of the system (Lutz et al., 2008). Perner et al. (2013) discussed the chemistry and microbiology of deep marine hydrothermal fluids from Irina II in the Logatchev field (14°45′N along the Mid-Atlantic Ridge). They suggest that sulfide, among oxygen, magnesium, hydrogen, methane chemistry (as well as temperature values) showed variations in minutes-scale time series for the hydrothermal fluids (Perner et al., 2013). Luther et al., (2008) utilized voltammetric micro-electrodes (similar to those used in this study) for the analysis of O_2 and H_2S in the seawater near a Riftia field. Riftia pachyptila is an organism that requires both sulfide and O_2 due to the need of survival of its chemosynthetic endosymbiot (Luther et al., 2008). The voltammetric data disclosed temporal variability of both sulfide and O_2, which vary up to two orders of magnitude and up to a factor of 3, respectively (Luther et al., 2008). Hydrothermal chimneys at the East Pacific Rise are inhabited by *Alvinella pompejana*, a thermotolerant worm that can survive thermally and chemically extreme conditions (Le Bris and Gaill, 2007). Apart from the sulfide temporal variability, thermal extremes have been recorded in chimneys inhabiting this worm with variations of more than 35^{o}C within less than 30 minutes (Le Bris and Gaill, 2007). The study of Luther et al. (2001b) suggests that the organism survives the chemical stress of sulfide toxicity by the formation of iron sulfide aqueous complexes, detoxifying its colony from deleterious amounts of sulfide (Luther III et al., 2001b).

Characterization of the sampling area

Yellowstone's hydrothermal system originates from the uplift of a mantle plume that formed a magmatic body, and consequent basaltic and rhyolitic volcanism (Huang et al., 2015). Studies have attributed the Yellowstone mantle plume to originate from partial melting of the mantle lithosphere due to upper mantle tectonics (Christiansen et al., 2002; Kelbert and Egbert, 2012). However, other observations show that the plume's routes are in the lower mantle (Pierce and Morgan, 2009). The basaltic partial melt that is formed as a consequence to the mantle plume, ascends to the upper crust forming basaltic volcanism, but also causes partial melting to the surrounding continental crust, causing silicic

volcanism expressed with rhyolite crystallization (Chang et al., 2007; Fournier, 1989). At present day, the presence of an active magma chamber (upper magma body) with a volume of ~4000km^3 at ~10km depth beneath the Yellowstone caldera is proven based on a conglomerate of both geophysical observations and modeling calculations (Chang et al., 2007; Eaton et al., 1975; Fournier, 1989; Husen et al., 2004a; Husen et al., 2004b), that lies above a magmatic body of basaltic composition (lower magma body) with a ~4.5 times larger volume (Huang et al., 2015). The cooling and consequent crystallization of the shallow batholith thermally charges the hydrothermal system of Yellowstone, with heat flow rates up to 2000 mW/m^2 (Morgan et al., 1977). Hydrogen sulfide is released from the magmatic chamber in its gaseous form (H_2S_g), being partitioned in the magmatic fluids exsolved from the magma (Scaillet et al., 1998), and transported through the hydrothermal system to the surface geothermal waters.

The hydrothermal cycling in Yellowstone is driven by the convection and advection of meteoric water that infiltrates through the pores and fractures of the bedrock lithology to a depth of 4-5km, where it reaches temperatures up to 430^{o}C that cause its upward convection (Fournier, 1989). The meteoric water comprises a part of the total fluid mass, as the magmatic source also provides a fraction of water that mixes with the meteoric component in varying proportions (Chiodini et al., 2012). The hydrologic properties of the hydrothermal system are influenced by the existing lithologic units of Yellowstone. The developed fracture network also contributes to the mobility of meteoric and magmatic water (Dobson et al., 2003). Deposition of volcanoclastic deposits has resulted in alternately overlapping bodies of permeable rhyolitic lava and relatively impermeable ash-flow tuff (Fournier, 1989). In detail, welded tuff and lava bodies show low matrix permeability but dense fracture network with high permeability. Combined, the two hydrological “modes” result in chaotic mobility of fluids, often with an episodic increase in the rates of fluid flow. This episodic pattern is a consequence of the fracture divergence to facilitate fluid flow followed by convergence and mineral deposition (Dobson et al., 2003).

Field observations of sulfur and other element systems in geothermal waters show that temporal variability in concentrations can be observed from minutes to years’ time

scales (Hurwitz et al., 2012; Hurwitz et al., 2008; Xu et al., 1998). Hurwitz et al., (2012) studied the temporal variability of major elements (Na^+, Cl^-, SiO_2, HCO_3^-) and water isotopes ($\delta^{18}O$, Tritium) in the geothermal waters of Geyser features in YNP. The findings showed that Grand Geyser showed minimal variability, whereas Old Faithful, Daisy, and Oblong Geysers showed small variability in the major chemistry and the isotopic signatures of oxygen and hydrogen. Finally, Aurum geyser showed the largest temporal variability in its water chemistry (Hurwitz et al., 2012). Xu et al. (1998) worked on the sulfur geochemistry of hydrothermal waters in Yellowstone National Park. They showed that Azure spring waters showed short term temporal variability of thiosulfate and sulfide for three sampling periods (up to 300min). They suggest that based on the variability of thiosulfate concentration among the Norris basin geothermal waters, subsurface oxidation of sulfide by dissolved oxygen is not a dominant process (only minor contribution). They propose SO_2 hydrolysis and S hydrolysis as sources of thiosulfate (Xu et al., 1998). Hurwitz et al. (2008) indicated the spatial and temporal geochemical trends of river solutes in the hydrothermal system of Yellowstone National Park. Observations showed that there is a significant variability in hours to days' scale in the concentrations of Cl^-, SO_4^{2-}, HCO_3^-, as well as to the HCO_3^-/Cl^- and SO_4^{2-}/Cl^- ratios (Hurwitz et al., 2008).

Here we present our observations in the geothermal waters of the hydrothermal features of Yellowstone National Park, with emphasis on the different ways that temporal variability of sulfide and other sulfur species can be expressed in an individual hydrothermal pool supporting microbial life. The intent of this paper is to determine the dynamics of sulfide delivery at finely resolved spatial and temporal scales, on par with the experience of individual microbes, in different springs at Yellowstone. Considering the steady-state assumption of sulfide levels in many field and lab studies that has been used so far, we investigated if small-scale temporal variability in the chemical microenvironment for microbes is another potential facet of these systems that could affect microbial physiology and ecology.

Methods

Water sampling and preparation

Geochemical analyses were conducted in hot springs located in Norris Basin, which held a variety of pH, temperature and chlorinity values (Table 4-1). Geothermal waters were sampled using a 3m-long pole with a 1-L nalgene (HDPE) bottle attached to it (Figure 4-1) to permit sampling at a safe distance away from the rim of each geothermal feature. Grab sampling served to collect material for chromatographic analyses for the determination of sulfur species chemical variability. In particular we investigated the variability of elemental sulfur (S_8), thiosulfate ($S_2O_3^{2-}$) and sulfite (SO_3^{2-}) species, separating these from sulfide analyses that took place using electrochemical techniques (see below). All of the geothermal springs studied (with the exception of Azure Spring), were grab sampled for the analyses of some or all of the above sulfur species. The grab sampling took place at various time points during our work at each spring within the same day, with the exception of Evening Primrose Spring where we conducted 2 visits and collected grab samples on two days.

The preparation of samples for elemental sulfur analysis using chromatographic techniques utilized 5ml of chloroform in a serum bottle for each 5ml of grab sample of each spring (added after the water sample had cooled), sealed and shaken. The high solubility of elemental sulfur in the immiscible-to-water chloroform causes the partitioning of the compound in the organic solvent and the ability to quantify it by analyzing the chloroform fraction (Henshaw et al., 1997). The non-pre-treated chloroform extraction method for zero valent sulfur analysis is considered to have a detection limit of 70μM of S^0, which apart from the elemental sulfur fraction, includes zero-valent sulfur derived from any amounts of polysulfide ions (S_n^{2-}) that might be in solution (Kamyshny et al., 2009). However, the electrochemical analyses showed no significant amounts of polysulfide ions in the geothermal springs during the period of analysis, meaning that the amounts of zero valent sulfur that have been quantified result mostly from elemental sulfur. It is known that chloroform extraction is not able to fully recover all forms of elemental sulfur, especially the portion that is biologically precipitated as more hydrophilic colloids (Janssen et al.,

1999). However, the protocol was used in preference to cyanolysis, Cr(III) reduction, or methanol extractions to balance specificity of the method for elemental sulfur forms, polysulfides, and sulfoxy compounds with field use precautions and preservation.

Sample derivatization using monobromobimane (MBB) was applied in grab samples for the stabilization of thiosulfate ($S_2O_3^{2-}$) and sulfite (SO_3^{2-}) intermediates and their consequent analysis in the lab (Rethmeier et al., 1997; Zopfi et al., 2004). The solutions used included 45mM MBB dissolved in acetonitrile, 500mM-50mM HEPES-EDTA at pH8 and 324mM methanesulfonic acid (MSA). An amount of 0.5ml of grab sample was fixed with 80μL of HEPES-EDTA buffer and 50μL of MBB in dark Zinser vials (1.5ml volume). After 30 minutes an amount of 50μL of MSA was added. The MBB and its derivatives are highly light sensitive so the derivatization took place under as restricted light conditions as possible.

Filtering of grab samples using a 0.2μm filter and addition of 0.5ml Zn-citrate for the removal of sulfide amounts took place in all samples designated for IC analysis for the determination of sulfate concentrations.

Table 4-1: Basic physical-chemical characteristics of the geothermal features sampled on September 2012. Geographic information after Ball et al. (2001) USGS Open File Report 01-49 (Ball et al., 2001).

Name	Latitude	Longitude	pH	T (°C)	T (°C) (Flow Cell)	Cl (mg/L)	SO_4 (mg/L)
West Nymph Creek Thermal Area							
Yellow Cinder Pool	44° 44' 41.0"	110° 44' 32.4"	2.42	80.3	64.5	0.6	551
Norris Geyser Basin							
Cinder Pool	44º 43’57.3”	110º 42’32.7”	4.08	---	72.8	593.7	104.5
Cistern Spring	44 º 43’23”	110 º 42’16”	4.66	---	74.6	475	89.5
Gibbon Geyser Basin - Sylvan Spring Area							
Evening Primrose Spring	44º 41’30”	110º 46’36”	5.61	79.0	70.4	487.9	139.8
Lower Geyser Basin							
Azure Spring (Source)	44º 33’39.7”	110º 49’55.9”	8.86*	77.2*	64.5*	293	48.45
Ojo Caliente (Source)	44º 33’46.1”	110º 50’16.9”	7.55	---	92.6	279.5	20.21

Table 4-1: Continued.

Name	Latitude	Longitude	pH	T (°C)	T (°C) (Flow Cell)	Cl (mg/L)	SO_4 (mg/L)
Crater Hills Area							
Sulphur Spring	44° 39' 17.2"	110° 28' 51.3"	3.79	88.9	73.0	763.4	544.6
Mark's Ugly Spring	44° 39' 12.0"	110° 29' 2.0"	1.78	68.9	79.6	8.8	2305
West Nymph (WNCTA)	44° 44' 44.6'	110° 44' 40.0"	5.74	57.8	---	---	---

*Measurements tool place in previous expedition in 2010

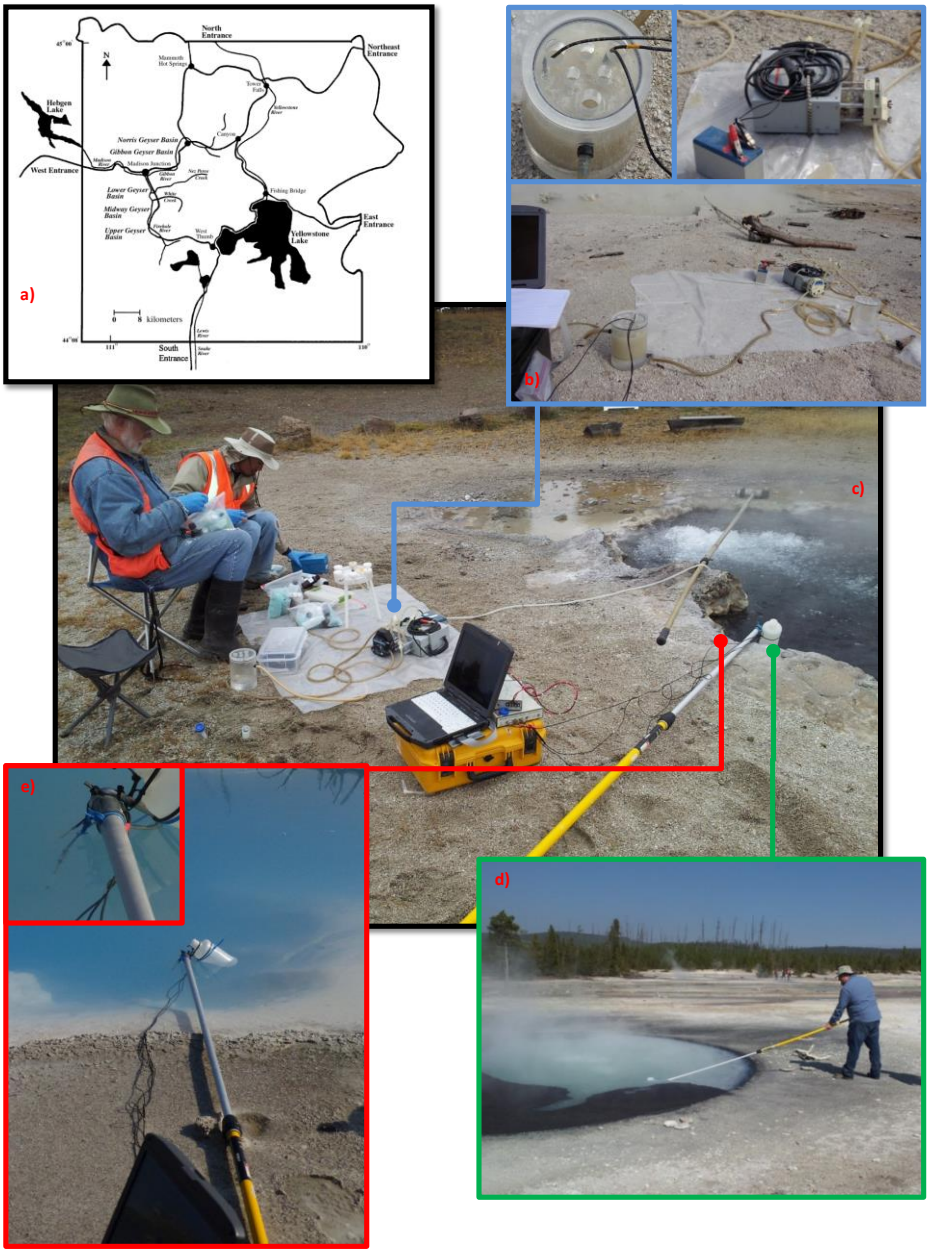

Figure 4-1: The map of Yellowstone National Park (a) indicates the basins including the geothermal springs studied. Field analysis included the electrochemical analysis of the geothermal waters in situ (direct contact of electrodes with the water; e) and ex situ (analysis of pumped water in a flow cell; b). The latter method gives a moving average analysis of the sulfide concentration as the water is temporarily mixing before it evacuates the cell. Grab sampling (d) and consequent derivatization of geothermal water assisted to the chromatographic determination of sulfur species (S_8, $S_2O_3^{2-}$, SO_3^{2-} and SO_4^{2-}). In situ electrochemical analysis in action in Ojo Caliente Spring (c).

Chromatography

Elemental Sulfur Analysis

The extracted zero-valent sulfur was detected with reverse phase HPLC, following an isocratic method with MeOH 100% as eluent at a flow rate of 1ml/min. Detection of S_8 took place at retention time of 3min, whereas the linear calibration curve was established using standard solutions of cyclo-octasulfur (S_8) with concentrations ranging from 5μM to 1mM S_8. A detailed list with the analyses of elemental sulfur in HPLC and the standard deviations for each replicate set is provided in Appendix C.

Thiosulfate/Sulfite Analysis

The MBB derivatized samples were analyzed in the lab using reverse phase HPLC using an Acclaim120, 5μM C18 column, with Acetic acid (0.25% v/v; pH 3.5) and MeOH 100% as the two eluents (Rethmeier et al., 1997; Zopfi et al., 2004). The detection took place using a Fluorescent detector (excitation at 380 nm; detection at 480 nm). Each run had a 45 min duration at a flow rate of 1ml/min, whereas the retention time for sulfite and thiosulfate were 14 and 18.5 min, respectively. A linear calibration curve was established for each run using standard solutions with concentrations ranging from 5μM to 1mM, for both $S_2O_3^{2-}$ and SO_3^{2-}. Detailed list with the analyses of thiosulfate and sulfite in HPLC and the standard deviations for each replicate set is provided in Appendix C. Concentrations were corrected for the dilution effect from the addition of the derivatization reagents.

Anions Analysis

Samples for anions analysis were re-filtered in the lab in order to separate the precipitated solids after the addition of Zn-citrate (5% w/w). The samples were analyzed using Ion Chromatography with an isocratic method at 1ml/min flow rate and 3.5mM CO_3^{2-} – 1mM HCO_3^- eluent, with a run time of 20 min. The column utilized was a Dionex IonPac AS14, coupled with an ASRS 4mm suppressor. The analytes of interest included fluoride,

chloride, nitrite, bromide, nitrate, phosphate and sulfate, and were quantified after standard protocols.

Electrochemical analysis

Electrochemical analyses showed effective temporal resolution for capturing the dynamic changes in concentration of S species over time, as the acquisition time has a duration between 3.4 to 5.4 seconds per analysis. The spatial resolution of the analysis was also important, as the chemical changes were captured on a scale of cubic micrometers, similar to the size of most prokaryote microbial cells.

Voltammetric signals are produced when electrochemically active analytes present in solution as dissolved species or particulate matter interact with the surface of a working electrode. This interaction is expressed as a half-reaction between the analyte and the Au-amalgam (Au-Hg alloy) on the electrode's surface. Electron flow (measured in Ampere) is proportional to the concentration of the analyte in solution, whereas the specific potential (measured in Volts) at which the half-reaction occurs gives information on the identity of the analyte. The voltammetric system consists of three electrodes: a silver/silver chloride reference electrode, a platinum counter electrode, and an Au-amalgam working electrode (Luther et al., 2008; Luther, 1995). The method used was cyclic voltammetry and involved the scanning of voltage from -0.1 to -1.8 V and back to -0.1V (compared to the reference electrode) at a scan rate of 1,000 mV/sec with or without a 2-s conditioning step. The conditioning step provides lower detection limits in cases where sulfide levels are very low. A number of sulfur species in aqueous and nanoparticulate form are electroactive at the surface of Au-amalgam electrodes, including H_2S, S_n^{2-}, S_8, $S_2O_3^{2-}$, $S_4O_6^{2-}$, and HSO_3^- (Boyd and Druschel, 2013; Luther III et al., 2001a). Voltammetric analyses were carried out with an Analytical Instrument Systems, Inc., DLK-60 potentiostat and computer controller. The voltammetric measurements involved two main types of analysis. The first one involved the *in-situ* analysis of the geothermal waters that was conducted by placing the three electrodes (working, counter and reference) directly in the aqueous environment (Figure 4-1). The analysis takes place in a volume of water that is attached to the surface

of the working electrode. Fick's law expresses the flux J_o of an electroactive compound O (such as sulfide) that passes through a cyclical electrode as shown in the equation (Bard and Faulkner, 2001):

$$-J_o(o,t) = \frac{i}{nFA} = D_o[\frac{dC_o(x,t)}{dt}] \quad (1)$$

where i is current (in Ampere or Coulombs/second), n is the number of electrons being transferred between the electroactive compound and the electrode (2 electrons for the sulfide electrochemical reaction), F is the Faraday constant (96485.3 Coulombs/mol) and A is the surface of the electrode (m^2). The current of the electrode is controlled by the surface of the electrode (and consequently the spherical sampling volume), the temperature, the electrical conductivity of the aqueous medium, the concentration of the compound, and time. The volume of water being analyzed (spherical sampling volume) was calculated using Fick's law (equation 1). We used the highest and one of the lowest sulfide signals found in our analyses in Yellowstone, which were 1430 μM sulfide (0.463μA) and 26.1 μM sulfide (0.021μA) from the in situ analyses of Ojo Caliente and Cinder Springs, respectively. The Fick's law equation was solved and the flux $J_{sulfide}$ values were calculated for both sulfidic current values. The flux shows the units mols $second^{-1}$ m^{-2}, as the above equation gives the 2 dimensional solution of the flux of the component of study. The geometrical expression of the flux is the area which is expanding from the point of the electrode and in which the electroactive compounds can be analyzed. However, when the flux $J_{sulfide}$ is multiplied by the time of analysis of 2.3 seconds (which is the time of deposition plus the time until the sulfide peak is first identified) and divided by the concentration (converted from microMolar to mols m^{-3}), the result is a number with meters as a unit. This is the one-dimensional solution of the equation, which expresses the (maximum) distance of an ion located in the water that can travel to the electrode surface within 2.3 seconds (analysis time), for a specific current and concentration of sulfide. Multiplying this number by 10^6, we have the diameter of the spherical volume of analysis in micrometers. All calculations are corresponding to a 100um diameter of the surface of the electrode (Appendix D).

The second analysis involved the *ex-situ* measurement of geothermal waters by placing the electrodes in a flow cell which pumped water from the spring with a 35-seconds delay, at a flow rate of 350ml/min and by mixing and homogenizing it within its 2L volume. Considering the flow rate and volume of the cell, the residence time of the solution in the flow cell was at ~5.7min, with the water being continuously released from the flow cell as more water was introduced.

The calibration of the instrument with respect to manganese (Mn^{2+}) took place in the field (using grab samples). Lab calibrations of sulfur species (mainly sulfide but also thiosulfate) to be quantified took place using a water bath-flow cell on the solutions of each geothermal spring and adjusting at the corresponding temperature and pH values. After the calibration curves for each compound was established, a correction was applied on these analyses based on the manganese analyses from the field based on the pilot-ion method (Slowey and Marvin-DiPasquale, 2012).

Variability of a voltammetric signal beyond standard instrumental error (typically within a few percent) can come from several sources when performing measurements in situ; a solution containing particles (minerals or other particles of organic or biological origin), gas bubbles, and fluid gradients that can be moving heterogeneously can all contribute to signal variability over time when the interaction of these things with the electrode occurs at a frequency lower than the scan times. Particles can affect electrochemical measurements when those particles are electroactive; for Au-amalgam electrodes this includes elemental sulfur, metal sulfide minerals, and metal oxides (Bura-Nakić et al., 2007; Bura-Nakić et al., 2015; Ciglenečki et al., 2005). The size of these particles is a key component of the signal they produce because the size of nanoparticles is linked directly to its ability to behave as a diffused molecule with respect to electrode reactions (Malik et al., 2010). Larger particles require physical (advective or actual compression of a mineral particle onto an electrode) processes to locate the particle onto the electrode for reaction, and the interaction will lack any diffusional current as the current associated with diffusion from the bulk would not be constant. Gas bubbles cannot directly interact with voltammetric electrodes, bubble interaction with any electrode in a 3-electrode system will interrupt the electron flow through the circuit and result in no signal

passing through the potentiostat. Gas bubbles rising in fluids do so at a significant velocity and can contribute to large fluid flow velocities in a tightly restricted area proximal to the bubble (bubble velocity ranges between 0.2 to 0.4m/sec in bubble diameter ranges up to 30mm)(Malenkov, 1968). It is a common experience with voltammetry in the lab to experience signals with exceptionally high noise (i.e. spurious, random signals of relatively high intensity) when scans are attempted with a gas flow on (gases such as N_2 or Ar are commonly used to occlude O_2 by bubbling through a solution). We conducted experiments in the lab to test the effect of bubbles on the voltammetric signal. Our results show that the sulfide signal during acquisition from a distal to a proximal location from the bubble stream changed less than 1%, a change much smaller than the sulfide signal variability observed in the geothermal springs studied. Furthermore, when the electrodes were placed directly above the bubble stream the signal was noisy and the acquisition was ineffective (see Appendix D).

Fluid flow can affect an electrode's current response by changing the transport of analyte to the electrode surface during the course of a measurement. Current response for an electrode can be ideally defined by the Butler-Volmer equation, in particular the approximation where there are no appreciable mass transfer effects (i.e, the concentration at the electrode surface and bulk are within 10%) which relates applied potential to current response for any reaction (Bard and Faulkner, 2001). This approximation is strengthened by the use of smaller radii electrodes and faster scan rates, to maximize how the thickness of the diffusion plate (area immediately next to the electrode where diffusive transport can limit current) relates to the radius of the electrode (Bockris and Reddy, 2000). Use of (micro)electrodes and the application of faster scan rates therefore should minimize, but not eliminate, effects of fluid flow variability on electrode response. To quantify the effect of changing solution flow past an electrode, the effect of flow rate on current can be described by the Levich equation:

$$i = knFCD^{2/3}r^{2/3}U^{1/2}v^{-1/6} \qquad (2)$$

where i is the current, k is a constant, n is the number of electrons transferred, F is Faraday's constant, C is the concentration of the electroactive species, D is the diffusion constant, r is the radius of the disk-shaped electrode, U is the flow rate, and v is the kinematic viscosity

of the solution (Luther et al., 2002). We utilized the Levich Equation (equation 2) in calculations for conditions similar to YNP (for this and more details on this calculated effect of fluid flow on current response, see Discussion section as well as Appendix D). Luther et al.(2002) also tested this experimentally for Mn^{2+} and HS^{-}, finding that there is up to 50% change in current sensitivity for flow rates up to 10 ml min-1 when using scan rates at 500 or 1000 mV min-1 (Luther et al., 2002). For more information, please see discussion below.

Fourier Transforms

Each dataset formed by the sulfide concentration of geothermal waters of every spring analyzed over time, was investigated using Fourier Transforms for the possible periodicity of sulfide variation over time. The algorithm used was the "FFT" in the Mathworks Matlab Software. Results are shown in Appendix C.

Geochemical kinetic modeling

Geochemical kinetic modeling was conducted for the investigation of the predicted distributions of sulfur intermediate species based on abiotic reaction pathways. The modeling was conducted using the Kinetiscope stochastic kinetics simulator (Hinsberg and Houle, 2017). The model's predictions on the distribution of intermediate species of sulfur were compared with those observed in YNP. Five principal reactions were utilized for the oxidation of sulfide to elemental sulfur, the formation and decomposition of polysulfide, the oxidation of polysulfide to thiosulfate and the decomposition of thiosulfate to sulfite (Table 4-2). Kinetic rate laws and k values for each reaction were extracted from the literature as well as calculated within the framework of this PhD thesis (see Chapter 3). Input values of the abundance of each species were as follows: H_2O, HSO_3^-, $S_2O_3^{2-}$, S_8 and SO_3^{2-} were 10^{-8}M, polysulfide was 10^{-6}M, H^+ was 10^{-5}M (pH 5) and O_2 was 10^{-4}M. Regarding the sulfide concentration, the highest and one of the lowest sulfide signals found

in our analyses in Yellowstone were utilized, corresponding to 1430 μM and 26.1 μM sulfide (0.021μA) from the in situ analyses of Ojo Caliente and Cinder Springs, respectively. Since these two extreme values showed two orders of magnitude difference, an intermediate value of 250 μM HS^- was selected as well.

Table 4-2: Abiotic chemical reactions and kinetic parameters utilized in the geochemical modeling of this study.

Reaction	**k value**	**Rate law**	**Notes**	**Reference**
$S_8 + 2\ H_2S \rightarrow 2\ S_5^{2-} + 4\ H^+$	4.50E-05	r= - 4.50E-05	Rate represents S_{8raffo} nanoparticles	Chapter 3
$8\ S_5^{2-} + 12\ O_2 \rightarrow 8\ S_2O_3^{2-} + 3\ S_8$	8	$r=k[S5--][O2]^{0.59}$	k value and stoichiometry multiplied by 8	Kleinjan et al. (2005b)
$8\ H_2S + 4\ O_2 \rightarrow S_8 + 8\ H_2O$	5.56E-03	$r=k[S_{tot}]^{1.34}[O2]^{0.56}$	k value and stoichiometry multiplied by 4	Chen and Morris (1972)
$8\ S_2O_3^{2-} + 4\ H^+ \rightarrow 4\ HSO_3^- + 4\ SO_3^{2-} + S_8$	2.64	$k=[H+][S203]^2$	k value and stoichiometry multiplied by 4	Xu and Schoonen, 1995 GCA
$2\ S_5^{2-} + 4\ H^+ \rightarrow S_8 + 2\ H_2S$	10		Estimation	n/a

Results

Fick's law calculations

The results from Fick's equation ($J_{sulfide}$: 3.055 10^{-4} and 1.385 10^{-5} mol sec^{-1} m^{-2}, for 1430 and 26.1 μM sulfide, respectively) helped us calculate a diameter (of the spherical volume of analysis) which ranged between 491 and 1221 μm, corresponding to a spherical volume between 6.21 10^{7} to 9.53 10^{8} μm^3. Considering the size of the water being analyzed, and comparing it with that of the average size of a microbial cell (1 micron diameter), we understand that the size of a cell is much smaller than the volume of water being analyzed. However, the use of the in situ electrode allows for an analysis reasonably close to the scale of a microbial cell or group of cells, with the ability to determine temporal variations at that spatial scale over seconds (Norlund et al., 2009).

Sulfide analyses

The summary of electrochemical analyses is presented as plots of sulfide concentration versus time, representing temporal variability of sulfide in Yellowstone geothermal waters (Figure 4-2). Section A and B of Figure 4-2 present this variability as sulfide concentration (μM) and intensity (μA) versus time (seconds), respectively. The difference between the two sections is related to the inability to calibrate the working electrodes with respect to sulfide in the field, either due to lack of Mn^{2+} spike solution, or due to the high acidity of the waters that resulted in inability to identify Mn^{2+} with the instrumentation (Mark's Ugly Pool). The electrochemical analyses had acquisition times of 3.4 and 5.4 seconds for zero deposition and 2 second deposition times, respectively. The condition of the deposition was determined as a function of the concentration of sulfide in the geothermal spring. Specifically, the 2 second deposition condition reduces the detection limit to lower sulfide concentrations. The in situ electrochemical analyses are represented in red color, whereas the ex situ analyses are represented in blue color. Fourier transforms

of these data showed no periodicity in the variation of sulfide over time in any of the springs over the time period measured.

The in situ voltammetric analyses of the geothermal springs showed large variability in the sulfide signal for some springs but not in others. In situ analyses of Cinder Pool showed a "wavy" pattern of increasing and decreasing amounts of sulfide starting from as low as 26.11μM up to 445.05μM, with a 'spiky' increase up to 524.62μM that lasted for one scan (Figure 4-2– b). Cistern Spring showed a constant concentration of sulfide at ~90μM for the first 750 seconds of acquisition, that changed suddenly to a much more chaotic variation over seconds' scale where sulfide concentrations ranged from 63.34 to 407.98μM (Figure 4-2– a). In situ analysis of Evening Primrose Spring indicated a baseline of sulfide content of ~30-50μM with spikes from 75.17 up to 749.86μM that lasted from seconds up to 1.5 minutes (Figure 4-2– c). Ojo Caliente Spring showed constant variation of the sulfide content in the geothermal waters with a steady increase over the period of analysis. The sulfide content increased from 157.48 to 1429.74μM over the duration of the acquisition (Figure 4-2– e). In situ analysis of Azure spring showed minimal variability in the intensity values with respect to sulfide, covering a range from 0.04 to 0.06 μA (Figure 4-2– g). Yellow Cinder Spring waters showed moderate variations in the sulfidic signal ranging from 0.41 to 0.63μA, with a few peaks in intensity with the most prominent reaching 0.72μA sulfide (Figure 4-2– h).

Geothermal springs analyzed by ex situ voltammetric methods showed less variability in sulfidic signatures overall but some springs still showed significant temporal variability. Ex situ analyses of the geothermal waters of Cinder Spring showed a constant character of ~100μM sulfide with almost no variation over time (Figure 4-2– b). Analyses of Cistern Spring geothermal waters showed a steady content of sulfide in the flow-cell water that started from as low as ~58μM and increased slowly up to ~110μM during the first 730 seconds, then exponentially increased up to ~442μM sulfide within 5 minutes, whereas it was preserved in the same levels with a small decline down to ~35μM sulfide for the following ~25 minutes (Figure 4-2– a). Ex situ analysis of Evening Primrose Spring indicated a constant amount of ~50μM sulfide for the whole period of acquisition, with the exception of an intense peak of 567.48μM that lasted only for a single scan (acquisition

time was 5.4 seconds) (Figure 4-2– c). The analyses of Sulfur Spring showed the most dynamic character in terms of sulfide temporal variation. (Figure 4-2– f). The total duration of acquisition was 5700 seconds, and a range of concentrations from a few nM up to 403.38μM sulfide with the high sulfide concentration "steps" showing duration from a few seconds up to ~7 minutes. The baseline was in the range of hundreds of nM. For the rest of the duration of acquisition the chemical signature of sulfide showed various temporal intervals of either below detection or concentration of ~100-150μM HS^-, while the duration and occurrence of each of the higher concentration intervals was completely random. Ex situ analysis in West Nymph Spring showed a peak at 271.01μM that lasted for ~30 seconds. The sulfide signature at the same spring showed smooth variations but showing a baseline that indicated sulfide concentrations at ~55 μM for 1 min period, while increased to ~81μM for a 3 min period (Figure 4-2– d). Yellow Cinder Spring waters showed a basement of sulfide intensity that averaged at 0.25μA, and was interrupted by two 1-minute-long pulses where sulfide intensity was increased up to 0.35μA (Figure 4-2– h). Ex situ analysis of Mark's Ugly Pool showed a low plateau of ~0.015μA for the first ~1300 seconds of the analysis, which were followed by an intense peak of 0.23μA and a consequent chaotic variability of peaks and drops of sulfide abundance, ranging from 0.04 to 0.23μA (Figure 4-2– i).

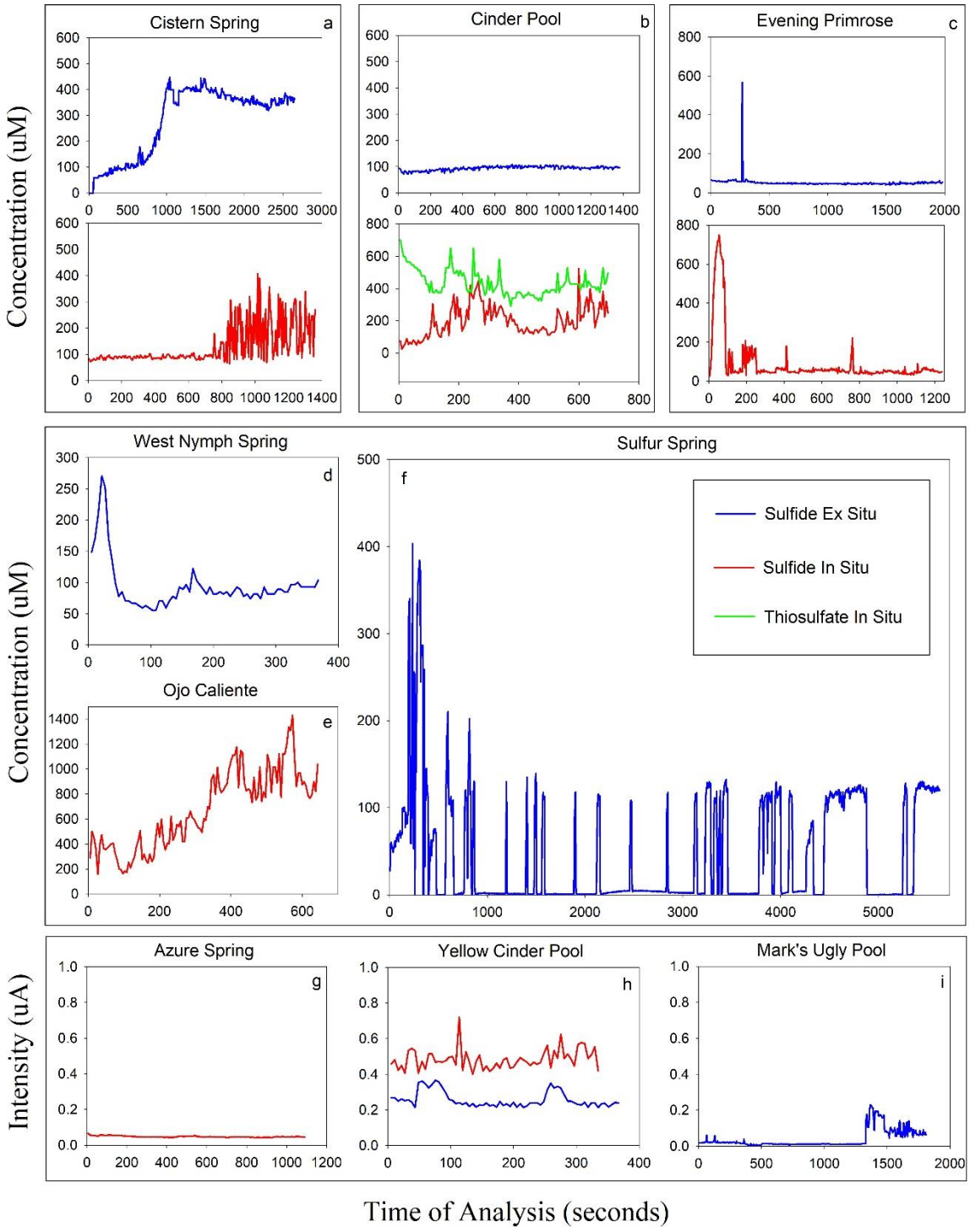

Figure 4-2: This is a summary of plots of temporal variability of sulfide in Yellowstone geothermal waters. Plots "a" through "f" present this variability as sulfide concentration (μM), whereas plots "g" through "i" present the variability as sulfide intensity (μA) versus time (seconds), respectively. The geothermal springs presented include: Cistern Spring (a),

Cinder Spring (b), Evening Primrose (c), West Nymph Spring (d), Ojo Caliente (e), Sulfur Spring (f), Azure Spring (g), Yellow Cinder Spring (h), and Mark's Ugly Pool (i).

Elemental sulfur and intermediates analyses

The voltammetric analyses showed the presence of elemental sulfur, polysulfide and thiosulfate in various geothermal springs (Appendix C). In situ analyses of Cistern Spring showed the presence of polysulfides, elemental sulfur and thiosulfate, the latter coinciding with the grab sample analyses (see below). Analyses at Evening Primrose using voltammetry showed the presence of thiosulfate, as well as colloidal elemental sulfur ($S_{8colloidal}$). $S_{8colloidal}$ was identified by the broad high intensity peaks that were being reduced in area and completely vanished within 2-4 scans, as the particle was consumed during its interaction with the working electrode (Appendix C). In situ voltammetric analyses of West Nymph Spring also showed peaks of thiosulfate and elemental sulfur. The above observations from electrochemical analysis coincide with the grab sampling analyses described below. However, in the cases of Mark's Ugly Spring and Yellow Cinder Pool (where elemental sulfur amounts were high enough for identification with voltammetry), the low pH conditions did not allow the electrochemical system to detect the peak of elemental sulfur (S_{8aq}) at potentials below -1V due to "proton shielding" (large peak area due to the interaction of the working electrode surface and the protons in solution).

The grab sample analyses for both elemental sulfur and the oxidized intermediates (sulfite and thiosulfate) showed different patterns of variability between them (Figure 4-3). Evening Primrose geothermal waters were grab sampled 7 times in total, at different times within two different days. Elemental sulfur analyses from grab samples from Evening Primrose ranged from 229.92 to 748.10μM S_8, whereas the thiosulfate and sulfite concentrations ranged from 349.74 to 368.70μM and 80.24 to 84.63μM, respectively. In-situ voltammetric analyses of the geothermal waters of Evening Primrose showed the presence of colloidal elemental sulfur ($S_{8colloidal}$), which was defined by a broad peak

centered ~ -1.2V with a high intensity that diminished over the following 3-5 scans as the colloid was decomposed by the reaction with the Au-Hg amalgam electrode. The detection of $S_{8colloidal}$ was random, and was linked to the probability of the particle to interact with the surface of the electrode. Elemental sulfur analyses in Ojo Caliente geothermal waters consisted of 0.40 to 0.55μM S_8, whereas the thiosulfate and sulfite ranged from 0.13 to 0.84μM and 6.28 to 8.51μM, respectively. Elemental sulfur analyses in Sulfur Spring samples ranged from 1.71 to 2.58μM S_8, while thiosulfate and sulfite analyses ranged from 0.24 to 0.40 μM and 12.4 to 13.5 μM, respectively. Mark's Ugly Pool showed elemental sulfur content ranging from 560.68 to 806.15μM S_8, while the thiosulfate and sulfite ranged from 2.09 to 2.58μM and 14.24 to 20.16μM, respectively. Cistern Spring analyses showed elemental sulfur content from 0.79 to 3.48μM S_8, thiosulfate ranging from 115.98 to 118.19μM and sulfite ranging from 52.9 to 57.2μM. West Nymph Spring analyses of elemental sulfur showed concentrations ranging from 44.46 to 86.20μM, whereas Yellow Cinder Pool showed an elemental sulfur content at 44.59μM S_8. Cinder pool analyses of thiosulfate and sulfite showed ranges from 2.20 to 2.48 and 19.6 to 21.7μM, respectively.

The variability of sulfur intermediates (elemental sulfur, thiosulfate, and sulfite) was evaluated and expressed as percentile difference between minimum and maximum concentration per spring. Regarding elemental sulfur, all springs showed statistically significant variability as shown in Figure 4-3 and Appendix C. Smallest variability was found at Ojo Caliente spring (36%) whereas the two springs with the largest variability were Cistern Spring and Evening Primrose (339% and 225%, respectively). The statistically significantly variable concentrations of thiosulfate correspond to Evening Primrose spring (5%) and Ojo Caliente (523%). Regarding their sulfite content, the geothermal springs showing statistically significant variability include Ojo Caliente (36%), Mark's Ugly (42%), and Cinder Pool (11%).

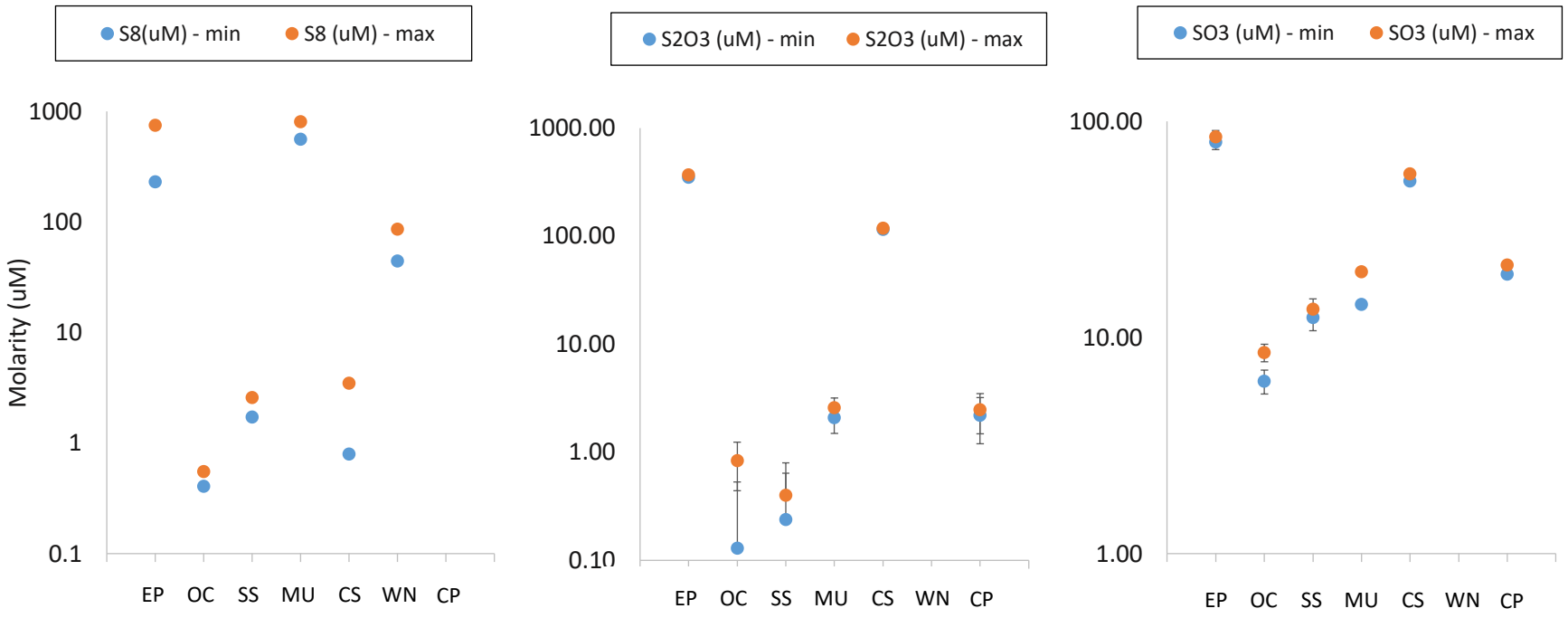

Figure 4-3: Variability in concentration (in μM S_8) of intermediate sulfur species (elemental sulfur, thiosulfate, sulfite) expressed as maximum and minimum concentrations per spring studied (derived from Appendix C). Error bars represent 2 standard deviations, whereas in the cases where the error bars are not apparent they are covered by the size of the symbol.

Discussion

Sulfide analyses

In general, the electrochemical analyses illustrate the temporal variability of sulfide signatures on the geothermal waters of YNP over second to minute time scales. This variability ranged vastly from minimal variability to extremely chaotic variability associated with different springs studied. The *in-situ* analyses depicted a more dynamic pattern in time for most of the springs in terms of the sulfide temporal variability, whereas the *ex-situ* analyses indicated a smoother evolution of sulfide concentration for some of the geothermal springs studied. During the ex situ analyses, the residence time of the fluid in the vessel can be assumed to mix the fluid as it comes in. This, in addition to the fact that the volume of the flow cell was 10^6 to 10^7 times larger than the volume of analysis for the in situ method (spherical sampling volume) suggest that this method of analysis (ex situ) could be considered a moving average of the sulfur chemical signature, at least for some of the springs studied (Figure 4-1). It is important to note that the in situ and ex situ analyses (for some pools that both types of acquisition are provided) are not simultaneous analyses. Analyses from some springs in this study showed a relatively smooth chemical signature (Cinder and Cistern springs, respectively – Figure 4-2). However, ex situ analyses at the rest of the springs studied showed sulfide concentration spikes that suggest something different than a moving average sulfide signature. Yellow Cinder Spring and Marks Ugly Pool showed steady baselines of low sulfide concentrations interrupted with pulses of increased concentrations for the former, and chaotic variability after ~1200 seconds of acquisition for the latter. The most chaotic pattern was shown at the *ex-situ* analysis of the Sulfur Spring where concentrations of sulfide were shown to change by orders of magnitude within seconds.

This study showed a dynamic variability on the sulfide signatures in the geothermal springs studied through the application of in situ and ex situ voltammetry; to properly evaluate the meaning of this we need to evaluate the possible processes that can cause signal changes from both chemical and physical change. The factors influencing voltammetric methods of analysis that can contribute to dynamic patterns of the

concentration of electroactive analytes include the chaotic movement of water (flow effect), presence of bubbles in the aqueous system of study (bubble effect) as well as presence and transport of particles (particle effect). To evaluate the hypothesis that signal variability is related to chemical heterogeneity of dissolved sulfide within the pools at the scale of the voltammetric electrode, we evaluated the scale of these effects under controlled laboratory conditions.

Fluid flow affects signal intensity by changing the mass of sulfide able to react at a voltammetric electrode by advectively transporting higher amounts of sulfide from the bulk solution to the electrode surface during the time of the measurement. The study of Luther et al. (2002) showed that an increase of the fluid flow cannot result in more than a 50% increase of the signal of the electrode (Luther et al., 2002). Specifically, the current increases up to 50% within the first 2ml/min increase of the flow rate, whereas after that the current reaches a plateau of steady values (Luther et al., 2002). For an increase of the fluid flow from zero to 1.2mL/min, Luther et al. showed a shift from 12 to 16nA which is a 33% increase on the signal (Luther et al., 2002). To determine how changes in advective flow in the ex-situ flow cell may have affected the sulfide signal, we performed experiments using a flow cell and changed the flow rate between 0.1 and 1.2 ml min^{-1} (same range as for the calculations mentioned above and using the exact solid state electrodes used in Yellowstone; see Appendix D). Our experiments showed the intensity of the current increased by 8.3% for the fluid flow increase from 0.1 to 1.2ml/min. The difference in increase percentage between our experiment and the observations of Luther et al. (2002) might originate due to differences in the geometry of the flow cell or other practical parameters, however the results are still comparable and suggest that flow rate changes used in this type of system result in relatively small differences beyond normal instrumental error in signal for either regular electrode reactions (as in O_2 to H_2O_2) or in plating reactions (HS^- to HgS over 2 seconds of deposition). Utilizing 2 seconds deposition condition would encourage larger analytical variability compared to the zero deposition mode.

Electrode reactions measured by voltammetry occur when a molecule is transported to, and reacts with, the surface of the working electrode. Surface interactions occur in the immediate vicinity of the electrode, transport of the molecules to the surface occurs first

within a spherical space surrounding the working electrode then as a function of diffusion from the bulk material to the spherical space. Fluid flow affects this by changing the timing of how ions are transported to the surface; at some point higher fluid flow stops affecting the reaction and therefore stops affecting the current response of the electrode to the analyte (Luther et al. 2002).

This plateau of values originates from the fact that the diffusion from the bulk influencing the electrode's response becomes insignificant at a specific flow rate. More specifically, the diffusion that influences the detection of an electroactive analyte from the electrodes surface shows two portions. The first is the bulk diffusion which dictates the rate with which the analyte will be delivered from the bulk of the solution to the spherical volume of analysis (that is the volume of aqueous solution that is in contact with the electrode's surface and is being analyzed by the electrode). The second is the diffusion from the spherical volume of analysis to the actual surface of the electrode where in our case the reaction between sulfide and Hg is taking place. The size of the spherical volume will change as a function of the fluid flow, with the size decreasing with increasing fluid flow in the medium where the analysis is taking place. Above a certain threshold value of the fluid flow, the size of the spherical volume of analysis becomes small enough for the second diffusion to be ineffective and essentially for the bulk diffusion to be the only diffusion being in effect. Therefore, above the threshold value above which the plateau is formed the conditions on the surface of the electrode will no longer be controlled by the rate of mass transport of the electroactive analyte to the electrode surface (Luther et al., 2002), rather by the bulk diffusion only.

The Levich Equation (equation 2) is a theoretical approach to determine the current response of an analyte based on diffusivity, electrode area, and flow rate; calculations suggest that the current response scales at a factor of 2.5 of signal change for an increase from 0.1 to 1.2ml/min fluid flow (see Methods and Appendix D for details). However this result is very different from the experimental observations of both Luther et al. (2002) as well as those of this work (Appendix D). The reason for that discrepancy lies along the line that the Levich equation assumes the maximum fluid velocity to be applied on the proximity to the surface of the working electrode, which is not always the case. The velocity (or flow) of the fluid measured within the experimental works shown refers to the

bulk fluid flow and not to the proximal-to-electrode flow. The reason for these two forms of fluid flow being different can be explained by the observations of a fluid medium passing through a pipe. The fluid dynamics of pipe flow shows that the fluid flow varies as a function of its distance from the walls of the tube. Viscosity effects taking place result in a parabolic distribution of velocity with velocity values increasing significantly with the increasing distance perpendicularly from the tube wall (Figure 4-4). The relationship of the flow rate with the geometric dimensions of the tube as well as other physical parameters is described as the Hagen-Poiseuille equation (equation 3):

$$\Delta P = \frac{8\mu L Q}{\pi R^4} \qquad (3)$$

with ΔP the pressure difference between two ends of the tube, L the length of the pipe, μ the dynamic viscosity, Q the volumetric flow rate, and R the radius of the tube. If this tube model is applied in the case of the working electrode, the R is the distance from the electrode's surface, whereas the Q is the fluid flow in the close proximity to the electrode's surface. Considering our system where the electrode surface can be represented by the tube walls, the fluid flow will decrease significantly in close proximity to the electrode's surface compared to the maximum (bulk) fluid flow that is controlled by the pump in both experimental reports (Appendix D; Luther et al., 2002).

In summary we conclude that based on the observations of our experimental work (similarly to the conclusions of Luther et al. 2002), the effect of fluid flow on the current of the working electrode is not of significant magnitude to describe the observed sulfide analyses and thus observed sulfide levels are not due to analytical artifacts from changes in the advective flow of waters in these springs.

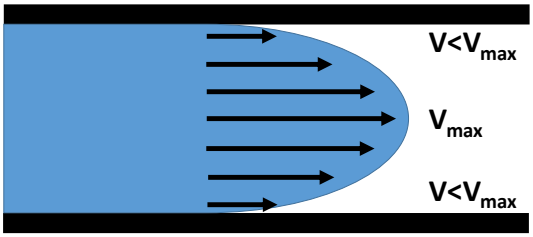

Figure 4-4: Velocity profile of a fluid moving through a pipe. The distribution of velocities increases with distance from the pipe's wall and is believed to show similar behavior as a function of the proximity of the fluid to the working electrode's surface.

The interaction of gas bubbles is able to affect substantially both the quality and quantity of the electrochemical signal. Direct interaction of a bubble would break the electrical cell, resulting to a lack of signal in a particular scan, whereas presence of a bubble stream in close proximity of the working electrode can potentially influence the intensity of the signal, possibly due to the huge flow velocities created in the proximity of the surface of the electrode as a bubble interface passes by that electrode. Therefore, we considered the effect of bubbles as part of the overall sulfide variability we observed in YNP. Bubbles could result in the transferring of an electroactive compound (such as sulfide) to the surface of the electrode. However, the flow velocity of bubbles ranges between 0.2-0.4m/sec for bubbles between 1 and 30 mm diameter (Malenkov, 1968). These values of bubble velocity are so high that within the time period of an electrochemical scan (3.4 seconds for no deposition or 5.4 seconds for 2 seconds deposition) a bubble with an average velocity of 0.3m/sec would have travelled across the diameter of the electrode surface (100μm) within 0.33 milliseconds. This is fast enough to significantly impact transport of species to the electroactive surface during a single scan. Voltammetric analyses of a 100μM sulfide anoxic solution at pH 10 took place in absence of N_2 bubble stream (control) as well as in presence of coarse bubble stream as a function of distance from the working electrode. The results indicated that the increase of the intensity of the sulfide signal as the bubble stream approached the working electrode was up to 22%, a factor much smaller than the orders of magnitude of variability we observe on the sulfide signal in YNP. The direct positioning

of the working electrode in the bubble stream resulted in a chaotic, noisy, signal which is easily identified and did not represent the voltammogram patters we analyzed in YNP. While bubble effects can cause significant signal variability, they could not cause the levels of variability in the patterns observed in our analyses at YNP. (See Appendix D).

Particles are able to contribute to the sulfide signal as follows: Physical collision of particles that mobilize sulfide adsorbed onto their surface causes sulfide to interact with (and be detected by) the electrode as the attached particles react on the electrode surface. Both in situ analyses at YNP and the literature suggest very characteristic voltammetric reduction peaks that correspond to interaction of particles with the electrode surface. The signal for elemental sulfur particles ($S_{8colloidal}$) acquired by voltammetric analysis is represented by a large peak centered around -1V, that within 3-4 scans has its intensity decrease rapidly due to the decomposition of the particle interacting with the surface of the electrode. This signal was observed in the in situ electrochemical analyses of the geothermal waters of Evening Primrose (Appendix C). Voltammetric signals similar to those of $S_{8colloidal}$ are found during the analysis of HgS, PbS, and S (among other) nanoparticles, as described by Bura-Nakic et al. (2007). The same workers correlated the particles' diameter with the surface area of the voltammetric peaks finding the peak area to be proportional to the size of the nanoparticle (Bura-Nakić et al., 2007). Furthermore, Bura-Nakic et al. (2015) have used additional electrochemical methods (chrono-amperometry) to quantify the size of sulfur nanoparticles, making electrochemical methods useful for the straightforward identification of particles and their size (Bura-Nakić et al., 2015).

The changes in sulfide signals observed in the geothermal features of YNP are beyond variations that can be attributed to gas bubbles, fluid flow and/or particles. Sulfide variability in this study seems to be attributed largely to actual changes in dissolved sulfide concentration. This variability is possibly related to formation of microgradients of aqueous sulfide (H_2S_{aq}) that originate due to bubbles of gaseous hydrogen sulfide (H_2S_g) being transported in a close proximity to the working electrode but without directly interacting with it (as the gas bubble would be apparent in the analysis by the noisy signal it would have formed). Due to the diffusion of sulfide from the gaseous sulfidic bubble to

the aqueous medium the generation of the observed intense sulfide peaks takes place. We hypothesize that these microgradients of H_2S_g are quickly disturbed by the upward rapid transfer of the bubble as well as by the dissolution of aqueous sulfide in the rest of the volume of water contained within the flow cell. Examples of sulfidic signals that show in a prevalent way the action of microgradients include the ex situ analyses of Sulfur Spring, but also the ex situ analyses of Yellow Cinder and Evening Primrose Springs. The voltammograms from Yellow Cinder and Evening Primrose (ex situ) showed one large spike of sulfide each, that similarly to Sulfur Spring, could result from sulfide microgradients (originating from gaseous sulfide bubble movement), however in a much smaller extent for these springs compared to the Sulfur Spring.

Elemental sulfur and intermediates analyses

The analyses of elemental sulfur, thiosulfate and sulfite have disclosed the existence of temporal variability which in some cases is comparable to that of sulfide data. This variability fluctuates within each intermediate or between sulfur, thiosulfate, and sulfite. Regarding thiosulfate analyses, Evening Primrose showed a 5% variability in terms of thiosulfate. This variability of the sulfoxy anions was shown to be for most cases lower compared to the variability of the rest of sulfur species studied. However, Ojo Caliente showed variability of thiosulfate up to 523%, the highest in terms of the variability percentage values estimated based on replicate grab sample analyses, being comparable to the electrochemical sulfide variability percentage values of 303% and 872% from the in situ and ex situ sulfide analyses from Evening Primrose, 356% from the in situ analyses of Cistern Spring, as well as the 752% and 875% from the ex situ analyses of Sulfur Spring and Mark's Ugly Spring, respectively. Sulfite variability was statistically significant at half of the springs studied, with analyses from Mark's Ugly Pool and Ojo Caliente showing sulfite variability at 42% and 36%, respectively. Cinder spring showed sulfite variability at 11%.

Sulfur intermediates show less variability compared to the variability of sulfide in the geothermal springs (Figure 4-3 and Appendix C). Overall, elemental sulfur shows the

most significant variability, with the S_8 content of Cistern spring and Evening Primrose reaching up to 339% and 225% variability, respectively. These values are comparable to the in situ and ex situ sulfide variability of Cistern spring (356% and 97%) and Evening Primrose (303% and 872%), respectively. Comparison of the elemental sulfur analyses within the various geothermal springs shows that between Ojo Caliente (lowest S_8 content) and Mark's Ugly Pool (highest S_8 content) we identify differences of up to 3 orders of magnitude. The very low pH values in Mark's Ugly Pool resulted in interfering with the potentials at which voltammetry scans can characterize elemental sulfur, therefore the chromatographic data were the only elemental sulfur information we have. In Evening Primrose Spring, the uniformity in concentration of both sulfur intermediates exists in the samples collected both from the spring directly and from the flow cell. Evening Primrose is known to incorporate amounts of $S_{8colloidal}$ (Kamyshny et al., 2014), which can be more available to detection by voltammetry than the dissolved S_{8aq}, showing scans of random occurrence as a function of the probability of interaction of the colloidal α-S_8 with the mercury electrode.

The fact that the variability of thiosulfate and sulfite is less than that of elemental sulfur for most of the geothermal springs studied (with all intermediates also showing various levels of concentrations between various springs), possibly originates from the geochemical kinetics of the reactions through which these intermediates are formed. Elemental sulfur is formed by inorganic or microbial oxidation of sulfide (Chen and Morris, 1972; Luther III et al., 2011)(Table 4-2):

$$8\ H_2S + 4\ O_2 \rightarrow S_8 + 8\ H_2O \qquad \text{(reaction 2)}$$

Consequently, elemental sulfur can quickly react with sulfide to form polysulfides, via the nucleophilic dissolution of S_8 (Figure 4-5). The kinetic rate law utilized corresponds to nanoparticulate elemental sulfur (S_{8raffo}) derived from Chapter 3 (reaction 1;Table 4-2). The polysulfides formed can further oxidize by O_2 to thiosulfate, in a rate four times quicker than that of sulfide oxidation (Figure 4-5; Table 4-2)(Kleinjan et al., 2005b):

$$8\ S_5^{2-} + 12\ O_2 \rightarrow 8\ S_2O_3^{2-} + 3S_8 \qquad \text{(reaction 3)}$$

Depending on the surface area of elemental sulfur reacting to form polysulfides, we would have different production rates of polysulfide and consequently thiosulfate (Figure 4-5). Additionally, thiosulfate (as well as sulfur and sulfite) can be produced or consumed not only via inorganic but also through microbially-catalyzed reactions (Figure 4-5 and Figure 4-6). Finally, thiosulfate can dissociate to elemental sulfur and sulfite (Table 4-2)(Xu et al., 1996):

$$8S_2O_3^{2-} + 4H^+ \rightarrow 4HSO_3^- + 4SO_3^{2-} + S_8 \qquad \text{(reaction 4)}$$

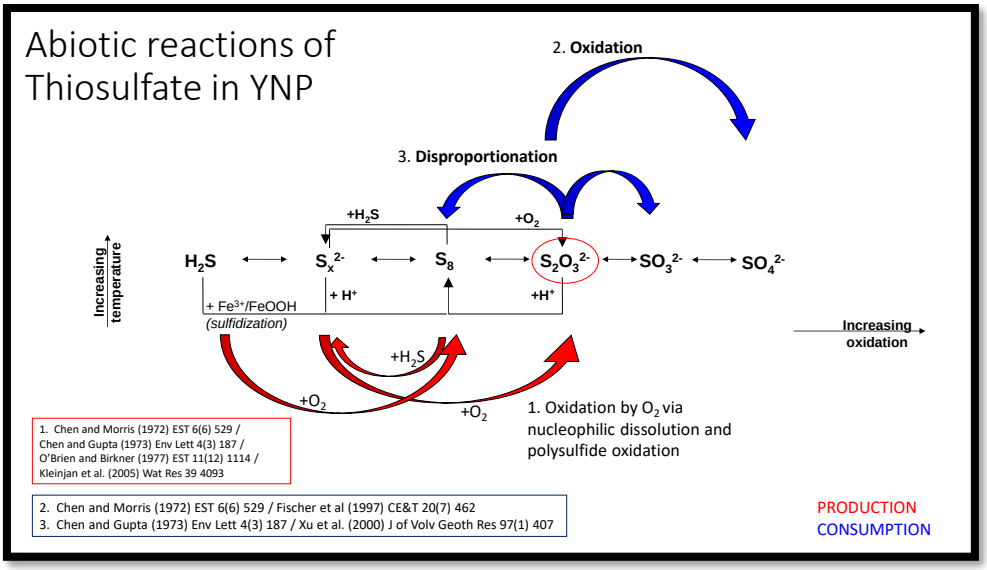

Figure 4-5: Abiotic reactions occurring in YNP which involve the production and consumption of thiosulfate.

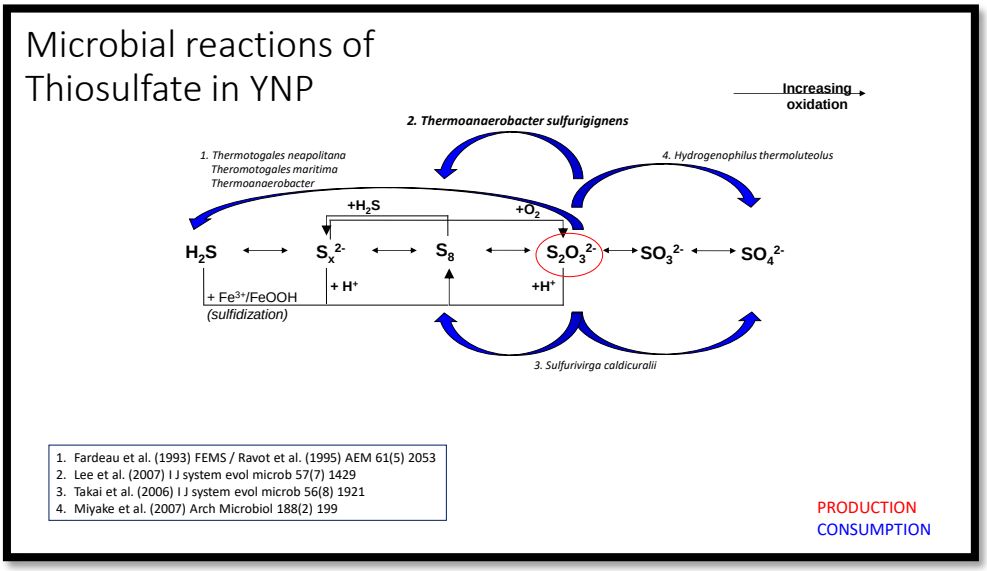

Figure 4-6: Microbial reactions occurring in YNP which involve the consumption of thiosulfate.

Geochemical kinetic modeling was conducted to determine the distribution of sulfoxy intermediates in the geothermal waters of YNP as a function of time from delivery of sulfide to depletion of sulfide or oxygen (Figure 4-7). The kinetic model incorporating the high sulfide scenario (scenario A) with a modeling concentration of 1430μM sulfide is shown in Figure 4-7-A. The sulfide-to-oxygen ratio was 14:3, based on the highest concentration of sulfide observed in Yellowstone during the analyses of this work, while the oxygen amounts were low simulating a partially oxygenated to O_2-limited water body of the geothermal springs studied. The pH dropped from 5 to 3.6. Sulfide concentrations decreased until all O_2 was consumed, since it was the limiting reactant, allowing for sulfide concentrations to stabilize at 1.28 10^{-3} M. Oxygen gets depleted after ~700 seconds. Elemental sulfur reaches negligible amounts (10^{-12}M) within 15 seconds, and is preserved at these levels throughout the simulation. Thiosulfate increase gradually at the first 500 seconds of the simulation, reaching concentrations up to 6.23 10^{-5}M, after the O_2 depletion. Polysulfides maintain a steady chemical signature over the whole duration of the simulation with slight increase from 10^{-6}M to 4.2 10^{-6}M as long as O_2 is present, while after O_2 depletion they stabilize at 4.2 10^{-6}M. Sulfite is very stable at 10^{-8} M while increases slowly only after O_2 has been depleted. The low sulfide scenario (26μM HS^-) shows the depletion of sulfide after 200 seconds of the simulation, while oxygen was preserved at a level of 7.9 10^{-5}M O_2 (sulfide to oxygen ratio at 0.26; Scenario B; Figure 4-7-B). Elemental sulfur showed an immediate decrease to trace amounts (10^{-13}M), while it increases rapidly from 10^{-13}M to 4.3 10^{-7}M immediately after the depletion of sulfide. Thiosulfate showed an increase immediately after the initiation of the simulation, reaching 1.07 10^{-5}M at the time when sulfide became depleted. The increase of thiosulfate was taking place as long as polysulfide was formed via the nucleophilic reaction. Polysulfide maintained its level at 10^{-6}M as long as reaction 1 was active, while it started a decreasing trend at sulfide depletion, until it reached negligible levels (10^{-13}M) at 10^6 seconds of the simulation. This drop is due to the ceasing of the nucleophilic dissolution that produced polysulfides, which are oxidized by O_2 to thiosulfate. The pH value dropped from 5 to 4.2. Furthermore, after the depletion of sulfide, thiosulfate would be preserved for almost 10^7 seconds before it would start dropping, forming S_8 and sulfite. Sulfite would be steady at 10^{-8} M for 10^2

seconds of the simulation (until sulfide became depleted), while after that it increased due to thiosulfate decomposition, reaching 6 10^{-6}M after 10^{8} seconds.

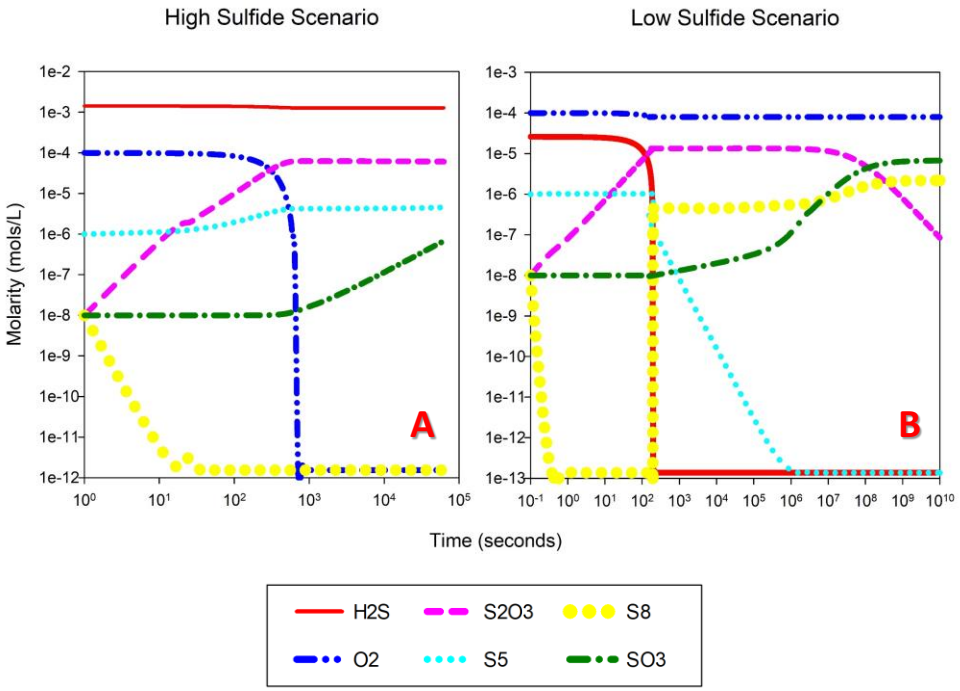

Figure 4-7: Chemical distribution of the sulfur species modelled using the Kinetiscope chemical kinetics simulator. The outcome of two different models is shown, corresponding to scenarios of high (A) and low (B) sulfide content. The legend displays all species incorporated in the geochemical models depicted as follows: Sulfide – red straight line, Thiosulfate – pink thick dashed line, Elemental sulfur – yellow thick dotted line, Oxygen – blue thick dash-dot-dot line, Polysulfide – kyan thin dashed line, Sulfite – dark green thick dash-dot line.

In both kinetic model scenarios (A and B) and for sulfide concentrations spanning 2 orders of magnitude, thiosulfate product amounts were within the same order of magnitude (6.2 10^{-5}M and 1.3 10^{-5}M $S_2O_3^{2-}$, for scenarios A and B, respectively), at least for part of the simulation (scenario B). This is an interesting finding considering the fact that thiosulfate production is closely associated to the oxidation of sulfide (reaction 2), the formation of polysulfides (reaction 1) and their consequent oxidation by molecular oxygen (reaction 3). For both A and B scenarios, thiosulfate is constantly increasing until either reactant of reaction 2, O_2 for scenario A or sulfide for scenario B, is completely spent. This means that the nucleophilic dissolution of S_8 (reaction 1) is fast enough to not be the rate limiting step in the sequence of reactions participating in the formation of thiosulfate (reaction 2 → reaction 1 → reaction 3). Therefore, as long as the two reactants (O_2, H_2S) of reaction 2 are abundant, thiosulfate is being formed. After the depletion of O_2 and sulfide in scenarios A and B, respectively, thiosulfate is decomposing to form sulfite. Specifically for scenario B, polysulfide is oxidizing to thiosulfate, while thiosulfate is decomposing to sulfite and elemental sulfur (reaction 3 → reaction 4).

Regarding polysulfide, it is shown from the kinetic modeling that this reduced S species serves as a cryptic intermediate of the oxidation pathway of sulfide to thiosulfate via the nucleophilic dissolution of S_8. Despite low levels of polysulfide at any time in these kinetic simulations (from undetectable to a few micromolar), significant thiosulfate is formed through the pathway of polysulfide formation (reaction 1) and oxidation (reaction 3). Further evidence of the importance of reaction 1 in this system has been indirectly shown in isotope analyses of the sulfur system in YNP. The work of Kamyshny et al. (2014) provided information on triple (^{32}S, ^{33}S, ^{34}S) isotope analyses on sulfide, zero-valent sulfur and sulfate on geothermal waters of YNP that suggest recycling of reduced sulfur species via abiotic redox transformations involve reaction 1 (Kamyshny et al., 2014). This isotopic fractionation was shown by Amrani et al. (2006) as an isotopic equilibrium between aqueous polysulfide species and the rest of the sulfur species in the system (Amrani et al., 2006).

Elemental sulfur was modeled in both scenarios A and B, and found to maintain concentrations ranging from negligible amounts up to 2.2 10^{-6}M. The models indicate that

as long as reaction 1 is active, elemental sulfur is not abundant, showing a “cryptic” behavior similar to that of polysulfide. When sulfide availability ceases, then elemental sulfur increases significantly over more than 6 orders of magnitude (Scenario B; Figure 4-7-B).

Even if the models predict the distribution of sulfur species intermediates as a function of time and sulfide-to-oxygen ratio, natural systems – particularly heterogeneous ones such as Yellowstone – are difficult to have their chemistry predicted. This difference of the chemical content of sulfur species between the field observations and the kinetic model can be due, at least in part, to the timescale of sulfide delivery to each system compared to the timescale of the reactions to achieve any sort of steady state condition. An example would be the random oxygenation of a geothermal spring due to water mixing. Meteoric water input via surface runoff to the spring would be spatially and temporally heterogeneous. Part of the geothermal water body would be oxygenated while the reaction pathway modelled in this work will initiate in a scenario similar to the scenario B, for a restricted period of time until the depletion of oxygen or the addition of sulfide will transition the chemistry towards scenario A. Chaotic delivery of sulfide or oxygenated water can fluctuate our chemical system between scenarios, effectively “restarting” the kinetic pathway (by the addition of a spike of sulfide or O_2). The whole volume of the geothermal water body might not reach homogeneity until reactions progress, therefore having both or even more chemical “scenarios” active in the same time in various locations of the water volume (spatial variability). All the above could result to the discontinuous formation of products of sulfide oxidation. This can explain the lack of consistency between the predicted concentrations of elemental sulfur in the models with those in the grab sample analyses. The models showed that elemental sulfur was negligible as long as reaction 1 was active, whereas chromatographic analyses on the grab samples indicated that elemental sulfur is preserved in the geothermal springs studied, even if S_8 shows temporal variations in its concentration.

However, intermediates of both thiosulfate and sulfite show less variability in some cases possibly because they are formed as products of reactions that are later parts of the chemical pathway described (reaction 3 and 4) compared to the earlier reactions involving

elemental sulfur (reaction 1, reaction 2, reverse reaction 1). The chaotic occurrence of "peaks" and "valleys" of sulfide and oxygen concentration in specific geothermal waters due to chaotic gas input for sulfide and chaotic oxygen input for O_2 also affect the concentrations of all sulfur intermediates as they are linked via the proposed reaction framework (Figure 4-5).

Biogeochemical implications

When the chemistry of a microbial habitat evolves, the communities respond to that change either by changing their structure, their metabolic activity, or their local abundance. This response has been shown to exist in either hours' scale (Van Der Gast et al., 2004), days scale (Becks et al., 2005), or months scale (Haack et al., 2004). Regarding the geothermal system of Yellowstone, the evolution of chemistry in some springs shows significant variability over seconds or even minutes' scales while in other springs the chemistry displays limited variability. Considering the vast spectrum of dynamic behavior of the springs studied, the Yellowstone ecosystem potentially engulfs an even wider array of chemical conditions for the microbes to live in than if one considered chemical conditions as stable over time. Dynamic conditions might not only promote microbial diversity but also pose an environmental stressor affecting microbial ecology inhabiting each geothermal spring. Yellowstone geothermal springs are an example where environmental conditions drive a remarkable diversity of the Archaea domain (Barns et al., 1994; Meyer-Dombard et al., 2005; Wang et al., 2011). Archaea are distinguished for their capacity for survival in extreme environments (high temperature, acidity, salinity and anoxia)(Valentine, 2007). In many cases this stress (also called chronic energy stress) is the key factor for allowing for the evolution of this domain (Valentine, 2007). Archaea can alternate between "survival mode" and "replication mode", ranging their physiological activities from strict replacement of key macromolecules to advanced activities (such as motility) and growth/replication (Valentine, 2007). Observed differences in the timing of chemical dynamics in the sulfur system (Figure 4-2) may provide key study sites for assessing the timing of these modes in specific communities of archaea.

Swingley et al. (2012) studied the metabolic shifts that occur in microbial ecosystems as a function of spatial variability of chemical compounds and physical parameters (temperature) in a geothermal feature of Yellowstone (Swingley et al., 2012). The chaotic delivery of sulfide to the electrode (Figure 4-2) defines a spatial dimension to the variability closer to what single microbial cells or groups of cells experience. The variation of sulfide concentrations in the point where the cell is located originates from the

evolution of microgradients of H_2S_{aq} due to the upward movement of gaseous H_2S. This mobility of microgradients translates to an evolution of sulfide concentrations at the point of analysis which we represented simply by a “chocolate chip cookie” model. Assuming that the chocolate chips are sulfide and the cookie is the background concentration of the aqueous medium, a single bite of the chocolate chip cookie represents a voltammetric scan or an interaction of the microbial cell with its aqueous environment. Depending on the size of the bite the amount of chocolate chip cookie consumed can vary. In the case of a very small “bite” we will taste either the cookie or the chocolate chips, individually. Therefore, depending on the scale of analysis with the electrochemical instrument used in this study (spherical sampling volume; in situ versus ex situ), we receive a sulfidic signal that represents either a more constant chemical signature or a more dynamic and temporally evolving chemical signature. Since the scale of microbial cells is not as large as that of the surface of our working electrode, the chemical interactions of the microbial cell is represented accurately by the “very small bite” scenario described above where the taste of chocolate chip (sulfide signal) will be present (intense signal of sulfide) or absent (background sulfide content). The evolution of “bites” or chemical interactions will take place in a chaotic manner resulting in a possible environmental stressor from sulfide towards the microbial cells.

Conclusions

Yellowstone geothermal springs exhibit dramatic differences in the temporal variability of sulfide and sulfur intermediates at spatial scales analogous to microbial cells or pods of cells (Norland et al., 1987). This analytical observation from voltammetry is not explained by the chaotic movement of water, bubbles or particles, but from real chemical variability occurring at the spherical sampling volume of analysis attached to the electrode's surface. Sulfide concentrations determined by electrochemical analyses show a chaotic pattern in their fluctuation over time that is not correlated with the method of analysis (*in situ* or *ex situ*) nor the physical-chemical signature of each spring (T, pH, and chlorinity). This chaos in sulfide temporal signatures likely originates from a combination of random degassing from the magmatic chamber, followed by mobility of H_2S_g bubbles that move upward and dissolve in the aqueous medium, creating microgradients of H_2S_{aq} which are captured by the voltammetric analyses and are depicted as chaotic sulfidic signals. Elemental sulfur concentrations as quantified from the chromatographic analyses show variability within each spring, as well as vast variability between various springs. Elemental sulfur is produced by the oxidation of sulfide by molecular oxygen, the acidification of polysulfides and the disproportionation of thiosulfate. The variability of sulfur intermediates is influenced by the delivery of O_2 and sulfide in each spring. The variability in sulfide as well as the sulfur species intermediates might pose a potential stress to microbial communities of the geothermal springs as it can result in significant variation of metabolic component availability to the microorganisms present. Furthermore, the chemical variability in time and space found in these springs combines with the complexity of sulfur speciation to create a wide array of possible chemical settings for microbial communities. In any case of physical-chemical variability that poses stress to the ecosystem, life will have to incorporate organisms that have developed survival mechanisms to cope with this stress. We propose that significant sulfide variability over small spatial and temporal scales is an ecological stressor capable of influencing single cell physiology and community adaptation.

References

Akerman, N., Price, R., Pichler, T. and Amend, J. (2011) Energy sources for chemolithotrophs in an arsenic-and iron-rich shallow-sea hydrothermal system. Geobiology 9, 436-445.

Amend, J.P., McCollom, T.M., Hentscher, M. and Bach, W. (2011) Catabolic and anabolic energy for chemolithoautotrophs in deep-sea hydrothermal systems hosted in different rock types. Geochimica et Cosmochimica Acta 75, 5736-5748.

Amrani, A., Kamyshny, A., Lev, O. and Aizenshtat, Z. (2006) Sulfur stable isotope distribution of polysulfide anions in an (NH4) 2S n aqueous solution. Inorganic chemistry 45, 1427-1429.

Ball, J.W., Nordstrom, D.K., McCleskey, R.B., Schoonen, M.A. and Xu, Y. (2001) Water-chemistry and on-site Sulfur-speciation data for selected springs in Yellowstone National Park, Wyoming, 1996-1998., USGS Open-File Report, Boulder, Colorado.

Bard, A.J. and Faulkner, L.R. (2001) Electrochemical Methods: Fundamentals and Applications. Wiley, New York

Barns, S.M., Fundyga, R.E., Jeffries, M.W. and Pace, N.R. (1994) Remarkable archaeal diversity detected in a Yellowstone National Park hot spring environment. Proceedings of the National Academy of Sciences 91, 1609-1613.

Becks, L., Hilker, F.M., Malchow, H., Jürgens, K. and Arndt, H. (2005) Experimental demonstration of chaos in a microbial food web. Nature 435, 1226-1229.

Bockris, J.O.M. and Reddy, A.K. (2000) Modern electrochemistry 2B: electrodics in chemistry, engineering, biology and environmental science. Springer Science & Business Media.

Botero, L.M., Brown, K.B., Brumefield, S., Burr, M., Castenholz, R.W., Young, M. and McDermott, T.R. (2004) Thermobaculum terrenum gen. nov., sp. nov.: a non-phototrophic gram-positive thermophile representing an environmental clone group related to the Chloroflexi (green non-sulfur bacteria) and Thermomicrobia. Archives of microbiology 181, 269-277.

Boyd, E.S. and Druschel, G.K. (2013) Involvement of Intermediate Sulfur Species in Biological Reduction of Elemental Sulfur under Acidic, Hydrothermal Conditions. Applied and environmental microbiology 79, 2061-2068.

Boyd, E.S., Jackson, R.A., Encarnacion, G., Zahn, J.A., Beard, T., Leavitt, W.D., Pi, Y., Zhang, C.L., Pearson, A. and Geesey, G.G. (2007) Isolation, characterization, and ecology of sulfur-respiring Crenarchaea inhabiting acid-sulfate-chloride-containing geothermal springs in Yellowstone National Park. Applied and environmental microbiology 73, 6669-6677.

Buisman, C.J., Jspeert, P.I., Hof, A., Janssen, A.J., Hagen, R.T. and Lettinga, G. (1991) Kinetic parameters of a mixed culture oxidizing sulfide and sulfur with oxygen. Biotechnology and bioengineering 38, 813-820.

Bura-Nakić, E., Krznarić, D., Jurašin, D., Helz, G.R. and Ciglenečki, I. (2007) Voltammetric characterization of metal sulfide particles and nanoparticles in model solutions and natural waters. Analytica Chimica Acta 594, 44-51.

Bura-Nakić, E., Marguš, M., Jurašin, D., Milanović, I. and Ciglenečki-Jušić, I. (2015) Chronoamperometric study of elemental sulphur (S) nanoparticles (NPs) in NaCl water solution: new methodology for S NPs sizing and detection. Geochemical transactions 16, 1.

Castenholz, R.W. (1977) The effect of sulfide on the blue-green algae of hot springs II. Yellowstone National Park. Microbial Ecology 3, 79-105.

Chang, W.-L., Smith, R.B., Wicks, C., Farrell, J.M. and Puskas, C.M. (2007) Accelerated uplift and magmatic intrusion of the Yellowstone caldera, 2004 to 2006. Science 318, 952-956.

Chen, K.Y. and Gupta, S.K. (1973) Formation of polysulfides in aqueous solution. Environmental letters 4, 187-200.

Chen, K.Y. and Morris, J.C. (1972) Kinetics of oxidation of aqueous sulfide by oxygen. Environmental Science & Technology 6, 529-537.

Chiodini, G., Caliro, S., Lowenstern, J.B., Evans, W.C., Bergfeld, D., Tassi, F. and Tedesco, D. (2012) Insights from fumarole gas geochemistry on the origin of hydrothermal fluids on the Yellowstone Plateau. Geochimica et Cosmochimica Acta 89, 265-278.

Christiansen, R.L., Foulger, G. and Evans, J.R. (2002) Upper-mantle origin of the Yellowstone hotspot. Geological Society of America Bulletin 114, 1245-1256.

Ciglenečki, I., Krznarić, D. and Helz, G.R. (2005) Voltammetry of copper sulfide particles and nanoparticles: investigation of the cluster hypothesis. Environmental science & technology 39, 7492-7498.

Dahl, C. and Prange, A. (2006) Bacterial sulfur globules: occurrence, structure and metabolism, Inclusions in prokaryotes. Springer, pp. 21-51.

Dobson, P.F., Kneafsey, T.J., Hulen, J. and Simmons, A. (2003) Porosity, permeability, and fluid flow in the Yellowstone geothermal system, Wyoming. Journal of volcanology and geothermal research 123, 313-324.

Eaton, G.P., Christiansen, R.L., Iyer, H., Pitt, A.D., Mabey, D.R., Blank, H.R., Zietz, I. and Gettings, M.E. (1975) Magma beneath Yellowstone National Park. Science 188, 787-796.

Farquhar, J., Wing, B., McKeegan, K., Harris, J., Cartigny, P. and Thiemens, M. (2002) Mass-independent sulfur of inclusions in diamond and sulfur recycling on early Earth. Science 298, 2369-2372.

Foote, C.S. and Peters, J.W. (1971) Chemistry of singlet oxygen. XIV. Reactive intermediate in sulfide photooxidation. Journal of the American Chemical Society 93, 3795-3796.

Fournier, R.O. (1989) Geochemistry and dynamics of the Yellowstone National Park hydrothermal system. Annual Review of Earth and Planetary Sciences 17, 13.

Garcia, A.A. and Druschel, G.K. (2014) Elemental sulfur coarsening kinetics. Geochemical transactions 15, 11.

George, G.N., Gnida, M., Bazylinski, D.A., Prince, R.C. and Pickering, I.J. (2008) X-ray absorption spectroscopy as a probe of microbial sulfur biochemistry: the nature of bacterial sulfur globules revisited. Journal of bacteriology 190, 6376-6383.

Gu, C.L. and Foote, C.S. (1982) Chemistry of singlet oxygen. 38. Temperature effect on the photooxidation of sulfides. Journal of the American Chemical Society 104, 6060-6063.

Haack, S.K., Fogarty, L.R., West, T.G., Alm, E.W., McGuire, J.T., Long, D.T., Hyndman, D.W. and Forney, L.J. (2004) Spatial and temporal changes in microbial

community structure associated with recharge-influenced chemical gradients in a contaminated aquifer. Environmental microbiology 6, 438-448.

Habicht, K.S., Canfield, D.E. and Rethmeier, J.o. (1998) Sulfur isotope fractionation during bacterial reduction and disproportionation of thiosulfate and sulfite. Geochimica et Cosmochimica Acta 62, 2585-2595.

Hallberg, K.B., Dopson, M. and Lindström, E.B. (1996) Reduced sulfur compound oxidation by Thiobacillus caldus. Journal of bacteriology 178, 6-11.

Hardisty, D.S., Olyphant, G.A., Bell, J.B., Johnson, A.P. and Pratt, L.M. (2013) Acidophilic sulfur disproportionation. Geochimica et Cosmochimica Acta 113, 136-151.

Henshaw, P.F., Bewtra, J.K. and Biswas, N. (1997) Extraction of elemental sulfur from an aqueous suspension for analysis by high-performance liquid chromatography. Analytical chemistry 69, 3119-3123.

Hinsberg, W. and Houle, F. (2017) Kinetiscope - A stochastic kinetics simulator.

Holm, N.G. (1992) Why are hydrothermal systems proposed as plausible environments for the origin of life?, Marine Hydrothermal Systems and the Origin of Life. Springer, pp. 5-14.

Huang, H.-H., Lin, F.-C., Schmandt, B., Farrell, J., Smith, R.B. and Tsai, V.C. (2015) The Yellowstone magmatic system from the mantle plume to the upper crust. Science 348, 773-776.

Hurwitz, S., Hunt, A.G. and Evans, W.C. (2012) Temporal variations of geyser water chemistry in the Upper Geyser Basin, Yellowstone National Park, USA. Geochemistry, Geophysics, Geosystems 13.

Hurwitz, S., Kumar, A., Taylor, R. and Heasler, H. (2008) Climate-induced variations of geyser periodicity in Yellowstone National Park, USA. Geology 36, 451-454.

Husen, S., Smith, R.B. and Waite, G.P. (2004a) Evidence for gas and magmatic sources beneath the Yellowstone volcanic field from seismic tomographic imaging. Journal of Volcanology and Geothermal Research 131, 397-410.

Husen, S., Taylor, R., Smith, R. and Healser, H. (2004b) Changes in geyser eruption behavior and remotely triggered seismicity in Yellowstone National Park produced by the 2002 M 7.9 Denali fault earthquake, Alaska. Geology 32, 537-540.

Inskeep, W.P., Jay, Z.J., Tringe, S.G., Herrgård, M.J., Rusch, D.B., Committee, Y.M.P.S. and Members, W.G. (2013) The YNP metagenome project: environmental parameters responsible for microbial distribution in the Yellowstone geothermal ecosystem. Frontiers in microbiology 4.

Janssen, A., Lettinga, G. and De Keizer, A. (1999) Removal of hydrogen sulphide from wastewater and waste gases by biological conversion to elemental sulphur: colloidal and interfacial aspects of biologically produced sulphur particles. Colloids and Surfaces A: Physicochemical and Engineering Aspects 151, 389-397.

Johnston, F. and McAmish, L. (1973) A study of the rates of sulfur production in acid thiosulfate solutions using S-35. Journal of Colloid and Interface Science 42, 112-119.

Kamp, A., Stief, P. and Schulz-Vogt, H.N. (2006) Anaerobic sulfide oxidation with nitrate by a freshwater Beggiatoa enrichment culture. Applied and environmental microbiology 72, 4755-4760.

Kamyshny, A., Borkenstein, C.G. and Ferdelman, T.G. (2009) Protocol for Quantitative Detection of Elemental Sulfur and Polysulfide Zero-Valent Sulfur Distribution in Natural Aquatic Samples. Geostandards and Geoanalytical Research 33, 415-435.

Kamyshny, A., Druschel, G., Mansaray, Z.F. and Farquhar, J. (2014) Multiple sulfur isotopes fractionations associated with abiotic sulfur transformations in Yellowstone National Park geothermal springs. Geochemical transactions 15, 7.

Kamyshny, A., Goifman, A., Gun, J., Rizkov, D. and Lev, O. (2004) Equilibrium distribution of polysulfide ions in aqueous solutions at 25 C: a new approach for the study of polysulfides' equilibria. Environmental science & technology 38, 6633-6644.

Kelbert, A. and Egbert, G. (2012) Crust and upper mantle electrical conductivity beneath the Yellowstone Hotspot Track. Geology 40, 447-450.

Kelly, D. (1989) Oxidation of sulphur compounds, in: Cole, J.A.F., S. (Ed.), Society for General Microbiology Symposium 42. Cambridge University Press, pp. 65-98.

Kleinjan, W.E., de Keizer, A. and Janssen, A.J. (2003) Biologically produced sulfur, Elemental sulfur and sulfur-rich compounds I. Springer, pp. 167-188.

Kleinjan, W.E., de Keizer, A. and Janssen, A.J. (2005a) Equilibrium of the reaction between dissolved sodium sulfide and biologically produced sulfur. Colloids and Surfaces B: Biointerfaces 43, 228-237.

Kleinjan, W.E., de Keizer, A. and Janssen, A.J. (2005b) Kinetics of the chemical oxidation of polysulfide anions in aqueous solution. Water research 39, 4093-4100.

Knickerbocker, C., Nordstrom, D. and Southam, G. (2000) The role of "blebbing" in overcoming the hydrophobic barrier during biooxidation of elemental sulfur by Thiobacillus thiooxidans. Chemical Geology 169, 425-433.

LaRowe, D.E., Dale, A.W., Aguilera, D.R., L'Heureux, I., Amend, J.P. and Regnier, P. (2014) Modeling microbial reaction rates in a submarine hydrothermal vent chimney wall. Geochimica et cosmochimica acta 124, 72-97.

Le Bris, N. and Gaill, F. (2007) How does the annelid Alvinella pompejana deal with an extreme hydrothermal environment?, Life in Extreme Environments. Springer, pp. 315-339.

Lee, Y.-J., Prange, A., Lichtenberg, H., Rohde, M., Dashti, M. and Wiegel, J. (2007) In situ analysis of sulfur species in sulfur globules produced from thiosulfate by Thermoanaerobacter sulfurigignens and Thermoanaerobacterium thermosulfurigenes. Journal of bacteriology 189, 7525-7529.

Luther, G.W., Bono, A.B., Taillefert, M. and Cary, S.C. (2002) A Continuous Flow Electrochemical Cell for Analysis of Chemical Species and Ions at High Pressure: Laboratory, Shipboard, and Hydrothermal Vent Results, Environmental Electrochemistry. American Chemical Society, pp. 54-72.

Luther, G.W., Glazer, B.T., Ma, S., Trouwborst, R.E., Moore, T.S., Metzger, E., Kraiya, C., Waite, T.J., Druschel, G. and Sundby, B. (2008) Use of voltammetric solid-state (micro) electrodes for studying biogeochemical processes: laboratory measurements to real time measurements with an in situ electrochemical analyzer (ISEA). Marine Chemistry 108, 221-235.

Luther III, G.W., Findlay, A.J., MacDonald, D.J., Owings, S.M., Hanson, T.E., Beinart, R.A. and Girguis, P.R. (2011) Thermodynamics and kinetics of sulfide oxidation by oxygen: a look at inorganically controlled reactions and biologically mediated processes in the environment. Frontiers in microbiology 2.

Luther III, G.W., Glazer, B.T., Hohmann, L., Popp, J.I., Taillefert, M., Rozan, T.F., Brendel, P.J., Theberge, S.M. and Nuzzio, D.B. (2001a) Sulfur speciation monitored in situ with solid state gold amalgam voltammetric microelectrodes: polysulfides as a special case in sediments, microbial mats and hydrothermal vent watersPresented at the Whistler 2000 Speciation Symposium, Whistler Resort, BC, Canada, June 25–July 1, 2000. Electronic Supplementary Information available. See http://www. rsc. org/suppdata/em/b0/b006499h. Journal of Environmental Monitoring 3, 61-66.

Luther III, G.W., Rozan, T.F., Taillefert, M. and Nuzzio, D.B. (2001b) Chemical speciation drives hydrothermal vent ecology. Nature 410, 813.

Luther, P.J.B.a.G.W.I. (1995) Development of a Gold Amalgam Voltammetric Microelectrode for the Determination of Dissolved Fe, Mn, O2, and S(-II) in Porewaters of Marine and Freshwater Sediments. Environmental Science & Technology 29, 751-761.

Lutz, R.A., Shank, T.M., Luther III, G.W., Vetriani, C., Tolstoy, M., Nuzzio, D.B., Moore, T.S., Waldhauser, F., Crespo-Medina, M. and Chatziefthimiou, A.D. (2008) Interrelationships between vent fluid chemistry, temperature, seismic activity, and biological community structure at a mussel-dominated, deep-sea hydrothermal vent along the East Pacific Rise. Journal of Shellfish Research 27, 177-190.

Macur, R., Jay, Z., Taylor, W., Kozubal, M., Kocar, B. and Inskeep, W. (2013) Microbial community structure and sulfur biogeochemistry in mildly-acidic sulfidic geothermal springs in Yellowstone National Park. Geobiology 11, 86-99.

Malenkov, I. (1968) Motion of large gas bubbles ascending in a liquid. Journal of Applied Mechanics and Technical Physics 9, 750-754.

Malik, R., Burch, D., Bazant, M. and Ceder, G. (2010) Particle size dependence of the ionic diffusivity. Nano letters 10, 4123-4127.

Meulenberg, R., Pronk, J.T., Hazeu, W., Bos, P. and Kuenen, J.G. (1992) Oxidation of reduced sulphur compounds by intact cells of Thiobacillus acidophilus. Archives of microbiology 157, 161-168.

Meyer-Dombard, D., Shock, E. and Amend, J. (2005) Archaeal and bacterial communities in geochemically diverse hot springs of Yellowstone National Park, USA. Geobiology 3, 211-227.

Millero, F.J., Hubinger, S., Fernandez, M. and Garnett, S. (1987) Oxidation of H2S in seawater as a function of temperature, pH, and ionic strength. Environmental science & technology 21, 439-443.

Milucka, J., Ferdelman, T.G., Polerecky, L., Franzke, D., Wegener, G., Schmid, M., Lieberwirth, I., Wagner, M., Widdel, F. and Kuypers, M.M. (2012) Zero-valent sulphur is a key intermediate in marine methane oxidation. Nature 491, 541.

Morgan, P., Blackwell, D.D., Spafford, R.E. and Smith, R.B. (1977) Heat flow measurements in Yellowstone Lake and the thermal structure of the Yellowstone caldera. Journal of Geophysical Research 82, 3719-3732.

Nakagawa, T. and Fukui, M. (2003) Molecular characterization of community structures and sulfur metabolism within microbial streamers in Japanese hot springs. Applied and environmental microbiology 69, 7044-7057.

Nordstrom, D.K., McCleskey, R.B. and Ball, J.W. (2009) Sulfur geochemistry of hydrothermal waters in Yellowstone National Park: IV Acid–sulfate waters. Applied Geochemistry 24, 191-207.

Norland, S., Heldal, M. and Tumyr, O. (1987) On the relation between dry matter and volume of bacteria. Microbial Ecology 13, 95-101.

Norlund, K.L.I., Southam, G., Tyliszczak, T., Hu, Y., Karunakaran, C., Obst, M., Hitchcock, A.P. and Warren, L.A. (2009) Microbial Architecture of Environmental Sulfur Processes: A Novel Syntrophic Sulfur-Metabolizing Consortia. Environmental Science & Technology 43, 8781-8786.

O'Brien, D.J. and Birkner, F.B. (1977) Kinetics of oxygenation of reduced sulfur species in aqueous solution. Environmental Science & Technology 11, 1114-1120.

Okabe, S., Ito, T., Sugita, K. and Satoh, H. (2005) Succession of internal sulfur cycles and sulfur-oxidizing bacterial communities in microaerophilic wastewater biofilms. Applied and environmental microbiology 71, 2520-2529.

Oppenheimer, C., Scaillet, B. and Martin, R.S. (2011) Sulfur degassing from volcanoes: source conditions, surveillance, plume chemistry and earth system impacts. Reviews in Mineralogy and Geochemistry 73, 363-421.

Pasteris, J.D., Freeman, J.J., Goffredi, S.K. and Buck, K.R. (2001) Raman spectroscopic and laser scanning confocal microscopic analysis of sulfur in living sulfur-precipitating marine bacteria. Chemical Geology 180, 3-18.

Perner, M., Gonnella, G., Hourdez, S., Böhnke, S., Kurtz, S. and Girguis, P. (2013) In situ chemistry and microbial community compositions in five deep-sea hydrothermal fluid samples from Irina II in the Logatchev field. Environmental microbiology 15, 1551-1560.

Pierce, K.L. and Morgan, L.A. (2009) Is the track of the Yellowstone hotspot driven by a deep mantle plume?—Review of volcanism, faulting, and uplift in light of new data. Journal of Volcanology and Geothermal Research 188, 1-25.

Prange, A., Chauvistre, R., Modrow, H., Hormes, J., Trüper, H.G. and Dahl, C. (2002) Quantitative speciation of sulfur in bacterial sulfur globules: X-ray absorption spectroscopy reveals at least three different species of sulfur. Microbiology 148, 267-276.

Raven, M.R., Adkins, J.F., Werne, J.P., Lyons, T.W. and Sessions, A.L. (2015) Sulfur isotopic composition of individual organic compounds from Cariaco Basin sediments. Organic Geochemistry 80, 53-59.

Rethmeier, J., Rabenstein, A., Langer, M. and Fischer, U. (1997) Detection of traces of oxidized and reduced sulfur compounds in small samples by combination of different high-performance liquid chromatography methods. Journal of chromatography A 760, 295-302.

Rickard, D. and Luther, G.W. (2007) Chemistry of Iron Sulfides. Chemical Reviews 107, 514-562.

Scaillet, B., Clemente, B., Evans, B.W. and Pichavant, M. (1998) Redox control of sulfur degassing in silicic magmas. Journal of Geophysical Research: Solid Earth 103, 23937-23949.

Schauder, R. and Müller, E. (1993) Polysulfide as a possible substrate for sulfur-reducing bacteria. Archives of microbiology 160, 377-382.

Schrenk, M.O., Kelley, D.S., Delaney, J.R. and Baross, J.A. (2003) Incidence and diversity of microorganisms within the walls of an active deep-sea sulfide chimney. Applied and Environmental Microbiology 69, 3580-3592.

Schubotz, F., Meyer-Dombard, D., Bradley, A., Fredricks, H., Hinrichs, K.U., Shock, E. and Summons, R. (2013) Spatial and temporal variability of biomarkers and microbial diversity reveal metabolic and community flexibility in Streamer Biofilm Communities in the Lower Geyser Basin, Yellowstone National Park. Geobiology 11, 549-569.

Schulz, H.N. and Schulz, H.D. (2005) Large sulfur bacteria and the formation of phosphorite. Science 307, 416-418.

Shock, E.L., Holland, M., Amend, J.P., Osburn, G. and Fischer, T.P. (2010) Quantifying inorganic sources of geochemical energy in hydrothermal ecosystems, Yellowstone National Park, USA. Geochimica et Cosmochimica Acta 74, 4005-4043.

Shock, E.L. and Schulte, M.D. (1998) Organic synthesis during fluid mixing in hydrothermal systems. Journal of Geophysical Research: Planets (1991–2012) 103, 28513-28527.

Shock, E.L.H., M; Meyer-Dombard, D R; Amend, J P (2005) Geochemical sources of energy for microbial metabolism in hydrothermal ecosystems: Obsidian Pool, Yellowstone National Park. Geothermal Biology and Geochemistry in Yellowstone National Park, 95-110.

Sievert, S.M., Brinkhoff, T., Muyzer, G., Ziebis, W. and Kuever, J. (1999) Spatial heterogeneity of bacterial populations along an environmental gradient at a shallow submarine hydrothermal vent near Milos Island (Greece). Applied and environmental microbiology 65, 3834-3842.

Sievert, S.M., Wieringa, E., Wirsen, C.O. and Taylor, C.D. (2007) Growth and mechanism of filamentous-sulfur formation by Candidatus Arcobacter sulfidicus in opposing oxygen-sulfide gradients. Environmental microbiology 9, 271-276.

Skirnisdottir, S., Hreggvidsson, G.O., Hjörleifsdottir, S., Marteinsson, V.T., Petursdottir, S.K., Holst, O. and Kristjansson, J.K. (2000) Influence of sulfide and temperature on species composition and community structure of hot spring microbial mats. Applied and environmental microbiology 66, 2835-2841.

Slowey, A.J. and Marvin-DiPasquale, M. (2012) How to overcome inter-electrode variability and instability to quantify dissolved oxygen, Fe (II), Mn (II), and S (−II) in undisturbed soils and sediments using voltammetry. Geochemical transactions 13, 1-20.

Spear, J.R., Walker, J.J., McCollom, T.M. and Pace, N.R. (2005) Hydrogen and bioenergetics in the Yellowstone geothermal ecosystem. Proceedings of the National Academy of Sciences of the United States of America 102, 2555-2560.

Stefess, G., Torremans, R., De Schrijver, R., Robertson, L. and Kuenen, J. (1996) Quantitative measurement of sulphur formation by steady-state and transient-state continuous cultures of autotrophic Thiobacillus species. Applied microbiology and biotechnology 45, 169-175.

Steudel, R. (1996) Mechanism for the formation of elemental sulfur from aqueous sulfide in chemical and microbiological desulfurization processes. Industrial & engineering chemistry research 35, 1417-1423.

Steudel, R. (2003) Aqueous sulfur sols, Elemental Sulfur and Sulfur-Rich Compounds I. Springer, pp. 153-166.

Steudel, R. and Holdt, G. (1988) Solubilization of elemental sulfur in water by cationic and anionic surfactants. Angewandte Chemie International Edition 27, 1358-1359.

Swingley, W.D., D'Arcy, R., Shock, E.L., Alsop, E.B., Falenski, H.D., Havig, J.R. and Raymond, J. (2012) Coordinating environmental genomics and geochemistry reveals metabolic transitions in a hot spring ecosystem. PloS one 7, e38108.

Taylor, C.D. and Wirsen, C.O. (1997) Microbiology and ecology of filamentous sulfur formation. Science 277, 1483-1485.

Taylor, C.D., Wirsen, C.O. and Gaill, F. (1999) Rapid microbial production of filamentous sulfur mats at hydrothermal vents. Applied and Environmental Microbiology 65, 2253-2255.

Thamdrup, B., Finster, K., Hansen, J.W. and Bak, F. (1993) Bacterial disproportionation of elemental sulfur coupled to chemical reduction of iron or manganese. Applied and environmental microbiology 59, 101-108.

Truper, H. and Fischer, U. (1982) Anaerobic oxidation of sulphur compounds as electron donors for bacterial photosynthesis. Philosophical Transactions of the Royal Society B: Biological Sciences 298, 529-542.

Ueno, Y. (2014) Coping with low ocean sulfate. Science 346, 703-704.

Valentine, D.L. (2007) Adaptations to energy stress dictate the ecology and evolution of the Archaea. Nature Reviews Microbiology 5, 316-323.

van den Ende, F.P. and van Gemerden, H. (1993) Sulfide oxidation under oxygen limitation by a Thiobacillus thioparus isolated from a marine microbial mat. FEMS microbiology ecology 13, 69-77.

Van Der Gast, C.J., Whiteley, A.S. and Thompson, I.P. (2004) Temporal dynamics and degradation activity of an bacterial inoculum for treating waste metal-working fluid. Environmental Microbiology 6, 254-263.

Visser, J.M., Robertson, L.A., Van Verseveld, H.W. and Kuenen, J.G. (1997) Sulfur production by obligately chemolithoautotrophic thiobacillus species. Applied and Environmental Microbiology 63, 2300-2305.

Wang, Y., Boyd, E., Crane, S., Lu-Irving, P., Krabbenhoft, D., King, S., Dighton, J., Geesey, G. and Barkay, T. (2011) Environmental conditions constrain the distribution and diversity of archaeal merA in Yellowstone National Park, Wyoming, USA. Microbial ecology 62, 739-752.

Wilbanks, E.G., Jaekel, U., Salman, V., Humphrey, P.T., Eisen, J.A., Facciotti, M.T., Buckley, D.H., Zinder, S.H., Druschel, G.K. and Fike, D.A. (2014) Microscale sulfur cycling in the phototrophic pink berry consortia of the Sippewissett Salt Marsh. Environmental microbiology 16, 3398-3415.

Xu, Y., Schoonen, M., Nordstrom, D., Cunningham, K. and Ball, J. (1998) Sulfur geochemistry of hydrothermal waters in Yellowstone National Park: I. The origin of thiosulfate in hot spring waters. Geochimica et Cosmochimica Acta 62, 3729-3743.

Xu, Y., Schoonen, M.A. and Strongin, D.R. (1996) Thiosulfate oxidation: Catalysis of synthetic sphalerite doped with transition metals. Geochimica et cosmochimica acta 60, 4701-4710.

Yücel, M., Sievert, S.M., Vetriani, C., Foustoukos, D.I., Giovannelli, D. and Le Bris, N. (2013) Eco-geochemical dynamics of a shallow-water hydrothermal vent system at Milos Island, Aegean Sea (Eastern Mediterranean). Chemical Geology 356, 11-20.

Zerkle, A.L., Farquhar, J., Johnston, D.T., Cox, R.P. and Canfield, D.E. (2009) Fractionation of multiple sulfur isotopes during phototrophic oxidation of sulfide and elemental sulfur by a green sulfur bacterium. Geochimica et Cosmochimica Acta 73, 291-306.

Zopfi, J., Ferdelman, T. and Fossing, H. (2004) Distribution and fate of sulfur intermediates—sulfite, tetrathionate, thiosulfate, and elemental sulfur—in marine sediments. Geological Society of America Special Papers 379, 97-116.

APPENDIX-A – ELEMENTAL SULFUR

Solid Sulfur mineralogy, crystallography and vibrational spectra

Sulfur occupies the chemical system with the vastest amount of allotropes in the solid phase (Meyer, 1964, 1976; Steudel and Eckert, 2003). Allotropes are called two or more solids of an element that differ in their crystallographic structure, as displayed in differences in XRD and molecular analyses. In low pressures, the elemental sulfur system displays allotropes both as: Unbranched cyclic molecules, with the sizes of the ring molecules ranging between 6 and 20 sulfur atoms. Polymeric ("branched") molecules of sulfur with varying number of sulfur atoms per molecule, where the molecule conformation is that of a coil (or helix). A summary of the various solid forms of sulfur as well as their molecular, crystallographic and vibrational properties is presented in Table A-1.

Unbranched cyclic sulfur molecules

There are 20 crystalline ring allotropes of sulfur which include: " S_6, S_7 (α, β, γ, δ), S_8 (α, β, γ), S_9 (α, β), S_{10}, $S_6.S_{10}$, S_{11}, S_{12}, S_{13}, S_{14}, S_{15}, endo-S_{18}, exo-S_{18}, and S_{20}". The Greek letters used as prefixes (i.e. α-S_8) indicate a variation in the packing pattern of unit cells between same size and same conformation molecules. In the case of the two forms of cyclo-octadecasulfur (S_{18}), endo- and exo- prefixes disclose two different conformations of S_{18}. The $S_6.S_{10}$ allotrope consists of two different molecules bound together in a stoichiometric ratio. Below a basic description of each molecule is provided.

Cyclo-hexasulfur – S_6

Cyclo-hexasulfur crystals show an orange-yellow color and a hexagonal prismatic shape. It crystallizes in the rhombohedral crystal system and its space group is R$\bar{3}$-C_{3i}^2. The unit cell includes one molecule of S_6, while it has a C_{3i} symmetry. The dimensions of the unit cell are a=b=1081.8pm, and c=428.0pm. The molecule shows a chair conformation (Meyer, 1976), which based on theoretical calculations is proven to be energetically the most favorable compared to other isomeric forms. There has been no other hexasulfur ring allotrope found nor synthesized. The compact structure of the molecule results in many short distance intermolecular contacts, and consequently to high density of the material (Steudel and Eckert, 2003). The S_6 allotrope has been investigated in terms of its Raman vibrational data at -90^{o}C. The spectrum indicated two stretching vibration bands at 448 and 471cm^{-1}, two bending vibration bands at 202 and 262cm^{-1}, as well as two librational lattice bands at 79 and 106cm^{-1} (Eckert and Steudel, 2003).

Cyclo-heptasulfur – S_7

Initial XRD analyses suggested a chair conformation for S_7, whereas molecular spectroscopies (Infrared, Raman) disclosed the four different allotropes of cyclo-heptasulfur (α-S_7, β-S_7, γ-S_7, δ-S_7). The α-S_7 allotrope shows crystals with shape similar to a needle or lancet, of an intense yellow color (Meyer, 1976). β-S_7 is a decomposition product of δ-S7. Allotropes γ-S_7 and δ-S_7 have been characterized more thoroughly in terms of their mineralogy (Steudel and Eckert, 2003).

γ-S_7 forms crystals in the monoclinic group with space group characteristics $P2_1/n\text{-}C_{2h}^5$. The unit cell of γ-S7 is comprised of four ring molecules. Its dimensions are a=968.0pm, b=764.1pm, c=940.9pm, and β=102.08^o (Steudel and Eckert, 2003).

δ -S_7 crystals are block shaped, forming tetragonal-bipyramidal and sarcophagus-like shapes (Steudel and Eckert, 2003). The δ-S_7 allotrope crystallizes in the monoclinic crystal group, with crystal space group $P2_1/n\text{-}C_{2h}^2$. There are eight molecules of S_7 included in the unit cell of δ-S_7. The dimensions of the unit cell are a= 1510.5pm, b= 599.8pm, c=1509.6pm, and β=92.15^o. Theoretical calculations indicated slightly lower lattice energy of δ-S_7 compared to the lattice energy calculated for γ-S_7 (Steudel and Eckert, 2003).

Both γ-S_7 and δ-S_7 show very similar molecular structures with chair conformation and symmetry C1. The characteristic of these two allotropes is a very large bond length 217.5pm between the S6 and S7 atoms. The repulsion caused by their $3p_\pi$ lone pairs, results in the large distance between these two atoms as well as to the high reactivity (due to low stability) of the S_7 molecule (Steudel and Eckert, 2003).

The various allotropes of S_7 show very similar Raman spectra, as they have been characterized at -100°C. A few characteristic peaks that they share are 480-481cm^{-1}, 459-460cm^{-1}, 419-420cm^{-1}, 400cm^{-1}, 285cm^{-1}, 79-80cm^{-1}, and 39-41cm^{-1}. Some characteristic Raman bands that can help distinguish between them are the 514 and 355cm^{-1} bands for α-S_7, 182 and 47cm^{-1} bands for β-S_7, 292, 71 and 62cm^{-1} peaks for γ-S_7, and the 201cm^{-1} band corresponding to the δ-S_7 allotrope (Eckert and Steudel, 2003). Infrared absorbance investigation for the α-S_7 solid (analysis at -100^{o}C) showed the very strong peaks at 513,

400, and 270 cm^{-1}, as well as the strong bands at 480 and 235cm^{-1} (Eckert and Steudel, 2003).

Allotropes of S_8

Cyclo-octasulfur forms three allotropes in nature, α-S_8, β-S_8 and γ-S_8. The orthorhombic α-S_8 is the most common form of elemental sulfur in solid phase, as it is the only phase stable at standard temperatures and pressures (STP). The β-S_8 allotrope is crystallizing in the monoclinic crystal group and can be formed either by heating α-S_8 above 369K, or by crystallization due to magma cooling below 393K (Steudel and Eckert, 2003).

All three allotropes of S_8 (α, β, γ) are built by the same shape of the cyclo-octasulfur ring molecule. The crown shaped puckered conformation of cyclo-octasulfur is characterized by a D4d symmetry due to alternation of dihedral angles (Steudel and Eckert, 2003).

In α-S_8 the crystallographic group is orthorhombic whereas the space group is Fddd-D_{2h}^{24}. Each four sulfur atoms form two groups that are placed in two parallel planes, forming the crown-shaped puckered conformation. The c crystallographic axis is perpendicular to those two planes. The unit cell contains four molecules of cyclo-octasulfur, while its dimensions are a=1046.4pm, b=1286.6pm, and c=2448.6pm (Meyer, 1976; Steudel and Eckert, 2003). The molecular symmetry is C2. This allotrope shows a large number of intermolecular contacts, that is 12 contacts per four non-equivalent sulfur atoms in each S_8 ring. In particular, these contacts show short intermolecular distances, less than 370pm, leading to the high stability of this allotrope in STP (Steudel and Eckert, 2003).

The β-S_8 allotrope shows crystals of yellow color, with needle-like shape and twinning. The crystallization takes place in the monoclinic crystal group, and space group $P2_1/c$-C_{2h}^5. The crown shape puckered conformation is similar to that of α-S_8, however with a flattening effect due to intermolecular forces. The symmetry of the crystals of this allotrope is D_{4d} symmetry with the two thirds of the amount of the rings being normal, whereas the one third being disordered by a 45^o rotation along the a axis. The unit cell incorporates six

molecules of cyclo-octasulfur (four normal and two pseudocentered), while the cell dimensions are a=1092.6pm, b=1085.2pm, c=1079.0pm, and β=95.9º (Meyer, 1976; Steudel and Eckert, 2003).

The γ-S_8 allotrope shows crystals of light yellow color with a needle-like prismatic shape. The crystal group is monoclinic, whereas the crystal space group is P2/c-C_{2h}^4. The crystals of γ-S_8 show a "sheared penny roll" arrangement. The molecule of cyclo-octasulfur in this allotrope displays a pseudo-hexagonal close-packed structure. The unit cell includes four molecules, whereas its dimensions are a=845.5pm, b=1305.2pm, c=926.7pm, and β=124.9º (Meyer, 1976; Steudel and Eckert, 2003). The bond lengths in γ-S_8 vary significantly, much more than the variation found in the bond lengths of α-S_8 and β-S_8 (Steudel and Eckert, 2003).

The Raman and Infrared signature of the allotropes of α-S_8 is comprised by a multitude of vibrations. These are proportional to the amount of molecules per unit cell of the mineral, the size of each molecule as well as its degree of freedom. For α-S_8, a total number of 96 vibrations have been calculated and characterized, which include (Eckert and Steudel, 2003):

- 72 intramolecular vibrations, as well as
- 24 intermolecular vibrations (lattice phonons), which can further be divided into
    - 12 librational modes (due to molecular rotations)
    - 9 translational models
    - 3 acoustic phonons

The principal Raman vibration bands of α-S_8 are at 476 and 218.5cm^{-1}, due to stretching (V1) and bending (V2) vibrations, respectively. Infrared absorbance at 471 and 243cm^{-1} originates from stretching (V5) and bending (V4) vibrations, respectively. Another bending vibration that causes absorbance in the Infrared spectrum is at 191cm^{-1} (V6). More Raman bands of α-S_8 at 86, 152.5, 248, 444, and 476cm^{-1} are a result of torsional (V9), bending (V8 and V11), as well as stretching (V10 and V7) vibrations, respectively (Eckert and Steudel, 2003).

The crystallographic geometry of β-S_8 crystals, which includes the two-fold disorder of part of the one third of the cyclo-octasulfur molecules in its unit cell, influences its Raman spectra. Even though the Raman spectrum of β-S_8 at 373K at the stretching and bending vibration range is similar to the spectrum of α-S_8, the torsional and external vibration range at the same temperature results to a broad band with a few distinguishable peaks at 34, 42, and 82cm^{-1}. The broad band is expected due to the conformation disorder that characterizes β-S_8. Interestingly, when the Raman spectra were acquired at 40K – way below 198K which marks the order-disorder transition – both stretching-bending as well as torsional-external vibration bands of β-S_8 showed completely different spectral signatures compared to the 373K homologues, that allow β-S_8 to be distinguished from α-S_8 in temperature conditions below the order-disorder transition (Eckert and Steudel, 2003).

Allotropes of S_9

Cyclo-nonasulfur salts show a deep yellow color and form needle shapes (Steudel and Eckert, 2003). The allotropes α-S_9 and β-S_9 have been identified via Raman spectroscopic analyses. The α-S_9 allotrope crystallizes in the monoclinic crystal group, with space group being $P2_1/n$. It is of the least symmetrical allotropes of elemental sulfur, showing enhanced variability in bond lengths and torsion angles (Lesté-Lasserre and Harpp, 1999). The symmetry of the unit cell is C1, but is close to C2. Two molecules are incorporated in each unit cell, which shows dimensions a=790.2pm, b=1390.8pm, c=1694.8pm, and β=103.2^o at 173K. The β-S_9 allotrope has been studied only with Raman spectroscopy suggesting same conformation of the molecule as of α-S_9 (Steudel and Eckert, 2003). The two allotropes of cyclo-nonasulfur show similar raman spectra with seven bands at the range of 414 to 485cm^{-1} that originate from S-S bond stretching vibrations. Some representative bands include 454, and 436cm^{-1} for α-S_9, as well as 460, 454, and 437cm^{-1} for β-S_9. Also, bands at 181 and 188cm^{-1} originate from the S-S-S bending vibrations of β- and α-S_9, respectively (Eckert and Steudel, 2003).

Cyclo-decasulfur – S_{10}

Cyclo-decasulfur salts have an intense yellow color (Lesté-Lasserre, 2001), while crystalize in the monoclinic crystal group, with space group being C2/c-C_{2h}^6 (Steudel and Eckert, 2003). The unit cell includes four rings with a C2 symmetry. The dimensions of the unit cell are a=1253.3pm, b=1027.5pm, and c=1277.6pm, at 163K. The molecular symmetry of S_{10} is found to be D_2, based on single crystal XRD, as well as quantum chemical calculations (Steudel and Eckert, 2003). The only symmetrical elements in S_{10} are the three orthogonal two fold axes of rotation (Lesté-Lasserre, 2001). This result was surprising due to the fact that a D_{5d} symmetry was expected for S_{10}, based on the trend of having D_{3d} symmetry for S_6 and D_{4d} symmetry for S_8 (Steudel and Eckert, 2003). For the cyclo-decasulfur the S-S bond stretching vibrations are depicted in the region of 400 to 500cm^{-1} for the Raman (487, 469, 243, 179, 131 and 100cm^{-1}) and Infrared (239, 220, and 204cm^{-1}) spectroscopy. The rest of the vibrational modes are reflected at wavenumbers less than 260cm^{-1} (Eckert and Steudel, 2003). Cyclo-decasulfur shows high reactivity for sulfurization reactions of dienes and olefins, producing polysulfidic molecules (Lesté-Lasserre and Harpp, 1999).

Allotrope $S_6.S_{10}$

This allotrope of elemental sulfur shows an intense orange-yellow color in its solid form, with opaque, plate-like, hexagonal crystals. It crystallizes in the monoclinic crystal system, with crystal space group I2/a (which is an alternative of C2/n). The unit cell of this allotrope includes two molecules of each S_6 and S_{10}, with the crystal structure being comprised by layers of S_6 and S_{10} molecules, alternating each other. The dimensions of the unit cell are a=1954.1pm, b=943.1pm, c=883.1pm, and β=105.1°. The molecular conformation and mean bond parameters of $S_6.S_{10}$ are same as those of S_6 and S_{10} individually. However, the site symmetry of S_6 is reduced from C_{3i} to C_i (Steudel and Eckert, 2003). The Raman and Infrared spectra of the $S_6.S_{10}$ allotrope are composed by the addition of the spectra of S_6 and S_{10}, respectively (Eckert and Steudel, 2003).

Cyclo-undecasulfur – S_{11}

Cyclo-undecasulfur (S_{11}) forms crystals of a yellow color, appearing as rod-like rhombic-bipyramids. The unit cell of the crystal of S_{11} contains eight rings of S11, and belongs to the orthorhombic system. The space group is $Pca2_1$-C_{2v}^5) with unit cell dimensions being a=1493.3pm, b=832.1pm, and c=1808.6pm at 163K. The molecular symmetry is approximately C2. The odd number of sulfur atoms in this molecule result to the large bond of 208 or 211pm (depending on the molecule of S_{11} observed in the unit cell). Also, the torsion angles of 141º and 137º (for each molecule studied in the unit cell, respectively) are the largest in the elemental sulfur rings system (Steudel and Eckert, 2003). Cyclo-undecasulfur shows Infrared and Raman spectra that incorporate vibration bands in the range of 410 to 480cm^{-1}, (S-S bond stretching) and at bands below 290cm^{-1} (bending, torsion and lattice vibrations)(Eckert and Steudel, 2003).

Cyclo-dodecasulfur – S_{12}

Precipitation of cyclo-dodecasulfur (S_{12}) forms needles of a pale yellowish color (Lesté-Lasserre, 2001). The unit cell of the crystal of S_{12} contains two molecules in its structure with a molecular symmetry of C1h. The unit cell parameters are a=472.5pm, b=910.4pm, and c=1453.0pm. The space group in which the S_{12} solid form crystallizes is Pnnn-D_{2h}^{12}, and belongs to the orthorhombic group. The atoms in the S_{12} molecule are positioned in three parallel layers, with 6 atoms occupying the intermediate layer, whereas the upper and lower layers hosting 3 atoms of sulfur each (Steudel and Eckert, 2003). Cyclo-dodecasulfur is considered the second most stable allotrope after cyclo-octasulfur (Lesté-Lasserre, 2001). Based on the observed pattern of molecular symmetry in smaller sulfur rings (D3d and D4d molecular symmetries in S_6 and S_8, respectively), a higher molecular symmetry would have been expected in orthorhombic S_{12}. However, X-ray diffraction analyses on S_{12} revealed D3d conformation, which was proven by quantum chemical calculations to have been energetically more stable than the assumed D6d symmetry (Raghavachari et al., 1990). The torsion angles in such a symmetry would have

been 129°, far larger from the value of 88° of the actual torsion angles in the D3d symmetry, which is much closer to the optimum 90° value (Meyer, 1976; Steudel and Eckert, 2003). The torsion angles influence the stability of a molecule, by causing larger bond lengths – and therefore weaker bonds –as torsion angles increase (Steudel and Eckert, 2003). The Infrared spectrum for S_{12} indicates the following strong bands at 465, 265, 250, and 165cm^{-1}. The Raman signature of S_{12} incorporates peaks with strong signals at 460, 449, 127, 67, 63, 43 and 31cm^{-1} (Eckert and Steudel, 2003).

Cyclo-tridecasulfur – S_{13}

Crystals of cyclo-tridecasulfur have a hexagonal plate shape and yellow color. The crystallographic system of S_{13} is monoclinic, with a space group $P2_1/c\text{-}C_{2h}^5$. The unit cell includes 8 molecules forming C1 symmetry. The parameters of the unit cell are a=1295.0pm, b=1236.0pm, c=1761.0pm, and β=110.41° at 163K. The only symmetry element this crystal has is a twofold rotation axis, which intersects the longest S-S bond of the ring. This large bond has a length of 209pm and is encapsulated by two short bonds (199pm)(Steudel and Eckert, 2003). Similarly to S_{11}, cyclo-tridecasulfur Raman peaks that originate from S-S bond stretching vibrations are located at high wavenumber bands (between 385 and 500cm^{-1}), whereas bending, torsion and lattice vibrations result into peaks with wavenumbers less than 290cm^{-1} (Eckert and Steudel, 2003).

Cyclo-tetradecasulfur – S_{14}

The crystals of cyclo-tetradecasulfur are deep yellow, while they form rod-like crystallites. This molecule crystalizes in the triclinic system, with a space group of $P\bar{1}\text{-}C_i^1$ (Steudel and Eckert, 2003). The unit cell is comprised of two ring molecules, and it shows approximate C_s symmetry (Steudel et al., 1998). Its dimensions are a=546.9pm, b=966.2pm, c=1433.1pm, α=95.97°, β=98.96°, and γ=100.43° at 173K. The only symmetry element is a mirror plane that intersects atoms S2 and S9. The average torsion angle is ~93°

which is close to the optimum value of 90^{o}, characterizing this compound stable (days before decomposition in STP)(Steudel and Eckert, 2003). The narrow range of bond lengths in cyclo-tetradecasulfur results to the consequent narrow band width (440 to 485cm^{-1}) resulting from S-S stretching Raman vibrations. Two characteristic peaks of S_{14} within that range are at 468 and 460cm^{-1}. The bending vibrations result to the peaks 234, 198, and 163cm^{-1} among others, whereas bending, torsion and lattice vibrations result to peaks such as 128, 90, 69, 61, 57, 47 and 34cm^{-1} (Eckert and Steudel, 2003).

Cyclo-pentadecasulfur – S_{15}

The solid form of cyclo-pentadecasulfur has been obtained only as a mixture with other elemental sulfur rings, and has been characterized as lemon-yellow powder or as light-yellow flakes. No single crystal growth of S_{15} has been successful. The only molecular information gained is in $S_{15(aq)}$ in aqueous solutions by Raman and UV spectroscopy. The spectroscopic studies suggested an average bond length at 207pm. Theoretical calculations suggest C2 symmetry in the S_{15} ring, with bond angles ranging from 104.1^{o} to 109.4^{o} as well as torsion angles ranging from 77.1^{o} to 112.3^{o} (Steudel and Eckert, 2003). An indication of the bond lengths being between 203 and 209pm in S_{15}, is that the S-S bond stretching vibrations in this allotrope does not exceed the 400 to 495cm^{-1} range. Theoretical calculations have confirmed the bond length range (Eckert and Steudel, 2003).

Cyclo-octadecasulfur – S_{18}

This form of sulfur is found in two allotropes, endo-S_{18} and exo-S_{18} (previously called α-S_{18} and β-S_{18}, respectively). The comparison between the two allotropes of S_{18} shows that the molecules are similar in terms of their crystal structure, whereas they differ in their molecular conformation. More specifically, two torsion angles have opposite sign in endo-S_{18} from the exact same angles in exo-S_{18}. Using the Greek suffix endo- (ένδο- meaning inner) and exo- (έξω- meaning outer), the descriptions describe the torsion angles tilting the sulfur atoms more "inner" (closer to) or "outer" (away from) the center of the molecule, forming the endo- and exo-conformation, respectively. The rest of the molecule in both conformations is shown to have its atoms located in two planes that are almost parallel (Steudel and Eckert, 2003).

Endo-S_{18} crystallizes in the orthorhombic group and its space group is $P2_12_12_1$-D_2^4. A C_{2h} symmetry is achieved, with symmetrical elements including a two-fold rotation axis and a mirror plane, perpendicular to each other. The unit cell includes four molecules, while its dimensions are a=2115.2pm, b=1144.1pm, and c=758.1pm (Steudel and Eckert, 2003). The color of its crystals are intense lemon-yellow and their shape is that of rhombic plates (Steudel and Eckert, 2003).

Exo-S_{18} crystallizes in the monoclinic group with space group $P2_1/n$-C_{2h}^2. The symmetry of this conformer is Ci, with the only symmetry element as an inversion center. The unit cell includes two molecules of S_{18}, while its dimensions are a=1075.0pm, b=725.0pm, c=1225.0pm, and β=92.3^o (Steudel and Eckert, 2003).

Endo-S_{18} shows 4 Raman bands in the 400-500cm^{-1} range, corresponding to stretching vibrations. Endo-S_{18} does not have any vibrational bands between 300 and 400cm^{-1}, whereas it shows more bands less than 300cm^{-1} corresponding to bending and torsion vibrations (Eckert and Steudel, 2003).

Cyclo-eicosasulfur – S_{20}

Cyclo-eicosasulfur shows pale-yellow rods in its solid form (Lesté-Lasserre, 2001). It crystallizes in the orthorhombic system, with a space group Pbcn (D_{2h}^{14}). The unit cell includes four molecules, while its dimensions are a=1858.0pm, b=1318.1pm, and c=860pm (Meyer, 1976; Steudel and Eckert, 2003). The molecular symmetry of S_{20} is D_2. The elements of symmetry include two two-fold (in-plane) rotational axes that are perpendicular to a C_2 axis. Sulfur atoms in S_{20} are located in two (nearly) parallel planes with the distance between them being very small. This makes S_{20} an almost flat ring molecule. One bond with large length at 210pm is responsible for the low thermal stability of the molecule, which decomposes in solution in STP (Steudel and Eckert, 2003). S_{20} shows 8 Raman bands in the 400-500cm^{-1} range, corresponding to stretching vibrations of the S-S bonds. It does not exhibit any bands in the range between 300 and 400cm^{-1}, as opposing to the band range less than 300cm^{-1} where characteristic peaks of bending and torsion vibrations are found (Eckert and Steudel, 2003).

Crystalline polymeric sulfur allotropes

Three forms of polymeric sulfur exist in STP, including fibrous (S_ψ or ψ-sulfur), second fibrous sulfur ($S_{\omega 1}$ or ω_1-sulfur) and laminal sulfur ($S_{\omega 2}$ or ω_2-sulfur). Also, there is microcrystalline sulfur (S_μ or μ-sulfur) which is characterized by insolubility to organic solvents (even to CS_2). All polymeric sulfur allotropes consist of helix (or coil) conformation and incorporate 10^4-10^6 atoms of sulfur in their (macro)molecules (Steudel and Eckert, 2003).

Fibrous sulfur – Sψ

The stretching of liquid sulfur results in the formation of fibrous S_ψ. The material evolves after days to a mixture of S_ψ with a fraction of cyclo-octasulfur as well as traces of cyclo-heptasulfur. Fibrous sulfur is characterized as a chain molecule that incorporates ten atoms in the "unit cell", with length of 1370pm. Within this length the chain forms three turns, following a helical conformation. Bond length is 206.6pm whereas the torsion angle is 85.3°. The bond length is similar to the cyclo-octasulfur and cyclo-dodecasulfur which are characterized as most stable within the group of ring allotropes. Fibrous sulfur (S_ψ) forms crystals in the monoclinic crystal group. The unit cell consists of 8 parallel helical chains of 10 sulfur atoms each, with both right-handed and left-handed rotation. The space group is P2=C_2^1. The unit cell shows dimensions a=1760pm, b=925pm, c=1380pm, and β=113° (Steudel and Eckert, 2003). Fibrous sulfur (S_ψ) Raman investigations show two peaks at 453 and 418cm^{-1} due to stretching vibrations, as well as a peak at 273cm^{-1} due to bending vibrations (Eckert and Steudel, 2003).

Second fibrous sulfur ($S_{\omega 1}$) and laminar sulfur ($S_{\omega 2}$)

Crystals of the second fibrous sulfur are formed in the orthorhombic crystal system, with space group Pccn-D_{2h}^{10}. The unit cell incorporates four helical chains of ten sulfur atoms each, with the chains being parallel between them and to the C axis. However, alternating helical chains show opposite turns. The dimensions of the unit cell are a=902.0pm, b=833.0pm, and c=458.0pm. The similarity of the unit cell of the $S_{\omega 1}$ with the fibrous sulfur (S_ψ), gave it its name of second fibrous sulfur (Steudel and Eckert, 2003). Second fibrous sulfur ($S_{\omega 1}$) Raman spectroscopy shows a strong peak at 458cm^{-1} and a weak peak at 430cm^{-1} due to stretching vibrations, whereas a very weak bending vibration exists at 268cm^{-1} (Eckert and Steudel, 2003).

This allotrope crystallizes in the tetragonal crystal system. Its crystal space group is $I\bar{4}$-S_4^2. The unit cell dimensions are a=b=458pm, and c=1632pm. The structure of its unit cell is

such that the helical chains being perpendicular to the C axis. Furthermore, from the four molecules comprising each unit cell, one of them is perpendicular to the other three. The opposite turns of the helical chains between parallel layers assists to the achieving of the closest packing for $S_{\omega 2}$. The structure of this molecule is named “cross-grained plywood” structure (Steudel and Eckert, 2003). Laminal sulfur ($S_{\omega 2}$) Raman analyses indicate strong peak at 458cm^{-1} and a weak peak at 424cm^{-1} due to stretching vibrations, as well as two weak peaks at 280 and 268cm^{-1}, originating from bending vibrations (Eckert and Steudel, 2003).

Table A-1: Mineralogy, crystallography and vibrational data for solid sulfur allotropes.

Sulfur atoms	Chemical formula	Crystal system	Unit cell dimentions	Symmetry	Raman bands	Infrared bands
6	S_6	rhombohedral	a=b=1081.8pm, and c=428.0pm	C3i	471, 448, 262, 202, 106 and 79cm^{-1}	
7	α-S_7	n/a	n/a	n/a	514 and 355cm^{-1}	513, 400, 480, 270 and 235cm^{-1}
	β-S_7	n/a	n/a	n/a	182 and 47cm^{-1}	n/a
	γ-S_7	monoclinic	a=968.0pm, b=764.1pm, c=940.9pm, and β=102.08º	C1	292, 71 and 62cm^{-1}	n/a
	δ-S_7	monoclinic	a= 1510.5pm, b= 599.8pm, c=1509.6pm, and β=92.15º	C1	201cm^{-1}	n/a

Table A-1: Continued

Sulfur atoms	Chemical formula	Crystal system	Unit cell dimentions	Symmetry	Raman bands	Infrared bands
8	α-S_8	orthorhombic	a=1046.4pm, b=1286.6pm, and c=2448.6pm	C2	476 and 218.5cm^{-1}	471 and 243cm^{-1}
	β-S_8	monoclinic	a=1092.6pm, b=1085.2pm, c=1079.0pm, and β=95.9°	n/a	82. 42 and 34cm^{-1}	n/a
	γ-S_8	monoclinic	a=845.5pm, b=1305.2pm, c=926.7pm, and β=124.9°	n/a	n/a	n/a
9	α-S_9	monoclinic	a=790.2pm, b=1390.8pm, c=1694.8pm, and β=103.2°	C1	436, 454 and 188cm^{-1}	n/a
	β-S_9	n/a	n/a	n/a	437, 454, 460 and 181cm^{-1}	n/a
10	S_{10}	monoclinic	a=1253.3pm, b=1027.5pm, and c=1277.6pm	C2	487, 469, 243, 179, 131 and 100cm^{-1}	239, 220, and 204cm^{-1}

Table A-1: Continued

Sulfur Atoms	Chemical Formula	Crystal System	Unit Cell Dimentions	Symmetry	Raman Bands	Infrared Bands
11	S_{11}	orthorhombic	a=1493.3pm, b=832.1pm, and c=1808.6pm	C2	n/a	n/a
12	S_{12}	orthorhombic	a=472.5pm, b=910.4pm, and c=1453.0pm	n/a	460, 449, 127, 67, 63, 43 and 31cm^{-1}	465, 265, 250, and 165cm^{-1}
13	S_{13}	monoclinic	a=1295.0pm, b=1236.0pm, c=1761.0pm, and β=110.41°	C1	n/a	n/a
14	S_{14}	triclinic	a=546.9pm, b=966.2pm, c=1433.1pm, α=95.97°, β=98.96°, and γ=100.43°	C_s	468, 460, 234, 198, and 163cm^{-1}	n/a
15	S_{15}	n/a	n/a	n/a	n/a	n/a
16	$S_6.S_{10}$	n/a	a=1954.1pm, b=943.1pm, c=883.1pm, and β=105.1°	n/a	combination of S_{10} and S_6	n/a

Table A-1: Continued

Sulfur atoms	Chemical formula	Crystal system	Unit cell dimentions	Symmetry	Raman bands	Infrared bands
18	endo-S_{18}	orthorhombic	a=2115.2pm, b=1144.1pm, and c=758.1pm	C_{2h}	n/a	n/a
	exo-S_{18}	monoclinic	a=1075.0pm, b=725.0pm, c=1225.0pm, and β=92.3°	Ci	n/a	n/a
20	S_{20}	orthorhombic	a=1858.0pm, b=1318.1pm, and c=860pm	n/a	n/a	n/a
∞	Fibrous sulfur (S_{ψ})	monoclinic	a=1760pm, b=925pm, c=1380pm, and β=113°	n/a	453, 418 and 273cm^{-1}	n/a
∞	Second fibrous sulfur ($S_{\omega 1}$)	orthorhombic	a=902.0pm, b=833.0pm, and c=458.0pm	n/a	458 and 430cm^{-1}	n/a
∞	Laminar sulfur ($S_{\omega 2}$)	tetragonal	a=b=458pm, and c=1632pm	n/a	458, 424cm^{-1}	n/a

References

Eckert, B. and Steudel, R. (2003) Molecular spectra of sulfur molecules and solid sulfur allotropes, Elemental Sulfur und Sulfur-Rich Compounds II. Springer, pp. 31-98.

Lesté-Lasserre, P. (2001) Sulfur Allotrope Chemistry, Department of Chemistry. McGill University, Montreal, Quebec, CA.

Lesté-Lasserre, P. and Harpp, D.N. (1999) Sulfur allotrope chemistry—S10 an effective two-sulfur transfer reagent. Tetrahedron Letters 40, 7961-7964.

Meyer, B. (1964) Solid allotropes of sulfur. Chemical Reviews 64, 429-451.

Meyer, B. (1976) Elemental sulfur. Chemical Reviews 76, 367-388.

Raghavachari, K., Rohlfing, C.M. and Binkley, J.S. (1990) Structures and stabilities of sulfur clusters. The Journal of Chemical Physics 93, 5862-5874.

Steudel, R. and Eckert, B. (2003) Solid sulfur allotropes, Elemental sulfur and sulfur-rich compounds I. Springer, pp. 1-80.

Steudel, R., Schumann, O., Buschmann, J. and Luger, P. (1998) A New Allotrope of Elemental Sulfur: Convenient Preparation of cyclo-S14 from S8. Angewandte Chemie International Edition 37, 2377-2378.

APPENDIX-B – KINETICS PROJECT

Raw data from the kinetics study on the consumption of $S_{8weimarn}$ by sulfide

Table B-1: Raw data from the kinetics study of the nucleophilic dissolution of $S_{8weimarn}$ by sulfide.

DIAMETER (NM)	PH	SULFIDE (M)	I (M)	SSA (DM-1)	-MOLAR(S_8)/SEC	-MOLAR(S8)/SEC/DM^{-1}	2SIGMA	T (^oC)
Surface area effect								
244.7	7.4	0.0030	0.0803	2451559.7	2.10E-07	8.58E-14	5.31E-08	25
259.1	7.4	0.0030	0.0803	2315643.9	2.40E-07	1.04E-13	8.25E-08	25
278.3	7.4	0.0030	0.0803	2156252.1	2.48E-07	1.15E-13	4.01E-08	25
311.1	7.4	0.0030	0.0803	1928671.3	2.26E-07	1.17E-13	4.86E-08	25
353.5	7.4	0.0030	0.0803	1697283.3	2.18E-07	1.28E-13	1.43E-08	25
447.9	7.4	0.0030	0.0803	1339569.8	1.82E-07	1.36E-13	2.04E-08	25
468.4	7.4	0.0030	0.0803	1280884.0	1.80E-07	1.41E-13	1.96E-08	25
525.9	7.4	0.0030	0.0803	1140930.2	1.70E-07	1.49E-13	7.54E-08	25
653.1	7.4	0.0030	0.0803	918667.3	1.35E-07	1.47E-13	4.55E-08	25
Sulfide effect								
375.4	11.8	0.0028	0.0803	1598313.5	1.30E-07	8.13E-14	6.40E-08	25
382.2	11.8	0.0040	0.0803	1569710.0	1.69E-07	1.08E-13	1.45E-08	25
378.1	11.9	0.0070	0.0803	1586747.9	1.93E-07	1.21E-13	8.04E-08	25
387.7	11.9	0.0100	0.0803	1547554.0	2.56E-07	1.65E-13	3.45E-08	25
365.8	12.1	0.0200	0.0803	1640155.4	2.93E-07	1.79E-13	7.59E-09	25
354.9	12.3	0.0300	0.0803	1690740.0	3.49E-07	2.07E-13	6.29E-08	25
382.2	12.6	0.0400	0.0803	1569710.0	3.50E-07	2.23E-13	1.35E-07	25

Table B-1: Continued

Diameter (nm)	pH	Sulfide (M)	I (M)	SSA (dm-1)	-Molar(S_8)/sec	-Molar(S8)/sec/dm^{-1}	2sigma	T (oC)
pH effect								
644.5	8.0	0.0017	0.1000	930954.2	2.44E-07	2.62E-13	1.05E-07	25
517.8	10.0	0.0017	0.0980	1158748.6	3.72E-07	3.21E-13	2.60E-08	25
667.4	7.1	0.0017	0.1390	899011.1	1.67E-07	1.86E-13	4.04E-08	25
616.4	7.1	0.0017	0.1390	973393.9	1.53E-07	1.57E-13	4.31E-08	25
Ionic strength effect								
301.1	10.4	0.0100	0.5928	1992693.5	4.98E-07	2.50E-13	6.42E-09	25
296.4	10.4	0.0100	0.1048	2024291.5	5.59E-07	2.76E-13	1.63E-07	25
281.1	10.4	0.0100	0.1948	2134471.7	5.94E-07	2.78E-13	9.49E-08	25
293.5	10.4	0.0100	0.1408	2044293.0	6.68E-07	3.27E-13	9.34E-08	25
287.1	10.4	0.0100	0.5688	2089864.2	6.43E-07	3.08E-13	3.67E-08	25
346.7	10.4	0.0100	0.5918	1730774.6	1.52E-07	8.76E-14	9.32E-08	25
333.7	10.4	0.0100	0.1688	1798191.1	3.97E-07	2.21E-13	5.74E-08	25
310.0	10.4	0.0100	0.5688	1935483.9	2.45E-08	1.26E-14	1.98E-08	25
352.1	10.4	0.0100	0.0688	1703877.5	1.40E-07	8.21E-14	1.78E-08	25
280.7	10.4	0.0100	0.0588	2137513.4	6.62E-07	3.10E-13	3.86E-08	25
297.0	10.4	0.0100	0.0588	2020202.0	7.54E-07	3.73E-13	5.49E-08	25
358.3	10.4	0.0100	0.0588	1674600.3	8.50E-08	5.08E-14	2.17E-08	25
338.5	10.4	0.0100	0.0588	1772751.0	3.07E-07	1.73E-13	2.07E-08	25

Table B-1: Continued

Diameter (nm)	pH	Sulfide (M)	I (M)	SSA (dm-1)	-Molar(S_8)/sec	-Molar(S8)/sec/dm^{-1}	2sigma	T (oC)
$S_{8weimarn}$ T effect								
387.7	11.9	0.0100	0.0803	1547554.0	2.61E-07	1.69E-13	4.53E-08	27
422.2	11.9	0.0100	0.0803	1421127.4	5.57E-07	3.92E-13	2.46E-07	40
506.5	11.9	0.0100	0.0803	1184600.2	9.53E-07	8.05E-13	2.62E-07	40
440.0	11.9	0.0100	0.0803	1363636.4	5.26E-07	3.86E-13	2.51E-08	30
431.4	11.9	0.0100	0.0803	1390820.6	1.62E-06	1.17E-12	6.93E-08	55
340.1	11.9	0.0100	0.0803	1764187.0	2.15E-06	1.22E-12	2.83E-07	65
$S_{8weimarn-SDS}$ T effect								
289.6	7.4	0.0030	0.1211	2071823.2	2.62E-07	1.26E-13	6.97E-08	25
304.2	7.4	0.0030	0.1211	1972386.6	5.19E-07	2.63E-13	1.25E-07	35
247.9	7.4	0.0030	0.1211	2420330.8	1.64E-07	6.78E-14	3.29E-07	7.5
241.8	7.4	0.0030	0.1211	2481389.6	3.17E-07	1.28E-13	2.93E-08	30
$S_{8weimarn-SDS}$ H_2S effect								
433.0	11.9	0.0100	0.1211	1385681.3	9.88E-07	7.13E-13	1.71E-07	25
400.9	11.8	0.0050	0.1211	1496632.6	5.57E-07	3.72E-13	9.51E-08	25
374.4	12.1	0.0200	0.1211	1602564.1	9.54E-07	5.96E-13	9.52E-08	25

Table B-2: Processed raw data used for the calculation of the kinetic rate law of $S_{8weimarn}$ consumption via multiple linear regression. NOTE: the $S_{8weimarn}$ rates used for the calculations of the kinetic rate law are all SSA-normalized.

pH	LOG(H2S)	LOG(I)	LOG(rate)	Reciprocal of T
7.408	-2.529	-1.095	-13.066	0.040
7.408	-2.529	-1.095	-12.984	0.040
7.408	-2.529	-1.095	-12.939	0.040
7.408	-2.529	-1.095	-12.932	0.040
7.408	-2.529	-1.095	-12.892	0.040
7.408	-2.529	-1.095	-12.866	0.040
7.408	-2.529	-1.095	-12.852	0.040
7.408	-2.529	-1.095	-12.827	0.040
7.408	-2.529	-1.095	-12.834	0.040
11.794	-2.558	-1.095	-13.090	0.040
11.819	-2.398	-1.095	-12.968	0.040
11.880	-2.155	-1.095	-12.916	0.040
11.941	-2.000	-1.095	-12.782	0.040
12.145	-1.699	-1.095	-12.748	0.040
12.349	-1.523	-1.095	-12.685	0.040
12.553	-1.398	-1.095	-12.652	0.040
8.000	-2.771	-1.000	-12.582	0.040
10.000	-2.771	-1.009	-12.494	0.040
7.110	-2.771	-0.857	-12.731	0.040
7.110	-2.771	-0.857	-12.804	0.040
10.447	-2.000	-0.227	-12.602	0.040
10.447	-2.000	-0.980	-12.559	0.040
10.447	-2.000	-0.710	-12.555	0.040
10.447	-2.000	-0.851	-12.486	0.040
10.447	-2.000	-0.245	-12.512	0.040
10.447	-2.000	-0.228	-13.057	0.040

Table B-2: Continued

PH	LOG(H2S)	LOG(I)	LOG(RATE)	RECIPROCAL OF T
10.447	-2.000	-0.773	-12.656	0.040
10.447	-2.000	-0.245	-13.898	0.040
10.447	-2.000	-1.162	-13.086	0.040
10.447	-2.000	-1.231	-12.509	0.040
10.447	-2.000	-1.231	-12.428	0.040
10.447	-2.000	-1.231	-13.294	0.040
10.447	-2.000	-1.231	-12.762	0.040
11.941	-2.000	-1.095	-12.772	0.037
11.941	-2.000	-1.095	-12.406	0.025
11.941	-2.000	-1.095	-12.094	0.025
11.941	-2.000	-1.095	-12.413	0.033
11.941	-2.000	-1.095	-11.933	0.018
11.941	-2.000	-1.095	-11.914	0.015

Raw data from the kinetics study on the consumption of S_{8raffo} by sulfide

Table B-3: Raw data from the kinetics study of the nucleophilic dissolution of S_{8raffo} by sulfide.

DIAMETER (NM)	PH	SULFIDE (M)	I (M)	SSA (DM-1)	-MICROMOLAR(S0)/SEC	-MOLAR(S8)/SEC	2SIGMA	T (OC)
Surface Area effect								
1392.9	8.5	0.0050	0.0401	430756.0	1.43E+02	1.79E-05	9.23E-06	25
1254.0	8.5	0.0050	0.0401	478468.9	1.87E+02	2.34E-05	6.74E-06	25
952.2	8.5	0.0050	0.0401	630119.7	3.94E+02	4.92E-05	3.57E-06	25
1513.9	8.5	0.0050	0.0401	396327.4	1.63E+02	2.03E-05	7.26E-06	25
1036.3	8.5	0.0050	0.0401	578982.9	1.47E+02	1.84E-05	6.53E-06	25
943.1	8.5	0.0050	0.0401	636199.8	3.66E+02	4.58E-05	1.18E-05	25
316.7	8.5	0.0050	0.0401	1894537.4	1.01E+02	1.27E-05	4.20E-06	25
431.1	8.5	0.0050	0.0401	1391788.4	5.62E+01	7.03E-06	4.66E-06	25
379.5	8.5	0.0050	0.0401	1581027.7	6.56E+01	8.19E-06	1.08E-06	25
410.8	8.5	0.0050	0.0401	1460564.8	4.05E+01	5.07E-06	8.07E-07	25
513.0	8.5	0.0050	0.0401	1169590.6	1.53E+01	1.91E-06	3.36E-07	25
411.7	8.5	0.0050	0.0401	1457371.9	1.19E+02	1.49E-05	1.79E-06	25
523.1	8.5	0.0050	0.0401	1146986.3	5.23E+01	6.54E-06	9.08E-07	25
583.8	8.5	0.0050	0.0401	1027749.2	5.83E+01	7.29E-06	3.25E-07	25
630.2	8.5	0.0050	0.0401	952078.7	3.29E+01	4.12E-06	1.40E-06	25
624.3	8.5	0.0050	0.0401	961076.4	2.15E+01	2.68E-06	7.76E-07	25
672.0	8.5	0.0050	0.0401	892857.1	1.42E+01	1.77E-06	9.65E-07	25
686.6	8.5	0.0050	0.0401	873871.2	6.74E+00	8.43E-07	1.00E-06	25
714.1	8.5	0.0050	0.0401	840218.5	6.38E+00	7.97E-07	6.51E-07	25

Table B-3: Continued

Diameter (nm)	pH	Sulfide (M)	I (M)	SSA (dm-1)	-microMolar(S0)/sec	-Molar(S8)/sec	2sigma	T (oC)
Surface Area effect (continued)								
1657.5	8.5	0.0050	0.0401	361991.0	7.87E+01	9.84E-06	9.33E-06	25
1009.6	8.5	0.0050	0.0401	594294.8	1.03E+02	1.29E-05	3.55E-06	25
429.4	8.5	0.0050	0.0401	1397298.6	2.42E+02	3.03E-05	9.76E-06	25
430.2	8.5	0.0050	0.0401	1394700.1	2.30E+02	2.87E-05	4.92E-06	25
442.9	8.5	0.0050	0.0401	1354707.6	1.91E+02	2.39E-05	4.15E-06	25
Sulfide effect								
732.9	13.0	0.0540	0.0294	818665.6	7.31E+01	9.14E-06	1.06E-06	25
802.1	12.6	0.0472	0.0294	748036.4	3.83E+01	4.79E-06	1.91E-06	25
847.4	12.2	0.0405	0.0294	708048.1	1.09E+02	1.37E-05	2.00E-06	25
796.3	11.4	0.0270	0.0294	753484.9	1.61E+02	2.01E-05	1.18E-06	25
720.0	11.0	0.0202	0.0294	833333.3	1.68E+02	2.10E-05	1.12E-05	25

Table B-3: Continued

Diameter (nm)	pH	Sulfide (M)	I (M)	SSA (dm-1)	-microMolar(S0)/sec	-Molar(S8)/sec	2sigma	T (oC)
Sulfide effect (continued)								
900.0	10.6	0.0135	0.0294	666666.7	1.20E+02	1.50E-05	2.21E-06	25
pH effect								
800.0	9.3	0.0017	0.0500	750000.0	1.10E+02	1.38E-05	1.58E-06	25
917.3	7.7	0.0017	0.0700	654093.5	5.18E+01	6.47E-06	3.92E-07	25
729.8	10.0	0.0017	0.0500	822143.1	1.17E+02	1.46E-05	6.00E-07	25
726.1	8.0	0.0017	0.0500	826332.5	5.87E+01	7.33E-06	8.30E-07	25
Ionic strength effect								
1571.9	11.0	0.0202	0.2690	381703.7	4.58E+01	5.73E-06	2.21E-06	25
1510.0	11.0	0.0202	0.1231	397351.0	7.67E+01	9.59E-06	6.56E-07	25

Table B-3: Continued

Diameter (nm)	pH	Sulfide (M)	I (M)	SSA (dm-1)	-MicroMolar(S0)/sec	-Molar(S8)/sec	2sigma	T (oC)
Ionic strength effect (continued)								
1446.0	11.0	0.0202	0.0765	414937.8	9.50E+01	1.19E-05	3.61E-06	25
1511.0	11.0	0.0202	0.0542	397088.0	9.91E+01	1.24E-05	2.00E-06	25
1500.0	11.0	0.0202	0.0294	400000.0	1.52E+02	1.90E-05	5.10E-06	25
T effect								
1063.6	8.5	0.0050	0.0401	564121.9	3.34E+02	4.17E-05	1.05E-05	45
908.1	8.5	0.0050	0.0401	660720.2	2.65E+02	3.31E-05	1.30E-05	35
990.0	8.5	0.0050	0.0401	606060.6	2.04E+02	2.56E-05	6.76E-06	35
1009.6	8.5	0.0050	0.0401	594294.8	1.03E+02	1.29E-05	3.55E-06	25
1001.0	8.5	0.0050	0.0401	599400.6	5.28E+02	6.60E-05	6.91E-06	55

Table B-4: Processed raw data used for the calculation of the kinetic rate law of S_{8raffo} consumption via multiple linear regression. NOTE: The SSA column and the data from the SSA experiment were NOT utilized. The S_{8raffo} rate used was NOT surface area normalized.

ph	LOG(h2s)	LOG(i)	LOG(rate)	Reciprocal of T
12.951	-1.268	-1.532	-5.039	0.040
12.566	-1.326	-1.532	-5.320	0.040
12.183	-1.393	-1.532	-4.864	0.040
11.415	-1.569	-1.532	-4.697	0.040
11.030	-1.694	-1.532	-4.677	0.040
10.646	-1.870	-1.532	-4.823	0.040
9.300	-2.771	-1.301	-4.861	0.040
7.740	-2.771	-1.155	-5.189	0.040
10.000	-2.771	-1.301	-4.837	0.040
8.000	-2.771	-1.301	-5.135	0.040
11.030	-1.694	-0.570	-5.242	0.040
11.030	-1.694	-0.910	-5.018	0.040
11.030	-1.694	-1.117	-4.925	0.040
11.030	-1.694	-1.266	-4.907	0.040
11.030	-1.694	-1.532	-4.721	0.040
8.548	-2.301	-1.396	-4.380	0.022
8.548	-2.301	-1.396	-4.480	0.029
8.548	-2.301	-1.396	-4.593	0.029
8.548	-2.301	-1.396	-4.889	0.040
8.548	-2.301	-1.396	-4.181	0.018

Estimation of activation energy for $S_{8weimarn}$

ln(slope) = - Ea/R

-2246.3 * 2.303 = - Ea / (8.314 Joules/mol*K)

Ea = 43010.22507 Joules/mol

Ea= 10.27970185 kcal/mol

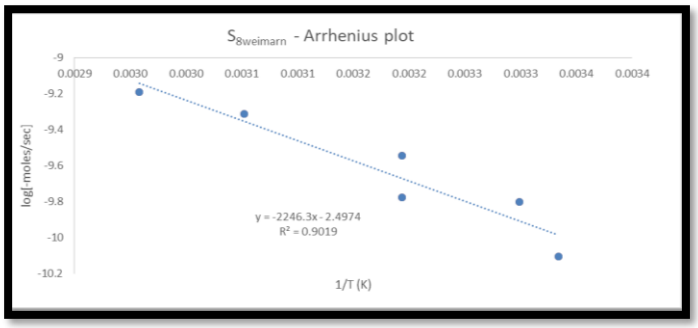

Figure B-1: Arrhenius plot for the nucleophilic dissolution of $S_{8weimarn}$ by sulfide.

Estimation of activation energy for $S_{8weimarn\text{-}SDS}$

ln(slope) = - Ea/R

-1401.2 *2.303 = - Ea / (8.314 Joules/mol*K)

Ea= 26828.97537 Joules/mol

Ea= 6.412286087 kcal/mol

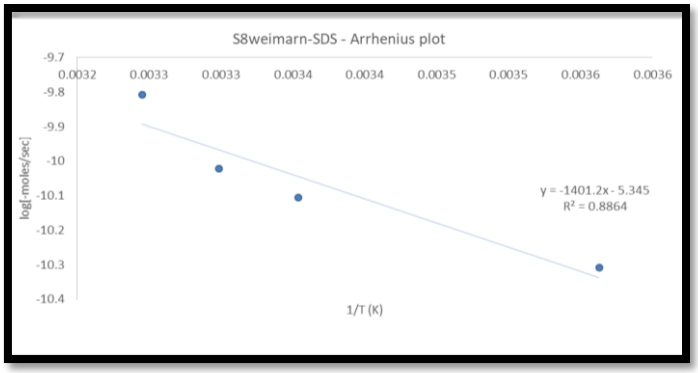

Figure B-2: Arrhenius plot for the nucleophilic dissolution of $S_{8weimarn\text{-}SDS}$ by sulfide.

Estimation of activation energy for S_{8raffo}

ln(slope) = - Ea/R

-2193.7 * 2.303 = - Ea / (8.314 Joules/mol*K)

Ea= 42003.08541 Joules/mol

Ea= 10.03898943 kcal/mol

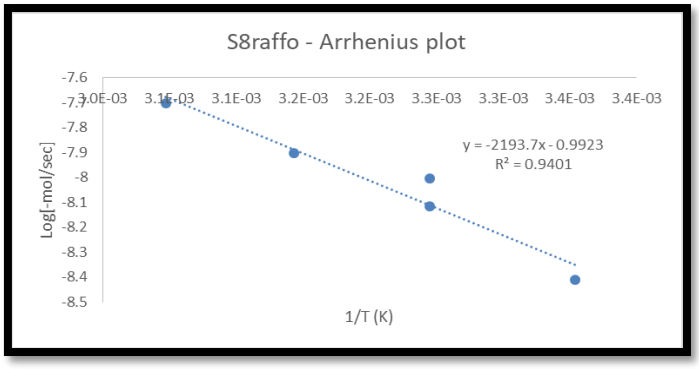

Figure B-3: Arrhenius plot for the nucleophilic dissolution of S_{8raffo} by sulfide.

Effect of ionic strength on the S_{8raffo} consumption rates

Table B-5: Data of S_{8raffo} consumption rate corresponding to specific values of square root of ionic strength.

minus-Rate [-Molar(S_8)/sec]	Square Root of Ionic strength
5.73E-06	0.519
9.59E-06	0.351
1.19E-05	0.277
1.24E-05	0.233
1.90E-05	0.171

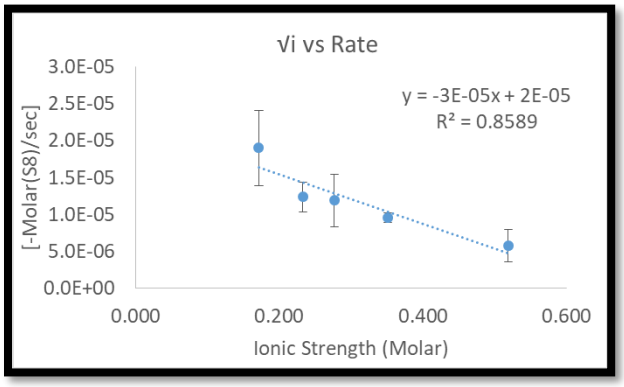

Figure B-4: Plot of square root of ionic strength versus rate of consumption of S_{8raffo}.

R code for multiple linear regression

Below is the code used in R software for the multiple linear regression modeling (calculation of kinetic rate laws).

```
library(foreign)

dat=read.table("C:/Weimarn.txt", header=TRUE)

summary(dat$ph)

summary(dat$h2s)

summary(dat$i)

summary(dat$nrate)

summary(dat$ret)

mod<-lm(nrate~ph+h2s+i+ret,data=dat)

summary(mod)
```

APPENDIX-C – YELLOWSTONE PROJECT

This appendix presents information regarding the physical and chemical characteristics of the geothermal features of Yellowstone National Park that were studied on September 2012.

Physical-chemical properties of the geothermal springs studied

Table C-1: Basic physical-chemical characteristics of the geothermal springs studied.

NAME	pH	T (°C)	T (°C) (Flow Cell)	Cl (mg/L)	SO_4 (mg/L)
WEST NYMPH CREEK THERMAL AREA					
Yellow Cinder Pool	2.42	80.3	64.5	0.60	551.00
NORRIS GEYSER BASIN					
Cinder Pool	4.08	---	72.8	593.66	104.48
Cistern Spring	4.66	---	74.6	475.00	89.50
GIBBON GEYSER BASIN - SYLVAN SPRING AREA					
Evening Primrose Spring	5.61	79.0	70.4	487.85	139.76
LOWER GEYSER BASIN					
Azure Spring - source	---	---	---	292.97	48.45
Ojo Caliente - source	7.55	---	92.6	279.47	20.21
CRATER HILLS AREA					
Sulphur Spring	3.79	88.9	73.0	763.43	544.56
Mark's Ugly Spring	1.79	68.9	79.6	8.82	2305.04
West Nymph Spring	5.74	57.8	---	---	---

Chemistry and temporal variability of the geothermal springs studied

Table C-2: Table showing the concentrations of elemental sulfur from the geothermal springs studied, as well as the calculated percentile variability of S_8 per geothermal spring. Variability was calculated as the % change between the max and the min concentrations of S_8.

SAMPLE	S_8 (µM)	2sigma	Variability (%)
EVENING PRIMROSE SPRING			
PR1'	233.45	0.18	225
PR2'	530.46	0.21	
PR3'	748.10	0.19	
PR4'	676.67	0.23	
PR5'	718.84	0.28	
PR1a (different day)	251.78	0.48	
PR2a (different day)	229.92	0.38	
OJO CALIENTE SPRING			
Ojo Caliente Pool	0.41	---	36
OC Drainage	0.55	---	
WEST NYMPH SPRING			
West Nymph 1	86.21	0.64	94
West Nymph 2	68.85	0.30	
West Nymph 4	44.47	0.24	
SULFUR SPRING			
SS1	1.87	0.05	51
SS2	2.59	0.15	
SS3	1.72	0.06	
YELLOW CINDER POOL			
YCP1	44.59	0.04	---
YCP2	---	---	

Table C-2: Continued

SAMPLE	S_8 (µM)	2sigma	Variability (%)
MARK'S UGLY SPRING			
Marks Ugly 1	560.69	0.21	44
Marks Ugly 2	806.15	0.38	
Marks Ugly 3	783.72	0.70	
CISTERN SPRING			
Cistern 1	1.29	0.06	339
Cistern 2	0.79	0.05	
Cistern 3	3.49	---	

Table C-3: Table showing the sulfoxy intermediate species concentrations from the geothermal springs studied, as well as the calculated percentile variability per species per geothermal spring. Also, the variability of the sulfide signature is also presented per spring, both for in situ and ex situ methods of acquisition. It is worth mentioning that the voltammetric variability was measured as the % change of sulfide concentration between two consecutive scans, whereas for the grab samples it was calculated as the % change between the max and the min concentrations.

SAMPLE	$S_2O_3^{2-}$(µM)	2sigma	Variability (%)	SO_3^{2-}(µM)	2sigma	Variability (%)	H_2S (Voltammetry) variability (%)	
							in situ	ex situ
EVENING PRIMROSE SPRING								
EPR #1a	356.58	1.39	5	84.14	4.88	5	303	872
EPR #1b	362.24	2.55		84.63	4.12			
EPR #1c	368.70	2.34		83.68	3.76			
EPR Flow cell a	355.61	0.65		81.31	2.54			
EPR Flow cell b	357.25	0.83		82.43	5.10			
EPR Flow cell c	349.74	1.33		80.24	6.09			
OJO CALIENTE SPRING								
OC #1	0.17	0.10	523	6.33	0.43	36	30	---
OC #2	0.31	0.30		6.28	0.77			
OC #3	0.13	0.15		7.00	0.48			
OC #4	0.42	0.25		8.33	1.16			
OC #5	0.84	0.40		8.51	1.45			
OC #6	0.47	0.25		7.40	0.97			

Table C-3: Continued

SAMPLE	$S_2O_3^{2-}$(µM)	2sigma	Variability (%)	SO_3^{2-}(µM)	2sigma	Variability (%)	H_2S (Voltammetry) variability (%)	
WEST NYMPH SPRING							IN SITU	EX SITU
West Nymph Spring	---	---	---	---	---	---	---	48
SULFUR SPRING								
Sulfur Spring a	---	0.13		13.50	1.10			
Sulfur Spring b	---	0.41	63	12.68	1.92	9	---	752
Sulfur Spring c	---	0.22		12.36	1.63			
YELLOW CINDER POOL								
Yellow Cinder Pool	---	---	---	---	---	---	71	65
MARK'S UGLY SPRING								
Marks Ugly a	2.09	0.48		20.16	0.23			
Marks Ugly b	2.58	0.61	23	14.24	0.53	42	---	875
Marks Ugly c	2.25	0.54		17.28	0.66			
CISTERN SPRING								
cistern spring a	115.98	9.10		56.39	5.79			
cistern spring b	118.19	8.74	2	52.91		8	356	97
cistern spring c	118.07	9.09		57.17	10.80			
CINDER POOL								
Cinder #1	2.48	1.05		19.60	0.20			
Cinder #3	2.20	1.02	13	21.03	0.20	11	230	23
Cinder #7	2.34	1.07		21.68	0.44			
AZURE SPRING								
Azure Spring	---	---	---	---	---	---	8	---

Electrochemical information indicating intermediate sulfur species in YNP

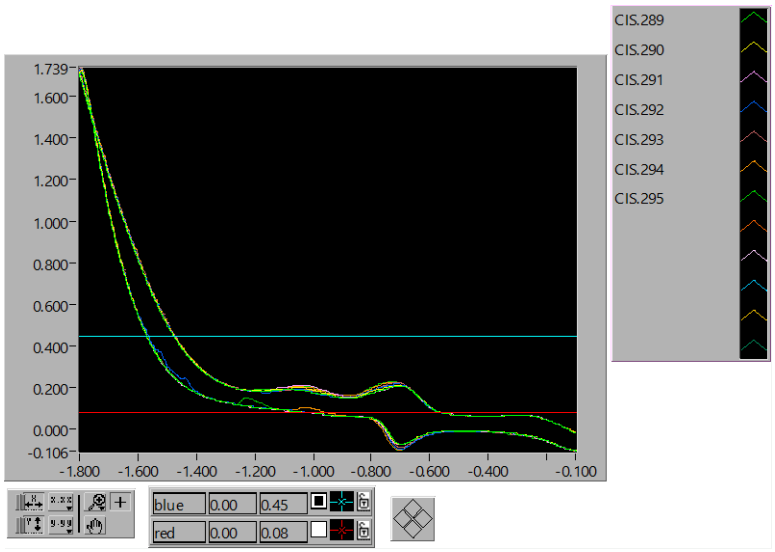

Figure C-1: Voltammograms from Cistern Spring indicating the presence of elemental sulfur (0.055µA at ~-1.1), polysulfides (-0.142µA, ~-0.65V) and thiosulfate (0.191µA at -0.15V) in addition to the sulfidic signal.

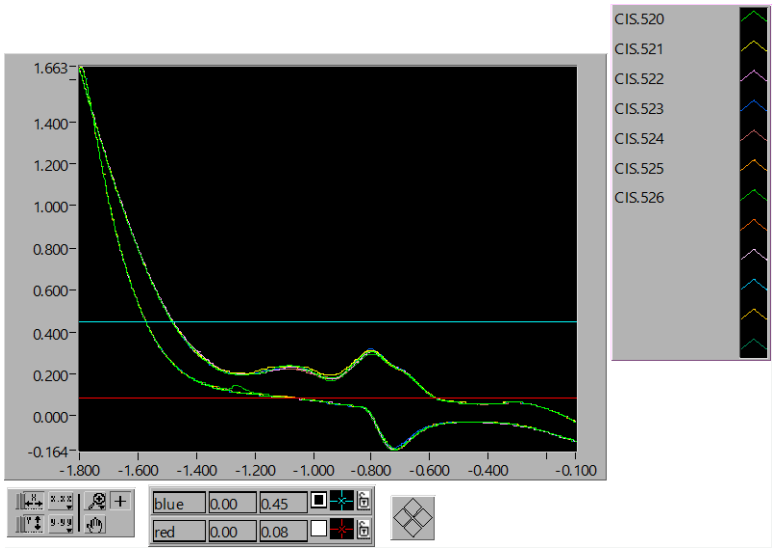

Figure C-2: Voltammograms from Cistern Spring indicating the presence of elemental sulfur, polysulfides and thiosulfate in addition to the sulfidic signal.

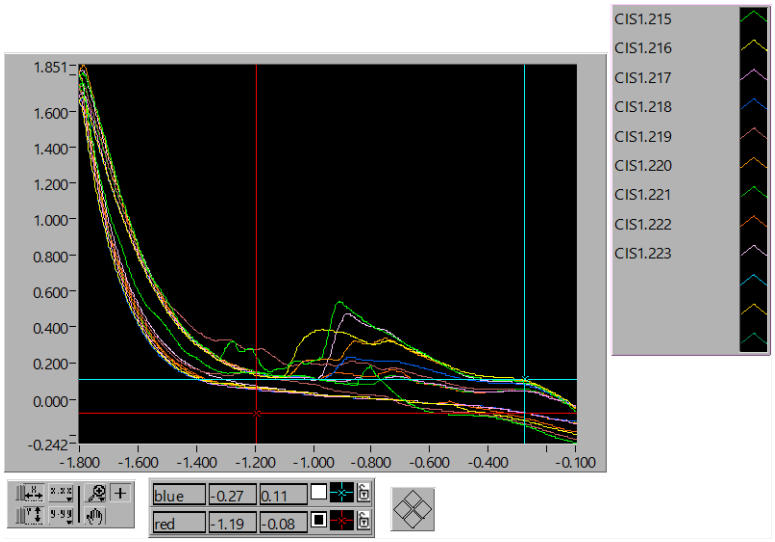

Figure C-3: Voltammograms from Cistern Spring indicating the presence of elemental sulfur, polysulfides and thiosulfate in addition to the sulfidic signal.

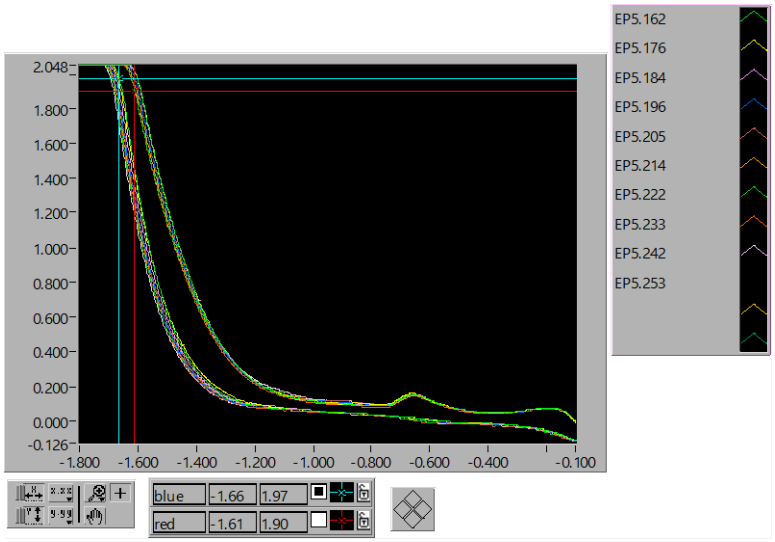

Figure C-4: Presence of thiosulfate (0.081μA at -0.15V) in the geothermal waters of Evening Primrose geothermal spring (ex situ acquisition).

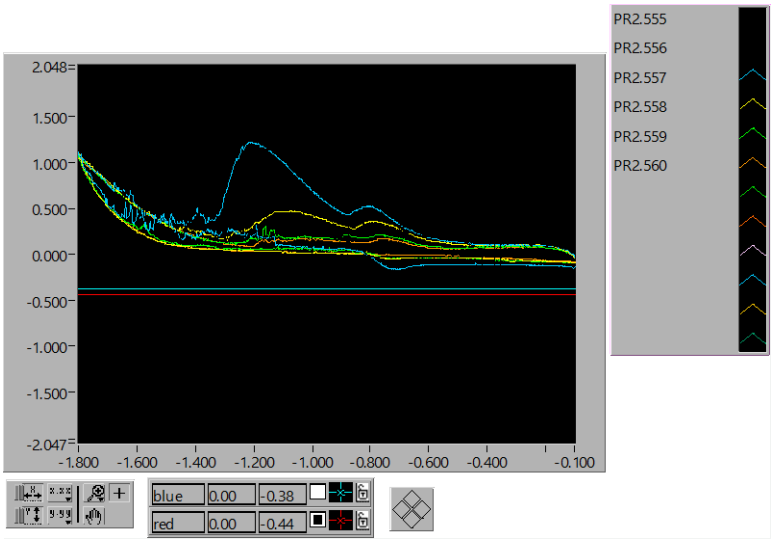
PR2.555
PR2.556
PR2.557
PR2.558
PR2.559
PR2.560
2.048
1.500
1.000
0.500
0.000
-0.500
-1.000
-1.500
-2.047
-1.800 -1.600 -1.400 -1.200 -1.000 -0.800 -0.600 -0.400 -0.100
blue 0.00 -0.38
red 0.00 -0.44

(a)

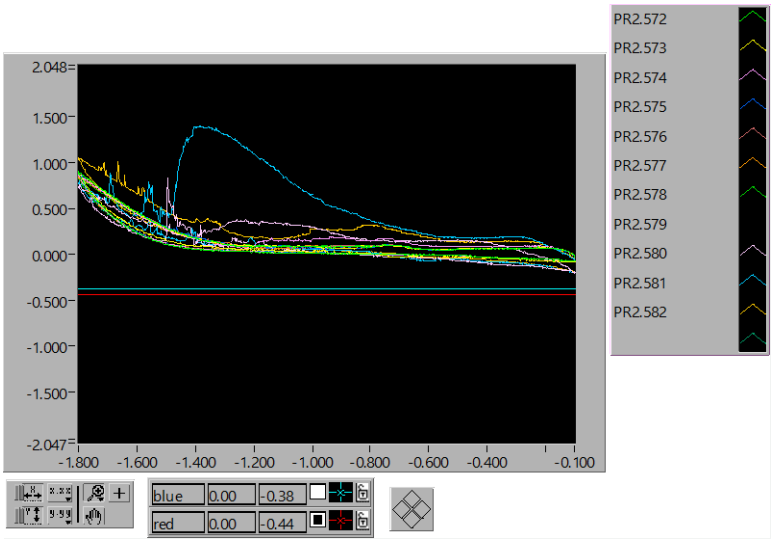
PR2.572
PR2.573
PR2.574
PR2.575
PR2.576
PR2.577
PR2.578
PR2.579
PR2.580
PR2.581
PR2.582
2.048
1.500
1.000
0.500
0.000
-0.500
-1.000
-1.500
-2.047
-1.800 -1.600 -1.400 -1.200 -1.000 -0.800 -0.600 -0.400 -0.100
blue 0.00 -0.38
red 0.00 -0.44

(b)

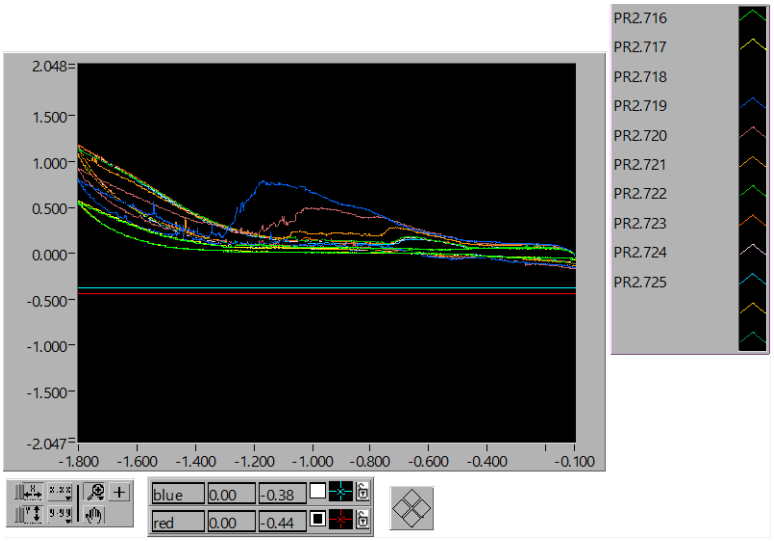
PR2.716
PR2.717
PR2.718
PR2.719
PR2.720
PR2.721
PR2.722
PR2.723
PR2.724
PR2.725
2.048
1.500
1.000
0.500
0.000
-0.500
-1.000
-1.500
-2.047
-1.800 -1.600 -1.400 -1.200 -1.000 -0.800 -0.600 -0.400 -0.100
blue 0.00 -0.38
red 0.00 -0.44

(c)

Figure C-5(a-c): The above three voltammograms show the existence of colloidal sulfur ($S_{8colloidal}$) in the geothermal waters of Evening Primrose (in situ acquisition). When $S_{8colloidal}$ interacts with the Hg-surface electrode, it forms a broad-high intensity peak which decreases in intensity and width dramatically over the consequetive scans due to the reductive decomposition of $S_{8colloidal}$ on the mercury surface.

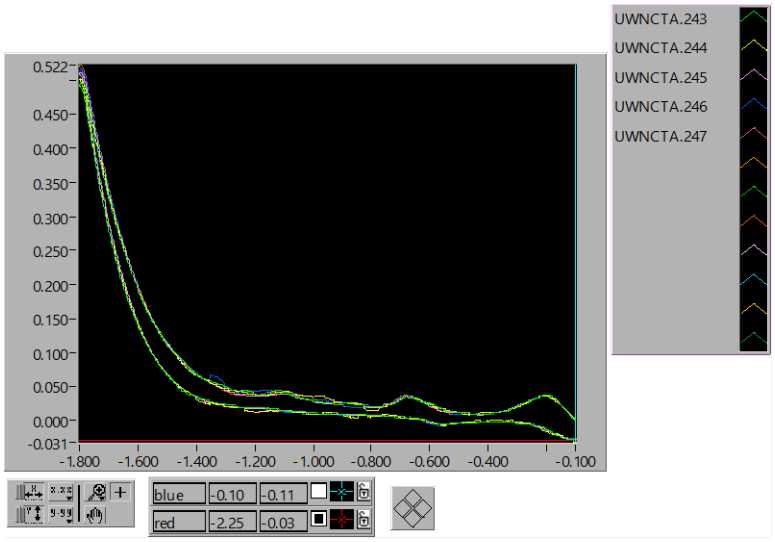

Figure C-6: Voltammogram from West Nymph geothermal spring indicating a thiosulfate (0.045µA at -0.15V) as well as an elemental sulfur (0.017µA at -1.2V) peak.

Fast Fourier Transformations on the sulfide signatures of the geothermal springs studied.

Periodicity was tested on all temporal sulfide data (both in situ and ex situ) from the geothermal springs studied. No periodicity was found to exist. The Fourier Transforms calculated using the "FFT" command in Matlab Software.

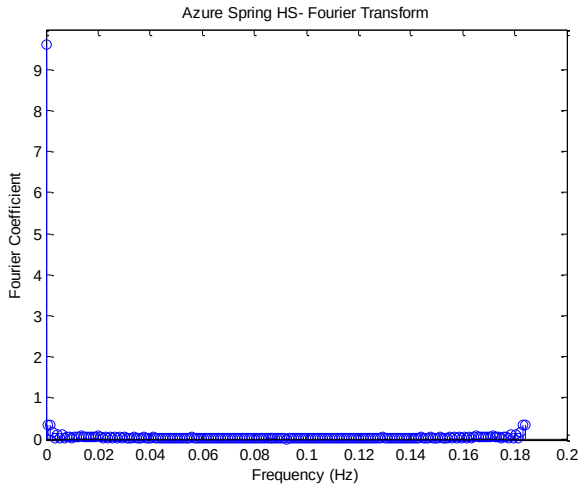

Figure C-7: FFT graph on the in situ sulfide temporal data from Azure Spring, YNP.

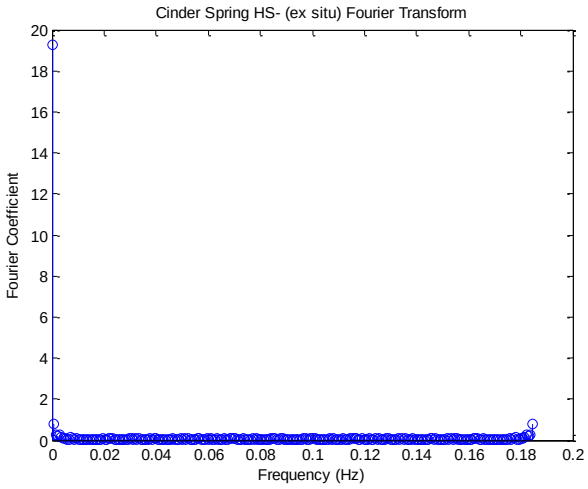

Figure C-8: FFT graph on the temporal sulfide data (ex situ) from Cinder Spring, YNP.

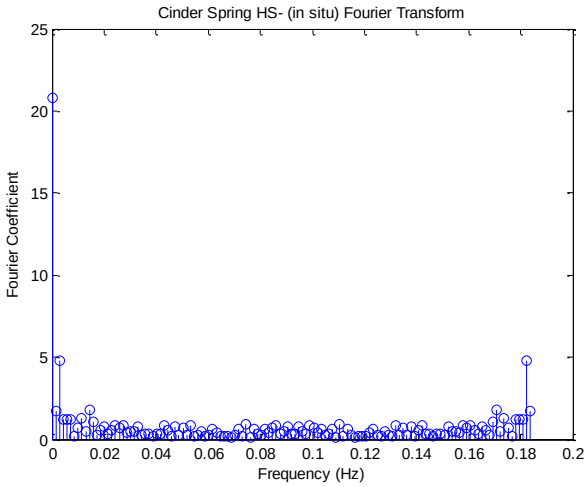

Figure C-9: FFT graph on the temporal sulfide data (in situ) from Cinder Spring, YNP.

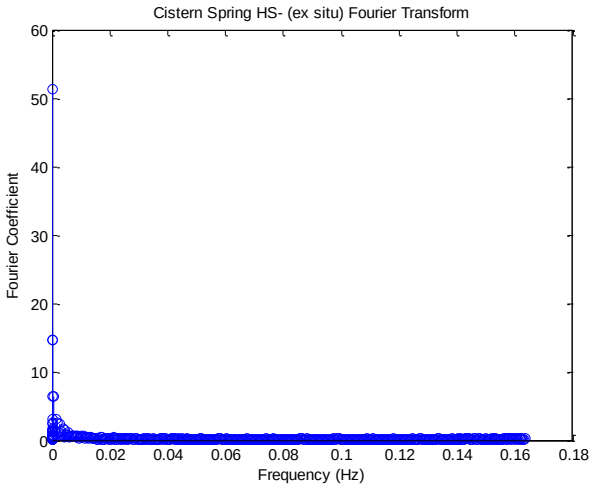

Figure C-10: FFT graph on the temporal sulfide data (ex situ) from Cistern Spring, YNP.

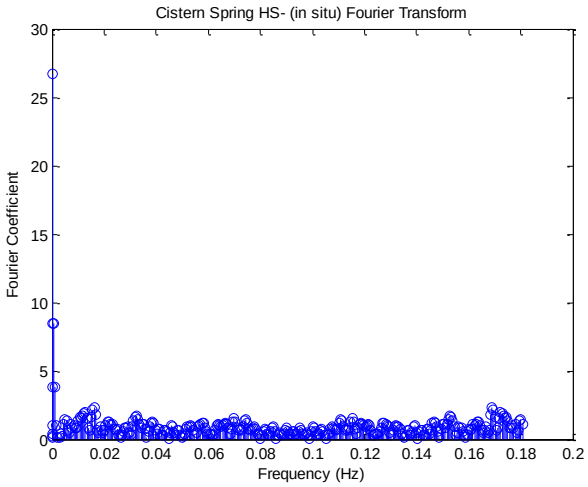

Figure C-11: FFT graph on the temporal sulfide data (in situ) from Cistern Spring, YNP.

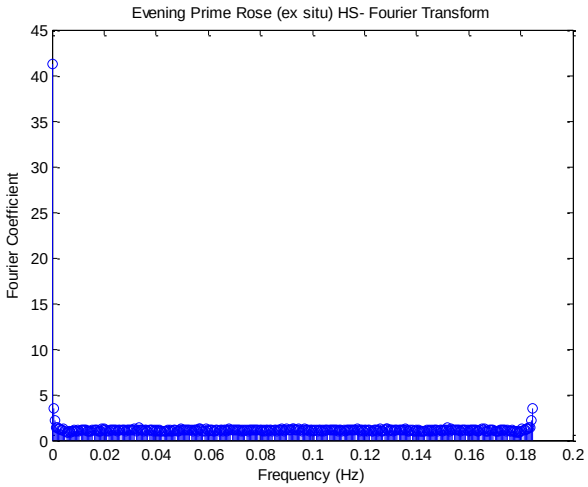

Figure C-12: FFT graph on the temporal sulfide data (ex situ) from Evening Primrose Spring, YNP.

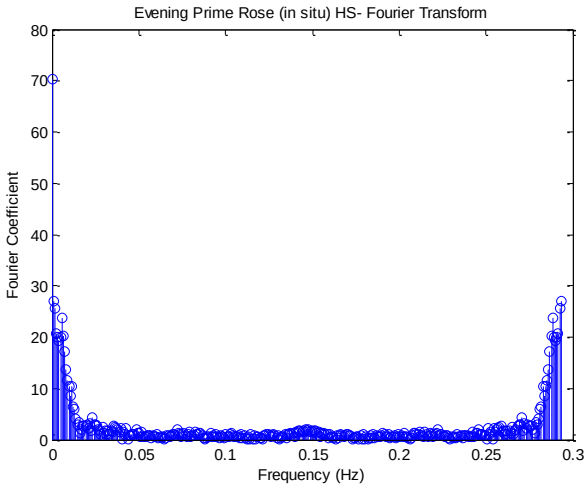

Figure C-13: FFT graph on the temporal sulfide data (in situ) from Evening Primrose Spring, YNP.

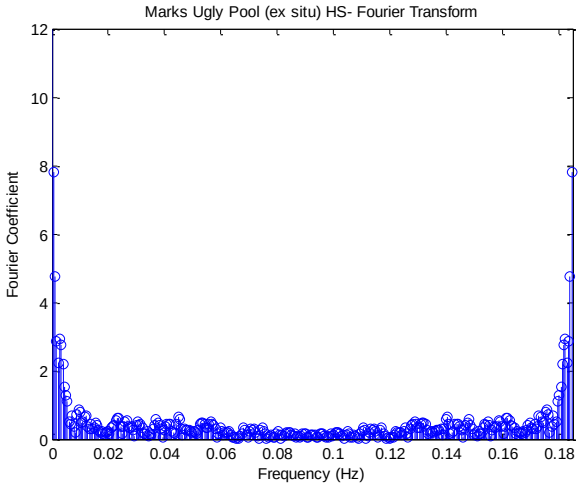

Figure C-14: FFT graph on the temporal sulfide data (ex situ) from Mark's Ugly Spring, YNP.

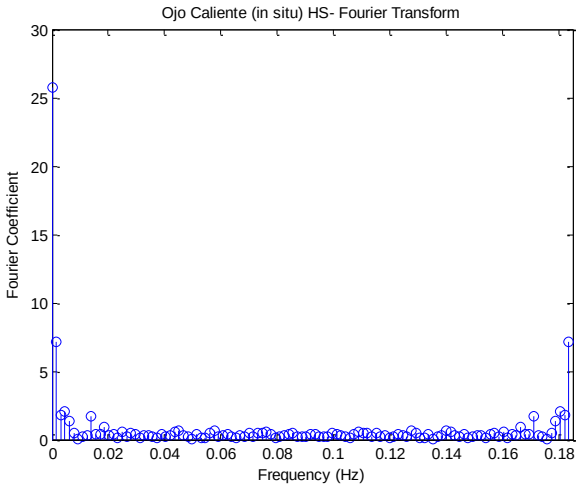

Figure C-15: FFT graph on the temporal sulfide data (in situ) from Ojo Caliente Spring, YNP.

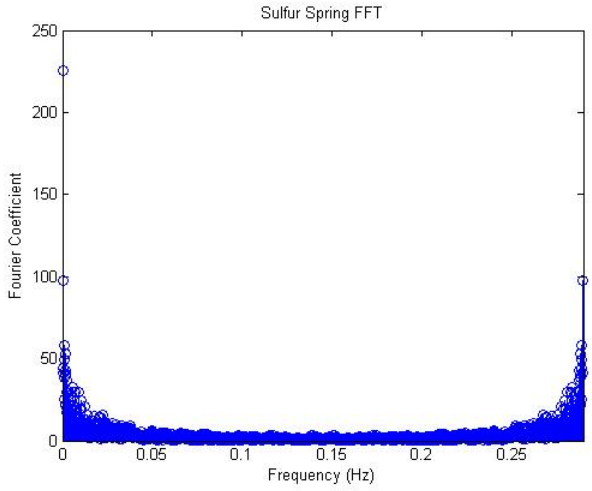

Figure C-16: FFT graph on the temporal sulfide data (ex situ) from Sulfur Spring, YNP.

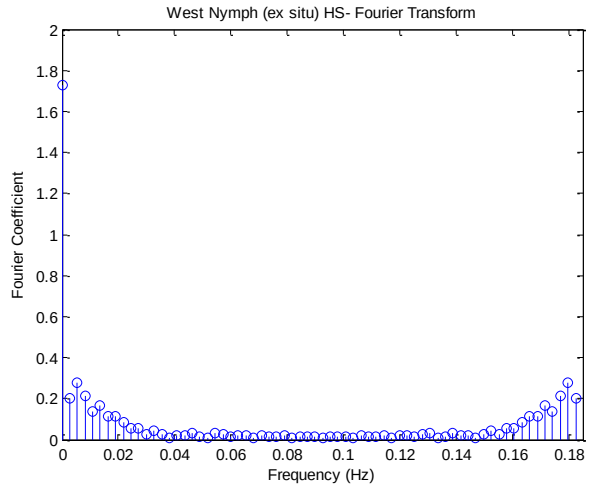

Figure C-17: FFT graph on the temporal sulfide data (ex situ) from West Nymph Spring, YNP.

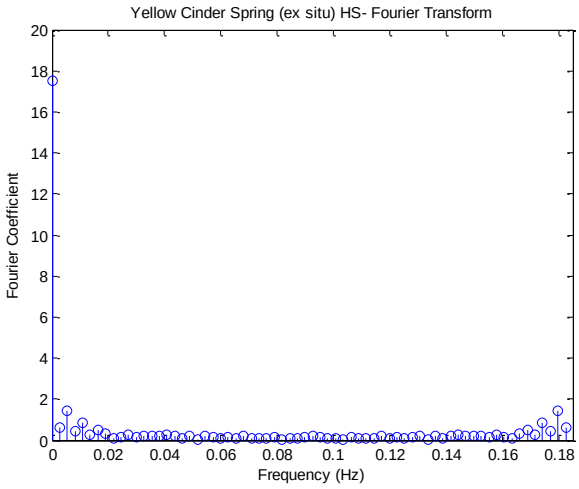

Figure C-18: FFT graph on the temporal sulfide data (ex situ) from Yellow Cinder Spring, YNP.

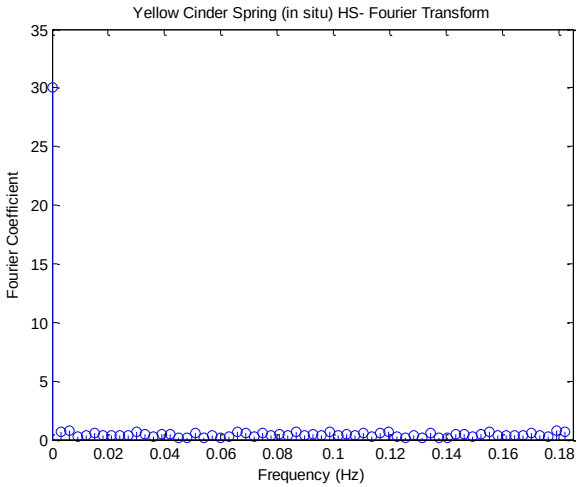

Figure C-19: FFT graph on the temporal sulfide data (in situ) from Yellow Cinder Spring, YNP.

APPENDIX-D – VOLTAMMETRY ELECTRODE ASSESSMENT

This appendix provides information from experiments and calculations related to the effect of bubble stream and fluid flow on the Hg-electrode response. Also the appendix incorporates the calculations of the minimum and maximum values of the spherical volume of analysis of the Hg-surface electrodes utilized in YNP.

Bubble stream effect

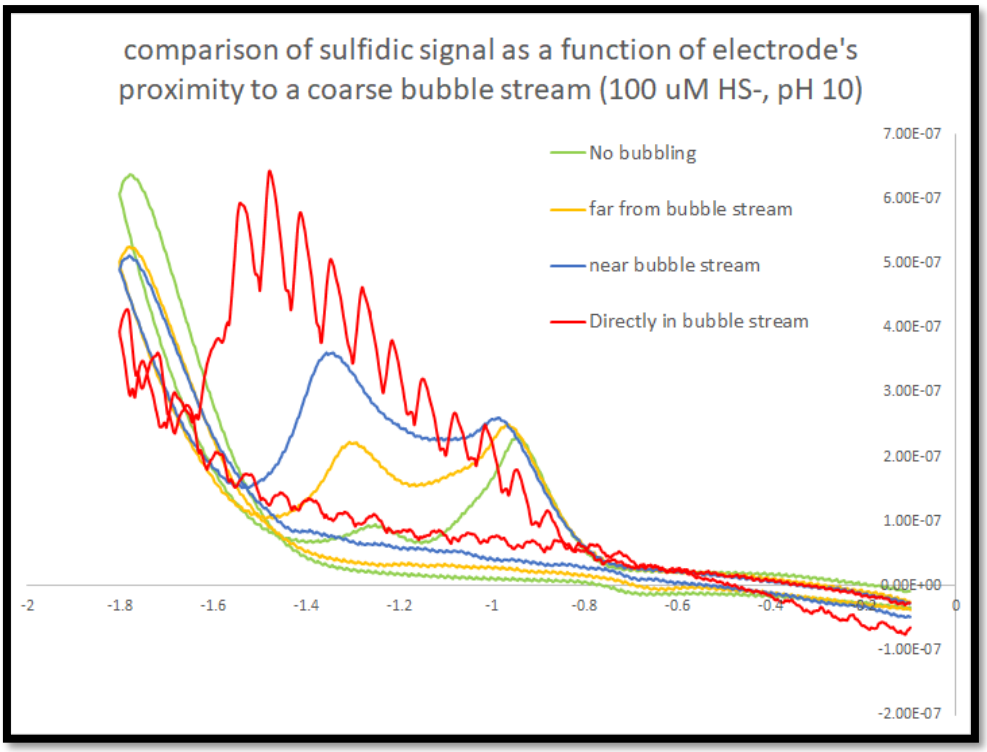

Figure D-1: Voltammetric experiments investigating the influence of the sulfidic signal of a 100µM HS^- solution (pH 10) as a function of the distance from a coarse N2 purging stream.

Fluid flow effect

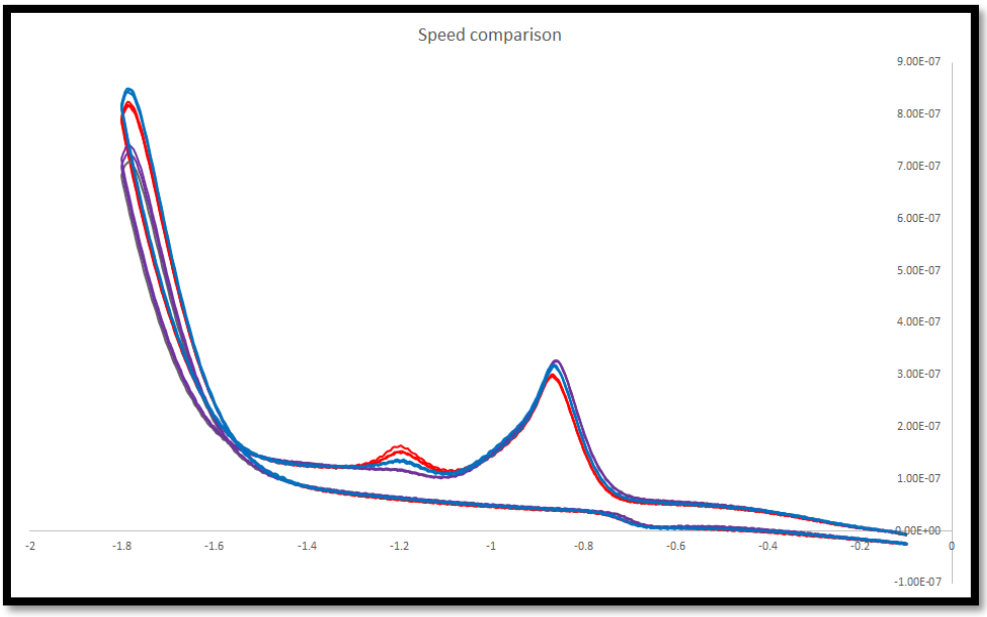

Figure D-2: The figure presents voltammetric experiments assessing the effect of fluid flow on the current response on the Hg-surface electrodes. 100µM HS^- added to degassed Eagle Creek Reservoir Water (22^{o}C). A Masterflex pump was utilized to manipulate the fluid flow in a flow cell system (50ml volume). After calibrations, the fluid flow was determined to be about 1.2 ml/min (fast flow – purple line), and less than 0.1ml/min (low flow – blue line). The red line represents no flow. The flow ratios are similar to flow cell and tubing used in YNP. The elemental sulfur peak increases in time as sulfide peak decreases. Changes in signal more due to oxidation during experiment than to flow changes.

Table D-1: Intensity (A) data from the interpretation of the above figure, as well as calculated percentile variability for each fluid flow rates are presented here.

I (A)	red (NO FLOW)	blue (SLOW)	purple (FAST)
base	3.05E-07	3.17E-07	3.27E-07
peak	7.24E-08	7.90E-08	7.50E-08
intensity	2.33E-07	2.38E-07	2.52E-07
% variability		**2.32%**	**8.34%**

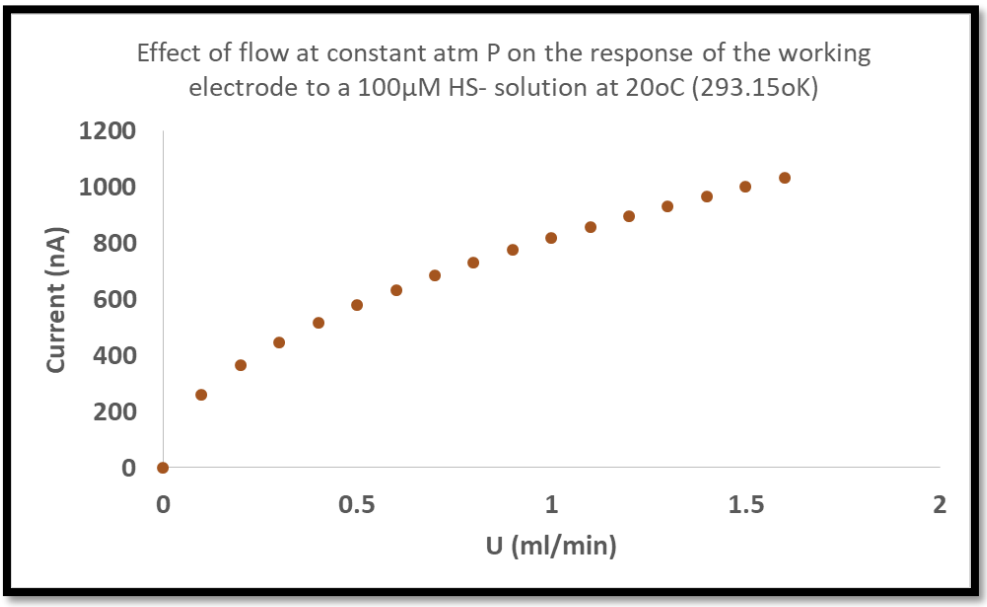

Figure D-3: Levich calculations on the effect of flow on the current of a working electrode are shown. Calculations considered a 100µM HS^- solution at 20^OC.

Table D-2: The table presents the percentile variability of current response of a working electrode as calculated based on the Levich equation, following an increase of fluid flow from 0.1 to 1.2ml/min.

I(nA)	Flow(ml/min)
258	0.1
895	1.2
246.90%	increase from 0.1 to 1.2ml/min fluid flow

Calculations of the spherical volume of analysis

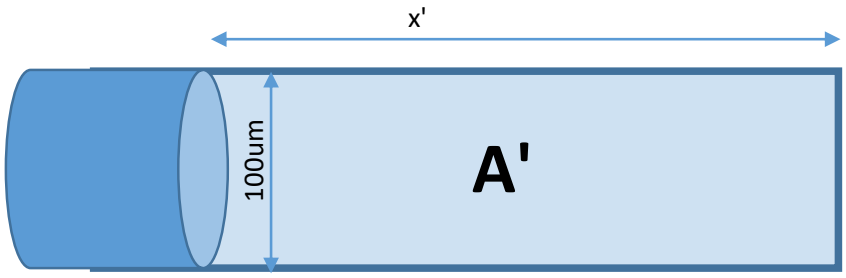

Figure D-4: This figure presents the two-dimensional geometry of the water attached on the surface of the Hg electrode (NOT the 3D geometry of the spherical volume of analysis) that is utilized in the following calculations (Table D-3, Table D-4 and Table D-5) for the estimation of the distance x' that serves as a diameter of the spherical volume of analysis to be calculated.

Table D-3: This "box" incorporates the 1st part of the calculations that took place in order to calculate the maximum and minimum values of the spherical volume of analysis for the Hg-surface electrodes utilized in YNP.

-J	**=**	**i** / **nFA**	**=**	**i** / **(2 * 96485.3 * 7.8539E-09)**	**Coulombs/second** / **(Coulombs/mol)* m^2**	**=**	**i** / **0.001515572**

working electrode	diameter	100	μm =	1.00E-04	m	
working electrode	radius	50	μm =	5.00E-05	m	

A = π * r^2 =	**7853.981634**	μm^2=	**7.85398E-09**	m^2

MAX. AND MIN. VALUES	
Intensity (uA)	**HS- (uM)**
0.463	1430
0.021	26.1

Table D-4: This "box" incorporates the 2nd part of the calculations that took place in order to calculate the minimum value of the spherical volume of analysis for the Hg-surface electrodes utilized in YNP.

(1)	**-J**	=	**i** / **nFA**	=	**0.000000463** / **0.001515588**	Coulombs/second / (Coulombs/mol)* m^2	= **0.0003055**	**mol/sec/m2**		

(2)	in a flux equal to (1) that corresponds to 1429.75uM sulfide we have for 2.3seconds: **0.00030549** mol/sec/m^2 x 2.3 seconds = **0.000702632 mol/m2**

(3)	Converting uM to mol/m3	1430	umol/l	=1.43	umol/ml =	1.43E-06	mol/cm^3 =	**1.42975**	**mol/m3**	

(4)	Dividing (2) by (3) :	0.000703 / 1.42975	mol/m2 / mol/m3	=	4.91E-04	meters or	4**91.7um**	

(5)	Volume, V = 4/3πr3 =	**6.21E+07** **um^3**

Table D-5: This "box" incorporates the 3rd part of the calculations that took place in order to calculate the maximum value of the spherical volume of analysis for the Hg-surface electrodes utilized in YNP.

(1)	**-J**	=	**i** / **nFA**	=	**0.000000021** / **0.001515588**	Coulombs/second = (Coulombs/mol)* m^2	**1.38562E-05**	**mol/sec/m2**

(2)	in a flux equal to (1) that corresponds to 26.10uM sulfide we have for 2.3seconds: 1.38562E-05 mol/sec/m^2 x 2.3 seconds = **3.18692E-05 mol/m2**

(3)	Converting uM to mol/m3:	26.1	umol/l	=0.03	umol/ml =	2.61E-08	mol/cm^3 =	**0.0261**	**mol/m3**

(4)	Dividing (2) by (3) :	3.19E-05 / 0.0261	mol/m2 / mol/m3	=	1.22E-03	meters or	**1221.04um**

(5)	Volume, V = 4/3πr3 =	**9.53E+08**	**um^3**

FOTIOS CHRISTOS KAFANTARIS

Research Interests

- My research focuses on the low temperature geochemistry of redox sensitive elements. I am especially interested in the redox transformations of sulfur, both inorganic and microbial. I am also interested in the influence of S species transformations on the S biogeochemical cycle and its interaction with other cycles, such as of carbon and metals.
- Within my PhD work I have been studying the coarsening processes of elemental sulfur nanoparticles and their nucleophilic dissolution by sulfide, where I have developed expertise on electrochemical, chromatographic, spectrophotometric and spectroscopic measurement techniques.

A. Professional Preparation

December 2017 — INDIANA UNIVERSITY – PURDUE UNIVERSITY INDIANAPOLIS

PhD Major: Applied Earth Sciences

(Advisor: Gregory Druschel)

Current project: Thermodynamics and kinetics of nucleophilic dissolution of elemental sulfur nanoparticles and its implications to sulfur cycling in near surface environments.

PhD Minor: Environmental Health Science

(Advisor: Steven Lacey)

Coursework completed: Environmental Toxicology; Environmental Health Risk Assessment; Air Pollution and the Environment; Environmental Science in Public Health.

September 2010 — IMPERIAL COLLEGE LONDON (UK)

MS in Petroleum Geoscience

Master's Thesis (Advisor: Mark A. Sephton): Organic Geochemistry and Shale Gas Potential of the Lower Carboniferous Black Shales of United Kingdom.

May 2009 UNIVERSITY OF ATHENS (GREECE)
BS Geology and Geo-environmental Studies
Diploma Thesis (Advisor: Athanasios Godelitsas): Mineralogical and Mineral-Chemical Investigation of Geological Materials with Increased Natural Radioactivity from Attica Area, Greece.

B. Positions and Honors

- 2016 IUPUI Graduate Office Travel Fellowship ($1000)
- 2016 Teaching Assistant (Indiana University Purdue University Indianapolis, IN, USA)
- 2012-2017 Research Assistant (Indiana University Purdue University Indianapolis, IN, USA) 2015 Teaching Assistant (Indiana University Purdue University Indianapolis, IN, USA)
- 2012 Geological Society of America Student Grant ($1700)
- 2012 Golden Key Academic Honors Society Student Award
- 2011 Hunt Scholarship for Earth Science Graduate Students ($2000)
- 2011-2012 Research Assistant (University of Texas at El Paso, TX, USA)
- 2010 Research Assistant (Imperial College London, London, UK)
- 2006-2009 Research Assistant (University of Athens, Athens, GR)

C. Research Experience

- 2012-present – Indiana University – Purdue University Indianapolis. Experimental work involving electrochemistry, liquid chromatography, and ion chromatography, utilization of anaerobic chamber for polysulfide chemical synthesis and synchrotron spectroscopies.

- 2011-2012 – University of Texas at El Paso. Experimental work involving microbial culturing and advanced isotope analysis techniques (column separation methods and Multiple-Collector Inductively Coupled Plasma Mass Spectrometry).
- 2009-2010 – Imperial College London. Experimental work in organic geochemistry utilizing Gas Chromatography – Mass Spectrometry and Pyrolysis – Fourier Transform Infrared Spectroscopy.
- 2006-2009 – University of Athens. Experimental work involving Gamma-ray Spectroscopy, X-ray diffraction analysis, Scanning Electron Microscopy, and X-ray Fluorescence Spectroscopy for the characterization of the radioactivity and mineralogy of geological materials.

D. Scientific Products

1. Walczak A. B., **Kafantaris F.-C. A.**, Druschel G. K., Yee N., and Young L. Y. (2016). Transformation of galena to pyromorphite produces bioavailable sulfur for neutrophilic chemoautotrophy. Geobiology. doi:10.1111/gbi.12199 (In press)
2. Wright Miriam C., Court Richard W., **Kafantaris Fotios-Christos A.**, Spathopoulos Fivos, and Sephton Mark A. (2015). A new rapid method for shale oil and shale gas assessment. Fuel. 153: 231-239.
3. Gilhooly William P., Fike David A., Druschel Gregory K., **Kafantaris Fotios-Christos A.**, Price Roy E., and Amend Jan P. (2014). Sulfur and oxygen isotope insights into sulfur cycling in shallow-sea hydrothermal vents, Milos, Greece. Geochemical Transactions. 14:12 (open access e-version only).
4. **Kafantaris Fotios-Christos A.** and Borrok David M. (2014). Zinc isotope fractionation during surface adsorption and intracellular incorporation by bacteria. Chemical Geology. 366: 42-51.

E. Selected Conference Contributions

1. Kafantaris F.-C. A., and Druschel G. (2017) "Geochemical Kinetics of Polysulfide Formation" Goldschmidt Conference, August 13-18 2017, Paris, France.
2. Kafantaris F.-C. A., Kurek M., Druschel G., Gilhooly III, W., Dvorski S. and Schmitt-Kopplin P. (2016) "Polysulfides reactivity and its role in cryptic sulfur cycling in

anoxic/euxinic basins". 2017 GSA Joint Northeastern/North-Central Section Meeting 19-21 March 2017, Pittsburgh PA (oral)

3. Kafantaris F.-C. A. and Druschel G. K. (2016) "Polysulfides reactivity and its role in sulfur cycling and sulfur-carbon interactions". AGU Fall Meeting Abstracts, 12-16 December 2016, San Francisco CA (oral)
4. Kafantaris F.-C. A., Druschel G., Dvorski S., Schmitt-Kopplin P. and Hu Y. (2015) "Reactivity of elemental sulfur nanoparticles and their role on the biogeochemical cycling of sulfur". 2015 GSA Annual Meeting, , November 1-4 2015, Baltimore, MA (oral)
5. Kafantaris F.-C. A. and Druschel G. K. (2014) "Reactivity of elemental sulfur nanoparticles and their role on the formation of sulfur intermediates". AGU Fall Meeting Abstracts, 15-19 December 2014, San Francisco CA (poster)
6. F.-C. A. Kafantaris, E.J. Crane III, E. Boyd and G. K. Druschel (2013) "Role of elemental sulfur size and surface character on the speciation and bioavailability of sulfur" In: 246th ACS National Meeting & Exposition, Indianapolis, IN (oral)
7. F.-C. A. Kafantaris, E.J. Crane III, and G. K. Druschel. (2013) "Geochemical dynamics in Yellowstone Springs: Sulfur chemistry changes at seconds-scale temporal resolution." In: 245th ACS National Meeting & Exposition, New Orleans, LA. Abstracts of Papers of the American Chemical Society. Vol. 245. 1155 16th St. NW, Washington DC 20036 USA: Amer Chemical Soc, 2013 (oral)
8. F.-C. Kafantaris and D. M. Borrok. (2012) "Zinc isotope fractionation during metabolic uptake by bacteria", Goldschmidt Conference, Jun. 24-29, Montreal, CA (oral)
9. D. M. Borrok, J. U. Navarrete, F.-C Kafantaris (2012) "A model for copper isotopic fractionation during weathering and transport", 2012 Goldschmidt Conference, Jun. 24-29, Montreal, CA (Keynote)
10. F.-C. Kafantaris and D. M. Borrok (2011) "Zinc isotope fractionation during surface adsorption by bacteria", 2011 American Geophysical Union Meeting, Dec. 5-9, San Fransisco, CA, USA, Abstract No B54D-02 (oral)